Development of atomistic and concurrent atomistic-continuum frameworks to model shock wave propagation and phonon transmission

by

Alexander S. Davis

A dissertation submitted to the Graduate Faculty of
Auburn University
in partial fulfillment of the
requirements for the Degree of
Doctor of Philosophy

Auburn, Alabama
May 6, 2023

Keywords: shock waves, moving window, molecular dynamics, atomistic-continuum, multiscale modeling

Approved by

Vinamra Agrawal, Assistant Professor of Aerospace Engineering
Russell Mailen, Assistant Professor of Aerospace Engineering
Suhasini Gururaja, Assistant Professor of Aerospace Engineering
Shuai Shao, Assistant Professor of Mechanical Engineering
Jeffrey Lloyd, Senior Research Scientist at the Army Research Laboratory
George Flowers, Dean of the Graduate School

Abstract

This dissertation is broadly divided into four primary topics which build upon each other and represent the main projects I worked on during my PhD. Furthermore, this work resulted in four peer-reviewed articles published in three different high-impact scientific journals – namely, *Computer Methods in Applied Mechanics and Engineering*, *Computational Materials Science*, and *Computational Mechanics*. The references for those papers are as follows: [1, 2, 3, 4]. I am extremely grateful for being given the opportunity to pursue this research while at Auburn.

In the first part of this dissertation, we develop a long-time moving window framework using Molecular Dynamics (MD) to model shock wave propagation through a one-dimensional monatomic chain. The moving window formulation follows the propagating shock front allowing us to model shock wave propagation much longer than conventional non-equilibrium MD (NEMD) simulations. This formulation also significantly decreases the required domain size and thus reduces the overall computational expense. The domain is divided into a purely atomistic *window* region containing the shock front flanked by boundary regions on either end which incorporate continuum shock conditions. Spurious wave reflections are removed by employing a damping band method using the Langevin thermostat applied locally to the particles in each boundary region. The moving window effect is achieved by adding/removing atoms to/from the window and boundary regions, and thus the shock wave front is focused at the center of the window region indefinitely. We simulate the shock through a one-dimensional monatomic chain using either the Lennard-Jones, modified Morse, or Embedded Atom Model (EAM) interatomic potential. We first perform verification studies to ensure proper implementation of the thermostat, potential functions, and damping band method, respectively. Next, we track the propagating shock and compare the actual shock velocity and average particle velocity to their corresponding analytical input values. From these comparisons, we optimize the linear shock Hugoniot relation for the given "lattice" orientation and compare these results to those in literature. When incorporated into the linear shock equation, these new Hugoniot parameters

are shown to produce a stationary wave front. Finally, we perform one-dimensional moving window simulations of an unsteady, structured shock up to a few nanoseconds and characterize the increase in the shock front's width.

While atomistic methods have successfully modeled different aspects of shock wave propagation in materials over the past several decades, they nevertheless suffer from limitations which restrict the total runtime and system size. Multiscale methods have been able to increase the length and time scales that can be modeled but employing such schemes to simulate wave propagation and evolution through engineering-scale domains is an active area of research. In the next part of this dissertation, we develop two distinct moving window approaches within a Concurrent Atomistic-Continuum (CAC) framework to model shock wave propagation through a one-dimensional monatomic chain. In the first method, the entire CAC system travels with the shock in a conveyor fashion and maintains the shock front in the middle of the overall domain. In the second method, the atomistic region follows the shock by the simultaneous coarsening and refinement of the continuum regions. The CAC and moving window frameworks are verified through dispersion relation studies and phonon wave packet tests. We achieve good agreement between the simulated shock velocities and the values obtained from theory with the conveyor technique, while the coarsen-refine technique allows us to follow the propagating wave front through a large-scale domain. This work showcases the ability of the CAC method to accurately simulate propagating shocks and also demonstrates how a moving window technique can be used in a multiscale framework to study highly nonlinear, transient phenomena.

The one-dimensional CAC shock wave studies demonstrate how coupled atomistic-continuum methods can describe large domains and model dynamic material behavior for a much lower computational cost than traditional atomistic techniques. However, these multiscale frameworks suffer from wave reflections at the atomistic-continuum interfaces due to the numerical discrepancy between the fine-scaled and coarse-scaled models. Such reflections are non-physical and may lead to unfavorable outcomes such as artificial heating in the atomistic region. In the third part of this dissertation, we develop a technique to allow the full spectrum of phonons to be incorporated into the coarse-scaled regions of a periodic concurrent atomistic-continuum (CAC) framework. This scheme tracks phonons generated at various time steps and

thus allows multiple high-frequency wave packets to travel between the atomistic and continuum regions. Simulations performed with this method demonstrate the ability of the technique to preserve the coherency of waves with a range of wavevectors as they propagate through the domain. This work has applications for systems with defined boundary conditions and may be extended to more complex problems involving waves randomly nucleated from an impact within a multiscale framework.

While the one-dimensional CAC moving window framework produced some very noteworthy results, the physical applications of this framework are limited because a 1D domain cannot support dislocations or transverse atomic motion. Thus, in the fourth part of this dissertation, we develop a two-dimensional CAC formulation to model shock wave propagation through a single-crystal lattice for long simulation times. To achieve this, we develop sophisticated algorithms for the boundary conditions, neighbor lists, governing equation, and parallelization scheme. Additionally, since shearing effects can modify atomic behavior in a two-dimensional system, we also implement Gaussian integration in order to obtain more accurate forces. We incorporate moving window methods to track an elastic shock for several nanoseconds, and such methods require advanced numerical techniques to dynamically coarsen/refine atomic planes. We compare our simulation results to analytical models as well as previous atomistic and CAC data and discuss the apparent effects of lattice orientation on the shock response of two FCC crystals. We then use the moving window techniques to perform parametric studies which analyze the shock front's structure. Finally, we compare the efficiency of our model to MD simulations. This two-dimensional work showcases the framework's capability for simulating dynamic shock evolution over long runtimes and opens the door to more complex studies involving shock propagation through composites and alloys.

In the Conclusion of this dissertation, we provide a summary of the aforementioned research endeavors and review their contributions to the broader scientific community. Additionally, we discuss our current work which involves modeling the behavior of medium entropy alloys using a large-scale, three-dimensional CAC framework.

Acknowledgments

First and foremost, I want to thank the Lord Jesus Christ for His unending love and grace, and without Whom, all of my accomplishments would be meaningless. My Catholic faith has been a continual source of joy while pursuing my academic goals, and I would like to thank my spiritual mentors at St. Michael's Catholic Church for always encouraging me to be humble, see life as a gift, and show kindness to everyone.

I could not have accomplished all of the work in this dissertation without the support and intellectual contributions of my advisor, Dr. Vinamra Agrawal, whose excellent guidance and persistent encouragement during my six years at Auburn contributed enormously to my research interests as well as my professional development. Dr. Agrawal, thank you so much for always pushing me to set and achieve high goals in scientific research – you made my PhD experience very memorable and rewarding. Additionally, I would like to thank my dissertation committee for their valuable inputs in these different projects: Dr. Russell Mailen, Dr. Suhasini Gururaja, Dr. Shuai Shao, and Dr. Jeffrey Lloyd. In particular, I am grateful to Dr. Lloyd for his considerable mentorship and instruction since my internship at the Army Research Lab during the summer of 2021. I would also like to thank my other mentors/collaborators at the Army Research Lab for providing extensive feedback on my work and guiding me towards my career goals: Dr. Betsy Rice and Dr. John Clayton. Finally, I would like to thank the professors I have had during graduate school who have really shown a passion for their subject matter and desired excellence in their students: Dr. Stephen Nichols, Dr. Joseph Majdalani, Dr. David Scarborough, Dr. Pradeep Lall, Dr. Hareesh Tippur, and Dr. Hans-Werner van Wyk.

I have made so many friends at Auburn (both inside and outside of school) who have encouraged me in my work but also brought me back down to earth when my head was full of equations, and I would just like to mention a few of them here: Roberto Perera, Midhan Siwakoti, Sam and Hannah Kawell, Yaeji Kim, Miles Blanchet, William and Kristen Priola, Ben and Lindsay Wisehaup, Evan and Ashton Stegner, Amanda Crutchfield, and Peyton Plessala.

My parents, siblings, and in-laws have also shown me so much support during these intense years, and I will never be able to fully repay them for their enduring love and encouragement: Steve and Amanda Davis, Mallory and Dom Zelenak, Ryan and Stephanie Wellman, Tom and Martha Benton, Isabella Benton, and Hart and Loryn Benton. Mom and Dad, the amount of love and encouragement you have given me throughout my entire life is unfathomable. I could not have asked for better parents, so from the bottom of my heart, thank you. Finally, I want to thank my wife Olivia for her patience and unceasing love throughout our journey so far. The most awe-inspiring moment I experienced during my graduate school years was watching our son Alexander being born during the midst of Covid-19 in September of 2020. I dedicate this dissertation and all the work I accomplished while pursuing my PhD to my wife and son.

This dissertation is based upon work supported by the National Science Foundation under Grant No. 1950488. Financial support was also provided by the U.S. Department of Defense through the National Defense Science and Engineering Graduate (NDSEG) Fellowship Program (F-1656215698). Simulations were performed using the Hopper and Easley computing clusters at Auburn University.

Table of Contents

List of Figures

List of Tables

List of Abbreviations

A-Atom	Average-Atom
A-C	Atomistic-Continuum
AFT	Atomistic Field Theory
Ag	Silver
Al	Aluminum
BD	Bridging Domain
BSM	Bridging Scale Method
CA	Continuum Atoms
CAC	Concurrent Atomistic-Continuum
CADD	Coupled Atomistic Discrete Dislocation
CLS	Coupling of Length Scales
CMM	Consistent Mass Matrix
Cu	Copper
DD	Dislocation Dynamics
DOF	Degree of Freedom
EAM	Embedded Atom Model

EOS Equation of State

FCC Face-Centered Cubic

FEM Finite Element Method

HEA High-Entropy Alloy

HEL Hugoniot Elastic Limit

IK Irving-Kirkwood

LAMMPS Large-Scale Atomic/Molecular Massively Parallel Simulator

LD Lattice Dynamics

LMM Lumped Mass Matrix

MD Molecular Dynamics

MEA Medium-Entropy Alloy

ML Machine Learning

MSST Multi-Scale Shock Technique

NEMD Non-Equilibrium Molecular Dynamics

Ni Nickel

QC Quasicontinuum

QH Quasi-Harmonic

SWF Shock Wave Front

TR Thermostat Region

WA Window Atoms

WR Window Region

Chapter 1

Introduction

1.1 Motivation

The behavior of shock waves in solids is an important scientific phenomenon that has been extensively studied for many decades; see, for example, [11, 21] and the references therein. Typically, a propagating shock occurs in a material under high strain rate loading conditions such as a high speed impact and can be fully characterized by the continuum governing equations. However, the shock response of a material at any length scale is inextricably linked to effects at lower length scales. At the macroscale, shock waves can lead to damage, plastic deformation, and fracture of the material. Figure 1.1 gives a schematic representation of spallation induced from a shock wave impact.

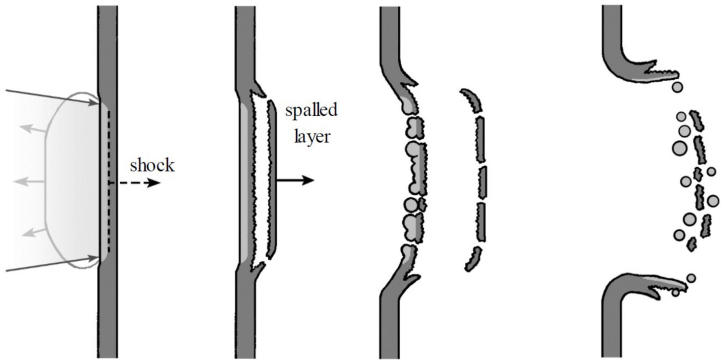

Figure 1.1: Partial melting, subsequent spall fracture, and debris ejection in laser shock-loaded iron. Pale grey represents molten metal [5][1].

[1]Reprinted from *Metals*, vol. 4, no. 4; T. De Rességuier, D. Loison, A. Dragon, and E. Lescoute; "Laser driven compression to investigate shock-induced melting of metals," pp. 490-502, 2014. Open access article. Figure obtained with permission from the terms and conditions of the Creative Commons Attribution license.

Phenomena such as spall fracture result from processes that occur at the microscale in which shocks interact with the microstructure and cause complex behavior such as scattering, grain rotations, pore collapse, phase transformations, dislocations, void generation, and grain crushing [22, 23, 24]. Fig. 1.2 shows dislocation lines generated during shock deformation in an atomistic simulation performed with LAMMPS (Large-scale Atomic/Molecular Massively Parallel Simulator).

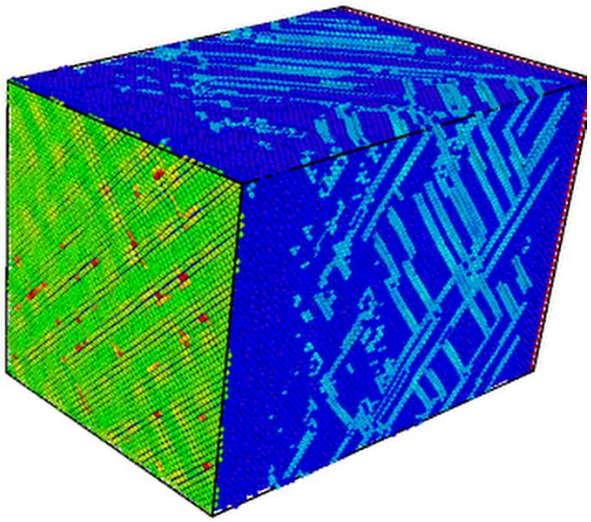

Figure 1.2: Image taken during a LAMMPS simulation of a piston-driven shock loaded along the [100] direction of a single-crystal copper lattice.

Very often, studies which examine shock wave propagation through a solid rely on *the continuum hypothesis*. This hypothesis says that materials are "composed of an infinitely divisible continuous medium, imbued with a constitutive behavior that remains unchanged regardless of how small the structure of interest may be" [25]. Although it conflicts with the atomic theory of matter, this assumption is valid for most practical engineering applications and greatly reduces the complexity of a system subjected to a shock wave impact. Additionally, this hypothesis allows one to represent a physical system in terms of continuum field theories such as the theory of elasticity or plasticity. Therefore, with this premise, shock waves can be described completely by the conservation of mass, momentum, and energy – often referred to as the Rankine-Hugoniot equations [26, 27].

The continuum hypothesis becomes insufficient, however, when a material's response to a given load depends on effects at the atomic scale as such effects cannot be incorporated

into the continuum model. This is especially true for damage and fracture that result from shock wave propagation as such macroscale phenomena are implicitly governed by microscale processes. Therefore, in order to fully understand shock waves at the continuum level, one must also be able to model and characterize them at the atomic level. However, atomistic shock simulations can suffer from, among other things, wave reflections due to limited domain sizes which drastically reduce the total runtime. The present work attempts to overcome these drawbacks by first developing a moving window atomistic framework to follow a propagating shock wave through a material. Such a framework facilitates very long-time simulations and thus permits a detailed study of the shock Hugoniot and shock front structure.

While contemporary atomistic methods have been very successful in modeling shock wave propagation and characterizing how defects influence shock behavior, even the largest benchmark simulations fall short of capturing continuum-level phenomena such as shock wave boundary layer interactions and the resulting scattered elastic waves. This is because limited computational resources restrict the total number of atoms that can realistically be incorporated into a microscale framework. Although computer processing power increases over time, physical limitations on computer architecture imply that simulations which model continuum events using purely atomistic techniques may never be possible.

Therefore, a *multiscale* scheme is needed which would be able to track a moving shock wave for a long time over a large domain as well as capture a shock's interaction with phonons and microstructural interfaces. Such a framework would locally retain atomistic information around a small region of interest (i.e. the shock wave front) and transition to continuum length scales throughout the rest of the domain. An example of such a multiscale framework can be seen in Fig. 1.3. Typically, the microscale domain is modeled using Density Functional Theory (quantum mechanics) or Molecular Dynamics (atomistics), and the continuum domain is modeled using finite element or finite volume techniques. The present work also expands the initial moving window atomistic scheme into a fully-coupled multiscale framework using the Concurrent Atomistic-Continuum (CAC) method to model realistic shock wave propagation through a material.

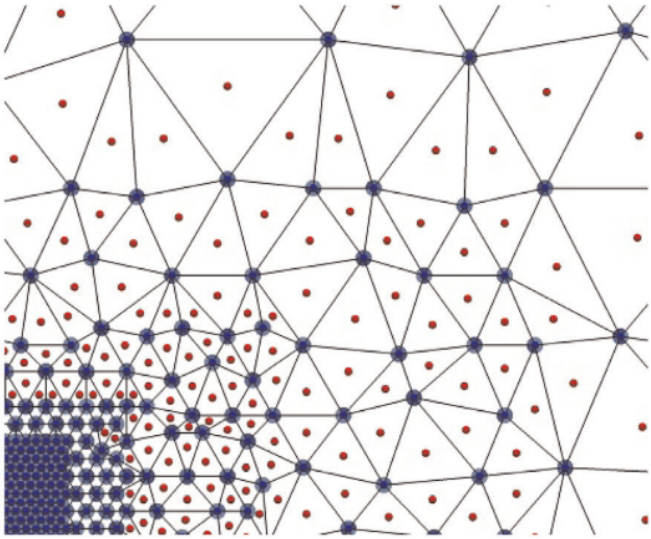

Figure 1.3: Non-uniform two-dimensional multiscale grid that is gradually coarsened around an atomistic core in the bottom left corner [6][2].

1.2 Atomistic framework

1.2.1 A brief history of NEMD shock wave simulations

For an in-depth insider analysis of the history of atomistic shock wave modeling up until 1993, please see [28]. Here, we provide a terse summary of that history and briefly discuss some of the advances made in the past three of decades since then.

One of the most powerful computational methods to simulate the motion of an atomistic system is Molecular Dynamics (MD). First invented in the mid 1950s by Alder and Wainwright [29, 30], MD uses classical Newtonian mechanics to describe a system of many interacting particles. In contrast to Monte Carlo, MD is capable of simulating the real-time evolution of an arrangement of atoms, including arrangements which exhibit non-equilibrium behavior [28]. As a result, MD is very effective at modeling shock wave propagation, and the most ubiquitous simulation technique for shocks is known as non-equilibrium MD (NEMD). NEMD shock simulations typically load the material using a flyer plate or moving piston, and they have been used over the past sixty years to study the mechanisms behind shock wave propagation at the microscale.

[2]Reprinted from *Journal of the Mechanics and Physics of Solids*, vol. 82; J.S. Amelang, G.N. Venturini, and D.M. Kochmann; "Summation rules for a fully nonlocal energy-based quasicontinuum method," pp. 378-413, 2015. Obtained with permission from Elsevier.

In fact, the first NEMD simulation of a shock-like event was performed by George Vineyard and his coworkers at Brookhaven National Laboratory in 1960 [31]. In this work, Vineyard simulated the radiation-damage cascade of 500 particles in a single-crystal copper lattice. All the computations were performed on an IBM 704 computer as seen in Fig. 1.4. Due to the limited number of atoms, the magnitude of the shock wave reflection once it reached the lattice surface had to be reduced. Vineyard accomplished this by applying a critical damping to the surface atoms, thus developing the first MD simulation to incorporate an "elastic-continuum" outflow boundary condition. The contributions of Vineyard and his research group in [31] laid the groundwork for the incorporation of finite central difference integration algorithms into MD, something which would not be formalized until 1967 by Verlet [32].

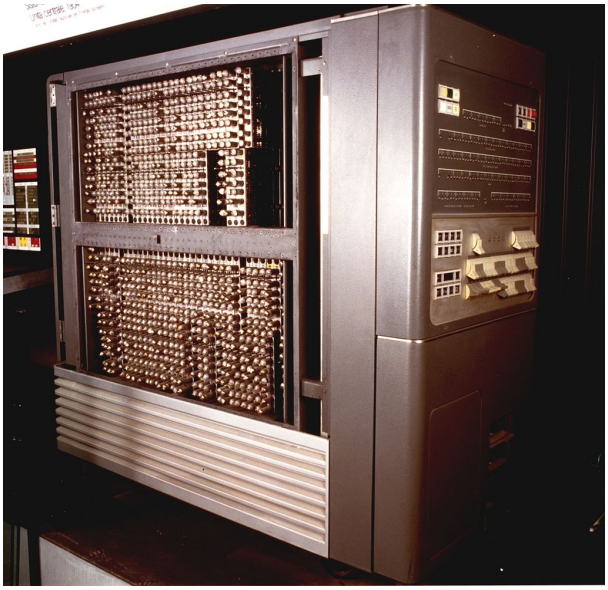

Figure 1.4: IBM 704 at the National Museum of Science and Technology, Milan[3].

The first study to use a continuous potential in MD to model a planar one-dimensional shock wave in a semi-infinite cubic lattice was performed in 1966 by Tsai and Beckett [33]. In this work, they constrained every atomic plane to move rigidly in the shock direction and justified this by saying that an exact balance of the transverse forces from neighboring atoms followed from lattice symmetry. As a result, their model could not account for transverse plastic flow or temperature equilibration, and hence their cubic lattice was equivalent to a semi-infinite,

[3]Open access figure. Museo della Scienza e della Tecnologia "Leonardo da Vinci", CC BY-SA 4.0, https://creativecommons.org/licenses/by-sa/4.0, via Wikimedia Commons.

one-dimensional chain of atoms. They found that although the shock velocity increased linearly with particle velocity (in qualitative agreement with the linear shock Hugoniot), the thickness of the shock front was not constant, and thus the shock wave profile was unsteady in time. These results called into question the validity of the shock Hugoniot equation of state (EOS) because the Hugoniot relations which use the conservation of mass, momentum, and energy to relate unshocked and shocked material depend implicitly on the manifestation of a steady wave.

To study this phenomenon further, George Duvall and his students published a series of papers in the late 1960s where they used MD to simulate shock propagation through a one-dimensional chain of particles [34, 35, 36]. In these works, they constrained all lattice points to move along the direction of shock propagation such that transverse waves could not arise. They observed that the particle velocities exhibited steady behavior (consistent with the Rankine-Hugoniot jump conditions for a continuum), but the thickness of the shock continually increased with time. They explained these findings by saying that in a nonlinear lattice which exhibits both frequency and amplitude dispersion, small changes propagate at different group speeds, so the region influenced by such changes increases linearly with time. These results seemed to concur with the findings in [33] thus causing further doubt about the effectiveness and legitimacy of the linear shock Hugoniot EOS.

To provide some clarity about this issue, Paskin and Dienes produced a paper in 1972 where they used MD to study realistic shock waves in a three-dimensional Lennard-Jones system [37]. In contrast to the earlier studies, however, Paskin and Dienes used larger piston velocities and thus produced stronger shock waves. They found that the Hugoniot for a shock propagating along the [100] direction of an FCC lattice was approximated by a linear relationship between shock velocity (U_S) and particle velocity (v): $U_S = C_0 + Sv$. Here, C_0 is the sound velocity in the material at zero stress, and S is the ratio of shock velocity to particle velocity. Additionally, they observed that the shock wave profile was steady. Paskin and Dienes performed several more MD studies after this initial work which seemed to confirm the steady nature of shock waves [38, 39, 40], but unfortunately they did not have the computational capability to study the structures produced by the propagating shock. Therefore, the mechanism

responsible for this phenomenon was not established, and the explanation as to why their results differed from those of earlier MD shock simulations was incomplete.

Since the equations of motion used in MD depend explicitly on the conservation equations of mass, momentum, and energy, the validity of the Hugoniot EOS in MD shock simulations centered on the steadiness of the shock wave. This controversy was finally resolved by Holian and Straub at Los Alamos National Lab in the late 1970s [41, 42]. Specifically in [42], they simulated shock waves in three-dimensional solids and observed that as the shock strength increased, the shock wave thickness transitioned from a regime of linear growth to a finite width (steady wave) when the initial temperature was nonzero. Therefore, the transition from unsteady to steady waves in three-dimensional lattices for shocks above a critical strength was found to be due to the "increase in coupling between vibrational excitations normal and transverse to the direction of shock wave propagation" [42]. Transverse atomic motion, which was explicitly neglected in the earlier work of Tsai and Beckett, was thus found to be the key to steady wave behavior in three-dimensional lattices [28]. Holian and Straub concluded that linear growth in shock thickness occurs for weak shocks in a "1D regime," and such phenomena should not be used as a basis for questioning the classical Hugoniot relations.

Straub and Holian expanded upon these findings in 1980 by performing MD simulations of an intermediate-strength shock wave in a perfect crystalline solid [43]. They discovered that, for low piston velocities, the propagating shock wave did not induce any plastic deformation in the material. Furthermore, for shocks produced with higher piston velocities (strong shocks), the wave train actually had two components: a fast-moving elastic wave which loaded the material and a slower-moving plastic wave. This "two-wave" phenomenon allowed them to understand the mechanisms behind shock-induced plastic deformation in great detail. However, because of limited computational capacity, they could not decipher the relationship between threshold shock strength and crystal yield strength. After the rapid increase in computing power during the subsequent decade, more studies were performed in the late 1980s and early 1990s which further characterized the difference between weak and strong shocks, formalized the mechanisms behind plastic wave behavior in solids, and investigated the shock Hugoniot and underlying kinetic relations [12, 44, 45, 46, 47, 48, 49].

The power of using extremely large-scale NEMD simulations to model plasticity induced by shock waves in solids was fully exhibited by Holian and Lomdahl in 1998 [19]. In this work, the group modeled shock wave propagation through an FCC cubic crystal consisting of 10 million atoms and showed that dislocations were produced throughout all available slip planes along the nonplanar shock front. These NEMD simulations were some of the first to showcase the complex nanostructure produced by strong shock waves, and they eliminated the possibility that slippage was merely an artifact of periodic boundary conditions. Additionally, their work suggested that defects present in an otherwise undisturbed material could generate transverse motion and hence plasticity once the shock wave propagated through them. Finally, this 10 million atom NEMD simulation showed that, in principle, such frameworks could be used to bridge length scales between the micro and macro world and thus inform continuum constitutive models.

In the past two decades, NEMD shock simulations have been expanded to very large-scale domains and used to model increasingly complex events [13, 50, 51, 52, 53, 54, 55, 56, 57, 58]. These simulations typically involve several millions of atoms ($\sim O(10^5 - 10^9)$) subjected to flyer-plate loading scenarios. Such simulations have been used to study void nucleation [55, 58, 59], dislocation generation [51, 60, 61, 62], twinning [63, 64, 65], and shock-induced spallation [53, 56, 66, 67, 68, 69]. However, because of limited domain sizes, NEMD shock methods still suffer from wave reflections off the domain boundary. Such incidents lead to transient effects and drastically reduce the total runtime. Additionally, NEMD shock simulations typically result in unrealistic strain rates ($10^{10} - 10^{12}\, s^{-1}$) [11]. Such strain rates are rare and orders of magnitude higher than those observed in experiments and practical scenarios ($10^6 - 10^8\, s^{-1}$).

1.2.2 Alternative atomistic techniques for shock wave modeling

To overcome some of the drawbacks with traditional NEMD methods, alternative atomistic frameworks have been developed since the early 2000s to model shock wave propagation. The first of these schemes is known as the *uniaxial Hugoniostat* [70, 71, 72, 73]. Initially proposed in 2000, the uniaxial Hugoniostat is an equilibrium MD method designed to reproduce the final

state of a shocked crystal. It achieves this by compressing the crystal instantaneously to its shocked state which is determined by the continuum governing equations. Then, the material is coupled to a thermostat which guarantees that the final Hugoniot state is reached. This method has been shown to replicate the shock Hugoniot curve as well as exhibit the dislocations and slip planes that are generated by a propagating shock. The uniaxial Hugoniostat is a very effective method for studying the state of a material in the aftermath of a shock wave, and it is an order of magnitude less computationally demanding than traditional NEMD simulations. Unfortunately, because this technique merely reproduces the final shocked state in the domain, the study of a shock's steadiness and structure as well as its interaction with defects is limited.

Another atomistic method which actually performs long-time shock wave simulations in the computational domain is the *Multi-Scale Shock Technique* (MSST) [74, 75]. Developed in 2003, MSST models shock wave propagation by combining MD with the one-dimensional Euler equations for compressible flow. As a result, MSST can simulate multiple shock waves that originate from material instabilities in the atomistic framework. In contradistinction to NEMD methods, MSST can perform dynamical simulations of propagating shock waves for very long runtimes ($\sim$ 5 ns). MSST is an extremely useful and robust method for atomistic shock wave modeling, and it has even been implemented into LAMMPS in recent years. However, while this technique permits the shock to be controlled based on prescribed continuum constraints, it does not allow information such as defects and heat to be transferred between atomistic and continuum regions. Therefore, the scalability of MSST to a fully-coupled atomistic-continuum scheme is restricted.

The final technique for simulating shock waves at the microscale could be broadly referred to as the *moving window method* [76, 77]. First formulated in 1997, this technique shifts the boundary conditions of the domain such that one is able to study a stationary wave front. To accomplish the shifting effect, a constant flux of material with a given density and velocity is fed into the simulation window by inserting a plane of atoms into the right boundary at regular time intervals. Local atomic energy fluctuations induced near the right boundary of the domain by the addition of atoms are dampened by a Langevin thermostat which is applied to each particle in a stadium region near the boundaries. The material flux through the computational domain

is automatically conserved once a stationary shock front is achieved. This method is able to examine the complex processes that occur behind the shock wave front indefinitely without continually inserting new atoms into the simulation cell. However, the scheme developed in [76] and [77] still initiates the shock wave using a moving piston, and such a method could not be readily incorporated into a coupled atomistic-continuum formulation.

1.2.3 A new moving window atomistic method for shock propagation

In this work, we first develop a long-time, moving window, atomistic framework using MD to model shock wave propagation through a one-dimensional monatomic chain. This framework employs techniques similar to those applied in the uniaxial Hugoniostat method by using the planar shock jump conditions and Hugoniot EOS to study the classic Riemann problem of a single propagating discontinuity. The domain is divided into an inner "window" region containing the shock front flanked by "thermostat" regions on either side. The thermostat regions are modeled after the *damping band* method presented in [78] which applies a Langevin thermostat locally to atoms in a *stadium* fashion and linearly increases the damping coefficient across the stadium region. Our method differs from [78] because it is purely atomistic and thus does not further couple the thermostat regions to outer continuum regions. The thermostat regions absorb and dissipate any impinging waves thus largely eliminating transient wave reflections. The atoms in the thermostat regions act as boundary conditions for atoms in the window region.

The motion of the domain is achieved by consistently adding and removing atoms to and from the thermostat and window regions. This moving window technique is similar in principle to moving boundary conditions used in works such as [79] and [80] to model dynamic crack propagation. Ordinarily, the simulation time of a shock propagating in an atomistic domain would be limited due to wave reflections off the boundary. The moving window formulation allows us to model the propagating shock much longer than conventional NEMD simulations by focusing the shock front at the center of the window region for the entire simulation. We emphasize that this first framework is not a true coupled atomistic-continuum scheme in that it lacks a continuum region with finite element-type mesh points. Therefore, the purely atomistic

formulation of the moving window technique is limited to ensuring that the small domain can follow a shock wave for a long time without artificial wave generation and reflection.

Next, we use this method to calculate the shock Hugoniot relation of single-crystal copper along the close packed lattice direction. Much work has been done on shock kinetic relations and the linear Hugoniot relationship between shock velocity and particle velocity. This includes extensive experimental calibration of the linear relation [12, 15] as well as theoretical investigations into the origins of the shock kinetic relation [81]. Additionally, many computational studies have been performed which use MD to measure the shock Hugoniot along different orientations of an FCC lattice [13, 14, 50, 82]. While the MD work has shown large anisotropic behavior for shock propagation along different crystal directions, experimental studies have shown no crystal orientation dependence of the shock velocity vs. particle velocity Hugoniot curve [83].

We start with the experimentally known shock Hugoniot parameters (C_0 and S) for polycrystalline bulk copper [12, 21, 15] and perform moving window simulations using particle velocities obtained from this linear relation. Next, we derive new empirical parameters of this EOS which produce stationary shock wave fronts in the one-dimensional monatomic chain. This new relation between shock velocity and particle velocity is defined as the shock Hugoniot curve along the close packed direction of a single-crystal copper lattice and compared to previous MD studies. Finally, we use this optimized Hugoniot data along with the moving window to follow a structured shock for a few nanoseconds and characterize the shock front's width. The shock's width is observed to increase with time which implies that the shock wave is unsteady. This is consistent with the findings of other early MD studies which used a one-dimensional chain of atoms to model shock wave propagation [28, 33, 34, 41, 84].

Although the moving window atomistic framework was presented in my 2020 master's thesis [85], this dissertation discusses new data obtained with the atomistic framework since then and elaborates on the significance of these results. These new data were also published in [1] in November of 2020.

1.3 Atomistic-continuum framework

Microscale modeling techniques such as MD clearly possess tremendous capability to simulate shock waves at lower length scales. Unfortunately, the applicability of MD deteriorates at the mesocale where the number of atoms required to characterize the system exceeds computational limitations. At the mesocale, however, the continuum hypothesis still fails, and thus the system cannot be described exclusively by continuum field theories. Therefore, there exists a need to develop frameworks which link the atomistic and continuum scales in order to accurately understand, describe, and simulate the motion and behavior of shock waves through materials. Figure 1.5 shows some of the different length and time scales in material modeling along with the experimental and computational techniques used at each level of analysis.

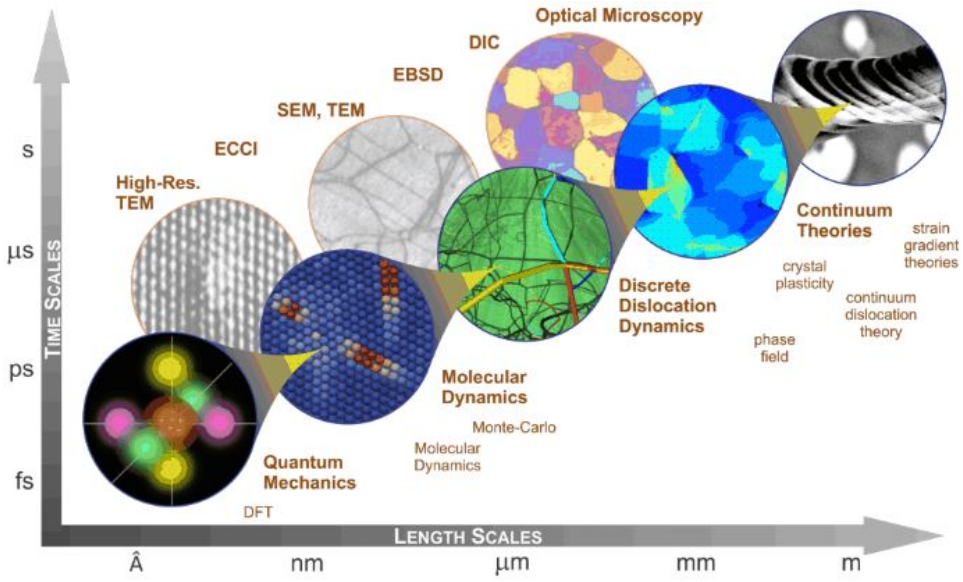

Figure 1.5: Multiscale categorization of material behavior [7].

1.3.1 Classification of multiscale techniques

Interest in developing coupled atomistic-continuum (A-C) frameworks for large-scale material modeling has been present in the scientific community since the early 1980s when Hardy derived formulas to relate local continuum properties such as mass density and momentum density to the masses, positions, and velocities of individual particles [86]. Hardy's formulas were similar to those presented in the work of Irving and Kirkwood from the 1950s [87], but

they had forms which could be easily incorporated into atomistic simulations. The first formal multiscale framework was developed in 1991 when Kohlhoff and his team used a combined finite-element and atomistic model to study crack propagation in BCC crystals [88]. In this work, they created an atomistic core with a surrounding continuum region and described this coupling in terms of non-local elasticity theory. This formulation became the standard-bearer for coupled atomistic-continuum models, and since that time, numerous methods have been established to connect these seemingly disparate levels of analysis. Such methods can be broadly divided into two distinct categories: *hierarchical* and *concurrent*.

Hierarchical methods presume a separation of spatial scales, and they formulate microscale information in terms of macroscale constitutive behavior. In other words, the lower-scale information is averaged and introduced into pure coarse-grained models in the form of constitutive equations. Some examples of hierarchical methods include multiple-level FEM [89, 90, 91], dislocation dynamics (DD) [92, 93, 94, 95], and the second gradient technique [96]. Specifically, DD simulates the motion of dislocations by treating them as continuum entities traveling in an elastic field. The interactions between these dislocations are described by constitutive relations, and the parameters can be derived, theoretically, from MD simulations. Because of this, the accuracy of DD is determined solely by how well these parameters in the constitutive relations describe the given system. This is a common limitation for all hierarchical techniques.

On the other hand, concurrent methods have been developed since the mid 1990s to overcome some of the drawbacks with hierarchical formulations. These concurrent schemes simultaneously integrate two different material descriptions into a single computational model. This is achieved by splitting up the given domain such that a continuum region flanks or surrounds an inner atomistic region. The atomistic region is very small compared to the continuum region and only envelops a given "region of interest" such as a dislocation or (as in our case) a shock wave front. As a result, concurrent schemes can describe very large domains for a comparatively lower computational cost than pure MD because the vast majority of the computational expense is associated with the small atomistic region. In this work, we incorporate the moving window formulation into a concurrent multiscale framework to model long-time shock

wave propagation through a material. Therefore, we present a brief introduction and analysis of existing concurrent schemes in the following section.

1.3.2 Existing concurrent multiscale schemes

In this review, we follow the work of Miller and Tadmor [9, 97] while making some reductions where necessary to avoid repetition and maintain relevancy. As stated in [97], concurrent multiscale schemes can be divided into two distinct methods: *energy-based* and *force-based*. In general, energy-based methods minimize a given energy functional to characterize the parameters of every atom/node in the system. By contrast, force-based methods solve the system by formulating a set of forces on every degree of freedom and then driving these forces to zero. Here, we briefly cover some of the most popular energy-based and force-based methods that exist today.

Coupling of Length Scales method

One of the first concurrent multiscale schemes to be developed was the Coupling of Length Scales (CLS) method [8, 98, 99, 100, 101]. CLS is an energy-based method which incorporates the MD equations of motion into an atomistic region and the finite-element equations of motion into a continuum region. As a result, a type of "handshaking" must be implemented in the interfacial zone between the atomistic and continuum regions as seen in Fig. 1.6. This handshake region is achieved by deriving the energy functional as the sum of the atomistic and continuum energies where the weights are modified as necessary in the interfacial zone. The atoms in the interfacial region are made neighbors with the nodes of the finite-element mesh, and this mesh is assumed to be a linear elastic material. The bulk elastic moduli correspond to the atomistic model, so the discrepancy at the atomistic-continuum boundary is minimized.

Bridging Domain method

The Bridging Domain (BD) method is an energy-based formulation developed in 2004 in which the atomistic and continuum regions overlap at the interfacial zone [102]. The energy functional is defined as a linear combination of the fine-scaled and coarse-scaled Hamiltonians, and the

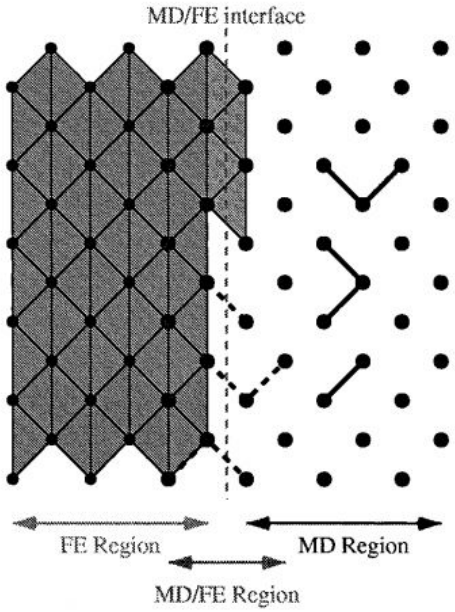

Figure 1.6: Illustration of the MD/FE handshake region for the CLS method [8][4].

constitutive equation in the coarse-scaled region is constructed via the Cauchy-Born rule. As a result, any atoms in the continuum domain must remain in that domain, so the BD method cannot be applied to diffusive phenomena in solids. Like CLS, the BD method incorporates a handshake region, and in the limit where the length of this region goes to zero, the CLS method is recovered. The BD method employs Lagrange multipliers in the handshake region to force consistency between the atomic and continuum displacements at the positions of atoms. This constrains both the atomistic and continuum models in the overlapping domain.

Bridging Scale method

The Bridging Scale Method (BSM) was first developed in 2003 and is an energy-based method which is distinct from the previous two schemes as it does not incorporate a handshake region [103, 104]. This is achieved because BSM does not separate the atomistic and continuum regions. Rather, both the atomistic and continuum displacement fields exist everywhere in the domain, and the displacement of each atom consists of a fine-scaled and coarse-scaled component. Figure 1.7 shows the interface region for BSM. The coarse-scaled displacements are

[4]Reprinted from *Computer Simulation of Materials at Atomic Level*, Ch. 11; R.E. Rudd and J.Q. Broughton; "Concurrent coupling of length scales in solid state systems," pp. 251-291, 2000. Obtained with permission from John Wiley and Sons, Ltd.

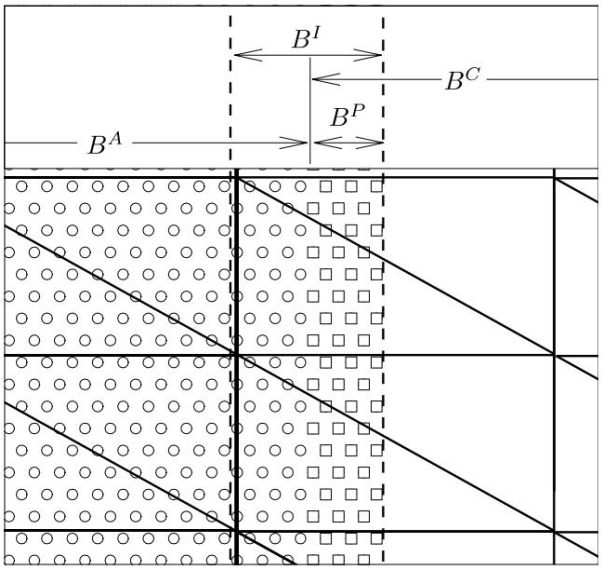

Figure 1.7: Illustration of the interface region for BSM [9][5]. There is not a handshake region and finite elements are populated throughout the body to store the coarse-grained displacements.

stored in a finite element mesh throughout the domain (all of B^A and B^C), while the fine-scaled displacements are only stored inside the atomistic domain (B^A). The fine-scaled displacements are obtained from MD by subtracting the component of the MD solution projected onto the coarse-scaled basis. Thus, a two-way information exchange exists where the fine-scaled MD values contribute to the internal force in the coarse-scaled equation, and the coarse-scaled values provide boundary information for the MD simulation. Because of this, it should be noted that using BSM to model complex phenomena like dislocations and deformations near surfaces can be non-trivial.

Coupled Atomistic Discrete Dislocation method

Developed in 2002 by Curtin and his team [78, 105, 106, 107, 108], the Coupled Atomistic Discrete Dislocation (CADD) method unifies atomistic techniques and continuum defect modeling schemes (such as DD) into one computational framework. CADD preserves atomistic resolution around a region of interest while simultaneously allowing continuum entities representing

[5]Reprinted from *Modelling and Simulation in Materials Science and Engineering*, vol. 17, no. 5; R.E. Miller and E.B. Tadmor; "A unified framework and performance benchmark of fourteen multiscale atomistic/continuum coupling methods," 2009. Obtained with permission from IOP Publishing, Ltd.

defects to interact directly with this region. Specifically, the coupling is achieved through superposition techniques consisting of three parts: (i) the atomistic domain, (ii) the DD domain, and (iii) the technique for detecting and passing dislocations between these two regions. In CADD, the defects in the coarse-scaled region are approximated as continuum entities with isotropic linear elastic fields. The total energy of the system is minimized using the conjugate gradient procedure, and complex strategies are implemented to allow dislocations to smoothly pass across the interfaces between the atomistic and DD regions. One of the disadvantages of CADD is that dislocations are curved in 3D, and hence the dislocation passing strategy becomes very complex at this dimension [109]. Additionally, CADD does not allow dislocation interactions nor does it allow heat conduction in the continuum or across the interface [110].

Quasicontinuum method

One of the most popular multiscale schemes is the Quasicontinuum (QC) method. Developed in 1996 by Tadmor and his coworkers [10, 111, 112, 113], QC does not have a handshake region and constrains atoms to deform along with the continuum displacement field. Elements in the coarse-scaled region represent nonlinear elastic crystals which follow the Cauchy-Born rule whereby the deformation gradient is applied to the undeformed lattice basis to achieve the crystal structure. The constraints introduced by the Cauchy-Born rule in the coarse-scaled regions eliminate extra atomistic degrees of freedom (DOFs), but such constraints also restrict continuum descriptions of dislocations and phonons unless an adaptive mesh scheme is implemented. As a result, the computational cost increases with increasing dislocations/phonons in traditional QC simulations. Many iterations of QC have been developed over the last two decades including cluster-QC [10], max-ent QC [113], fully non-local QC [6, 114, 115], and adaptive-mesh QC [116]. Specifically, cluster-QC approximates the force vector using summation rules which sample the lattice function over neighborhoods, or "clusters," of the representative atoms (nodes) in the coarse-scaled region. These clusters can be seen in Fig. 1.8.

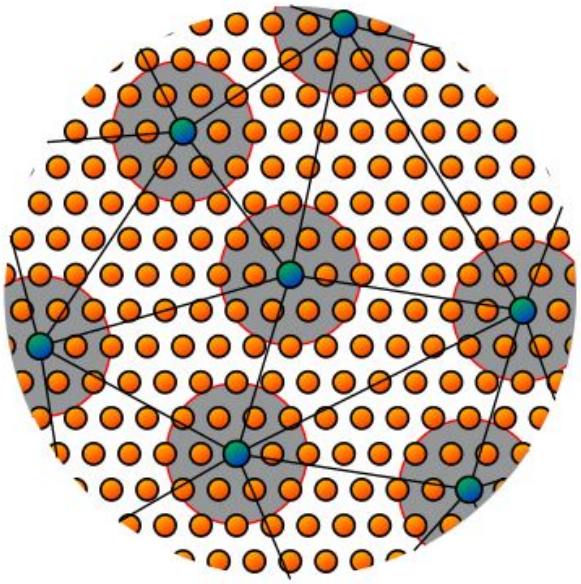

Figure 1.8: Clusters of atoms in triangulation of a crystal [10][6].

1.3.3 Limitations with previous schemes and an introduction to the CAC method

Reviewing these various concurrent multiscale methods shows us that combining atomistic and continuum models into a single framework significantly decreases the computational overhead because the continuum subdomain is much coarser than the atomistic subdomain. Hence, concurrent multiscale schemes can simulate very large systems for a much lower computational cost than pure MD. However, when modeling dynamical problems, concurrent frameworks can suffer from spurious wave reflections at the A-C interfaces causing an increase in energy inside the fine-scaled region. Such non-physical phenomena arise for the following reasons: (i) a difference in governing equations exists between the atomistic and continuum regions, (ii) the spectrum of the coarse-scaled model has a much smaller cutoff frequency than that of the fine-scaled model causing the A-C interface to appear rigid to incoming high-frequency waves, and (iii) the interface region cannot support thermal vibrations of particles.

Therefore, ensuring compatibility at the A-C interfaces is one of the primary challenges with developing and implementing concurrent multiscale frameworks. Although the methods discussed in the previous section have seen a lot of success in this area, many of them involve a

[6]Reprinted from *Journal of the Mechanics and Physics of Solids*, vol. 49, no. 9; J. Knap and M. Ortiz; "An analysis of the quasicontinuum method," pp. 1899-1923, 2001. Obtained with permission from Elsevier.

difference in material description across the interface, and most of them do not allow dislocation/phonon interactions or waves to travel into the continuum region [110]. Techniques which permit such interactions as well as admit dislocations to pass between the atomistic and continuum regions are needed in a concurrent scheme to realistically model shock wave propagation as well as study phenomena like phase transformations. Additionally, a framework which allows phonons to pass between the two regions would be capable of modeling the elastic waves generated after a shock wave impact.

The Concurrent Atomistic-Continuum (CAC) method has been developed over the past decade to overcome limitations inherent in other concurrent formulations [117, 118, 119, 120, 121, 122, 123, 124, 125, 126, 127, 128]. See Table 1.1 for a comparison of CAC with some of the schemes discussed in the previous section. Employing a unified multiscale framework built upon Atomistic Field Theory [129, 130], CAC extends the Irving-Kirkwood method for connecting the atomistic and hydrodynamical equations [87] to a two-level description of materials where the particle DOFs are included within each primitive unit cell. In this way, CAC follows the solid state physics model of crystals whereby the structure is continuous at the lattice level but discrete at the atomic level, and a single set of governing equations is used throughout the entire domain [128]. Hence, CAC not only supports dislocation/phonon interactions [120, 131], but it also allows dislocations and waves to pass from the atomistic region to the continuum region and vice versa [117, 126]. While CAC has been very successful at modeling material defects and their motion and is actively being applied to study dislocation evolution and interactions [132, 133, 134, 135], it has not yet been extended to model shock wave propagation through a material.

Table 1.1: Comparison of CAC with other multiscale methods.

Method	*CLS*	*BDM*	*CADD*	*QC*	*CAC*
Publication Year	1998	2004	2002	1996	2010
Handshake Region	Yes	Yes	No	No	No
Statics	No	Yes	Yes	Yes	Yes
Dynamics	Yes	Yes	Yes	Yes	Yes
Finite Temp Non-Equilibrium Dynamics	No	Yes	No	Yes	Yes
Dislocations in Continuum	No	No	Yes	No	Yes
Dislocations across Interface	No	No	Yes	No	Yes
Dislocation/Phonon Interactions	No	No	No	No	Yes

1.4 Objectives and research significance

The objective of the present work is to develop long-time, moving window, atomistic and multiscale frameworks to model shock wave propagation through various materials. Specifically, we study the classic Riemann problem of a single traveling discontinuity. In the atomistic framework, we characterize the shock wave using the planar shock jump conditions and Hugoniot EOS and employ the moving window technique established in [1] to follow the wave front for very long simulation times. In the multiscale CAC framework, we characterize the shock wave using the nonlinear Eulerian thermoelastic equations for shock compression of single crystals [136, 137] and employ the moving window in two distinct ways: (i) by tracking the shock front in a conveyor fashion and (ii) by simultaneously refining the coarse-scaled region and coarsening the fine-scaled region at the speed at which the shock wave advances. These moving window techniques allow us to model a propagating shock much longer than conventional NEMD simulations by focusing the shock front at the center of the fine-scaled region for the entire simulation. As a result, we can track the shock front and characterize its structure over time scales that are typically prohibitive.

During impact simulations, a shock wave may interact with a microstructural interface and produce transient high-frequency waves which travel throughout the domain. In most concurrent multiscale formulations, these waves would reflect off the A-C interfaces due to the numerical incompatibility between the atomistic and continuum regions. Such phonons would then travel back into the fine-scaled region and cause artificial heating which could potentially undermine the results of the simulation. Therefore, a scheme which could pass multiple high-frequency waves across the A-C interface in a multiscale setting would be invaluable. In this dissertation, we also develop a Lattice Dynamics (LD) technique based upon the work in [126] to update the particle displacements in the continuum region given multiple short-wavelength phonons nucleated in the atomistic region. This is achieved by taking two sets of Fourier transforms during the time integration algorithm and storing the amplitude coefficients in a "master" array. Such a technique serves as a strong foundation towards solving the complex problem of incompatibility at the A-C interfaces of a concurrent framework.

Finally, in this work, we have also expanded the one-dimensional CAC framework to two dimensions. While the one-dimensional monatomic CAC framework is very useful for studying simple shocks and testing new numerical methods, its physical applications are limited because it cannot support dislocations and transverse atomic motion. Scaling the framework up to 2D was a big undertaking as it required updating the boundary conditions, neighbor lists, unit cells, and CAC governing equation. Additionally, since shearing effects could influence the particle behavior, the integration technique required updating. As a result of all these modifications, the computational expense significantly increased, so we also revised the parallelization scheme. Despite its complexity, this higher-dimensional CAC framework will be very valuable to the multiscale modeling community for its potential to simulate nonlinear events, and we show the results from our simulations in this work.

1.5 Outline of dissertation

This dissertation is organized as follows:

- **Chapter 2**

    1. Derives the shock wave jump equations, Hugoniot relationship, and thermodynamic expression for temperature in the shocked material.
    2. Discusses the nonlinear Eulerian thermoelastic equations for shock wave propagation through anisotropic single crystals derived in [136].
    3. Outlines the problem statement.
    4. Describes the framework's geometry and boundary conditions.
    5. Presents the potentials and thermostats used in the simulations.

- **Chapter 3**

    1. Outlines the atomistic moving window and discusses how the shock is initialized in the fine-scaled domain.
    2. Presents results from verification studies performed with the atomistic framework.

3. Discusses atomistic shock wave propagation and structure results [1].

- **Chapter 4**

  1. Reviews the governing equations and finite element implementation of CAC.
  2. Outlines the CAC moving window method and discusses how the shock is initialized in the multiscale domain.

- **Chapter 5**

  1. Presents results from dispersion relation and phonon wave packet studies performed with the one-dimensional CAC framework.
  2. Presents shock wave and structure results obtained with the one-dimensional CAC moving window framework.

- **Chapter 6**

  1. Derives the Lattice Dynamics formulation for passing high-frequency phonon waves across length scales within the CAC framework.
  2. Enhances this technique to be used with multiple waves in a periodic domain.
  3. Presents results from one-dimensional wave packet simulations performed with the wave passing method.

- **Chapter 7**

  1. Discusses the formulation of the two-dimensional CAC framework.
  2. Presents shock wave results obtained with the two-dimensional CAC moving window framework.

- **Chapter 8**

  1. Provides a conclusion and summary of the dissertation.
  2. Discusses the scientific contributions of this work.
  3. Considers current and future research on this topic.

- **Appendix**

    1. Presents further verification results for both the atomistic and CAC frameworks.
    2. Gives unsolicited advice to future engineering students by elaborating on the lessons I learned while pursuing my PhD.

Chapter 2

Mathematical Background and Domain Formulation

Before discussing the details of the various projects, we first provide a mathematical overview of our framework.

In Chs. 3 - 5, we consider an elastic monatomic chain with no defects under compression by an ideal one-dimensional (i.e. longitudinal) shock wave (the two-dimensional formulation will be analyzed separately in Ch. 7). Mathematically, we represent the shock as a propagating discontinuity across which there exists a jump in particle velocity (v), stress (σ), strain (ϵ), and temperature (θ). Material quantities ahead of the shock front have the superscript $-$, and quantities behind the shock front have the superscript $+$. In each simulation, particles ahead of the shock front are assumed to be at zero mean particle velocity, unstressed, unstrained, and at room temperature (295 K), and the shock propagates at a natural velocity U_S. The notation $[\![\cdot]\!]$ denotes the change in a given quantity $(\cdot)$ across the shock front. Some of the analysis in this chapter can also be found in [11, 21, 85], but we reiterate pertinent derivations/equations/explanations as well as add more details where necessary for the sake of completeness and clarity.

2.1 Hugoniot shock wave equations

To obtain the results presented in Ch. 3 as well as some of the results in Ch. 7, we simulate a propagating shock wave using the conservation of momentum, continuity equation, Hugoniot EOS, and a thermodynamic relationship derived from the shock Hugoniot and release isentrope. Figure 2.1 provides an illustration of a shock passing through a body Ω. We assume that the boundary of the shock wave front is contained within the boundary of the material. This creates

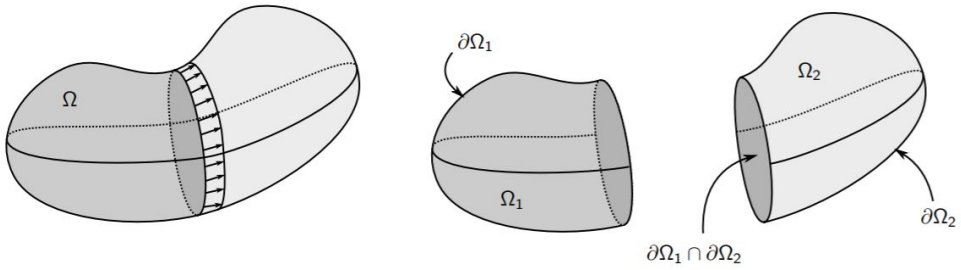

Figure 2.1: Discontinuous wave propagating through a three-dimensional material.

a partitioning $\Omega = \Omega_1 \cap \Omega_2$ of the body into two regions on either side of the discontinuity where the displacements are continuous.

2.1.1 Continuity jump equation

Consider a point $\mathbf{s}$ on the discontinuity which moves with the discontinuity in time. Here, $\dot{\mathbf{s}}$ is the velocity of the discontinuity at the point $\mathbf{s}$. The material neither creates a void nor

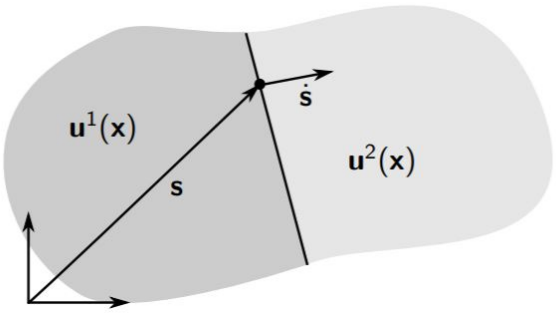

Figure 2.2: Point $\mathbf{s}$ on the discontinuity propagating through the material with velocity $\dot{\mathbf{s}}$.

interpenetrates itself, so the displacement is continuous at $\mathbf{s}(t)$ for all time:

$$\mathbf{u}^1(\mathbf{s}, t) = \mathbf{u}^2(\mathbf{s}, t). \tag{2.1}$$

Taking the total derivative of each side with respect to time and using index notation, we get the following:

$$\begin{aligned} \frac{d}{dt} u_i^1(\mathbf{s}(t), t) &= \frac{d}{dt} u_i^2(\mathbf{s}(t), t) \\ \frac{\partial u_i^1}{\partial s_j} \frac{ds_j}{dt} + \frac{\partial u_i^1}{\partial t} &= \frac{\partial u_i^2}{\partial s_j} \frac{ds_j}{dt} + \frac{\partial u_i^2}{\partial t} \\ \epsilon_{ij}^1 \dot{s}_j + v_i^1 &= \epsilon_{ij}^2 \dot{s}_j + v_i^2 \end{aligned} \tag{2.2}$$

where ϵ and v denote strain and particle velocity respectively. Then, we can write Eq. (2.2) as

$$[\![\epsilon_{ij}]\!]\dot{s}_j + [\![v_i]\!] = 0. \tag{2.3}$$

2.1.2 Momentum jump equation

The integral of the total force ($\mathbf{t} = \sigma\mathbf{n}$) over the boundary of the body equals the time derivative of the total momentum of the body as shown below:

$$\int_{\partial\Omega} \sigma_{ij} n_j dA = \frac{d}{dt}\int_{\Omega} \rho v_i dV \tag{2.4}$$

where σ and ρ represent stress and density respectively. For the left-hand side of the Eq. (2.4), we apply the divergence theorem to the two sub-bodies on either side of the discontinuity. Using index notation, we get the following:

$$\begin{aligned}
\int_{\Omega} \sigma_{ij,j} dV &= \int_{\Omega_1} \sigma_{ij,j} dV + \int_{\Omega_2} \sigma_{ij,j} dV \\
&= \int_{\partial\Omega} \sigma_{ij} n_j dA + \int_{\partial\Omega_1 \cap \partial\Omega_2} \sigma^1_{ij,j} n^1_j dA + \int_{\partial\Omega_1 \cap \partial\Omega_2} \sigma^2_{ij,j} n^2_j dA \\
&= \int_{\partial\Omega} \sigma_{ij} n_j dA + \int_{\partial\Omega_1 \cap \partial\Omega_2} [\![\sigma_{ij,j}]\!] n_j dA
\end{aligned} \tag{2.5}$$

where $\sigma_{ij,j} = \text{div}(\sigma)$. Hence, the left-hand side of Eq. (2.4) can be rewritten as

$$\int_{\partial\Omega} \sigma_{ij} n_j dA = \int_{\Omega} \sigma_{ij,j} dV - \int_{\partial\Omega_1 \cap \partial\Omega_2} [\![\sigma_{ij,j}]\!] n_j dA. \tag{2.6}$$

Next, we apply Reynold's transport theorem to the right-hand side of Eq. (2.4) to get

$$\frac{d}{dt}\int_{\Omega_1} \rho v_i dV = \int_{\Omega_1} \frac{\partial}{\partial t} \rho v_i dV + \int_{\partial\Omega_1} \rho v_i \dot{s}_j n_j dA \tag{2.7}$$

where $\dot{s}_j$ is the boundary velocity. Thus, we can write

$$\begin{aligned}\frac{d}{dt}\int_\Omega \rho v_i dV &= \int_\Omega \frac{\partial}{\partial t}\rho v_i dV + \int_{\partial\Omega_1} \rho^1 v_i^1 \dot{s}_j n_j^1 dA + \int_{\partial\Omega_2} \rho^2 v_i^2 \dot{s}_j n_j^2 dA \\ &= \int_\Omega \frac{\partial}{\partial t}\rho v_i dV + \int_{\partial\Omega_1\cap\partial\Omega_2} [\![\rho v_i]\!] \dot{s}_j n_j dA. \end{aligned} \tag{2.8}$$

Combining Eqs. (2.6) and (2.8), we get the following:

$$\int_\Omega \sigma_{ij,j} dV - \int_{\partial\Omega_1\cap\partial\Omega_2} [\![\sigma_{ij,j}]\!] n_j dA = \int_\Omega \frac{\partial}{\partial t}\rho v_i dV + \int_{\partial\Omega_1\cap\partial\Omega_2} [\![\rho v_i]\!] \dot{s}_j n_j dA \tag{2.9}$$

which we can rewrite as

$$\int_\Omega \left[\sigma_{ij,j} - \frac{\partial}{\partial t}\rho v_i\right] dV = \int_{\partial\Omega_1\cap\partial\Omega_2} \left([\![\sigma_{ij,j}]\!] + [\![\rho v_i]\!]\dot{s}_j\right) n_j dA. \tag{2.10}$$

Eq. (2.10) is true for *all* subregions of Ω, and it must hold true for all $\Omega \subset (\Omega_1 \cup \Omega_2)$. This only occurs if the integrand is zero. Then, the right hand side must hold for all subsets of the boundary. By the fundamental lemma, we have the following jump condition:

$$[\![\sigma_{ij}]\!] n_j + [\![\rho v_i]\!] \dot{s}_j n_j = 0. \tag{2.11}$$

2.1.3 Reduction to 1D and the linear shock Hugoniot

Consider the propagation of a discontinuity in a plane-strain or plane-stress material as shown in Fig. 2.3. In this case, we let the velocity of the discontinuity $\dot{\mathbf{s}} = U_S$ be in the positive

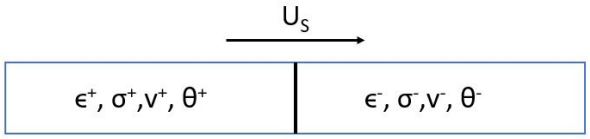

Figure 2.3: Discontinuous wave propagating through a one-dimensional material.

x direction only. Substituting the velocity U_S into Eq. (2.3), we get the one-dimensional continuity jump condition:

$$[\![\epsilon]\!] U_S + [\![v]\!] = 0 \tag{2.12}$$

where ϵ is the longitudinal strain, and v is the particle velocity. Next, substituting U_S into Eq. (2.11), we get the one-dimensional momentum jump condition:

$$[\![\sigma]\!] + \rho U_S [\![v]\!] = 0 \tag{2.13}$$

where σ is the longitudinal stress. We assume that the wave does not significantly affect the material properties, so $\rho^+ = \rho^- = \rho$.

The shock jump equations are supplemented by an empirically observed linear relation between shock velocity and particle velocity [11]:

$$U_s = C_0 + S[\![v]\!]. \tag{2.14}$$

Here, S is a dimensionless, empirical parameter representing the slope of the shock velocity vs. particle velocity Hugoniot curve, and C_0 is the sound velocity in the material at zero stress. Equation (2.14) was first presented in [138] and used to fit data for twenty-three metals. However, [15] tabulated Hugoniot data which offered linear fits for many different types of materials. In some cases – for example, materials with phase transitions, porosity, or molecular bonding – the linear relation can break down [139]. However, even in those instances, the linear relation is still used, at least for representing the data over part of the range.

Equations (2.12), (2.13), and (2.14) lead to the standard Hugoniot stress-strain relationship given by

$$\sigma = \frac{\rho C_0^2 [\![\epsilon]\!]}{(1 + S[\![\epsilon]\!])^2} \tag{2.15}$$

where compression strain is considered positive. The Hugoniot stress-strain relationship forms the basis of modern equations of state. In this work, we use the Hugoniot EOS (Eq. 2.15) for the sake of simplicity and to quickly compute shocked states.

2.1.4 Temperature

In this subsection, we summarize the analysis from [11]. As a shock wave moves through a solid, the material behind the wave front gets compressed, and this causes the temperature in

the shocked material to rise. We assume the thermodynamic process at the shock front to be adiabatic and the release from the shocked state to the initial state to be isentropic. For solid materials, the release isentrope and shock Hugoniot are nearly the same. Fig. 2.4 shows a material shocked from an initial state at atmospheric pressure to pressure P_1. Points P_1 and V_1

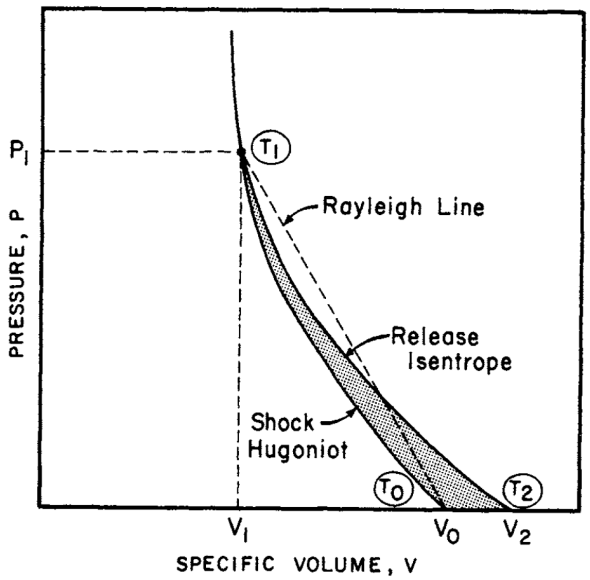

Figure 2.4: Shock Hugoniot and release isentrope leading to temperatures T_1 and T_2 [11][7].

are on the shock Hugoniot, and unloading follows the release isentrope to point 2. It is apparent that T_2 is higher than T_0, and thus V_2 is higher than V_0. This irreversibility produces a loss of energy as shown by the grey area. We can calculate the rise in temperature behind the shock using the Grüneisen EOS and thermodynamic relationships.

Using the first law of thermodynamics:

$$dE = \delta Q - \delta W \tag{2.16}$$

where

$$\delta W = PdV \tag{2.17}$$

and

$$\delta Q = TdS, \tag{2.18}$$

[7]Reprinted from *Dynamic Behavior of Materials*, Ch. 5; M.A. Meyers, 1994. Obtained with permission from John Wiley and Sons, Ltd.

we obtain the following expression:

$$dE = TdS - PdV. \tag{2.19}$$

We can use this to calculate a thermodynamic expression for TdS:

$$\begin{aligned} S &= f(T,V) \\ dS &= \left(\frac{\partial S}{\partial T}\right)_V dT + \left(\frac{\partial S}{\partial V}\right)_T dV \\ TdS &= T\left(\frac{\partial S}{\partial T}\right)_V dT + T\left(\frac{\partial S}{\partial V}\right)_T dV, \end{aligned} \tag{2.20}$$

where we know that

$$C_V = \left(\frac{\partial E}{\partial T}\right)_V = T\left(\frac{\partial S}{\partial T}\right)_V \tag{2.21}$$

is the volumetric specific heat capacity. Then, from the second Maxwell relation

$$dA = -PdV - SdT, \tag{2.22}$$

we get the following:

$$\left(\frac{\partial P}{\partial T}\right)_V = \left(\frac{\partial S}{\partial V}\right)_T. \tag{2.23}$$

Substituting Eqs. (2.21) and (2.23) into Eq. (2.20) gives

$$TdS = C_V dT + T\left(\frac{\partial P}{\partial T}\right)_V dV. \tag{2.24}$$

We now apply the Grüneisen equation

$$\frac{\Gamma_1}{V} = \left(\frac{\partial P}{\partial E}\right)_V \tag{2.25}$$

to get the following identity:

$$\left(\frac{\partial P}{\partial T}\right)_V = \left(\frac{\partial P}{\partial E}\right)_V \left(\frac{\partial E}{\partial T}\right)_V = \frac{\Gamma_1}{V} C_V \tag{2.26}$$

where Γ_1 is the first-order Grüneisen parameter for the material. Next, we substitute Eqs. (2.24) and (2.26) into Eq. (2.19),

$$dE = C_V dT + T\frac{\Gamma_1}{V}C_V dV - PdV. \tag{2.27}$$

For a Hugoniot shock process, we know that

$$\Delta E = (E_1 - E_0) = \frac{1}{2}(P_1 + P_0)(V_0 - V). \tag{2.28}$$

Expressing the change in internal energy with volume along the Hugoniot, we can rewrite Eqs. (2.27) and (2.28) as follows:

$$\left(\frac{dE}{dV}\right)_H = C_V\left(\frac{dT}{dV}\right)_H + \frac{\Gamma_1 T C_V}{V} - P \tag{2.29}$$

$$\left(\frac{dE}{dV}\right)_H = \frac{1}{2}\left(\frac{dP}{dV}\right)_H (V_0 - V) - \frac{P}{2}. \tag{2.30}$$

Substituting Eq. (2.30) into Eq. (2.29), we get an expression for the temperature T,

$$C_V\left(\frac{dT}{dV}\right)_H + \frac{\Gamma_1 T C_V}{V} = \frac{1}{2}\left(\frac{dP}{dV}\right)_H (V_0 - V) + \frac{P}{2} \tag{2.31}$$

which is a differential equation of the form $Ay' + By = F(V)$. Writing Eq. (2.31) in terms of ϵ and σ and letting $\theta = T$, we arrive at the shock heat equation:

$$C_V\left(\frac{d\theta}{d\epsilon}\right)_H - \frac{\Gamma_1 \theta C_V}{1-\epsilon} = \frac{\epsilon}{2}\left(\frac{d\sigma}{d\epsilon}\right)_H - \frac{\sigma}{2}. \tag{2.32}$$

We use this equation to solve for the jump in temperature across the shock wave front.

2.2 Nonlinear Eulerian thermoelastic theory for shock waves in anisotropic crystals

To characterize the shock wave in the 1D and 2D CAC frameworks, we use the nonlinear Eulerian thermoelastic shock equations derived in [136, 137] for anisotropic crystals. Nonlinear elastic constitutive models of material behavior which do not account for slippage and plasticity

are generally idealizations because even small uniaxial compressive strains can cause ductile materials to reach the experimental Hugoniot elastic limit (HEL). However, such elastic formulations can be practically applied to defect-free atomistic and multiscale simulations of ductile solids since these domains may be shocked to finite strains over relatively short time scales and small volumes [137, 140]. Furthermore, we note that nonlinear elastic models may be used to describe the finite compression of some strong crystals like diamond since the HEL of such materials is very large. To see an extensive derivation of the Eulerian formulation for shock waves, we refer the reader to [136] as we merely provide an overview here.

For uniaxial loading, the '11' component of the deformation gradient behind the shock front is given as follows:

$$F_{11} = \frac{\partial x}{\partial X} = 1 + \frac{\partial u}{\partial X} = 1 + \epsilon = J \tag{2.33}$$

where u is the displacement, ϵ is the strain, and J is the Jacobian determinant. We simulate compressive shocks, for which $0 < F \leq 1$ and $-1 < \epsilon \leq 0$, propagating with a positive velocity $U_S > 0$. Then, the only nonzero component of the Eulerian strain is

$$D = D_{11} = \frac{1}{2}\left(1 - F_{11}^{-2}\right) = \frac{1}{2}\left[1 - \frac{1}{(1+\epsilon)^2}\right]. \tag{2.34}$$

Also, for uniaxial strain along the positive x-direction, we have the following:

$$\begin{aligned} P &= -\sigma_{11} \\ J &= F_{11} = (1 - 2D)^{-1/2} \end{aligned} \tag{2.35}$$

where P is the axial shock stress. In this case, the term *Eulerian* refers to a strain that is a function of the inverse deformation gradient and not necessarily one in spatial coordinates. Therefore, the strain tensor D is Eulerian but refers to material coordinates, so it can be used in simulations of anisotropic materials [136]. As stated in [141], the choice between Lagrangian and Eulerian is a matter of convenience, but the Eulerian formulation gives simpler expressions when modeling large compressions.

It is well known that a planar shock wave propagating through an unstressed solid with velocity U_S can be described by the Rankine-Hugoniot equations [21, 27, 142]

$$\begin{aligned}
[\![P]\!] - \rho_0 U_s [\![v]\!] &= 0 \\
[\![v]\!] - U_s [\![1 - J]\!] &= 0 \\
[\![U]\!] - \frac{1}{2}\rho_0 [\![v^2]\!] &= 0
\end{aligned} \tag{2.36}$$

where ρ_0, v, and U denote density, particle velocity, and energy respectively. As shown in [136], analytical solutions to the planar shock problem can be derived when the material's internal energy is a linear function of entropy. Assuming uniaxial strain, the Eulerian fourth-order internal energy function and conjugate thermodynamic stress are given by [137]

$$\hat{U} = \frac{1}{2}C_{11}D^2 + \frac{1}{6}\hat{C}_{111}D^3 + \frac{1}{24}\hat{C}_{1111}D^4 - \theta_0\left(\Gamma_1 D + \frac{1}{2}\hat{\Gamma}_{11}D^2 - 1\right)\eta \tag{2.37}$$

$$\hat{S} = -J^3 P = \frac{\partial \hat{U}}{\partial D}. \tag{2.38}$$

Here, $\theta_0 > 0$ and $\eta = 0$ are the respective temperature and entropy ahead of the shock front, C_{11} is the second-order elastic constant, and Γ_1 is the first-order Grüneisen parameter. The Eulerian third-order elastic constant, Eulerian fourth-order elastic constant, and Eulerian second-order Grüneisen parameter are obtained by the relations [136, 143, 144]

$$\hat{C}_{111} = C_{111} + 12C_{11} \tag{2.39}$$

$$\hat{C}_{1111} = C_{1111} - 18C_{111} - 318C_{11} \tag{2.40}$$

$$\hat{\Gamma}_{11} = \Gamma_{11} + 4\Gamma_1 \tag{2.41}$$

where $\Gamma_{11} = \Gamma_1$ assuming that $\rho\Gamma_\beta = \rho_0\Gamma_{0\beta} =$ constant [136, 145].

Solving Eqs. (2.35), (2.36), (2.37), and (2.38) simultaneously gives the following fifth-order polynomials for entropy η generated across the shock front [136]:

$$\eta(D) = \sum_{k=0}^{5} b_k D^k \tag{2.42}$$

$$b_0 = b_1 = b_2 = 0 \tag{2.43}$$

$$b_3 = \frac{1}{12\theta_0}\left(\hat{C}_{111} - 9C_{11}\right) \tag{2.44}$$

$$b_4 = \frac{1}{24\theta_0}\left[\hat{C}_{1111} - 9\hat{C}_{111} - 6C_{11} + \Gamma_1\left(\hat{C}_{111} - 9C_{11}\right)\right] \tag{2.45}$$

$$b_5 = \frac{1}{48\theta_0}\left[-6\hat{C}_{1111} - 6\hat{C}_{111} - 9C_{11} + \Gamma_1\left(\hat{C}_{1111} - 6\hat{C}_{111} - 33C_{11}\right) + \Gamma_1^2\left(\hat{C}_{111} - 9C_{11}\right)\right]. \tag{2.46}$$

Substituting these polynomials into Eq. (2.37), we can obtain the following expression for the fifth-order conjugate stress (Eq. 2.38) [136]:

$$\hat{S} = \frac{\partial \hat{U}}{\partial D} = C_{11}D + \frac{1}{2}\hat{C}_{111}D^2 + \left(\frac{1}{6}\hat{C}_{1111} - \theta_0\Gamma_1 b_3\right)D^3 - \theta_0 D^4\left[\left(\Gamma_1 b_4 + \hat{\Gamma}_{11}b_3\right) + \left(\Gamma_1 b_5 + \hat{\Gamma}_{11}b_4\right)D\right]. \tag{2.47}$$

From this conjugate stress, we can then use Eqs. (2.35b) and (2.38) to get an expression for the shock stress P:

$$P = -\left(1 - 2D\right)^{3/2}\hat{S}. \tag{2.48}$$

Finally, the particle velocity v and temperature θ behind the shock front as well as the shock velocity U_S can be obtained from Eqs. (2.36a), (2.36b), (2.37), and (2.48):

$$v = \left\{\left(\frac{\hat{S}}{\rho_0}\right)\left[(1-2D) - (1-2D)^{3/2}\right]\right\}^{1/2} \tag{2.49}$$

$$U_S = v\left[1 - (1-2D)^{-1/2}\right]^{-1} \tag{2.50}$$

$$\theta = \frac{\partial \hat{U}}{\partial \eta} = \theta_0 \left(1 - \Gamma_1 D - \frac{1}{2} \hat{\Gamma}_{11} D^2 \right). \tag{2.51}$$

For every shock simulation in Ch. 5, we use the third-order expressions of Eqs. (2.49), (2.50), and (2.51). However, for the simulations in Ch. 7, we use the fourth-order expressions.

2.3 Riemann problem statement

The material is described by the state variables v, ϵ, and θ on either side of the shock front as well as the shock velocity U_S. Given an initial strain ϵ^-, a final strain ϵ^+, and state (v^-, θ^-) of the unshocked material, either the Hugoniot equations [Eqs. (2.12), (2.14), and (2.32)] or the Eulerian equations [Eqs. (2.49), (2.50), and (2.51)] can be used to compute U_S and state (v^+, θ^+) of the shocked material. We incorporate these parameters into moving window atomistic and CAC frameworks to simulate long-time shock wave propagation given continuum shock states ahead of and behind the shock front. Specifically, we study the classic Riemann problem of a single propagating discontinuity with constant states on either side as shown in Fig. 2.5.

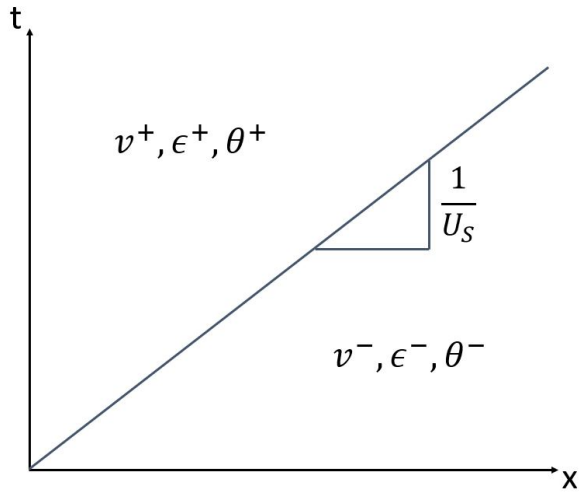

Figure 2.5: Riemann problem of a shock wave with constant states ahead of and behind the shock front.

Section 1.2.1 discussed some of the NEMD simulations performed in the 1960s and 70s which modeled shock waves in 1D. It should be emphasized that all of these works examined shock propagation along the [100] lattice direction. More recent studies have measured

the shock Hugoniot along different orientations of a monatomic lattice and discovered large anisotropic behavior along the various crystal directions [13, 14, 50, 82]. Specifically, [50] found that shocks propagating along the [110] direction exhibited a leading solitary wave train, spreading out as time progressed, which was not observed in the other cases. Along this orientation, the atoms displaced primarily in the shock direction and very little, if at all, in the transverse directions. The article concluded that shocks along the [110] direction exhibited effectively 1D behavior comparable to what had been observed in cases of a one-dimensional chain of hard rods [41].

Building upon this, in Chs. 3 and 5, we relate a shock wave propagating through a one-dimensional chain of *close-packed* particles to a planar elastic shock propagating along the [110] direction of a single-crystal lattice. We maintain low particle velocities as well as temperatures below the melting temperature of the material to study weak shocks. This minimizes plastic behavior such as void nucleation and subsequent dislocation generation in the shocked region. We note, however, that some plasticity and slippage may still occur. Since the one-dimensional framework is fundamentally incapable of capturing plastic effects (and the associated transverse atomic displacements), we should still expect to observe the shock front increase in thickness over time.

2.4 Computational setup

2.4.1 Geometry and boundary conditions

The one-dimensional framework is implemented using an in-house C++ code. The monatomic chain consists of N particles which are split into three regions as seen in Fig. 2.6. The particles in each coarse-scaled (continuum) region are separated by a distance of nr_0 and are referred to as *nodes* in the present work. Here, n is some positive integer, and r_0 is the equilibrium spacing determined by the potential function. These two coarse-scaled regions flank the inner fine-scaled (atomistic) region on either side. The particles in the fine-scaled region are separated by a distance of r_0 and are referred to as *atoms* in the present work. Because CAC produces a unified atomistic-continuum framework using a single set of governing equations, the atoms

and nodes have identical properties with the only difference being their inter-particle spacing and mass. Hence, all force calculations are fully nonlocal, and the interatomic potential is the only constitutive relation [123]. As a result, the particles at the atomistic-continuum interfaces ($x_{A,0}$ and $x_{A,F}$) interact with each other directly without generating ghost forces [127, 146].

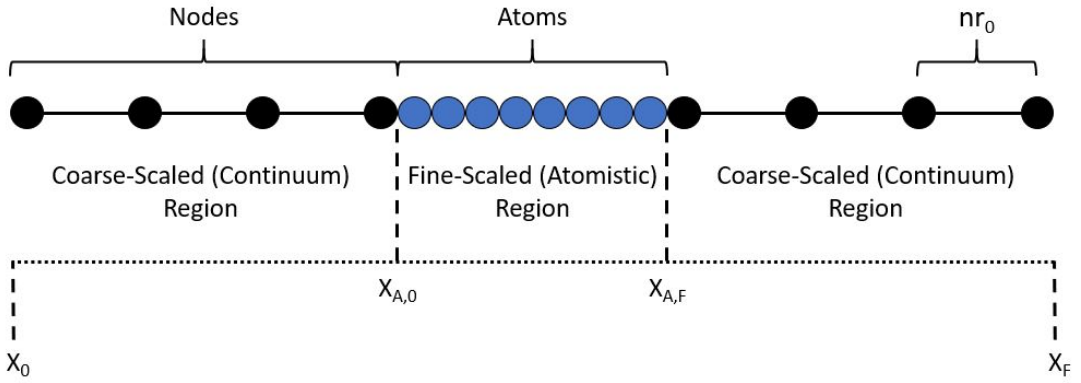

Figure 2.6: Schematic of the one-dimensional CAC domain.

For verification tests and non-shock simulations, we employ either standard fixed or periodic boundary conditions. However, when modeling a propagating shock wave, the two coarse-scaled regions have distinct particle velocities, strains, and temperatures. Therefore, to avoid introducing non-physical forces into the domain, a semi-periodic boundary condition method is employed during shock simulations. Specifically, the nodes at the ends of the chain (x_0 and x_F) are made neighbors with the nodes at the interfaces ($x_{A,0}$ and $x_{A,F}$ respectively). The atoms and nodes at the A-C interfaces interact with each other directly as in non-shock simulations.

We note that for purely atomistic simulations, only the fine-scaled region is used. In these simulations, the equilibrium spacing between each particle in the domain is r_0, and the classic MD equations of motion are employed. As with the CAC framework, standard boundary conditions are used for non-shock simulations while semi-periodic boundary conditions are used for shock simulations.

2.4.2 Integration algorithm

The CAC governing equation (Eq. 4.18) is a second-order ordinary differential equation in time, and we solve it using the velocity Verlet algorithm [147] as seen below:

$$\begin{aligned}
\mathbf{x}_i\left(t+\Delta t\right) &= \mathbf{x}_i\left(t\right) + \mathbf{v}_i\left(t\right)\Delta t + \frac{\mathbf{f}_i\left(t\right)}{2m}\Delta t^2 \\
\mathbf{v}_i\left(t+\frac{\Delta t}{2}\right) &= \mathbf{v}_i\left(t\right) + \frac{\Delta t}{2}\frac{\mathbf{f}_i\left(t\right)}{m} \\
\mathbf{f}_i\left(t+\Delta t\right) &= \mathbf{f}_i\left[\mathbf{x}_i\left(t+\Delta t\right)\right] \\
\mathbf{v}_i\left(t+\Delta t\right) &= \mathbf{v}_i\left(t+\frac{\Delta t}{2}\right) + \frac{\Delta t}{2}\frac{\mathbf{f}_i\left(t+\Delta t\right)}{m}.
\end{aligned} \tag{2.52}$$

Here, $\mathbf{x}_i$, $\mathbf{v}_i$, and $\mathbf{f}_i$ denote the position of the i^{th} particle, its velocity, and the net force acting on it respectively. The time step used in the integration algorithm is chosen to be $\Delta t = 0.001$ ps in order to minimize numerical error. The velocity Verlet algorithm is adapted in the presence of the Langevin thermostat as explained in Sec. 2.4.4.

2.4.3 Interatomic potentials

We use the Lennard-Jones, modified Morse, and Embedded Atom Model (EAM) interatomic potential functions for pure MD force calculations and the modified Morse potential to calculate the integrand of the internal force density (Eq. 4.14) in CAC simulations. Without loss of generality, all atomistic simulations as well as the CAC verification studies in Sec. 5.1 and the Appendix are performed using only the parameters for Cu.

The Lennard-Jones potential only considers first nearest-neighbor interactions and is represented most commonly as follows [32, 148]:

$$\Pi(r_{ij}) = 4\epsilon\left[\left(\frac{\sigma}{r_{ij}}\right)^{12} - \left(\frac{\sigma}{r_{ij}}\right)^{6}\right] = \epsilon\left[\left(\frac{r_0}{r_{ij}}\right)^{12} - 2\left(\frac{r_0}{r_{ij}}\right)^{6}\right] \tag{2.53}$$

where ϵ is the depth of the potential well, σ is the finite distance at which the inter-particle potential is zero, $r_{ij} = |x_i - x_j|$ is the absolute distance between particle i and j, and r_0 is

the distance at which the potential reaches the minimum. The parameters for Cu are given as follows: $\epsilon = 0.415$ eV and $\sigma = 2.277$ Å [149].

Like Lennard-Jones, the modified Morse potential [20] only considers first nearest neighbor interactions. The expression is given by

$$\Pi(r_{ij}) = \frac{D_0}{2B-1}\left[e^{-2A\sqrt{B}(r_{ij}-r_0)} - 2Be^{-A(r_{ij}-r_0)/\sqrt{B}}\right]. \tag{2.54}$$

MacDonald and MacDonald [20] modified the standard Morse potential to improve the agreement with experimental values for the thermal expansion of materials. Atomistic shock simulations are only performed with Cu while CAC shock simulations are performed with the following FCC metals: Cu, Al, Ag, and Ni. Additionally, we use Cu and Al for the two-dimensional CAC shock simulations discussed in Sec. 7. The parameters for these materials are given in Table 2.1 where we note that each r_0 is equivalent to the equilibrium spacing along the [110] lattice direction of that particular element.

Table 2.1: Material constants and Morse parameters of four different FCC metals [20].

Element	*mass (u)*	ρ_0 *(g/cm^3)*	Γ_1	r_0 *(Å)*	α *(Å^{-1})*	D_0 *(eV)*	*B*
Cu	63.55	8.96	5.5486	2.5471	1.1857	0.5869	2.265
Al	26.98	2.70	6.2753	2.8485	1.1611	0.3976	2.5
Ag	107.87	10.49	5.9773	2.8765	1.1255	0.4915	2.3
Ni	58.69	8.90	6.4699	2.4849	1.3909	0.6144	2.4

The expression for the Grüneisen constant Γ_1 of a perfect crystal with pair interactions in *d*-dimensional space is given as follows [150]:

$$\Gamma_1 = -\frac{1}{2d}\frac{\Pi'''(r_0)r_0^2 + (d-1)\left[\Pi''(r_0)r_0 - \Pi'(r_0)\right]}{\Pi''(r_0)r_0 + (d-1)\Pi'(r_0)} \tag{2.55}$$

where Π is the interatomic potential. For a one-dimensional chain, this equation reduces to

$$\Gamma_1 = -\frac{1}{2}\frac{\Pi'''(r_0)r_0^2}{\Pi''(r_0)r_0}. \tag{2.56}$$

We use Eq. (2.56) to obtain the Grüneisen constants given in Table 2.1. As seen, the Γ_1 values for a 1D chain are about 3x the experimental constants of a three-dimensional crystal.

Finally, the EAM potential is given by the following equation [151]:

$$\Pi(r_{ij}) = F\left(\sum_{i\neq j}\rho\left(r_{ij}\right)\right) + \frac{1}{2}\sum_{i\neq j}V\left(r_{ij}\right) \tag{2.57}$$

where the net force on a given particle is now a function of all the atoms/nodes/lattice points within a cutoff radius r_c. In Eq. (2.57), V is a pair-wise potential function, ρ is the contribution to the electron charge density from particle *j* at the location of particle *i*, and *F* is an embedding function that represents the energy required to place particle *i* into the electron cloud [152]. We use the EAM potential file produced by Mishin for atomistic simulations [153].

2.4.4 Thermostat

We impose and maintain temperature in the domain using the Langevin thermostat. The Langevin thermostat is stochastic and thus adds a random force to the particle motion along with a damping term ζ. The one-dimensional equations of motion of this thermostat for a particle *i* are as follows:

$$\begin{aligned}
\mathbf{f}_i^{tot}\left(t\right) &= \mathbf{f}_i\left(t\right) - \zeta m\mathbf{v}_i\left(t\right) + \sqrt{\frac{2k_B\theta\zeta m}{\Delta t}}\tilde{\mathbf{h}}_i\left(t\right) \\
\left\langle\tilde{\mathbf{h}}_i\left(t\right)\right\rangle &= \mathbf{0} \\
\left\langle\tilde{\mathbf{h}}_{i,\alpha}\tilde{\mathbf{h}}_{i,\beta}\left(t\right)\right\rangle &= \delta_{\alpha\beta}
\end{aligned} \tag{2.58}$$

where α and β denote Cartesian components, k_B is Boltzmann's constant, and $\tilde{\mathbf{h}}_i$ is a Gaussian random variable with a mean of zero and a variance of one. Since Langevin is local in nature, the target temperatures θ^+ and θ^- are specified for each particle. We modify the velocity Verlet algorithm in the presence of the Langevin thermostat by performing the discretization used in

LAMMPS [154]:

$$\begin{aligned}
\mathbf{v}_i\left(t+\frac{\Delta t}{2}\right) &= \mathbf{v}_i(t) - \frac{\Delta t}{2}\left[\frac{\nabla_i \Pi(t)}{m} + \zeta \mathbf{v}_i(t)\right] + \sqrt{\frac{\Delta t k_B \theta \zeta}{m}}\tilde{\mathbf{h}}_i \\
\mathbf{x}_i(t+\Delta t) &= \mathbf{x}_i(t) + \mathbf{v}_i\left(t+\frac{\Delta t}{2}\right)\Delta t \\
\mathbf{v}_i\left(t+\Delta t\right) &= \mathbf{v}_i\left(t+\frac{\Delta t}{2}\right) - \frac{\Delta t}{2}\left[\frac{\nabla_i \Pi(t+\Delta t)}{m} + \zeta \mathbf{v}_i\left(t+\frac{\Delta t}{2}\right)\right] + \sqrt{\frac{\Delta t k_B \theta \zeta}{m}}\tilde{\mathbf{h}}_i.
\end{aligned} \tag{2.59}$$

We note that because of the Verlet scheme, the time step in each velocity update is now $\frac{\Delta t}{2}$ rather than Δt. As per Langevin's requirements, we generate a different random variable for each particle during each velocity update.

Chapter 3

Results with the 1D Atomistic Framework

In this chapter, we present verification studies and shock wave propagation results obtained with the one-dimensional atomistic framework. These results have also been published in *Computer Methods in Applied Mechanics and Engineering* [1].

3.1 1D atomistic moving window

In traditional NEMD shock wave simulations, the shock front cannot travel far before encountering a boundary, and this vastly limits the overall simulation time. In the present work, we address this problem by implementing a moving window method which is similar in principle to moving boundary conditions used in [79] and [80] to model dynamic crack propagation. Both of these works use a finite number of particles to model a crack in an infinite strip so that the crack reaches steady state. The infinite strip is achieved by pasting crystals ahead of the crack tip and cutting broken crystals away from the other end as the crack advances through the medium. As a result, the crack always remains at the center of the simulation cell without reaching the boundary. Additionally, energy absorption regions are created on the leading and trailing edges of the grid to dissipate any elastic waves emanating from the crack.

Incorporation of a shock wave into the moving window framework is inspired from [76] and [77] where a constant flux of material with a given density and velocity is fed into the simulation window by inserting a plane of atoms into the right boundary at regular time intervals. Unlike our framework, this moving window technique utilizes piston-driven simulations to generate a shock wave. Like our framework, however, this method imposes self-consistently

obtained boundary conditions laterally to the direction of shock front propagation and thus brings the shock wave to rest within a finite-length simulation domain. Therefore, the moving window method of [76] and [77] is able to treat the complex processes occurring behind the shock wave front indefinitely without the number of atoms included in the simulation cell continually increasing. We introduce a modified version of this moving window technique into our formulation to eliminate wave reflections and thus follow the propagating shock front for long simulation times.

3.1.1 Atomistic geometry

When performing shock wave simulations with the moving window in a purely atomistic setting, only the fine-scaled region of Fig. 2.6 is used, and we divide it into three sections as shown in Fig. 3.1. The outer atoms (orange circles) constitute the *thermostat regions* (TRs) while the inner atoms (blue circles) constitute the *window region* (WR). The WR is governed by the classic MD equations of motion, and the Langevin thermostat is applied exclusively to the two TRs in order for the entire domain to reach the desired temperature [78]. Semi-periodic boundary conditions are employed as detailed in Sec. 2.4.1. In this case, however, the thermostat atoms at the ends of the fine-scaled chain ($x_{A,0}$ and $x_{A,F}$) are made neighbors with the thermostat atoms at the TR/WR interfaces ($x_{WR,0}$ and $x_{WR,F}$ respectively). The atoms at the TR/WR interfaces interact with each other normally.

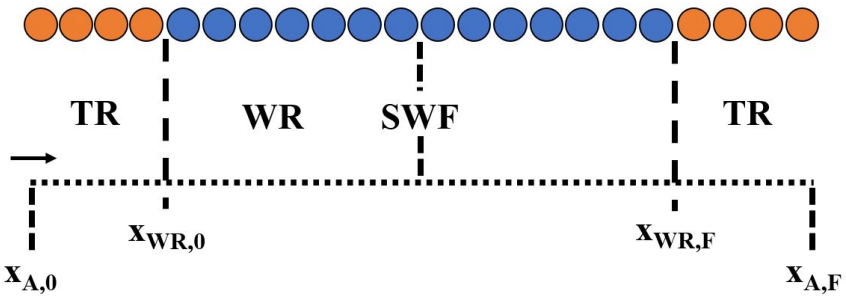

Figure 3.1: Domain geometry for atomistic shock simulations.

To minimize artificial kapitza resistance across the TR boundaries as well as efficiently absorb impinging transient waves, we specify the damping factor ζ in the Langevin thermostat

to be a function of position relative to each TR/WR interface. Specifically, we utilize the equation developed in [78] to linearly ramp damping in each TR as the distance from the TR/WR interface increases. This equation is given as follows:

$$\zeta = \zeta_0 \left[1 - \frac{d\left(x_i\right)}{l} \right] \tag{3.1}$$

where ζ_0 equals the maximum damping (one-half the Debye frequency), and l is the length of the given TR. Additionally, $d(x_i)$ is the minimum absolute distance from atom i at position x to the end of the fine-scaled chain (either point $x_{A,0}$ or $x_{A,F}$). Thus, for atoms in the TRs, the damping coefficient varies linearly from zero at the TR/WR interfaces to ζ_0 at the ends of the chain. This allows transient waves to enter the TRs and slowly be absorbed as they propagate to the ends of the chain. Such a technique reduces spurious wave reflections and thus prevents artificial heating in the WR [78, 155].

3.1.2 Atomistic moving window mechanism

A schematic of the atomistic moving window technique is shown in Fig. 3.2. The shock wave originates at the center of the WR as detailed in Sec. 3.1.3 and immediately begins propagating forward into the unshocked material. After the shock has traveled a distance of one equilibrium lattice spacing r_0, atom N_1 is set equal to atom N_2, atom N_2 is set equal to atom N_3, and so on down the chain up to and including atom $N_{Total} - 1$. This process effectively removes the thermostat atom at $x_{A,0}$ and simultaneously shifts every atom to the position of its nearest right neighbor. During this shifting mechanism, the window atom at the left TR/WR boundary becomes a thermostat atom, and the thermostat atom at the right TR/WR boundary becomes a window atom.

As a result of this process, atom N_{Total} is effectively removed, and hence the atomic position at $x_{A,F}$ is vacant. Therefore, we insert a new N_{Total} atom into the chain with position $x_{Total} = x_{Total-1} + r_0$ (unstrained system), velocity $v^- = 0$ km/s, and acceleration $a^- = 0$ km/s^2. Local atomic energy fluctuations induced near $x_{A,F}$ by the insertion of atom N_{Total} are dampened by the Langevin thermostat as in [77]. This shifting/insertion method constitutes the

moving window formulation for a one-dimensional purely atomistic framework, and it occurs iteratively with a frequency of $\tau^{-1} = U_S/r_0$ as the simulation progresses. The moving window maintains the shock front at the center of the WR indefinitely instead of the shock propagating forward to the right boundary and dissipating.

Figure 3.2: Mechanism of the atomistic moving window technique.

3.1.3 Initialization of the atomistic shock wave

Typically, shock waves are generated by subjecting the computational domain to flyer-plate loading scenarios leading to very high strain rates in the shocked material. The atomistic formulation, by contrast, initializes the shock wave using techniques inspired from the uniaxial Hugoniostat method [70, 71, 72, 73]. Specifically, we employ the Hugoniot jump conditions to characterize the shock wave and then couple a thermostat to a portion of the domain, so the correct temperature is obtained. Our framework differs from the Hugoniostat method, however, because the thermostat is only applied to the prescribed TRs which allows us to simulate the evolution of the shock front over time and evaluate its structure.

To maintain consistency, we always define the shock wave front (SWF) to originate at the center of the WR. All the particles to the right of the SWF constitute the unshocked material, while all the particles to the left of the SWF constitute the shocked material. For every shock wave simulation, the unshocked state of the material is specified as follows: ($v^- = 0$ km/s, $\epsilon^- = 0, \theta^- = 298$ K). We note that the Hugoniot parameters are typically reported for a material with this initial state [21]. Nonetheless, the framework would still be valid for other unshocked

states, provided that suitable Hugoniot parameters of Eq. (2.14) could be obtained. The initial temperature is imposed inside the right TR ensuring that all of the unshocked material maintains a mean temperature of 298 K [78].

We choose an initial shock wave velocity and use Eqs. (2.12) and (2.14) to obtain the strain and mean particle velocity for the shocked material. This mean particle velocity represents a new equilibrium velocity for atoms in the shocked region, and the integration algorithm is updated accordingly. The imposed strain causes the shocked region to compress uniaxially, and the atoms obey the Cauchy-Born rule such that their new positions follow the overall strain of the shocked region [156]. The non-zero particle velocity and compressive strain cause the shocked region to reach the final Hugoniot state and produce a forward-propagating shock wave beginning at the center of the WR. The temperature rise is calculated from Eq. (2.32) and imposed in the left TR, so the entire shocked region achieves this temperature. The parameters (v^+, ϵ^+, θ^+) represent the entire state of the shocked material.

We note that the size and position of the TRs are chosen such that they are far away from the SWF (the non-equilibrium region). As discussed in [19], the shock velocity vs. particle velocity Hugoniot relation links a given initial equilibrium state to all possible final equilibrium states for planar shock waves. Hence, the thermostat bands are in regions of "local" equilibrium. As shown in [70], a thermostat coupled to a strained system in the shocked state will cause the system to reach an equilibrium temperature appropriate to the final state of the Hugoniot. Therefore, we can validly apply a thermostat to a strained section in a local equilibrium region far from the SWF to achieve the desired temperature in the shocked material.

3.2 1D atomistic verification studies

In the remaining sections of this chapter, we present verification studies and shock propagation results for the one-dimensional atomistic framework. As discussed in Sec. 1.2.3, I have obtained new results with the atomistic framework since presenting it for my master's thesis [85]. In each chapter after this, we focus on the CAC framework exclusively.

We perform three sets of verifications with the atomistic framework to ensure that (i) the Langevin thermostat maintains the desired equilibrium temperature, (ii) the potential functions

accurately represent mechanical properties, and (iii) there are no spurious reflections or artifact waves at the TR/WR interfaces. For the sake of brevity, details on (i) and (ii) are presented in Appxs. A.1 and A.2 respectively. In Appx. A.1, we found that the Langevin thermostat maintained a canonical ensemble for a range of different input temperatures. This effect was observed regardless of the potential function used. In Appx. A.2, we found that the Lennard-Jones and modified Morse potentials gave accurate tangent moduli values for a range of input temperatures, and the EAM potential accurately represented both the cohesive energy and bulk modulus of Cu at 0 K.

We conduct the third *steady state* verification using the atomistic framework from Fig. 3.1. To do this, we first explored how changing the length of the TRs as well as the damping factor ζ influenced the system's ability to achieve steady state and obtain canonical temperature fluctuations. We varied the length of each TR from 3 to 500 atoms and the damping factor from 0.1 to 1.0 times the Debye frequency (ω_D) of Cu. First, we found that each TR needed to be at least the range of the forces as a shorter length failed to dampen energetic pulses and resulted in wave reflections into the WR. Hence, we perform all atomistic simulations with 100 atoms in each TR to ensure that transient phenomena are properly dissipated during long-time simulations. Additionally, we found that the optimal value for ζ_0 was one-half the Debye frequency. A smaller ζ_0 (weak damping) failed to achieve a canonical ensemble in the WR, while a larger ζ_0 (hyper damping) resulted in large fluctuations in the WR [157]. These findings are consistent with results previously obtained for the CADD framework [78]. Therefore, we always use a maximum damping of $\frac{1}{2}\omega_D$ with the Langevin thermostat.

To ensure that the TR/WR interfaces are not introducing spurious waves into the WR, we prescribe the same continuum states to both TRs. In other words, the problem has now moved either to the left or the right of the shock front in Fig. 2.5. The average particle velocity of the system should remain equal to the initial input value with little to no increase in the average amplitude. A change in the average particle velocity would indicate that the system is not reaching equilibrium, while a large increase in amplitude would mean that energy is being artificially added to the WR. Additionally, after a reasonable interval of time, no traveling waves

should appear in the WR. Such artifacts would mean that waves are not being smoothly absorbed into the TRs and are instead reflecting off the TR/WR interfaces. The presence of these waves could also mean that the periodic boundary conditions are improperly implemented.

We conduct steady state simulations for a one-dimensional monatomic chain of 10,000 Cu atoms using the Lennard-Jones, modified Morse, and EAM potential functions. The Langevin thermostat is applied in each TR with $\zeta = \frac{1}{2}\omega_D$. We test the ability of the TRs to equilibrate the system to the average input particle velocity and properly absorb energetic pulses. Specifically, we perform these studies for the following mean input particle velocities: 0, 3, 6, 9, and 12 Å/ps. The first set of results can be seen in Fig. 3.3, where we plot the average particle velocity of the domain vs. time. The total runtime for each simulation was 3,000 ps. We observe that the system maintains the initial mean particle velocity for the duration of the simulation for every interatomic potential. From these results, we conclude that the WR achieves steady state for long-time simulations.

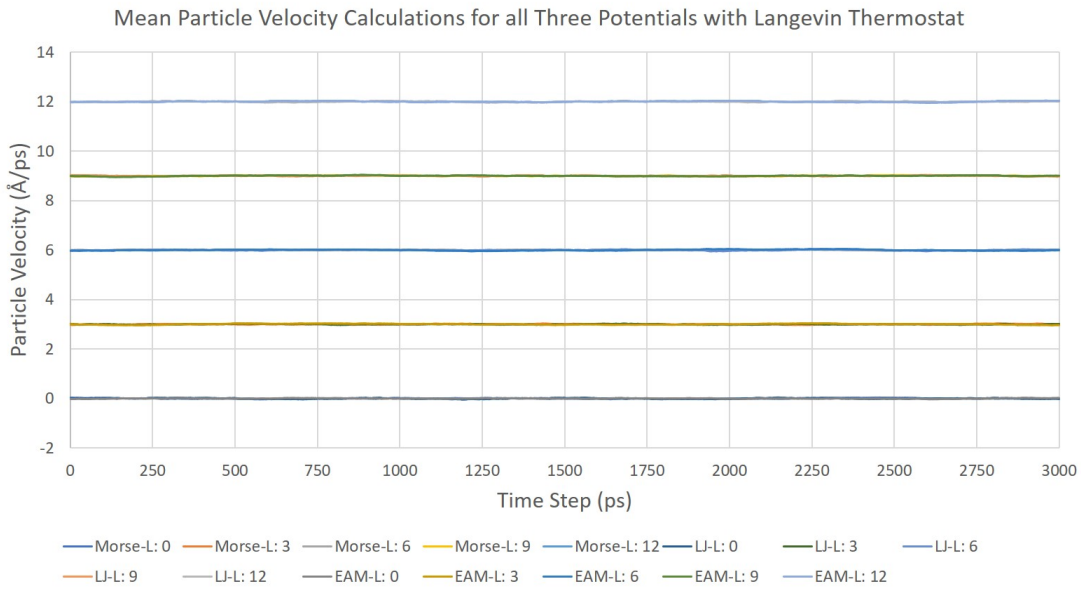

Figure 3.3: Average particle velocity vs. time for 1D atomistic domains with various potentials and input velocities.

Finally, we confirm that the average amplitude of the particle velocities remains relatively constant and no large traveling waves appear throughout the duration of the simulation. Figure 3.4 shows three different particle velocity vs. particle number plots for all three potentials. In each of these graphs, we plot the velocity of each particle at 0 ps and overlay that with

the velocity of each particle at 3,000 ps for each input velocity (0, 3, 6, 9, and 12 Å/ps). We observe that in each case, the amplitude of the particle velocities does not increase as the simulation evolves in time. In fact, the two sets of data overlap each other almost identically indicating that no artificial energy is being introduced into the WR. (We also note that no large traveling waves were observed in the WR over the entire runtime). These results confirm that any waves or pulses encountering the TR/WR interfaces are traveling smoothly into the TRs and eventually being dampened out. Additionally, the data establish that the periodic boundary conditions used in the TRs are implemented correctly.

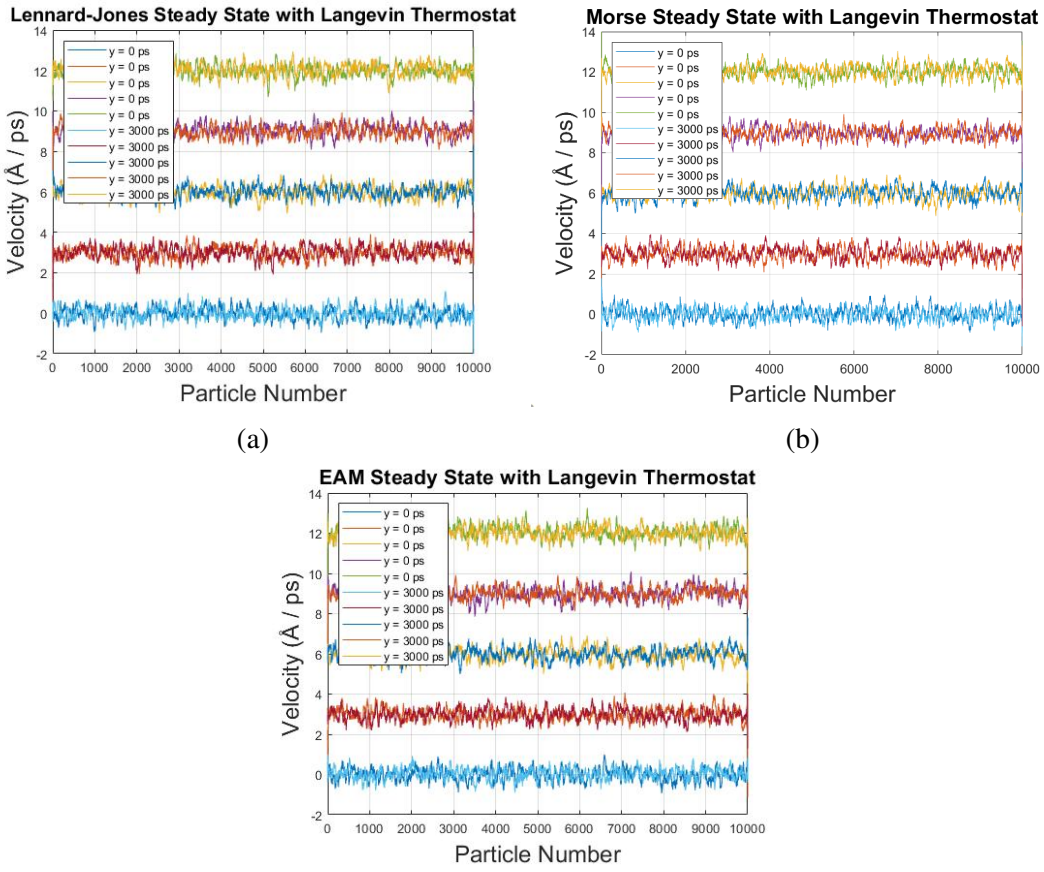

Figure 3.4: One-dimensional atomistic steady state plots using the Langevin thermostat in each TR with the (a) Lennard-Jones, (b) modified Morse, and (c) EAM potentials.

3.3 Shock Hugoniot results

3.3.1 Moving window shock simulations using the experimental Hugoniot parameters

We perform long-time moving window shock wave simulations through an idealized, one-dimensional, "close-packed" chain of Cu particles. The fine-scaled domain contains a total of 10,000 atoms with 9,800 atoms in the WR and 100 atoms in each TR to ensure smooth damping for long-time simulations. Semi-periodic boundary conditions are enforced as described in Sec. 2.4.1, the moving window is applied as detailed in Sec. 3.1.2, and the shock is initialized using the technique described in Sec. 3.1.3. Each simulation is performed for 3 ns in order to track the motion and evolution of the fully-developed wave front. We conduct the first set of simulations with several different shock wave velocities using the experimental Hugoniot parameters for polycrystalline Cu ($C_0 = 3.94$ km/s and $S = 1.49$ [12]). These values serve as an initial guess, and we will derive parameters which produce stationary shocks in Sec. 3.3.2. Fig. 3.5 shows the velocity profile of a moving window shock simulation for an input velocity of U_S = 50 Å/ps (5.0 km/s). In this case, we overlay the initial shock wave with its successive positions in 100 ps increments, so we see the evolution of the wave front over a period of 1,000 ps.

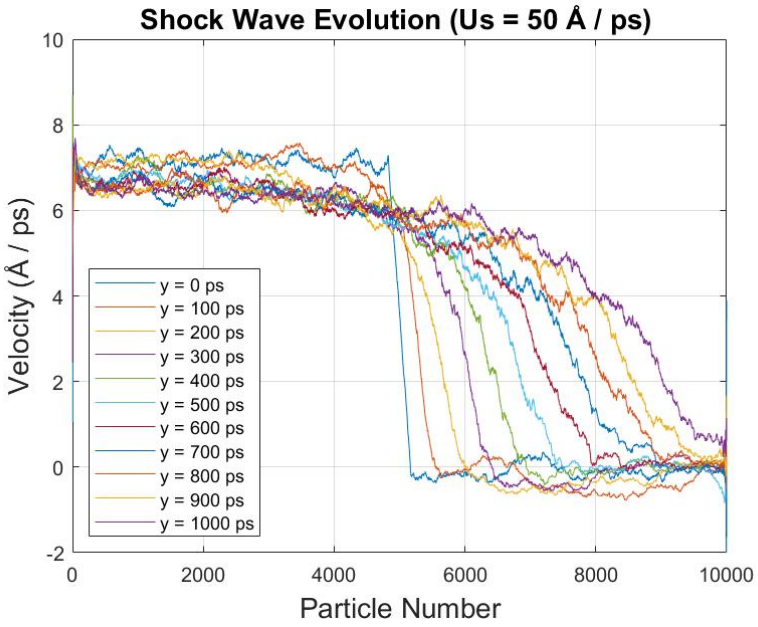

Figure 3.5: Propagation of a shock wave using the EAM potential for an input shock velocity of 50 Å/ps (5.0 km/s). This simulation was performed using the experimental shock Hugoniot parameters for bulk Cu [12].

The moving window method should maintain the shock front at the center of the WR throughout the entire simulation. However, this is not observed in Fig. 3.5 because the experimental Hugoniot parameters of Eq. (2.14) used in our initial guess are derived for a shock traveling through polycrystalline bulk Cu. Several MD studies have measured the shock Hugoniot along the different orientations of a single-crystal Cu lattice and discovered large anisotropic behavior along the different crystal directions [13, 14, 50, 82]. Since the interatomic potentials used in this work have an equilibrium spacing equal to the spacing along the [110] (close packed) direction of a Cu crystal, our initial Hugoniot is not suitable for the current framework. Such anisotropic behavior exists because plane-plane collisions propagate the shock faster along the close packed direction than along the other two directions [13, 14]. Therefore, the moving window update frequency is too slow, and this causes the shock wave to drift forward towards the right boundary.

This drifting effect is also observed by plotting the shock front position vs. time for the following input shock velocities: 47, 50, 54, 58 and 60 Å/ps. In Fig. 3.6 we observe that, in each case, the shock wave travels to the right, and the speed of this forward motion increases with increasing input shock velocity. (The figure terminates at 500 ps because the 60 Å/ps shock encountered the boundary around this time). These results imply that the WR is "falling behind" the forward propagating shock. This lack of agreement between the shock wave velocity and moving window frequency becomes more pronounced as the input shock velocity increases. Therefore, we must calculate a new shock Hugoniot suitable for our framework by plotting the observed shock velocity vs. particle velocity directly behind the shock front. We refer to this new Hugoniot as the '[110]' Hugoniot. These results are presented in Sec. 3.3.2.

3.3.2 [110] shock Hugoniot calculations

To derive new Hugoniot EOS parameters for our close-packed framework, we analyze moving window shock simulations using all three potentials for the following input shock velocities: 47, 50, 54, 58, and 60 Å/ps. We track the position of the SWF as well as the mean particle velocity behind the SWF until the shock impinges upon the right TR/WR interface (analysis after this point is invalid because the shock gets absorbed). To accomplish this, we fit the

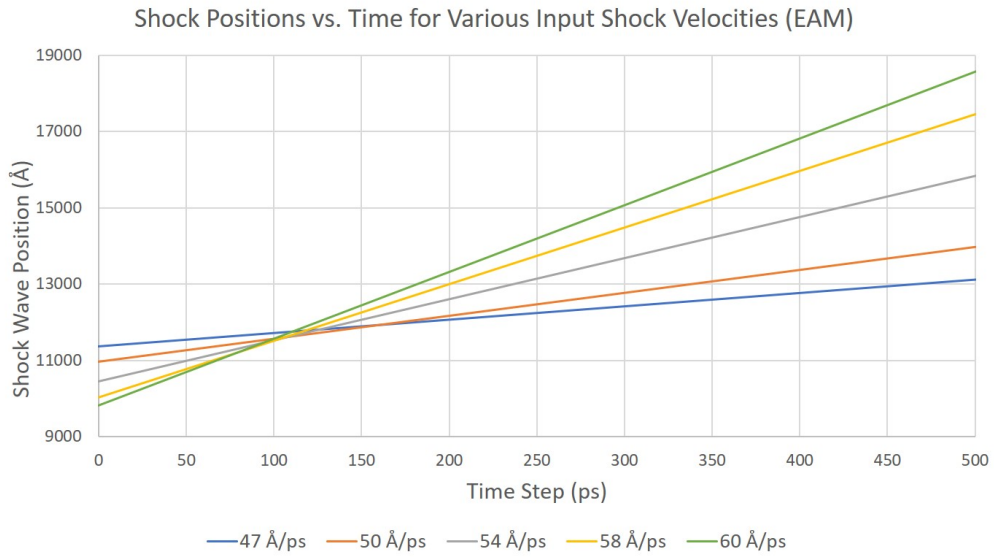

Figure 3.6: Position vs. time of the shock front for various input shock velocities using the EAM potential. Here, we use the experimental shock Hugoniot parameters for bulk Cu [12].

shock's particle velocity profile to a hyperbolic tangent function in MATLAB (using the Curve Fitting tool) for different time steps.

Fig. 3.7 shows a snapshot at 35 ps of a propagating shock with an input velocity of 60 Å/ps (6.0 km/s). We observe four main components in this shock profile: (i) the mean particle velocity in the shocked material (v^+) derived from Eq. (2.14), (ii) the actual mean particle velocity behind the SWF obtained from MD, (iii) the position of the SWF (which is drifting forward), and (iv) the mean particle velocity input by the user in the unshocked material ($v^- = 0$ km/s). We notice that the actual v^+ has a mean value which is slightly higher than that of the analytical v^+. This causes the actual ϵ^+ in the shocked material to be higher than the analytical ϵ^+ which results in a forward propagating shock wave. Therefore, because we used the experimental Hugoniot parameters for polycrystalline Cu in our moving window simulations, the shock values (v^+, ϵ^+, and U_S) obtained from MD with our one-dimensional framework are different from those calculated using the jump conditions. We use these new MD parameters to derive the shock Hugoniot for the close packed monatomic chain.

Fig. 3.8 presents Hugoniot curves of the average shock velocity vs. particle velocity along the close packed, or [110], lattice direction for all three potentials. These Hugoniots were obtained from the five shock wave trials mentioned previously, but we emphasize that

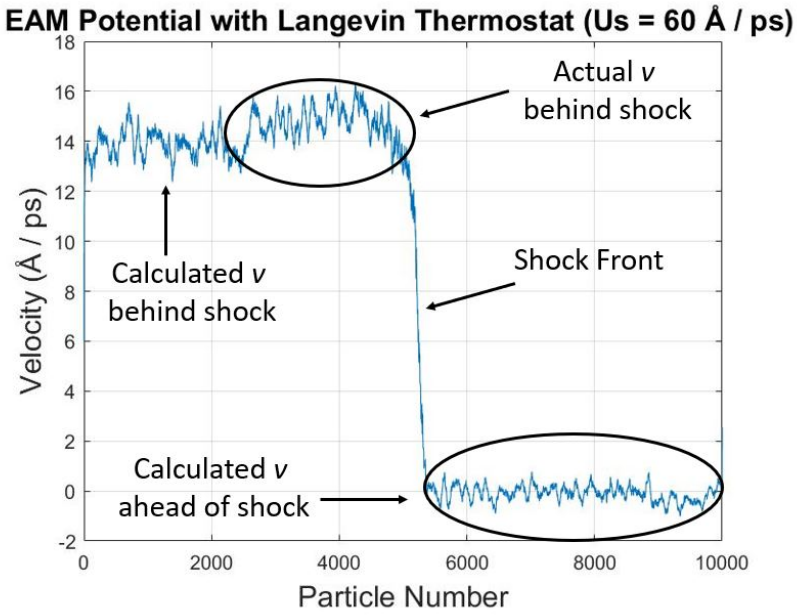

Figure 3.7: Snapshot at 35 ps of a propagating shock with a velocity of 60 Å/ps (6.0 km/s).

the results in Fig. 3.8 are the *calculated* mean shock/particle velocities from MD and *not* their input values. As a comparison, the linear fits to the experimental data of bulk Cu by [12] ($U_S = 3.94 + 1.49v$) as well as NEMD shock simulation results for the [110] direction of perfect single-crystal Cu by [13] and [14] are also plotted in Fig. 3.8. For each potential, the slope of the linear fit is the new S value while the y-intercept is the new C_0 value.

The results from Fig. 3.8 imply that single-crystal Cu is a highly anisotropic material as the shock velocity vs. particle velocity [110] shock Hugoniots for all three potentials deviate significantly from the experimental Hugoniot data. Our findings corroborate the anisotropic nature of shock Hugoniots along different lattice orientations of Cu observed in NEMD simulations [13, 14, 50] as well as MSST simulations [82]. The higher shock wave speeds along the [110] direction are due to plane-plane collisions that propagate the shock faster than along the [100] direction as mentioned previously.

Our simulation results using the Morse and EAM potentials are in good agreement with both Bringa's [13] and Lin's [14] NEMD results for the low particle velocities studied with the atomistic moving window method ($v < 1.6$ km/s). The slopes of the Hugoniots (S values) obtained from these two potentials are very similar to the Hugoniot slopes from the two NEMD studies, but we do observe slight deviations from Bringa's results in the higher velocity region.

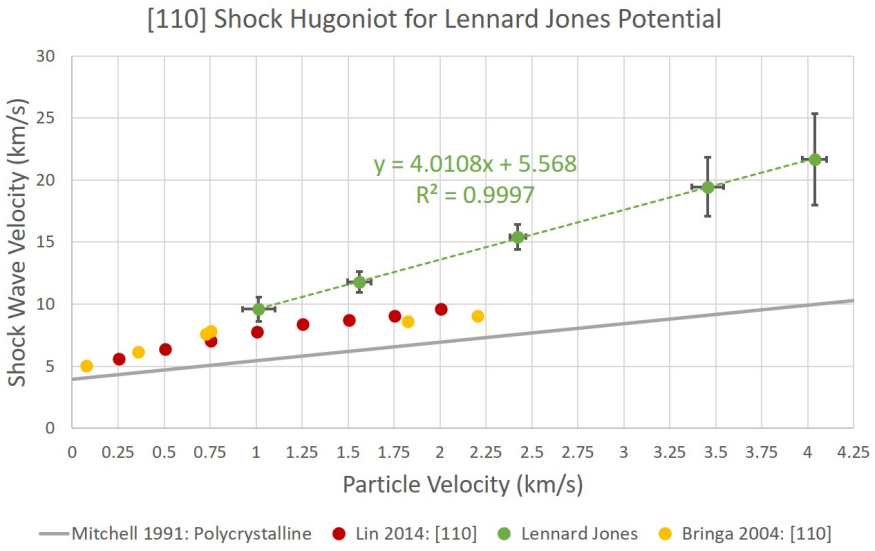

(a)

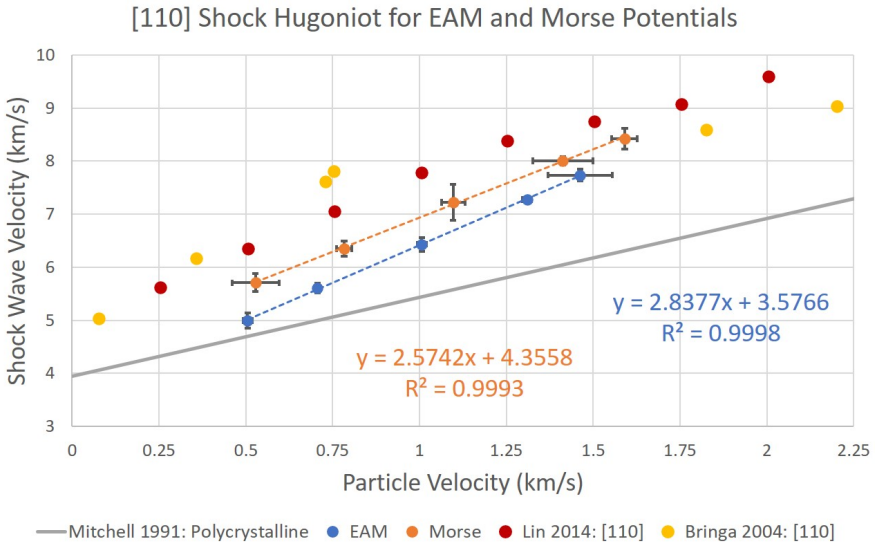

(b)

Figure 3.8: Shock velocity (U_S) vs. particle velocity (v) along the [110] crystal direction of Cu using the (a) Lennard-Jones potential and (b) EAM and Morse potentials. These are compared to other NEMD simulation results for a shock along the [110] direction of a Cu lattice found in [13] and [14]. Additionally, we plot experimental Hugoniot data of bulk Cu from [12].

This is attributed to the higher temperature in the unshocked region (298 K) employed in the current simulations. Lin used an initial temperature of 300 K which is why our moving window results agree more with the results in [14] over the full range of particle velocities studied. The shock wave velocities (and thus C_0 values) obtained with the Morse and EAM potentials are slightly lower than the shock velocities from the NEMD studies, and this could be attributed to small transverse effects in a bulk crystal which are unaccounted for in our one-dimensional monatomic chain.

The same correlation is not observed when using the Lennard-Jones potential which produced shock velocities and particle velocities much higher than those in the NEMD simulations. These high shock velocities would result in plastic behavior which cannot be captured in a one-dimensional chain. Additionally, the slope of the Hugoniot curve obtained from the Lennard-Jones potential is much higher than the slopes from any of the other data sets. Finally we note that Lennard-Jones is, in general, a poor model for Cu. Therefore, we perform all further atomistic moving window simulations using only the Morse and EAM potentials.

The modified Morse and EAM [110] shock Hugoniot results in Fig. 3.8 are in good agreement with the [110] NEMD Hugoniot results, and this provides further confirmation that a shock propagating through a one-dimensional chain of "closed packed" Cu atoms is comparable to a planar shock moving along the [110] direction of a single-crystal Cu lattice. Additionally, these results show that the atomistic moving window formulation presented in this work can be used with multiple interatomic potential functions. We observe that EAM produces C_0 and S values of approximately 3.577 km/s and 2.84 respectively while Morse produces values of 4.356 km/s and 2.57 respectively. We define these as the new empirical parameters of our linear shock Hugoniot and use them to produce a stationary wave front in Sec. 3.3.3.

3.3.3 Moving window shock simulations with the new [110] Hugoniot

In Fig. 3.9a, we present the time evolution of a 50 Å/ps (5.0 km/s) shock wave over 1,000 ps in increments of 100 ps (the total runtime was 3,000 ps). This simulation uses the EAM potential and introduces the new [110] Hugoniot parameters for EAM into Eq. (2.14). We performed the same MD simulations using the modified Morse potential with its new Hugoniot

parameters and saw similar results, so we only present and discuss data for the EAM potential here. In Fig. 3.9a, we achieve much better agreement between the input shock velocity and MD shock velocity than attained in Sec. 3.3.1. The shock front is now remaining stationary in the atomistic domain and not drifting towards the right TR/WR interface.

It is apparent that when using the new [110] shock Hugoniot parameters, the midpoint of the shock front maintains its position at the center of the WR much longer than when using the experimental Hugoniot parameters which assume that the shock propagates along the [100] lattice direction of a bulk crystal. This effect is even more noticeable in Fig. 3.9b where we plot the shock front position vs. time from the new Hugoniot simulations and compare these results to Fig. 3.6. Whereas the shock fronts were all drifting forward before, they are now remaining stationary (as evidenced by the horizontal data points) throughout the duration of each simulation. Therefore, the moving window update frequency now matches the shock velocity, so the atomistic domain is properly following the propagating shock front.

For all of the shock simulations with the new [110] Hugoniot parameters, we do observe an increase in the shock thickness over time. This effect is evident in Fig. 3.9a. Although the midpoint of the shock front remains relatively stationary, the shock "spreads out" across the WR at higher time steps. This is a consequence of the shock developing a structure as it propagates. A structured shock wave is a well-established and characterized phenomenon [158], and it has been observed in many other one-dimensional MD shock simulations [28, 33, 34, 41, 84]. As such, care must be taken to ensure that the WR is sufficiently large to account for the entire structured shock. Otherwise, the shock wave could potentially "leak" out of the WR and impinge on the TR/WR interfaces which could result in shock absorption and energy dissipation at higher time steps. Typically, 1D shock simulations result in a linear increase in the shock thickness (unsteady wave) while 3D shock simulations produce a constant shock thickness (steady wave) [42]. To understand this phenomenon further, we increase the size of the WR and perform additional shock simulations using the new [110] Hugoniot parameters. These results are presented in Sec. 3.4.

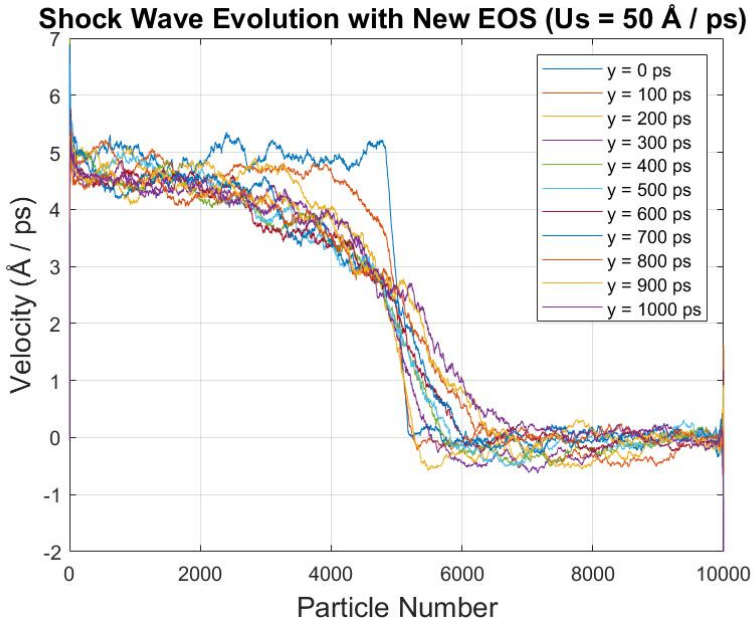

(a)

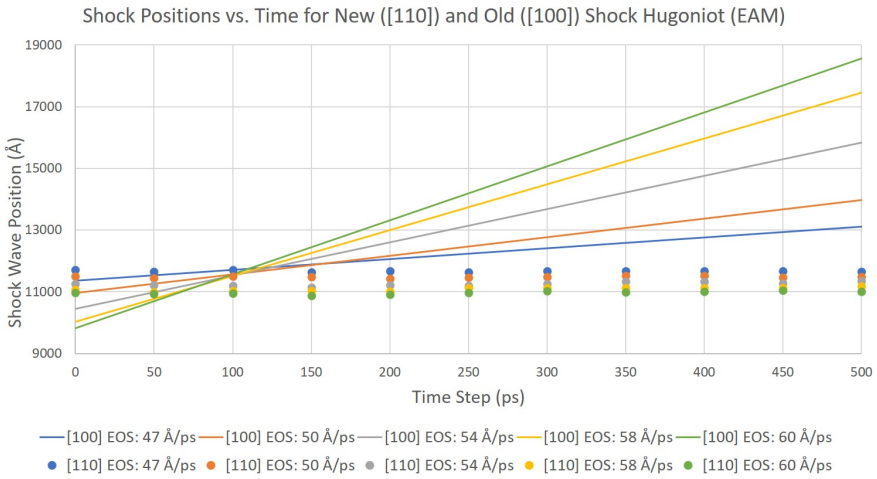

(b)

Figure 3.9: (a) Propagation of a shock wave using the EAM potential and incorporating the new [110] Hugoniot EOS parameters for EAM (U_S = 50 Å/ps). (b) Shock position vs. time when using the new [110] Hugoniot compared to the results from Fig. 3.6.

3.4 Atomistic shock wave structure results

As we saw in Sec. 3.3.3, the shock wave was remaining stationary but was also developing a structure and exhibiting a length scale. In [158], Chhabildas and Assay calculate an upper limit of 3.0 ns and a lower limit of 0.03 ns for the shock rise time (R_S) in Cu. Using the new shock Hugoniot for EAM, we perform long-time moving window simulations using the following input shock velocities: 47, 50, 54, 58, and 60 Å/ps. Assuming the upper limit of 3.0 ns for the shock rise time as well as the highest shock wave velocity of 60 Å/ps, we can obtain a maximum value for the shock thickness (T_S) as follows:

$$T_S = U_S \times R_S = 60\,\text{Å}/ps \times 3,000\,ps = 180,000\,\text{Å}. \tag{3.2}$$

Hence, we increase the atomistic domain size to 80,000 atoms ($\sim 204,500$ Å) and perform shock simulations with the new [110] Hugoniot EOS. (Again, we only show results for the EAM potential as the Morse potential produced similar results.) Velocity profiles for input shock velocities of 50 Å/ps and 60 Å/ps can be seen in Figs. 3.10a and 3.10b respectively.

For both shock wave trials, we clearly observe the shock wave maintaining its position at the center of the WR over time. Additionally, the entire structured shock is well-contained within the WR and thus not being absorbed and dampened by the TRs. However, as seen in Fig. 3.11, the shock wave thickness still increases throughout the entire runtime. For all five shock wave trials, the width increases linearly from 0 to 500 ps and then continues to gradually increase from 500 ps to the end of the simulation at 3,000 ps. Therefore, we conclude that the one-dimensional moving window atomistic framework produces unsteady waves in agreement with other one-dimensional NEMD shock simulations [28, 33, 34, 35, 36, 41, 42, 84]. Our results confirm that such unsteady behavior also occurs in a "close packed" atomistic chain assuming optimized [110] Hugoniot parameters (as opposed to experimental parameters) are incorporated into the linear shock Hugoniot.

We note that most of the NEMD "piston-based" shock studies which utilize a one-dimensional chain of atoms are limited to simulation times of $\leq$ 100 ps because the number of atoms that

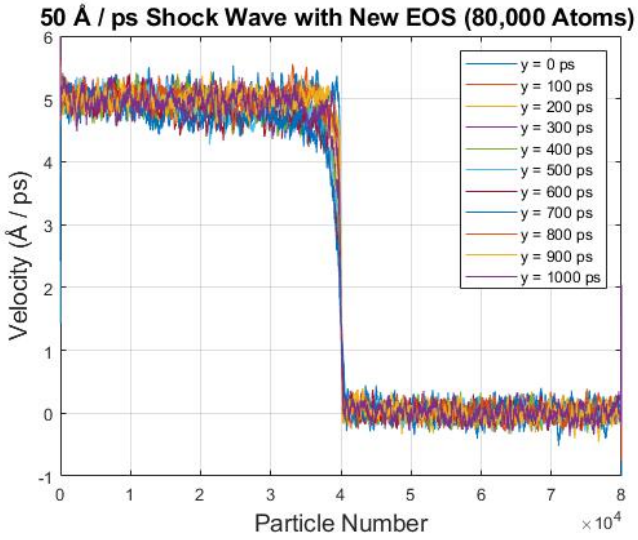

(a)

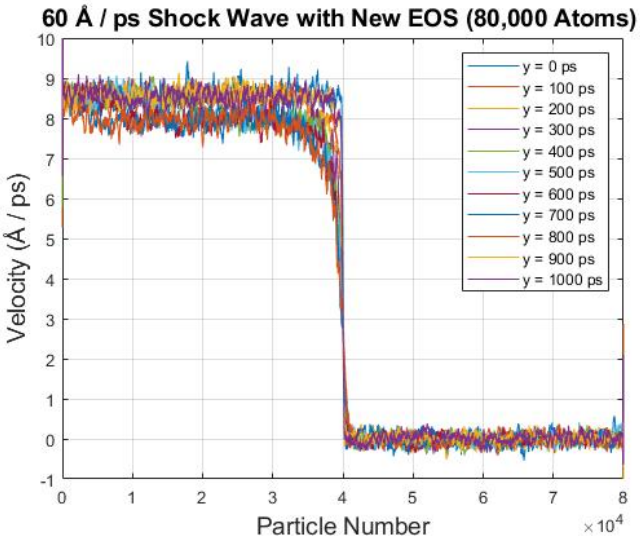

(b)

Figure 3.10: Propagation of the shock wave front using the EAM potential for input shock velocities of 50 and 60 Å/ ps (5.0 and 6.0 km/s). The atomistic domain now contains 80,000 total atoms.

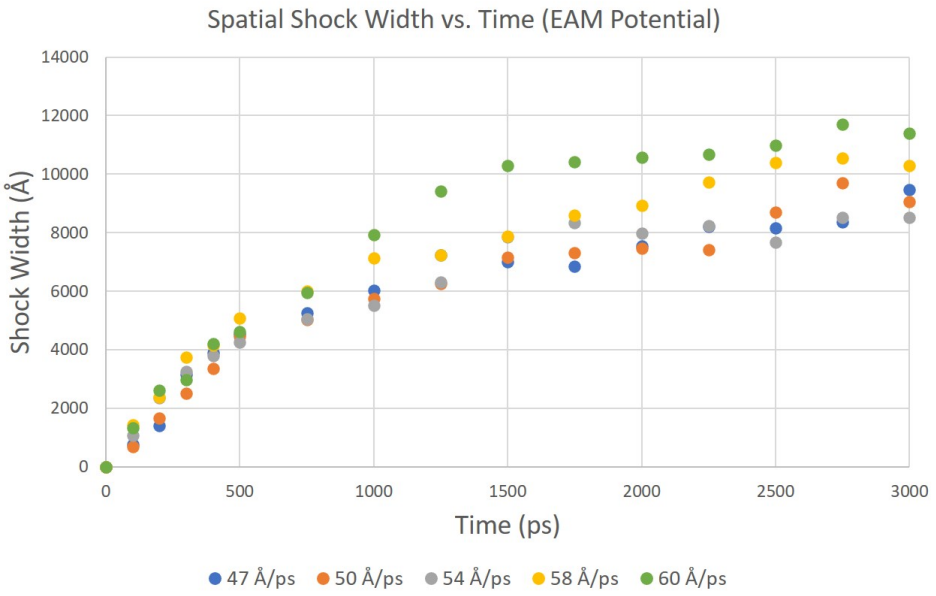

Figure 3.11: Spatial shock width vs. time for five different shock wave trials with the new [110] Hugoniot.

must be included grows as the shock front recedes from the piston face [77]. In such simulations, a linear increase in the spatial width of the shock front is observed, and we also observe this linear growth of the shock thickness up to 500 ps in the current moving window framework. However, as seen in Fig. 3.11, the shock width growth of the five trials begins to diverge after this point. This change in growth rate was not observed in previous one-dimensional NEMD simulations due to limited computational times, and such a phenomenon could be attributed to the minimal transverse motion which occurs for a shock propagating along the [110] lattice direction [50]. Nonetheless, such a change in the rate of increase of the shock width is an interesting result of long-time simulations and could be a topic of future study.

Chapter 4

Concurrent Atomistic-Continuum Method

In this chapter, we discuss the finite element implementation of Atomistic Field Theory and relate this formulation to our one-dimensional framework. Additionally, we present the moving window techniques for a multiscale domain.

4.1 Atomistic Field Theory

The preceding chapter presented results from the purely atomistic moving window framework. At the microscale, the behavior of matter is discrete and governed by the dynamics of individual particles. Hence, an atomistic system can be fully characterized in terms of the masses, positions, accelerations, and velocities of every particle in its domain. However, when attempting to simulate macroscopic phenomena, coarse-grained models are traditionally required because the number of particles that can realistically be incorporated into a given domain is restricted by limited computing power and memory.

Continuum mechanics is one of the earliest coarse-grained field theories and, in contradistinction to atomistics, treats matter as a homogeneous and continuous medium [159]. In continuum mechanics, the smallest structural unit is approximated as a point mass, and the system is described by local properties such as mass density, momentum density, energy density, local velocity, stress, and heat flux. These density functions are related to each other through constitutive relations (i.e. Hooke's Law and Fourier's Law) which serve as the governing equations in the given continuum model. Since atomistic information is ignored in continuum mechanics, the macroscopic material properties cannot be linked to particle motion at the nanoscale.

Rather, these material properties are obtained through macroscale experiments, and, as a result, continuum mechanics is not predictive.

Therefore, there exists a difference in material description between discrete particle dynamics at the microscale and averaged continuum behavior at the macroscale, and the goal of statistical mechanics is to connect these two levels of analysis. At the beginning of the 20^{th} century, Josiah Gibbs developed equilibrium statistical mechanics to successfully link atomic motion to static macroscopic variables [160]. Irving and Kirkwood extended this formalism in the 1950s to a non-equilibrium setting by expressing the continuity equation, motion equation, and energy transport equation in terms of microscopic molecular variables using ensemble averages [87]:

$$\bar{\mathbf{a}}\left(\mathbf{x},t\right) \equiv \left\langle \sum_{k=1}^{N} A(\mathbf{r}_k, \mathbf{v}_k)\delta(\mathbf{r}_k - \mathbf{x}) \right\rangle . \tag{4.1}$$

Here, $\bar{\mathbf{a}}\left(\mathbf{x},t\right)$ is an ensemble-averaged point function, $A(\mathbf{r}_k, \mathbf{v}_k)$ is a dynamic phase function, and $\mathbf{r}_k$ and $\mathbf{v}_k$ are the respective position and velocity of the k^{th} particle. In 1982, Hardy modified the Irving-Kirkwood (IK) methodology for use in MD simulations by implementing a general localization function for spatial averaging [86].

While the IK formalism is critically important for coarse-grained MD simulations, it does not consider the internal deformation of a primitive unit cell. Such internal deformation is a fundamental concept in solid state physics where the displacement of each atom in a polyatomic crystal is a function of both the continuous lattice motion and the discrete sub-lattice motion. Kirkwood, however, did foresee the IK formalism one day being expanded to support the internal degrees of freedom within molecules [161]. This development finally came in the 2000s when Youping Chen used ideas in solid state physics as well as Hardy's methodology to extend the IK formalism into a new framework for multiscale material modeling known as Atomistic Field Theory (AFT) [130]. AFT describes a crystalline system as a continuous collection of material points that each represent a unit cell. These material points are connected to the microscale directly by embedding a group of discrete atoms within each unit cell. Hence, the DOF for every unit cell is a function of the number of atoms inside of it.

Since AFT treats the various length scales of a material concurrently, one of the primary issues in this formulation is the decomposition strategy of atomic variables. AFT addresses this by decomposing the position of a given atom into its bulk lattice position and relative internal position:

$$\mathbf{R}^{k\xi} = \mathbf{R}^{k} + \Delta\mathbf{r}^{k\xi}. \tag{4.2}$$

In Eq. (4.2), $\mathbf{R}^{k\xi}$ is the position of the ξ^{th} atom in the k^{th} unit cell, $\mathbf{R}^{k}$ is the position of the k^{th} unit cell, and $\Delta\mathbf{r}^{k\xi}$ is the relative position between the ξ^{th} atom and the center of the k^{th} unit cell. In physical space, this decomposition is written as follows:

$$\mathbf{z} = \mathbf{x} + \mathbf{y} \tag{4.3}$$

where **z**, **x**, and **y** represent $\mathbf{R}^{k\xi}$, $\mathbf{R}^{k}$, and $\Delta\mathbf{r}^{k\xi}$ respectively. Using this decomposition technique, a new link can be established between the local density function $\mathbf{a}(\mathbf{x}, \mathbf{y}, t)$ in physical space and any dynamic function $\mathbf{A}(\mathbf{r}, \mathbf{p})$ in phase space [130]:

$$\begin{aligned}\mathbf{a}(\mathbf{x}, \mathbf{y}, t) &= \sum_{k=1}^{N_l}\sum_{\xi=1}^{N_a}\mathbf{A}(\mathbf{r}, \mathbf{p})\delta(\mathbf{R}^{k\xi} - \mathbf{z}) \\ &= \sum_{k=1}^{N_l}\sum_{\xi=1}^{N_a}\mathbf{A}(\mathbf{r}, \mathbf{p})\delta(\mathbf{R}^{k} - \mathbf{x})\bar{\delta}(\Delta\mathbf{r}^{k\xi} - \mathbf{y}).\end{aligned} \tag{4.4}$$

In Eq. (4.4), N_l is the total number of unit cells, N_a is the total number of atoms within each unit cell, and **r** and **p** are the atomic position and momenta respectively. Additionally, $\delta(\cdot)$ is the localization function which provides a link between phase space and physical space and can be either a Dirac delta function or a distribution of weighting functions.

AFT thus defines local properties of a material which are continuously distributed at the level of a unit cell but which are discrete within each unit cell. Taking the time derivative of the local density function in Eq. (4.4), one can derive field equations for the conservation of mass, the balance of linear momentum, and the conservation of energy [129]:

$$\frac{\partial\rho^{\alpha}}{\partial t} = -\nabla_{\mathbf{x}}\cdot(\rho^{\alpha}\mathbf{v}) - \nabla_{\mathbf{y}^{\alpha}}\cdot(\rho^{\alpha}\Delta\mathbf{v}^{\alpha}) \tag{4.5}$$

$$\frac{\partial \rho^{\alpha}\left(\mathbf{v}+\Delta\mathbf{v}^{\alpha}\right)}{\partial t} = \nabla_{\mathbf{x}} \cdot \left[\mathbf{t}^{\alpha} - \rho^{\alpha}\mathbf{v} \otimes \left(\mathbf{v}+\Delta\mathbf{v}^{\alpha}\right)\right] + \nabla_{\mathbf{y}^{\alpha}} \cdot \left[\boldsymbol{\tau}^{\alpha} - \rho^{\alpha}\Delta\mathbf{v}^{\alpha} \otimes \left(\mathbf{v}+\Delta\mathbf{v}^{\alpha}\right)\right] + \mathbf{f}^{\alpha} \tag{4.6}$$

$$\frac{\partial \rho^{\alpha} e^{\alpha}}{\partial t} = \nabla_{\mathbf{x}} \cdot \left[\mathbf{q}^{\alpha} + \mathbf{t}^{\alpha} \cdot \left(\mathbf{v}+\Delta\mathbf{v}^{\alpha}\right) - \mathbf{v}\rho^{\alpha}e^{\alpha}\right] + \nabla_{\mathbf{y}^{\alpha}} \cdot \left[\mathbf{j}^{\alpha} + \boldsymbol{\tau}^{\alpha} \cdot \left(\mathbf{v}+\Delta\mathbf{v}^{\alpha}\right) - \Delta\mathbf{v}^{\alpha}\rho^{\alpha}e^{\alpha}\right] + \mathbf{f}^{\alpha} \cdot \left(\mathbf{v}+\Delta\mathbf{v}^{\alpha}\right). \tag{4.7}$$

In the three previous governing equations, ρ^{α} is the local mass density, $\rho^{\alpha}(\mathbf{v}+\Delta\mathbf{v}^{\alpha})$ is the local density of linear momentum, and $\rho^{\alpha}e^{\alpha}$ is the local energy density. Additionally, $\mathbf{v}$ is the macroscopic velocity field, $\Delta\mathbf{v}^{\alpha}$ is the atomistic velocity associated with the internal deformation of a unit cell, $\mathbf{f}^{\alpha}$ is the external force field, and $\mathbf{t}^{\alpha}$ and $\mathbf{q}^{\alpha}$ are the respective momentum and heat flux caused by the homogeneous distortion of unit cells. Also, $\boldsymbol{\tau}^{\alpha}$ and $\mathbf{j}^{\alpha}$ are the respective momentum and heat flux caused by the restructuring of atoms within the unit cells, and they represent the stress and heat flux due to inhomogeneous behavior at the microscale.

For monatomic crystals, which we study in this work, $\mathbf{y}^{\alpha} = \mathbf{0}$ and $N_{\alpha} = 1$ (one atom per unit cell). Then, Eqs. (4.5), (4.6), and (4.7) reduce to the following [127]:

$$\frac{\partial \rho}{\partial t} = -\rho \nabla_{\mathbf{x}} \cdot \mathbf{v} \tag{4.8}$$

$$\rho \frac{\partial \mathbf{v}}{\partial t} = \nabla_{\mathbf{x}} \cdot \mathbf{t} + \mathbf{f}_{ext} \tag{4.9}$$

$$\rho \frac{\partial e}{\partial t} = \nabla_{\mathbf{x}} \cdot \mathbf{q} + \mathbf{t} : \nabla_{\mathbf{x}}\mathbf{v}. \tag{4.10}$$

For conservative systems, the AFT energy equation is equivalent to the AFT linear momentum equation. The AFT formalism facilitates discrete internal deformation within each unit cell and thus provides a mathematical foundation for the CAC method.

4.2 Finite element implementation of AFT

Equations (4.5), (4.6), and (4.7) represent the governing equations of AFT and are similar in form to the balance laws of classical continuum mechanics. As in continuum mechanics, the

analytical solution to these partial differential equations is not readily obtainable, and thus we utilize numerical schemes such as the finite element method (FEM) to solve them. Using the standard definitions of internal force density and kinetic temperature as derived in [162] and [163], we can rewrite the instantaneous balance equation of linear momentum as follows [164]:

$$\rho^{\alpha}\frac{d}{dt}\left(\mathbf{v}+\Delta\mathbf{v}^{\alpha}\right)=\mathbf{f}_{int}^{\alpha}(\mathbf{x})+\mathbf{f}_{ext}^{\alpha}(\mathbf{x})-\frac{m^{\alpha}k_{B}}{M\Delta V}\nabla_{\mathbf{x}}T^{\alpha} \tag{4.11}$$

where ρ^{α} is a volumetric mass density such that

$$\rho^{\alpha}(\mathbf{x},t)=\frac{m^{\alpha}}{\Delta V}. \tag{4.12}$$

In Eq. (4.11), $\mathbf{f}_{int}^{\alpha}(\mathbf{x})$ is the internal force density, $\mathbf{f}_{ext}^{\alpha}(\mathbf{x})$ is the external force density, m^{α} is the mass of the α^{th} atom, M is the total mass of the atoms within a unit cell, ΔV is the volume of the unit cell, T^{α} is the kinetic temperature, and k_B is the Boltzmann constant. If we let $\mathbf{f}_{temp}^{\alpha}(\mathbf{x})=-\frac{m^{\alpha}k_{B}}{M\Delta V}\nabla_{\mathbf{x}}T^{\alpha}$ and $\mathbf{f}^{\alpha}(\mathbf{x})=\mathbf{f}_{ext}^{\alpha}(\mathbf{x})+\mathbf{f}_{temp}^{\alpha}(\mathbf{x})$, then Eq. (4.11) becomes the following:

$$\rho^{\alpha}\ddot{\mathbf{u}}^{\alpha}(\mathbf{x})=\mathbf{f}_{int}^{\alpha}(\mathbf{x})+\mathbf{f}^{\alpha}(\mathbf{x}) \tag{4.13}$$

where $\mathbf{u}^{\alpha}(\mathbf{x})$ is the displacement of the α^{th} atom in the unit cell, and $\mathbf{f}^{\alpha}(\mathbf{x})$ is the external force density which now includes the effects of temperature. The most complex component of Eq. (4.13) is the internal force density which is generally defined as follows:

$$\mathbf{f}_{int}^{\alpha}(\mathbf{x})=\int_{\Omega(\mathbf{x}')}\sum_{\beta=1}^{N_a}\mathbf{f}\left[\mathbf{u}^{\alpha}(\mathbf{x})-\mathbf{u}^{\beta}(\mathbf{x}')\right]d\mathbf{x}'. \tag{4.14}$$

Hence, the internal force density is a nonlinear, nonlocal function of relative displacements between neighboring particles within a given cutoff radius, and it can be obtained exclusively from the interatomic potential function [165].

We calculate the numerical solution of the governing equation (Eq. 4.13) by discretizing the material with finite elements such that each element contains a collection of primitive unit cells. Furthermore, each finite element node represents a unit cell which is itself populated by

a group of atoms. At the lattice level, we use interpolation within an element to approximate the displacement field as follows [117]:

$$\hat{\mathbf{u}}^{\alpha}(\mathbf{x}) = \mathbf{\Phi}_{\xi}(\mathbf{x})\mathbf{U}_{\xi}^{\alpha}. \tag{4.15}$$

Here, $\hat{\mathbf{u}}^{\alpha}(\mathbf{x})$ is the displacement field for the α^{th} atom within a given element, $\mathbf{\Phi}_{\xi}(\mathbf{x})$ is the shape function (linear in this work), and $\mathbf{U}_{\xi}^{\alpha}$ is the displacement of the α^{th} atom within the ξ^{th} element node. We let $\xi = 1, 2, ..., n$ where n is the total number of nodes in the element.

Using the method of weighted residuals, we obtain the weak form of the governing equation by multiplying Eq. (4.13) with a weight function $\mathbf{\Phi}_{\eta}(\mathbf{x})$ and integrating over the entire domain:

$$\int_{\Omega(\mathbf{x})} \left[\rho^{\alpha}\mathbf{\Phi}_{\eta}(\mathbf{x})\ddot{\mathbf{u}}^{\alpha}(\mathbf{x})\right] d\mathbf{x} = \int_{\Omega(\mathbf{x})} \left[\mathbf{\Phi}_{\eta}(\mathbf{x})\mathbf{f}_{int}^{\alpha}(\mathbf{x})\right] d\mathbf{x} + \int_{\Omega(\mathbf{x})} \left[\mathbf{\Phi}_{\eta}(\mathbf{x})\mathbf{f}^{\alpha}(\mathbf{x})\right] d\mathbf{x}. \tag{4.16}$$

Specifically, the Galerkin method is used to obtain Eq. (4.16), so the weight function $\mathbf{\Phi}_{\eta}(\mathbf{x})$ equals the shape function $\mathbf{\Phi}_{\xi}(\mathbf{x})$ in this work. Substituting Eqs. (4.14) and (4.15) into Eq. (4.16), we get the following expression:

$$\int_{\Omega(\mathbf{x})} \left[\rho^{\alpha}\mathbf{\Phi}_{\eta}(\mathbf{x})\mathbf{\Phi}_{\xi}(\mathbf{x})\right] d\mathbf{x}\ddot{\mathbf{U}}_{\xi}^{\alpha} =$$

$$\int_{\Omega(\mathbf{x})} \mathbf{\Phi}_{\eta}(\mathbf{x}) \int_{\Omega(\mathbf{x}')} \sum_{\beta=1}^{N_a} \mathbf{f}\left[\mathbf{\Phi}_{\xi}(\mathbf{x})\mathbf{U}_{\xi}^{\alpha} - \mathbf{\Phi}_{\xi}(\mathbf{x}')\mathbf{U}_{\xi}^{\beta}\right] d\mathbf{x}' d\mathbf{x} + \int_{\Omega(\mathbf{x})} \left[\mathbf{\Phi}_{\eta}(\mathbf{x})\mathbf{f}^{\alpha}(\mathbf{x})\right] d\mathbf{x}. \tag{4.17}$$

Eq. (4.17) is the weak form of the governing equation and can be represented in matrix form as

$$\mathbf{M}^{\alpha}\ddot{\mathbf{U}}_{\xi}^{\alpha} = \mathbf{F}_{int}^{\alpha} + \mathbf{F}^{\alpha} \tag{4.18}$$

where

$$\mathbf{M}^{\alpha} = \int_{\Omega(\mathbf{x})} \left[\rho^{\alpha}\mathbf{\Phi}_{\eta}(\mathbf{x})\mathbf{\Phi}_{\xi}(\mathbf{x})\right] d\mathbf{x} \tag{4.19}$$

$$\mathbf{F}_{int}^{\alpha} = \int_{\Omega(\mathbf{x})} \mathbf{\Phi}_{\eta}(\mathbf{x}) \int_{\Omega(\mathbf{x}')} \sum_{\beta=1}^{N_a} \mathbf{f}\left[\mathbf{\Phi}_{\xi}(\mathbf{x})\mathbf{U}_{\xi}^{\alpha} - \mathbf{\Phi}_{\xi}(\mathbf{x}')\mathbf{U}_{\xi}^{\beta}\right] d\mathbf{x}' d\mathbf{x} \tag{4.20}$$

$$\mathbf{F}^{\alpha} = \int_{\Omega(\mathbf{x})} \left[\mathbf{\Phi}_{\eta}(\mathbf{x})\mathbf{f}^{\alpha}(\mathbf{x})\right] d\mathbf{x} = \int_{\Omega(\mathbf{x})} \mathbf{\Phi}_{\eta}(\mathbf{x}) \left[\mathbf{f}^{\alpha}_{ext}(\mathbf{x}) + \mathbf{f}^{\alpha}_{temp}(\mathbf{x})\right] d\mathbf{x}. \tag{4.21}$$

In the present formulation, we approximate the inertial term using the lumped mass matrix (LMM) [166]. Additionally, no external forces are applied and temperature is incorporated through the use of a thermostat as in [121] and [126]. The internal force density $\mathbf{F}^{\alpha}_{int}$ is the most computationally demanding term, and we evaluate it using either nodal (1D) or Gaussian (2D and 3D) integration techniques. Finally, the second order differential equation (Eq. 4.18) is solved through the velocity Verlet integration algorithm presented in Sec. 2.4.2.

By using this finite element implementation of AFT in conjunction with numerical integration, a majority of the degrees of freedom in the continuum regions are eliminated. For critical regions where atomistic behavior is important (i.e. a shock wave front), the finest mesh is used such that the element length is equal to the atomic equilibrium spacing r_0. In this way, CAC uses AFT to produce a unified theoretical framework between the atomistic and continuum regions. CAC frameworks are defined as AFT domains which contain both fine-scaled and coarse-scaled regions.

4.3 AFT finite element method in 1D

The governing equation derived in Sec. 4.2 describes a polyatomic crystalline lattice composed of three-dimensional elements. However, the framework in Ch. 5 simulates shock wave propagation through a one-dimensional monatomic chain. Therefore, in this section, we show how the AFT finite element equations are applied to a 1D linear element in the coarse-scaled region. Such an element can be seen in Fig. 4.1.

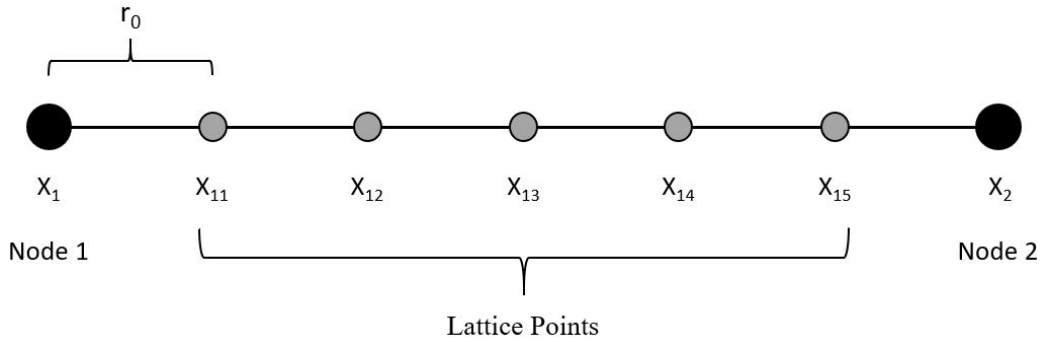

Figure 4.1: CAC coarse-scaled element for a one-dimensional monatomic chain.

This element has a length of $6r_0$ where r_0 is the close-packed lattice spacing. For monatomic crystalline materials, the CAC unit cell only contains one atom. Hence, the "unit cells" at positions x_1 and x_2 consist exclusively of nodes 1 and 2 respectively. Additionally, the element edge contains five lattice points whose positions are interpolated using Eq. (4.15) and which are excluded from the Verlet algorithm. We do not apply any external forces and temperature is incorporated through the Langevin thermostat, so the governing equation reduces to the following in 1D:

$$\mathbf{M}\ddot{\mathbf{U}} - \mathbf{F}^{int} = \mathbf{0} \tag{4.22}$$

where

$$\mathbf{M} = \int_{\Omega(x)} [\rho \mathbf{\Phi}(x) \mathbf{\Phi}(x)] \, dx \tag{4.23}$$

$$\mathbf{F}^{int} = \int_{\Omega(x)} \mathbf{\Phi}(x) \int_{\Omega(x')} \sum_{j=1}^{n_\alpha} f \left[\mathbf{\Phi}(x) U_i - \mathbf{\Phi}(x') U_j \right] dx' dx. \tag{4.24}$$

In Eq. (4.22), $\mathbf{M}$ is the complete mass matrix which is assembled from the LMM of each element in the domain. The standard LMM of a singular, two-node, one-dimensional element is defined as follows:

$$\mathbf{M}^e_{LMM} = \int_0^{L^e} [\rho^e \mathbf{\Phi}^e(x) \mathbf{\Phi}^e(x)] \, dx \approx \frac{m n^e}{2} \begin{bmatrix} 1 & 0 \\ 0 & 1 \end{bmatrix}. \tag{4.25}$$

Here, m is the atomic mass, n^e is the total number of particles and lattice points in the given element (where each particle gives one-half contribution), ρ^e is the atomic density of the element, L^e is the element length, and $\mathbf{\Phi}^e(x)$ is the standard linear shape function in 1D. For the coarse-scaled element in Fig. 4.1, the shape function at any position x along the length of the element would be as follows:

$$\mathbf{\Phi}(x) = [\phi_1(x) \quad \phi_2(x)] = \begin{bmatrix} \dfrac{x_2 - x}{x_2 - x_1} & \dfrac{x - x_1}{x_2 - x_1} \end{bmatrix} = \begin{bmatrix} \dfrac{1 - \xi}{2} & \dfrac{1 + \xi}{2} \end{bmatrix} \tag{4.26}$$

where

$$\xi = 2 \frac{x - x_C}{L^e}, \tag{4.27}$$

and x_C is the central coordinate of the element. We note that in the natural coordinate system, $\xi = -1$ at node 1, $\xi = 0$ at the central point of the element, and $\xi = 1$ at node 2. The coarse-scaled element in Fig. 4.1 has a length of $6r_0$ with two nodes and five lattice points, so its LMM is given as follows:

$$\mathbf{M}^e_{LMM} \approx \frac{6m}{2}\begin{bmatrix} 1 & 0 \\ 0 & 1 \end{bmatrix} = \begin{bmatrix} 3m & 0 \\ 0 & 3m \end{bmatrix}. \tag{4.28}$$

The terms $\ddot{\mathbf{U}}$ and $\mathbf{F}^{int}$ are vectors of the respective accelerations and net internal forces for each particle in the chain. In Eq. (4.24), n_α is the number of neighbors of particle i within a given cutoff radius, and f is the force as a function of relative displacements acting on the particle. If we let

$$f^{int}(x) = \int_{\Omega(x')} \sum_{j=1}^{n_\alpha} f\left[\mathbf{\Phi}(x)U_i - \mathbf{\Phi}(x')U_j\right] dx' \tag{4.29}$$

then we can rewrite Eq. (4.24) as follows:

$$\mathbf{F}^{int} = \int_{\Omega(x)} \mathbf{\Phi}(x) f^{int}(x) dx. \tag{4.30}$$

The force $f^{int}(x)$ on particle i at position x is obtained exclusively from the interatomic potential function, and the corresponding net force is obtained through numerical integration. When finding the force $f^{int}(x)$ for a node in the coarse-scaled region, the surrounding lattice points are taken as neighbors and used to calculate relative displacements.

The internal force density in Eq. (4.30) is calculated using numerical integration techniques, and two of the most popular methods are *nodal* integration and *Gaussian* integration. In nodal integration, the forces in the elements are approximated by the forces at the nodes.

Thus, for the element in Fig. 4.1, Eq. (4.30) would be evaluated as follows:

$$\begin{aligned}
\mathbf{F}^{int} &= w_1 \mathbf{\Phi}(x_1) f^{int}(x_1) + w_2 \mathbf{\Phi}(x_2) f^{int}(x_2) \\
&= (1) \begin{bmatrix} \frac{1-(-1)}{2} \\ \frac{1+(-1)}{2} \end{bmatrix} f^{int}(x_1) + (1) \begin{bmatrix} \frac{1-1}{2} \\ \frac{1+1}{2} \end{bmatrix} f^{int}(x_2) \\
&= \begin{bmatrix} 1 \\ 0 \end{bmatrix} f^{int}(x_1) + \begin{bmatrix} 0 \\ 1 \end{bmatrix} f^{int}(x_2) \\
&= \begin{bmatrix} f^{int}(x_1) \\ f^{int}(x_2) \end{bmatrix}
\end{aligned} \tag{4.31}$$

where $\mathbf{\Phi}(x_1)$ and $\mathbf{\Phi}(x_2)$ are the shape functions at x_1 and x_2, and w_1 and w_2 are the weights associated with nodes 1 and 2 respectively. Although nodal integration is less robust than other integration schemes, it can still produce accurate forces when using simple geometries.

In Gaussian integration, the force $\mathbf{F}^{int}$ is first split into two terms:

$$\mathbf{F}^{int} = \mathbf{FN}^{int} + \mathbf{FE}^{int} \tag{4.32}$$

where $\mathbf{FN}^{int}$ is the internal force density associated with the element nodes, and $\mathbf{FE}^{int}$ is the internal force density associated with the element edge. Gaussian quadratures are then taken in the physical space for each element. Thus, for the element in Fig. 4.1, each term in Eq. (4.32) would be evaluated as follows:

$$\begin{aligned}
\mathbf{FN}^{int} &= \mathbf{\Phi}(x_1) f^{int}(x_1) + \mathbf{\Phi}(x_2) f^{int}(x_2) \\
&= \begin{bmatrix} 1 \\ 0 \end{bmatrix} f^{int}(x_1) + \begin{bmatrix} 0 \\ 1 \end{bmatrix} f^{int}(x_2) \\
&= \begin{bmatrix} f^{int}(x_1) \\ f^{int}(x_2) \end{bmatrix}
\end{aligned} \tag{4.33}$$

$$
\begin{aligned}
\mathbf{FE}^{int} &= w_{IP_1}\mathbf{\Phi}(IP_1)f^{int}(IP_1) + w_{IP_2}\mathbf{\Phi}(IP_2)f^{int}(IP_2) \\
&= (1)\begin{bmatrix} \frac{1+0.57735}{2} \\ \frac{1-0.57735}{2} \end{bmatrix} f^{int}(IP_1) + (1)\begin{bmatrix} \frac{1-0.57735}{2} \\ \frac{1+0.57735}{2} \end{bmatrix} f^{int}(IP_2) \\
&= \begin{bmatrix} 0.78868 \\ 0.21133 \end{bmatrix} f^{int}(IP_1) + \begin{bmatrix} 0.21133 \\ 0.78868 \end{bmatrix} f^{int}(IP_2) \\
&= \begin{bmatrix} 0.78868 \cdot f^{int}(IP_1) + 0.21133 \cdot f^{int}(IP_2) \\ 0.21133 \cdot f^{int}(IP_1) + 0.78868 \cdot f^{int}(IP_2) \end{bmatrix}.
\end{aligned} \tag{4.34}
$$

In Eq. (4.34), IP_1 and IP_2 are the two Gaussian integration points in the element selected as $IP_1 = -\frac{1}{\sqrt{3}}$ and $IP_2 = +\frac{1}{\sqrt{3}}$ in the natural coordinate system with corresponding weights $w_{IP_1} = w_{IP_2} = 1$. We let these two integration points be equal to the nearest lattice points in the element and update the shape functions and weights accordingly. The forces $f^{int}(IP_1)$ and $f^{int}(IP_2)$ are obtained from relative displacements with the surrounding lattice points and nodes. We note that the linear shape functions will result in simple compression or extension in the coarse-scaled element causing the integration point forces to sum to zero. Hence, Gaussian integration reduces to nodal integration in the current one-dimensional framework, but this will not generally be the case for higher-dimensional systems (see Ch. 7).

For a one-dimensional monatomic chain with many elements, the internal force vector would be assembled from the individual force vectors of each element. In a CAC framework, this internal force vector would contain net forces for both atoms and nodes. The only difference in the atomistic force calculations would be the element length L^e (and thus n^e), as well as the fact that the neighbors of atoms are others atoms rather than lattice points. As a result, lattice point positions would not have to be interpolated during the calculation of $f^{int}(x)$ for particles in the fine-scaled region. Since Gaussian integration reduces to nodal integration in 1D, we use nodal integration when performing simulations with the 1D CAC framework.

4.4 CAC moving window in 1D

4.4.1 Geometry for a shock wave

When performing shock wave simulations with the moving window in a multiscale setting, we utilize the entire CAC framework from Fig. 2.6 and divide it into different regions as shown in Fig. 4.2. The outer particles (black and orange circles) constitute the *thermostat regions* (TRs), and these particles flank the interior atoms (blue circles) which constitute the *window region* (WR). We note that the two TRs encompass every continuum node as well as a small "band" of fine-scaled atoms at each A-C interface in order for the WR to achieve the correct canonical ensemble [78]. All the particles to the left of the shock wave front (SWF) constitute the shocked material while all the particles to the right constitute the unshocked material. Semi-periodic boundary conditions are employed as detailed in Sec. 2.4.1, and the particles at the thermostat and A-C interfaces interact with each other directly. As discussed in Sec. 3.1.1, the damping factor ζ in the Langevin thermostat increases linearly throughout each atomistic TR. The only difference here is that $\zeta = \zeta_0$ in the continuum TRs.

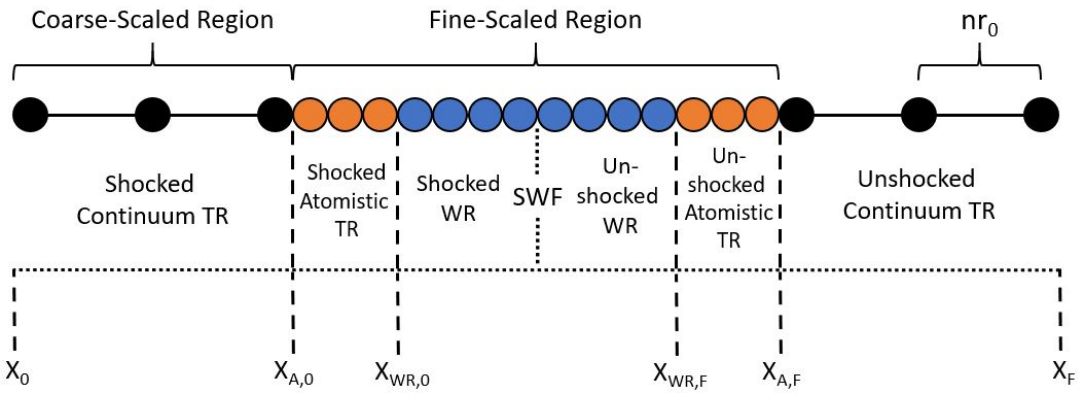

Figure 4.2: CAC geometry for one-dimensional moving window shock simulations.

With the 1D CAC framework, we employ two distinct moving window methods to track the propagating shock front: the *conveyor* technique and the *coarsen-refine* technique. These methods are described in the sections that follow.

4.4.2 Conveyor technique in 1D

A schematic of the moving window using the conveyor technique is shown in Fig. 4.3. The shock wave originates at the center of the WR as detailed in Sec. 4.4.4 and immediately begins propagating forward into the unshocked material. After the shock has traveled one equilibrium spacing r_0, the atomic parameters (initial position, displacement, velocity, and acceleration) of the first coarse-scaled particle in the chain (P_1) are set equal to the parameters of the lattice point immediately to its right (LP_{11}). The initial position of LP_{11} is stored, but its displacement, velocity, and acceleration must be interpolated using the linear shape function from Eq. (4.26) as shown in [123]:

$$\begin{aligned} U_{P_1} &\Rightarrow U_{LP_{11}} = \phi_1(x_{11})U_{P_1} + \phi_2(x_{11})U_{P_2} \\ \dot{U}_{P_1} &\Rightarrow \dot{U}_{LP_{11}} = \phi_1(x_{11})\dot{U}_{P_1} + \phi_2(x_{11})\dot{U}_{P_2} \\ \ddot{U}_{P_1} &\Rightarrow \ddot{U}_{LP_{11}} = \phi_1(x_{11})\ddot{U}_{P_1} + \phi_2(x_{11})\ddot{U}_{P_2} \end{aligned} \tag{4.35}$$

After this, the initial position of LP_{11} is set equal to the initial position of LP_{12} and so on throughout the first element until we reach the final lattice point in the element (LP_{1F}). Then, the initial position of LP_{1F} is set equal to the initial position of P_2. For lattice points, only the initial positions are updated because their displacements are interpolated during the Verlet algorithm. These steps get repeated throughout each coarse-scaled element in the chain, and in the fine-scaled region, the parameters of a given atom are set equal to the parameters of its right neighbor without any interpolation. Lastly, we assign the following values to the final particle in the chain (P_F):

$$\begin{aligned} X_{P_F} &= X_{P_F-1} + r_0 \\ U_{P_F} &= 0 \text{ km} \\ \dot{U}_{P_F} &= 0 \text{ km/sec} \\ \ddot{U}_{P_F} &= 0 \text{ km/sec}^2 \end{aligned} \tag{4.36}$$

where local atomic energy fluctuations induced near x_F are damped by the Langevin thermostat as in [77].

This shifting process occurs iteratively with a frequency of $\tau^{-1} = U_S/r_0$ and effectively allows the monatomic chain to "follow" the propagating shock wave. Therefore, if the simulated shock velocity matches the analytical shock velocity, the SWF should remain at the center of the WR throughout the entire simulation. We refer to this as a conveyor method because the chain moves in the positive x-direction with a constant velocity, and the coarse-scaled and fine-scaled regions always have the same respective lengths. Hence, no real refinement or coarsening of the domain takes place.

Due to the specified shifting frequency, the highest time resolution in the conveyor technique is r_0/U_S. This is solely because the region of interest in the domain is the SWF which travels with a known velocity of U_S. Phenomena with longer or shorter time scales would indeed be captured in the domain, but depending on their relative velocity, they may either outpace or fall behind the wave front and reflect off the A-C interfaces. The time resolution of the conveyor method could easily be increased by shifting the simulation cell more frequently. The only limiting factor would be the time step of the integration algorithm. Hence, the conveyor technique is highly adaptable to other dynamic behavior in materials such as crack growth or dislocation evolution.

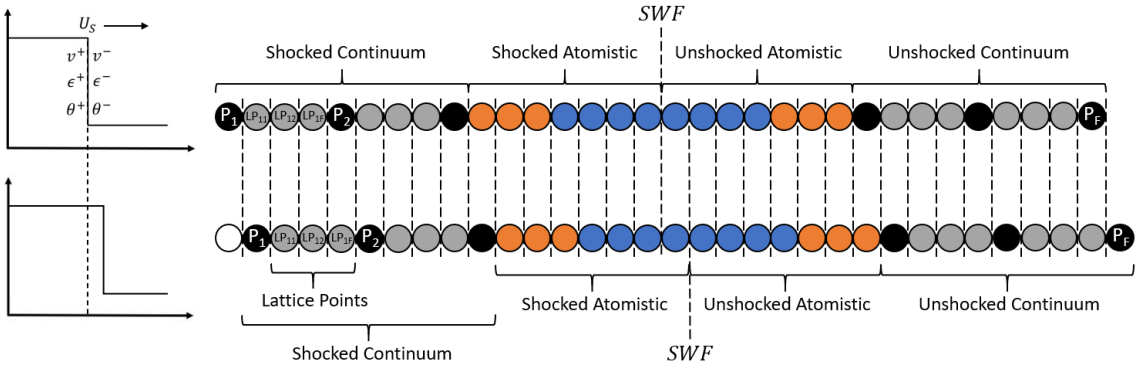

Figure 4.3: Moving window using the conveyor technique in 1D.

4.4.3 Coarsen-refine technique in 1D

A schematic of the one-dimensional moving window using the coarsen-refine technique is shown in Fig. 4.4. As in the conveyor technique, the SWF originates at the center of the WR and propagates into the unshocked material. In the coarsen-refine method, however, atoms near the left A-C interface become lattice points while lattice points near the right A-C interface become atoms. Therefore, the moving window update does not occur until the shock has traveled a distance of one element length nr_0. After this, the last node in the shocked continuum region (the node at the left A-C interface) becomes the second to last node in the shocked continuum region. Next, $n-1$ lattice points are assigned the initial positions of the corresponding $n-1$ atoms in the shocked atomistic region. Then, the first atom in the shocked atomistic region becomes the new A-C interface node and is assigned the initial position, displacement, velocity, and acceleration of the atom $n-1$ positions ahead of it. Effectively, a new continuum element has been created behind the SWF, and the shocked material has been coarsened.

This atomic parameter assignment occurs throughout the fine-scaled region as long as the current atom plus $n-1$ is less than or equal to the first node in the unshocked continuum region. After this point, each fine-scaled atom is assigned the parameters of the given lattice point $n-1$ positions ahead of it. As in the conveyor technique, the initial positions of the lattice points are stored, but their displacements, velocities, and accelerations must be interpolated. Finally, the second node in the unshocked continuum region maintains its parameters from the Verlet update, but it is now defined as the first node in the unshocked continuum region. Effectively, a continuum element ahead of the SWF has been transformed into atoms, and the unshocked material has been refined. After this entire process completes, the LMM is updated to reflect the modified mass distribution.

The coarsen-refine technique occurs iteratively with a frequency of $\tau^{-1} = U_S/nr_0$, and it is distinct from the conveyor method because the initial and final positions of the framework do not change. Rather, the entire monatomic chain remains stationary and only the boundaries of the atomistic region are updated. We also note that the interface atoms of the atomistic TR bands are shifted accordingly. As a result, the shocked continuum region lengthens, the

unshocked continuum region shortens, and the atomistic region tracks the SWF through the domain. For reasons similar to those mentioned in Sec. 4.4.2, the coarsen-refine technique introduces a time resolution of nr_0/U_S into the domain due to the update frequency. Therefore, while phenomena such as elastic waves or dislocations could drift out of the fine-scaled region, they would merely reflect off the boundary or be absorbed by the TRs while the WR tracked the shock.

The current coarsen-refine technique arises from a consideration of the balance between efficiency and accuracy. For example, merely refining the domain ahead of the wave front would result in total accuracy but no efficiency as the fine-scaled region would get larger and larger while the simulation evolved. This would defeat the purpose of the CAC method and significantly increase the computational load over time. Likewise, merely coarsening the domain behind the wave front would result in total efficiency but no accuracy as the fine-scaled region would get smaller and smaller while the shock approached the A-C interface. Thus, we strike a balance between these two extremes by coarsening and refining equally-sized portions of the domain at the same rate.

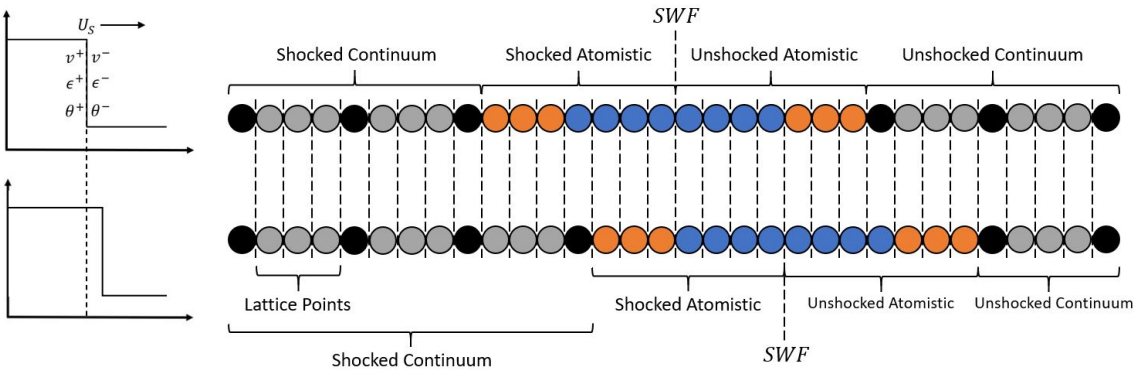

Figure 4.4: Moving window using the coarsen-refine technique in 1D.

4.4.4 Initialization of the shock wave

We choose a final strain ϵ^+ and use Eqs. (2.49) and (2.50) to obtain the mean particle velocity v^+ and shock front velocity U_S. This mean particle velocity represents a new equilibrium velocity for particles in the shocked region, and the integration algorithm is updated accordingly. The imposed strain causes the shocked region to experience uniaxial compression, and

the particles obey the Cauchy-Born rule such that their new positions follow the overall strain of the material. The non-zero particle velocity and compressive strain cause the shocked region to reach its final state and produce a forward-propagating shock wave beginning at the center of the WR. The temperature rise θ^+ is calculated from Eq. (2.51) and imposed in the left TR, so the entire shocked region achieves this temperature [78]. The fine-scaled TR bands are far enough away from the SWF (the non-equilibrium region) such that they are in regions of "local" equilibrium. This ensures the validity of applying thermostats onto strained sections of the domain [70].

Chapter 5

Results with the 1D CAC Framework

In this chapter, we present verification studies and shock wave propagation results obtained with the one-dimensional CAC framework. These results have also been published in *Computer Methods in Applied Mechanics and Engineering* [2].

5.1 CAC verification studies

For the sake of brevity, results from the first two verification studies are presented and discussed in Appxs. B.1 and B.2. In Appx. B.1, we performed force vs. displacement tests to verify that Eq. (4.24) was correctly implemented into the one-dimensional framework as well as ensure force matching at the A-C interfaces. We found that the spring constants of the fine-scaled, coarse-scaled, and CAC domains were nearly identical. Next, in Appx. B.2, we performed temperature equilibration tests to ensure that the thermostat damping method discussed in Sec. 3.1.1 maintained the correct temperature in the undamped WR. We found that the Langevin thermostat equilibrated the system to the given input temperature and maintained this temperature for the entire runtime.

5.1.1 Predicting phonon dispersion relations

The CAC method has been used previously to predict the dynamics of dislocations [120, 167, 168], cracks [169, 170, 171], and phase transformations [172]. Since this is the first attempt to extend CAC to simulate propagating shock waves and since we are incorporating a Langevin thermostat into portions of the domain to achieve the correct unshocked and shocked temperatures, we need to verify that our CAC framework can accurately predict properties of phonon

dynamics. Specifically, we need to ensure that the 1D CAC framework can reproduce the correct *dispersion relation* – a relationship between the wavevector and angular frequency.

Lattice dynamics and spectral energy density background

In crystalline materials, heat is classically conducted through lattice vibrations. At the quantum level, these lattice vibrations are characterized by phonons. Finite temperature is generated in a material through the vibration of atoms around their respective equilibrium positions, and these vibrations can be viewed as a gas of phonons. Because of the interatomic force field, these particle vibrations occur collectively and thus form traveling waves.

Based on the solution of the harmonic equation of motion, Lattice Dynamics (LD) represents a particle's displacement from equilibrium as a series of sinusoidal waves [173, 174]:

$$\mathbf{u}^{\alpha}(\mathbf{x},t) = \frac{1}{(N_l m^{\alpha})^{1/2}} \sum_{\mathbf{k},\nu} \mathbf{e}^{\alpha}_{\mathbf{k}\nu} Q_{\mathbf{k}\nu} exp\left[i\left(\mathbf{k}\cdot\mathbf{x} - \omega_{\mathbf{k}\nu} t\right)\right]. \tag{5.1}$$

Equation (5.1) decomposes the displacement of the α^{th} atom in the l^{th} unit cell at time t into a linear combination of the normal modes $Q_{\mathbf{k}\nu}$, and the linear decomposition originates from crystal symmetry. Each of the normal modes represents a wave that can be characterized by the phonon branch ν in the dispersion diagram along with the wavevector $\mathbf{k}$ and corresponding frequency $\omega_{\mathbf{k}\nu}$. Additionally, $\mathbf{e}^{\alpha}_{\mathbf{k}\nu}$ is the displacement (or *polarization*) vector which gives the direction in which each atom travels, m^{α} is the mass of the α^{th} atom in the l^{th} unit cell, N_l is the total number of unit cells in the domain, and $\mathbf{x}$ is the equilibrium position of the l^{th} unit cell. For a one-dimensional monatomic chain, there is only one atom per unit cell ($\alpha = 1$ and $N_l = N$ where N is the total number of atoms), each atom has the same mass ($m^{\alpha} = m$), displacement to the left is defined as negative while displacement to the right is defined as positive ($\mathbf{e}^{\alpha}_{\mathbf{k}\nu} = 1$), and there is only one phonon branch in the dispersion diagram ($\nu = 1$). Hence, in a one-dimensional setting, Eq. (5.1) reduces to the following:

$$u(x,t) = \frac{1}{(Nm)^{1/2}} \sum_{k} Q_k exp\left[i\left(k\cdot x - \omega_k t\right)\right]. \tag{5.2}$$

Although LD provides a fundamental description of phonon properties in perfect crystals at low temperatures, it cannot account for anharmonic behavior like phonon-phonon scattering. Finite temperature effects can be integrated into LD through quasi-harmonic methods, but such methods are typically unwieldy and impractical to implement [175, 176]. We need to verify that our CAC framework can produce the correct dispersion relation because this relation characterizes the dynamics of a crystalline system and provides a direct test of a given theoretical model [177]. CAC naturally incorporates anharmonic phenomena, and fortunately, alternative methods to LD have been developed to evaluate phonon properties of crystalline systems in MD settings. The most common technique is the calculation of the phonon spectral energy density, and a very robust equation for the spectral energy density comes from a 2010 paper by John A. Thomas and his coworkers [178]. Their derivation is summarized below.

The spectral energy density results from projecting the positions of atoms onto the normal modes of vibration $Q_{\mathbf{k}\nu}(t)$. The contribution to the normal-mode amplitude arising from $u_\xi^\alpha(\beta,t)$ – the displacement in the β^{th} direction of the α^{th} atom inside the ξ^{th} unit cell at time t – is given as follows:

$$Q_{\mathbf{k}\nu}^\alpha(\beta,t) = e_{\mathbf{k}\nu}^\alpha(\beta)\sqrt{\frac{m^\alpha}{N_l}} \times \left\{ \sum_\xi^{N_l} u_\xi^\alpha(\beta,t) \cdot exp\left[i\mathbf{k}\cdot\mathbf{x}_\xi(t_0)\right] \right\}, \tag{5.3}$$

where $e_{\mathbf{k}\nu}^\alpha$ is the corresponding component of the polarization vector, N_l is the total number of unit cells, $\mathbf{x}_\xi(t_0)$ is the equilibrium position of the ξ^{th} unit cell at t_0, and $\mathbf{k}$ and ν are the respective wavevector and phonon branch from before. The total normal-mode amplitude is

$$Q_{\mathbf{k}\nu}(t) = \sum_\beta \sum_\alpha^{N_\alpha} Q_{\mathbf{k}\nu}^\alpha(\beta,t), \tag{5.4}$$

and the average kinetic energy of normal mode $\mathbf{k}\nu$ is as follows:

$$\bar{T}_{\mathbf{k}\nu} = \sum_\beta \sum_\alpha^{N_\alpha} \bar{T}_{\mathbf{k}\nu}^\alpha(\beta) = \sum_\beta \sum_\alpha^{N_\alpha} \left\{ \frac{1}{2\tau_0} \int_0^{\tau_0} \left[\dot{Q}_{\mathbf{k}\nu}^{\alpha *}(\beta,t) \cdot \dot{Q}_{\mathbf{k}\nu}^\alpha(\beta,t) \right] dt \right\}, \tag{5.5}$$

where $\dot{Q}^{\alpha *}_{\mathbf{k}\nu}(\beta,t)$ is the complex conjugate of $\dot{Q}^{\alpha}_{\mathbf{k}\nu}(\beta,t)$. We transform the kinetic energy from the time domain to the frequency domain using Parseval's theorem [179] as follows:

$$\bar{T}_{\mathbf{k}\nu} = \sum_{\beta}\sum_{\alpha}^{N_\alpha} \frac{1}{4\tau_0}\left|\frac{1}{\sqrt{2\pi}}\int_0^{\tau_0}\left[\dot{Q}^{\alpha}_{\mathbf{k}\nu}(\beta,t)\cdot exp(-i\omega t)\right]dt\right|^2, \tag{5.6}$$

where $\omega = \omega_{\mathbf{k}\nu}$ is the angular frequency. If we substitute the time derivative of Eq. (5.3) into Eq. (5.6) and average over N_l, we get the spectral energy density:

$$\varphi(\mathbf{k},\omega) = \frac{1}{4\pi\tau_0 N_l}\sum_{\beta}\sum_{\alpha}^{N_\alpha} m^\alpha \left|\int_0^{\tau_0}\left\{\sum_{\xi}^{N_l}\dot{u}^{\alpha}_{\xi}(\beta,t)\times exp\left[i\mathbf{k}\cdot\mathbf{x}_{\xi}(t_0)-i\omega t\right]\right\}dt\right|^2. \tag{5.7}$$

Equation (5.7) is derived exclusively through LD, and the displacement vectors do not appear here because they are orthonormal. For a one-dimensional monatomic chain, Eq. (5.7) reduces to the following:

$$\varphi(k,\omega) = \frac{m}{4\pi\tau_0 N}\left|\int_0^{\tau_0}\left\{\sum_{n=1}^{N}\dot{u}_n(t)\times exp\left[ik\cdot x_n(t_0)-i\omega t\right]\right\}dt\right|^2. \tag{5.8}$$

The spectral energy density is defined as the average kinetic energy per unit cell as a function of wavevector and frequency. We use Eq. (5.8) to calculate the phonon dispersion curve of the one-dimensional CAC framework by postprocessing atomic velocities in the fine-scaled region and nodal velocities in the coarse-scaled regions.

Spectral energy density results

We test the ability of the CAC method to reproduce the accurate phonon dispersion relation by performing a spectral energy density calculation with the atomistic-continuum domain shown in Fig. 2.6. For this simulation, the monatomic chain contains 260 atoms in the fine-scaled region and 20 nodes in each coarse-scaled region for a total of 300 particles. The element length L in the coarse-scaled regions is defined as six times the equilibrium spacing ($6r_0$), and standard periodic boundary conditions are applied at x_0 and x_F.

The spectral energy density plot as well as the dispersion relation obtained analytically through LD using the modified Morse potential can be seen in Fig. 5.1. The dispersion relation for a one-dimensional monatomic crystal is given by the following standard equation:

$$\omega = \sqrt{\frac{4C}{m}} \left| sin\left(\frac{kr_0}{2}\right) \right| \tag{5.9}$$

where C is the elastic constant defined as the second derivative of the interatomic potential function at r_0 in this case. This simulation was performed at 10 K, and we note that the data is a little noisy because the Langevin thermostat is stochastic and thus generates a new random number for each particle at each time step. The frequency resolution on the vertical axis is 0.004 rad/ps, the wavevector resolution on the horizontal axis is 0.004, and the contours indicate the magnitude of the spectral energy density for each (k, ω) combination.

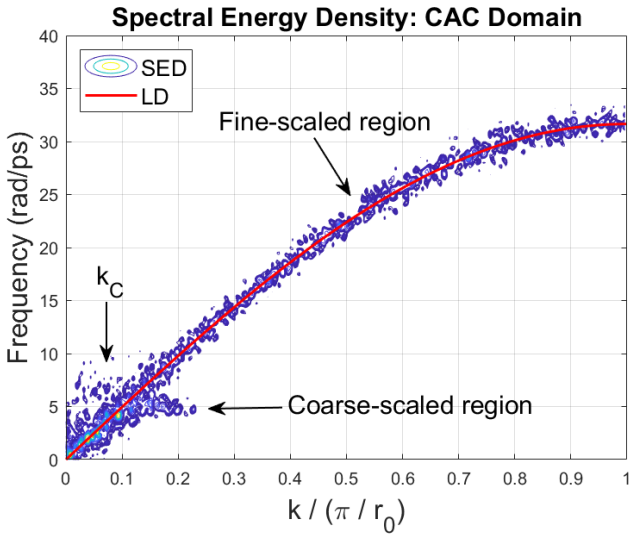

Figure 5.1: Phonon spectral energy density contour plot of a CAC monatomic chain calculated using the *Langevin* thermostat. The red line represents the analytical dispersion relation obtained from LD, and the simulation was performed at 10 K.

In Fig. 5.1, we observe that the phonon dispersion relation obtained in the fine-scaled region of the CAC framework is identical to that obtained from LD. This confirms that if modeled with the finest mesh ($L = r_0$), our CAC domain can accurately reproduce the exact dynamics of particles in an atomistic system. However, the dispersion relation for the coarse-scaled regions is only accurate for phonons whose wavevector is smaller than a critical value, k_C. This

occurs because the linear shape functions used in the coarse-scaled regions inhibit the transmission of small-wavelength phonons with wavevectors larger than k_C or wavelengths smaller than $2\pi/k_C$. The critical wavevector k_C for an allowed error ϵ is calculated by the element length ($L = nr_0$) in the coarse-scaled regions according to the following equation [180]:

$$k_C = \max_k \left\{ \left| sin\left(\frac{kr_0}{2}\right) - sin\left(\frac{kL}{2}\right) \right| \leq \epsilon \right\}. \tag{5.10}$$

For this equation to be valid, the length values must be in nanometers, so $r_0 = 0.25471$ nm and $L = 6r_0 = 1.5283$ nm in our case. We choose an allowable error of $\epsilon = 5\%$ which corresponds to a critical wavevector of $k_C = 0.064\frac{\pi}{r_0}$. Hence, only phonons with wavelengths longer than $\lambda_C = 2\pi/k_C = 7.96$ nm can pass into the coarse-scaled regions with a reflection of less than 5%. This is consistent with the plot in Fig. 5.1 where the difference between the dispersion relations of the fine-scaled and coarse-scaled regions is imperceptible for $k < k_C$.

Therefore, CAC can be used to accurately predict the dynamics of phonons with wavelengths longer than $2\pi/k_C$ even when linear shape functions are incorporated into the coarse-scaled regions. This implies that the current one-dimensional CAC framework can also produce accurate group velocities for phonon wave packets as discussed in Sec. 5.1.3. These results are consistent with spectral energy density plots obtained in previous works which use the CAC method for phonon heat transport and the prediction of phonon properties [121, 126, 180]. Increasing the temperature in the domain merely results in the contours of the spectral energy density having a greater magnitude due to the faster vibrational motion of particles.

5.1.2 Phonon wave packet reflections at the A-C interface

To visualize the transmission and reflection of waves at the A-C interfaces, we perform phonon wave packet studies using the one-dimensional CAC framework. We create the wave packet from a single branch of the dispersion relation obtained in Sec. 5.1.1 with a narrow frequency range and well-defined polarization. Specifically, for each phonon mode, we know the corresponding wavevector k and angular frequency ω from the LD dispersion relation or spectral

energy density plot, and we can generate a Gaussian wave packet by assigning an initial displacement U_n to the n^{th} particle as follows [181, 182, 183]:

$$U_n = A\epsilon(k)exp\left[ik(x_n - x_0)\right] exp\left[-(x_n - x_0)^2/\xi^2\right]. \tag{5.11}$$

In Eq. (5.11), A is the displacement amplitude, $\epsilon(k)$ is the polarization vector ($\epsilon(k) = 1$ in 1D), x_n is the position of the n^{th} particle, x_0 is the position of the particle at the center of the wave packet, and ξ is the spatial extent of the wave packet. The time-dependent displacement and velocity are calculated as follows:

$$U_n^* = U_n \times e^{-i\omega t} \tag{5.12}$$

$$V_n^* = \frac{dU_n^*}{dt} = -i\omega U_n \times e^{-i\omega t}, \tag{5.13}$$

and at $t = 0$, the initial velocity of the wave packet is given as [183]

$$V_n = \omega \times Imag(U_n). \tag{5.14}$$

After the wave packet is initialized in the atomistic region, it propagates into the undisturbed medium, so only the displacement and velocity at $t = 0$ (Eqs. 5.11 and 5.14) are used.

In Fig. 5.2, we present four sets of CAC simulation results with wave packets of the following four central wavevectors: $k = 0.01$, 0.05, 0.1, and $0.2\ \frac{\pi}{r_0}$. These wave packets are chosen to represent a range of values on the dispersion curve such that $k = 0.01\frac{\pi}{r_0}$ is in the atomistic-continuum overlap region, $k = 0.05\frac{\pi}{r_0}$ is slightly below the critical wavevector, $k = 0.1\frac{\pi}{r_0}$ is slightly above the critical wavevector, and $k = 0.2\frac{\pi}{r_0}$ is a short-wavelength phonon which cannot be modeled by the coarse-scaled region. We observe that the long-wavelength wave packet ($k = 0.01\frac{\pi}{r_0}$) achieves nearly complete transmission across the A-C interface, and the $k = 0.05\frac{\pi}{r_0}$ wave packet has only a small reflection. This shows that CAC can accurately incorporate phonon waves into the coarse-scaled regions when $k < k_C$. However, the shorter-wavelength wave packet ($k = 0.1\frac{\pi}{r_0}$) has less transmission at the A-C interface, while the

$k = 0.2\frac{\pi}{r_0}$ wave packet is completely reflected. This is because the wavelength corresponding to $k = 0.2\frac{\pi}{r_0}$ is smaller than what can be modeled by the coarse-scaled region using linear interpolation. The energy transmission of wave packets at the A-C interface for various wavevectors can be seen in Table 5.1.

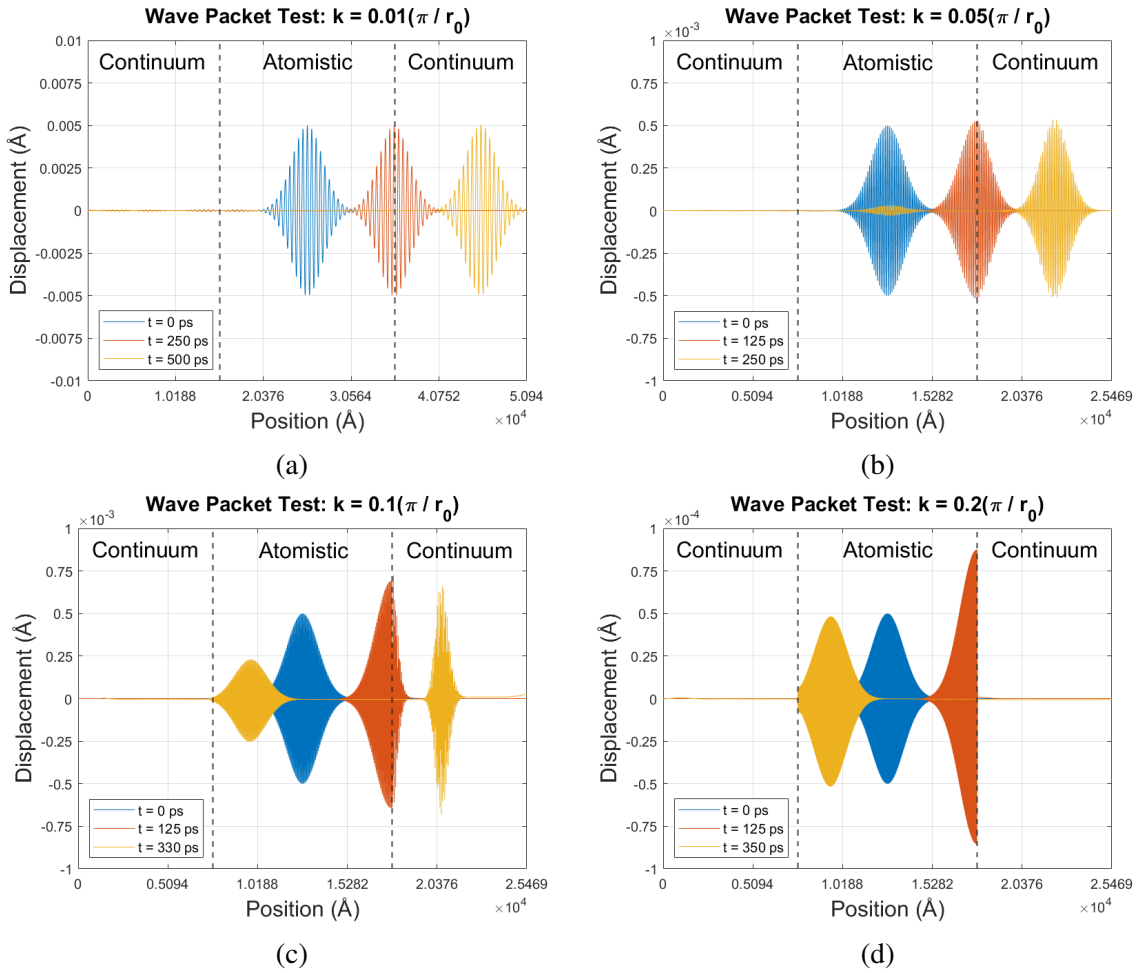

Figure 5.2: Phonon wave packet simulations performed with the following wavevectors: (a) $0.01\frac{\pi}{r_0}$ (b) $0.05\frac{\pi}{r_0}$, (c) $0.1\frac{\pi}{r_0}$, and (d) $0.2\frac{\pi}{r_0}$.

These phonon wave packet results confirm that the reflections at the A-C interface are a direct result of the numerical discrepancy between the atomistic and continuum regions as shown in previous studies [121, 126]. This mismatch is attributed to the dispersive nature of the frequency-wavevector relation which comes from the fact that the nonlocal internal force-displacement relationship is the only constitutive relation in CAC [117]. Hence, the coarse-scaled regions in CAC simulations impede elastic waves with wavelengths shorter than $2\pi/k_C$. To allow these short-wavelength (large wavevector) waves to pass smoothly from the atomistic

to the continuum region, the CAC finite element formulation would need to be modified to allow the full population of phonon waves to propagate across the A-C interface [126].

Table 5.1: Effect of wavevector on the energy transmission of a phonon wave packet traveling from the fine-scaled region to the coarse-scaled region.

$k\,/\,(\pi/r_0)$	$\%$ *energy transmission*
0.01	99.97
0.05	99.61
0.06	99.11
0.07	98.10
0.08	95.83
0.09	90.63
0.10	73.35
0.20	0.00

5.1.3 Moving window with phonon wave packets

To verify that the two CAC moving window methods described in Secs. 4.4.2 and 4.4.3 maintain a stationary wave at the center of the fine-scaled region and do not produce any spurious phenomena at the A-C interfaces, we perform moving window simulations with a phonon wave packet. We choose a medium-wavelength wave packet ($k = 0.2\frac{\pi}{r_0}$) such that the wave would ordinarily be reflected at the A-C interface if allowed to propagate freely. The only distinction with these simulations is that the Langevin thermostat is not applied to the domain – the particles are initially at rest.

Simulation results using the medium-wavelength wave packet both with and without the conveyor mechanism are presented in Fig. 5.3. We observe that this method effectively prevents the phonon wave packet from propagating forward, and the wave remains at the center of the atomistic region. Additionally, no spurious waves appeared at either A-C interface throughout the duration of the simulation. These results confirm that the conveyor moving window method works correctly and can track waves much longer than would be allowed in traditional MD simulations. Hence, when using the analytical shock velocity to determine the update frequency in shock simulations, the conveyor technique should accurately predict the actual speed U_S of the shock front.

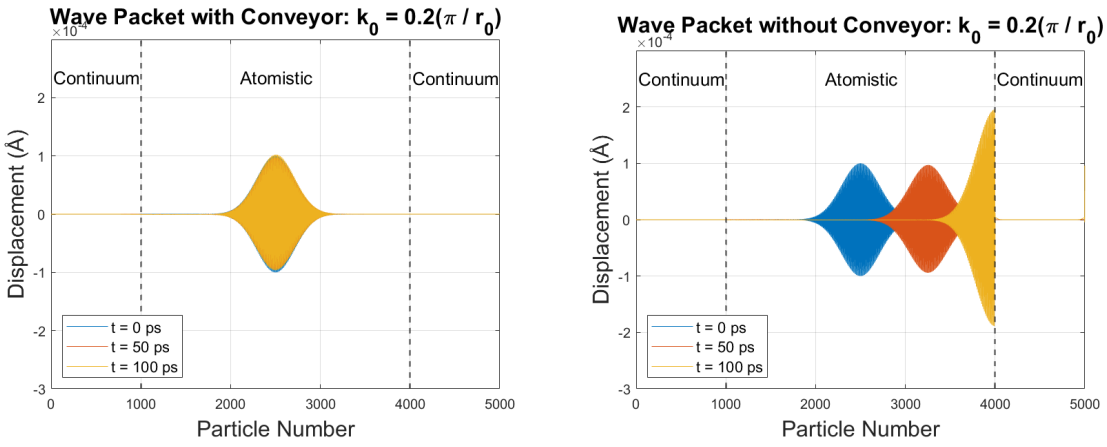

(a) (b)

Figure 5.3: Wave packet simulations performed both (a) with and (b) without the conveyor method.

When modeling a phonon wave packet with the conveyor method, the moving window update frequency is determined by the group velocity of the wave packet. In each simulation, we use the analytical group velocity given by $v_g = \frac{\partial \omega}{\partial k}$ to initialize the update frequency defined as $\tau^{-1} = v_g / r_0$. Then, we observe the drift in the propagating wave packet to calculate its actual group velocity. These analytical and simulated group velocities are plotted against the reduced wavevector in Fig. 5.4. Here, we see that the actual group velocity of the wave packet obtained from the conveyor method follows the analytical group velocity exactly over the full range of wavevectors. This confirms that the conveyor mechanism works correctly for both large and small wavelength waves and does not alter the wave speed in any nonphysical manner.

In Fig. 5.5, we present results of a wave packet simulation performed with the coarsen-refine technique. Here, the wave originates at the left of the domain and travels to the right over a period of 400 ps. The displacement profile of the wave packet at 0 ps, 200 ps, and 400 ps is shown, and the dotted lines represent the position of the left and right A-C interface at each time. We observe that the initial and final positions (x_0 and x_F) remain stationary while the atomistic region moves through the entire domain by the simultaneous coarsening of the left continuum region and refinement of the right continuum region. In effect, the left coarse-scaled region lengthens, and the right coarse-scaled region shortens as the simulation progresses in time. As a result, the fine-scaled region tracks the wave packet thus preventing

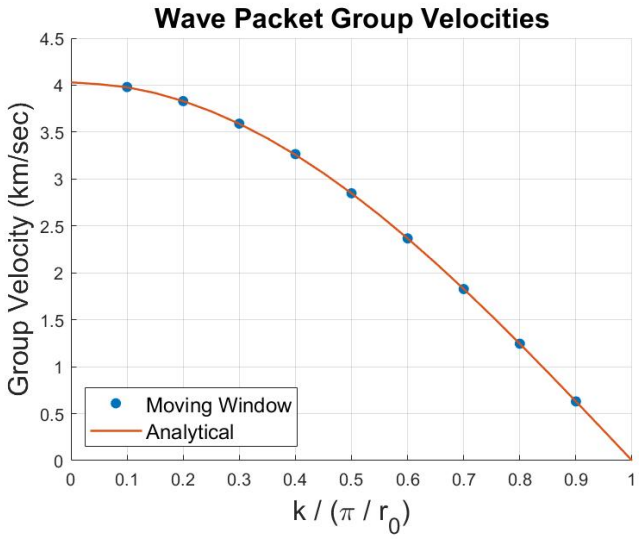

Figure 5.4: Analytical and simulated group velocities of phonon wave packets.

it from ever encountering an interface. The coarsen-refine technique allows one to efficiently follow a propagating wave.

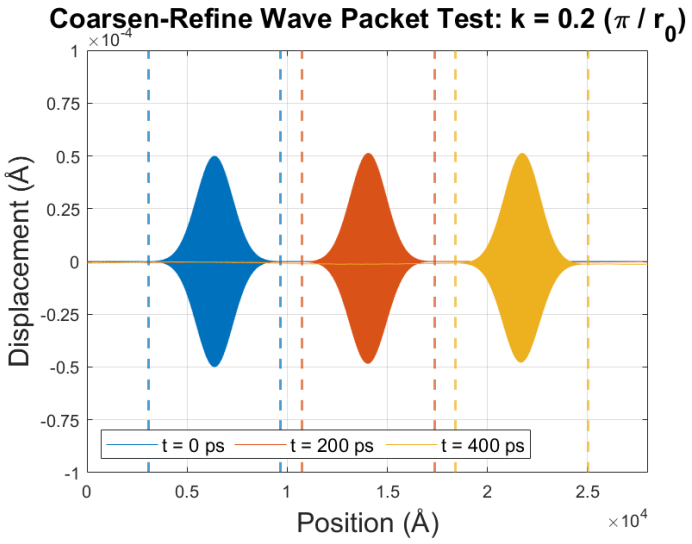

Figure 5.5: Time evolution of a phonon wave packet using the coarsen-refine technique.

5.2 One-dimensional CAC shock propagation results

In this section, we present results from shock wave simulations performed with both the conveyor and coarsen-refine moving window technique using the one-dimensional CAC domain from Fig. 4.2. Before conducting these studies, we had to determine an appropriate length for

the fine-scaled region to ensure that the structured shock front was fully-contained in this region and did not "spill over" into the coarse-scaled regions. The length of the fine-scaled region is determined by the spatial shock thickness (T_S) which is calculated from the shock velocity (U_S) and rise time (R_S) by the following equation: $T_S = U_S \times R_S$. Studies have shown a wide range in the shock rise times for small-domain FCC metals with lower limits of $\sim 10^{-3}$ ns [184] and upper limits of $\sim 10^{0}$ ns [158] for the same material. To be safe, we choose a rise time of $10^0 = 1.0$ ns. The materials studied are Cu, Al, Ag, and Ni with a maximum compressive strain of -0.1. Using a rise time of 1.0 ns with the analytical shock velocity obtained from $\epsilon^+ = -0.1$, we get the following upper limits of the shock thickness for Cu, Al, Ag, and Ni respectively: 55,170 Å ($\sim$21,660 atoms), 79,700 Å ($\sim$27,980 atoms), 42,680 Å ($\sim$14,838 atoms), and 70,700 Å ($\sim$28,452 atoms). Therefore, without loss of generality and to be extra precautious, we perform each shock simulation with 40,000 atoms in the fine-scaled region.

5.2.1 Conveyor method in 1D

We first simulate propagating shock waves in the CAC domain using the conveyor moving window technique described in Sec. 4.4.2. For these simulations, the left and right coarse-scaled regions each contain 20,000 nodes with an element length of $6r_0$ for a total of 80,000 particles in the domain. Additionally, each atomistic TR band contains 100 atoms where $\zeta = \zeta_0$ increases linearly throughout each band. The atomistic TRs are much longer than the force range to ensure that the WR achieves the correct temperature. Simulations are performed with Cu, Al, Ag, and Ni for final strains (ϵ^+) ranging from -0.01 to -0.1, and each simulation is allowed to run for 1.0 ns. Results from four of these simulations for $\epsilon^+ = -0.06$ are shown in Fig. 5.6. Here, the dotted lines represent the A-C interfaces, and we plot the velocity profile of the shock at 0.0 ns, 0.5 ns, and 1.0 ns.

For each of these shock simulations, v^+, U_S, and θ^+ are obtained using the 3rd-order Eulerian thermoelastic equations from Sec. 2.2 (Eqs. 2.49, 2.50, and 2.51 respectively). The Grüneisen constant Γ_1 and density ρ_0 are given in Sec. 2.4.3, and $\hat{\Gamma}_{11}$ is determined from Eq. (2.41). Additionally, the 2nd and 3rd order elastic constants are calculated from the equations developed by Born [185]. These equations allow one to compute the elastic constants of cubic

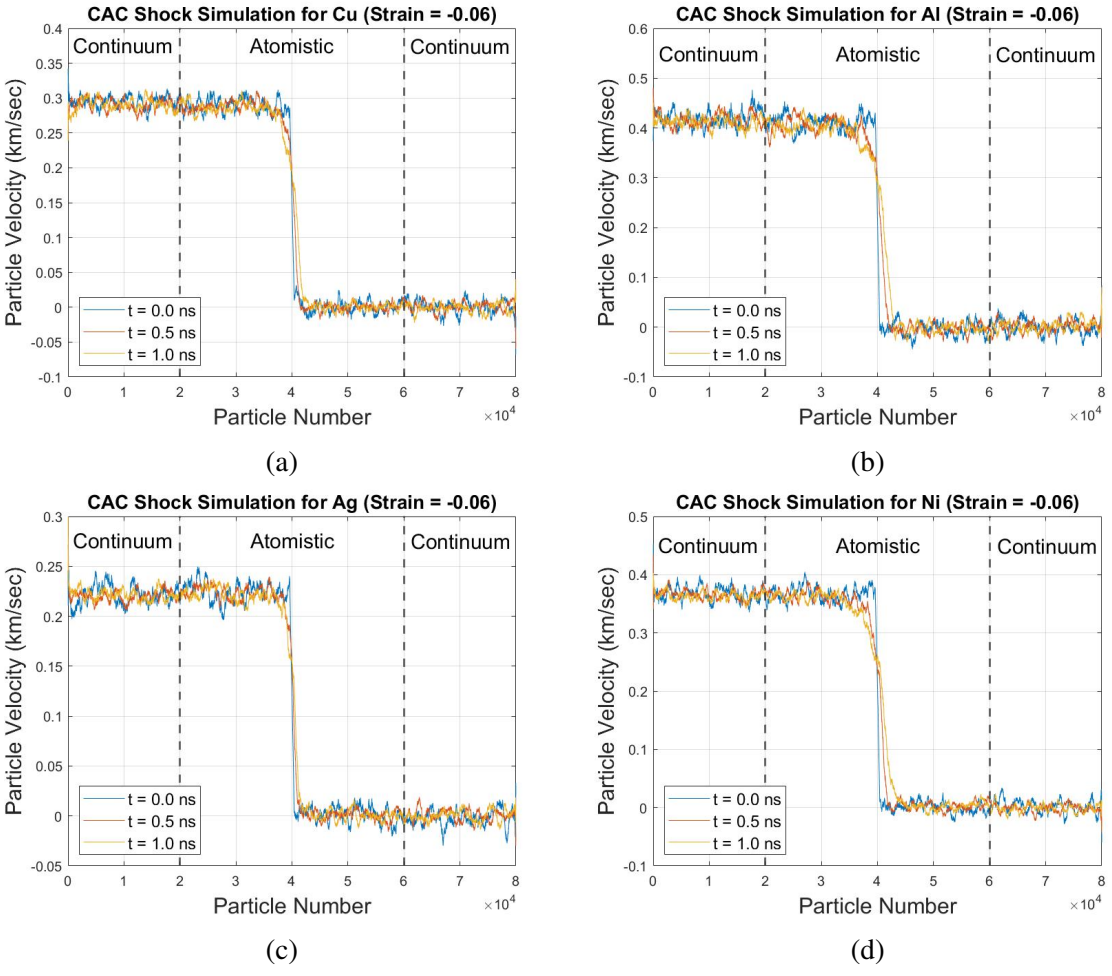

Figure 5.6: Velocity profiles of shock wave simulations performed with the 1D conveyor technique for ϵ^{+} = -0.06. Results are shown for the following four materials: (a) Cu, (b) Al, (c) Ag, and (d) Ni.

monatomic crystals whose atoms interact according to a central pairwise force law [186, 187, 188]:

$$C_{11} = \frac{a^4}{2V} \sum_j m_j^4 D_j^2 \Pi(r_j) \tag{5.15}$$

$$C_{111} = \frac{a^6}{2V} \sum_j m_j^6 D_j^3 \Pi(r_j). \tag{5.16}$$

Here, *a* is one-half the lattice parameter of the material, *V* is the volume per atom ($V = 2a^3$ for FCC crystals), and Π is the interatomic potential. Also,

$$r_j = \left[m_j^2 + n_j^2 + l_j^2\right]^{\frac{1}{2}} a \tag{5.17}$$

where m_j, n_j, and l_j are position coordinates of any atom in the lattice. Finally, D_j is an operator given as follows:

$$D_j = \frac{1}{r_j} \frac{d}{dr_j}. \tag{5.18}$$

With the modified Morse potential, r_0 is defined as the equilibrium spacing along the close packed direction of the lattice. Therefore, we calculate C_{11} and C_{111} using Eqs. (5.15) and (5.16) by summing over the first nearest neighbors of the 1D chain, and we find $\hat{C}_{111}$ from these constants using Eq. (2.39). Knowing Γ_1, $\hat{\Gamma}_{11}$, ρ_0, C_{11}, and $\hat{C}_{111}$, we can then obtain the analytical shock velocity U_S (as well as v^+ and θ^+) required to begin the simulation. As seen in Fig. 5.6, the shock front drifts over time from the center of the WR, and hence the simulated shock velocity deviates slightly from the analytical value. We fit the shock profile to a hyperbolic tangent function using MATLAB's Curve Fitting tool, and track the shock drift over 1.0 ns (with an equilibration time of 300 ps) to obtain the actual shock velocity. These results for all four elements over the full range of compressive strains studied can be seen in Fig. 5.7.

We observe in Fig. 5.7 that the shock velocity data obtained from the CAC simulations correspond well to the results obtained from 3rd-order Eulerian theory over the full range of strains. For all four materials, the actual shock velocity exceeds the analytical value by 2-3.5%. Specifically, the average errors for Cu, Al, Ag, and Ni are given respectively as follows: 2.33%,

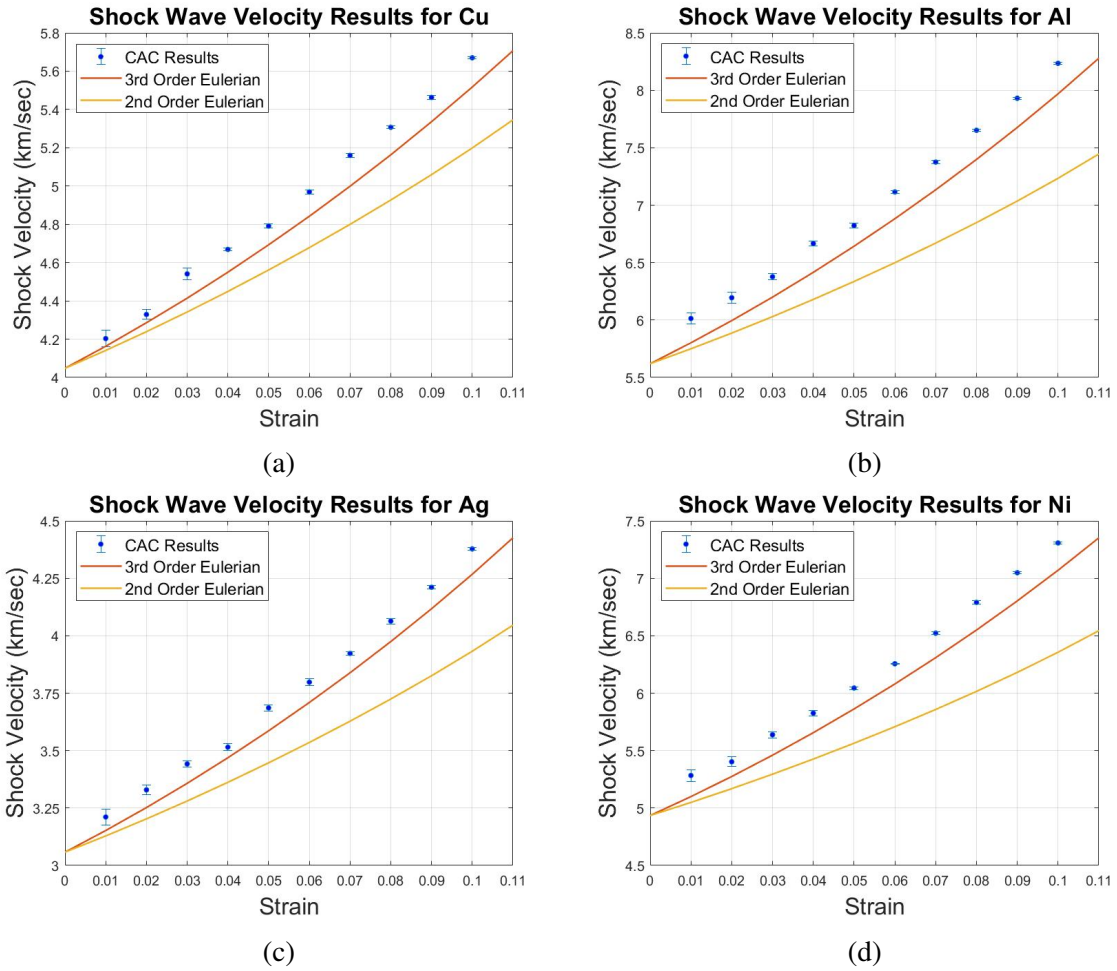

Figure 5.7: Simulated shock velocity (U_S) vs. strain (ϵ^+) data for (a) Cu, (b) Al, (c) Ag, and (d) Ni. Analytical results from 2nd and 3rd order Eulerian theory are also shown.

3.33%, 2.25%, 3.23%. These errors are attributed to the analytical approximation of the elastic constants in Eqs. (5.15) and (5.16) (in fact, [187] found that these equations slightly under-predicted the experimental elastic constants of a bulk lattice at room temperature). The stiffer CAC results may also be due to thermal effects and including fourth order terms in the Eulerian equations could further reduce the differences between simulation and theory. Nonetheless, the drift in the shock front is nearly imperceptible for many hundreds of picoseconds which shows that such errors are fairly small for this type of problem. Therefore, the conveyor method maintains a stationary wave front at the center of the WR with minimal deviation from the theoretical shock velocity.

To confirm the ability of the CAC framework to track the propagating shock for very long simulation times with this moving window technique, we conduct simulations using Cu, Al, Ag, and Ni with $\epsilon^+ = -0.06$ for 5 ns, where U_S and v^+ are assigned their computational values. Results from these simulations can be seen in Fig. 5.8. In each case, we observe the shock front remain stationary at the center of the WR while the spatial width of the shock front increases over time – implying that the shock wave is unsteady. This is expected because steady shock behavior is achieved through transverse atomic displacement which is impossible in a monatomic chain [28, 42, 19]. Hence, the conveyor technique allows the CAC domain to track a propagating shock much longer than traditional NEMD simulations. Additionally, each of these domains contains 80,000 particles and covers a total length of nearly $70\ \mu\mathrm{m}$. An equally sized atomistic domain would be composed of 280,000 atoms and thus require 3.5x more memory. Therefore, the CAC framework with the conveyor technique significantly reduces the computational overhead of large-domain simulations.

5.2.2 Coarsen-refine method in 1D

Next, we track a propagating shock in the CAC domain using the coarsen-refine moving window technique described in Sec. 4.4.3. In this case, however, the fine-scaled portion of the chain begins at the left boundary and is allowed to travel with the shock front through the entire domain by the simultaneous coarsening of the left continuum region and refinement of the right continuum region. Therefore, the shocked coarse-scaled region begins with 500 nodes,

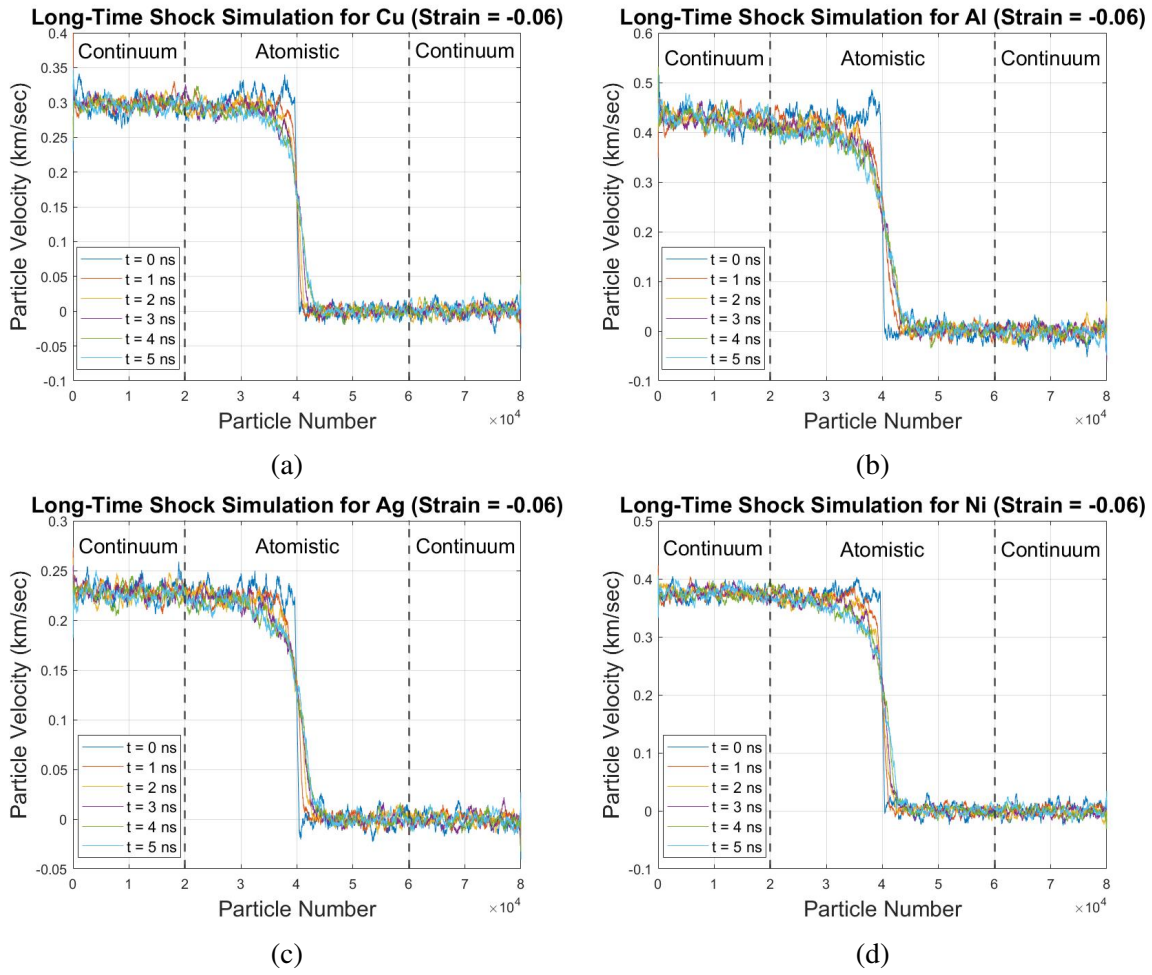

Figure 5.8: Velocity profiles of 1D CAC shock simulations performed with (a) Cu, (b) Al, (c) Ag, and (d) Ni for 5 ns ($\epsilon^{+} = -0.06$).

the unshocked coarse-scaled region begins with 39,500 nodes, and the fine-scaled region again contains 40,000 atoms for a total of 80,000 particles. The element length in each continuum region is $6r_0$ giving a total domain size of $\sim$ 709,367 Å. As before, each atomistic TR band contains 100 atoms. During the simulation, the left continuum region will grow, the right continuum region will shrink, and the atomistic region will remain at a constant length. Results of a simulation performed with Cu for $\epsilon^+ = -0.06$ are shown in Fig. 5.9.

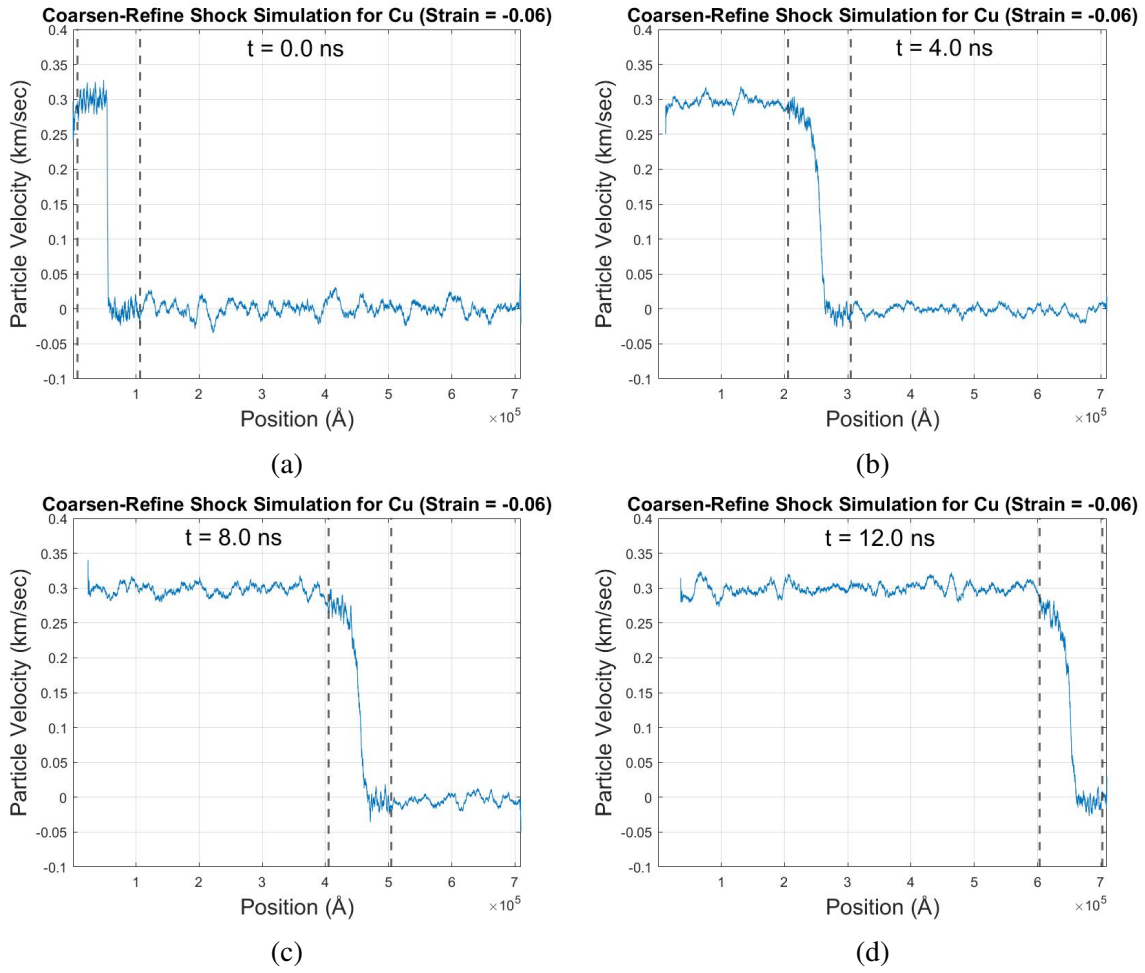

Figure 5.9: Velocity profile snapshots of a single propagating shock at the following times: (a) 0.0 ns, (b) 4.0 ns, (c) 8.0 ns, and (d) 12.0 ns. Here, ϵ^+ = -0.06, and the atomistic domain follows the shock front using the coarsen-refine technique. The dotted lines represent the one-dimensional A-C interfaces.

In these plots, we observe the evolution of the shock wave over 12.0 ns. The fine-scaled region successfully tracks the moving wave front through the entire CAC domain with minimal spurious behavior at the A-C interfaces. As expected, we observe compression of the material to the left of the shock wave while the rightmost point remains stationary. Hence,

using the coarsen-refine moving window technique in a CAC framework allows us to model shock propagation over engineering length scales and time frames. In contrast to the conveyor technique, the shock can now travel through the entire domain because the lengths of the continuum regions change. Previous studies have incorporated mesh refinement schemes into both finite element and atomistic-continuum frameworks [116, 123, 189, 190]. However, employing *simultaneous* coarsening/refinement methods to model highly non-equilibrium events like propagating shock waves is an active area of research. This work serves as a first step for using such a technique in a multiscale setting.

5.2.3 Shock front structure in 1D

In Figs. 5.8 and 5.9, we observe that the spatial width of the shock front increases over time – implying that the shock wave is unsteady. To understand this phenomenon further, we analyze the growth in shock front thickness over 5 ns for the four different materials. A plot of this data obtained for ϵ^+ = -0.06 is shown in Fig. 5.10. These results are in qualitative agreement with results from previous NEMD studies which modeled weak shock waves through materials in a one-dimensional setting and also observed unsteady wave behavior [28, 42, 19]. Additionally, we note that the growth rate of the shock width is approximately constant up to $\sim$1,000 ps and then slows down at higher time steps. This characteristic mirrors the results obtained previously in the moving window atomistic framework [1]. Finally, from this data, we obtain a lower bound of $\sim$0.003 ns and an upper bound of $\sim$0.3 ns for the shock rise time across each material. These values are very similar to the ranges observed in previous studies for small-domain FCC metals [158, 184].

5.2.4 Computational efficiency of the 1D CAC framework

Finally, we compare the computational cost of a shock simulation performed with CAC to an equally-sized MD simulation of a shock wave. MD simulations were conducted using an entirely fine-scaled domain. The runtime is calculated for a range of domain sizes, and the CAC framework always contains 40,000 atoms in the fine-scaled region. The results are summarized in Table 5.2. Here, the units represent hours of runtime required for every nanosecond of

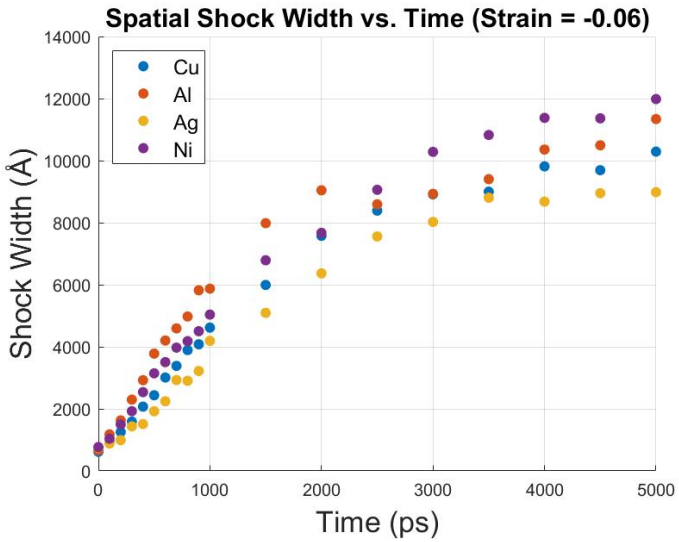

Figure 5.10: Growth in the spatial width of the shock wave front over 5 ns. Here, ϵ^+ = -0.06, and results are shown for Cu, Al, Ag, and Ni.

simulation time (h/ns), and each simulation was conducted with 40 processors. Notably, even the smallest CAC domain is already a factor of 2 faster than the pure MD system. For the longest domain, the speedup factor grows to nearly 6 even though there are only 4.67x as many atoms in the MD simulation as particles in the CAC simulation. This study illustrates benefits of using CAC with the moving window techniques to significantly reduce the total computational time of large-scale, nonlinear simulations.

Table 5.2: Simulation costs of the 1D CAC method against pure MD for various domain sizes. The number of particles required in CAC and number of atoms required in MD for the given domain length is shown (the CAC system always contains 40,000 atoms in the fine-scaled region).

Domain size (Å)	Particles (CAC)	Atoms (MD)	*h/ns (CAC)*	*h/ns (MD)*	*Speedup*
98,827	40,000	40,000	0.371	0.371	1.000
247,069	50,000	100,000	0.505	0.996	1.972
395,310	60,000	160,000	0.600	1.544	2.573
543,551	70,000	220,000	0.724	1.976	2.729
691,792	80,000	280,000	0.765	2.542	3.323
840,034	90,000	340,000	0.912	3.171	3.477
988,275	100,000	400,000	0.996	4.440	4.458
1,729,481	150,000	700,000	1.583	9.343	5.902

Chapter 6

Transmitting Multiple High-Frequency Phonons across Length Scales

In this chapter, we develop and present results for a technique to pass multiple high-frequency phonons between the atomistic and continuum regions of the CAC framework. These results have also been published in *Computational Materials Science* [3].

6.1 Wave passing background

Multiscale modeling techniques endeavor to link observable material behavior to effects at lower length scales. One of the central challenges with concurrent schemes is ensuring compatibility at the A-C interfaces so as to mitigate ghost forces in static systems and spurious wave behavior in dynamic systems [110]. Typically, such non-physical phenomena arise because the spectrum of the continuum model has a much smaller cutoff frequency than that of the atomistic model [97]. Although many techniques have been developed to reduce ghost forces in static frameworks [146, 191], the advancement of dynamic multiscale methods is nevertheless hindered by spurious wave reflections at the A-C interfaces.

To overcome this obstacle, most concurrent methods incorporate techniques to either minimize or absorb transient waves impinging on the A-C interfaces [78, 192, 193, 194]. An early scheme developed by [195] incorporates Langevin dynamics into the fine-scaled equations of motion and dampens specified particles in a "stadium" region around the inner atomistic core. Specifically, the method couples a one-dimensional atomistic domain to a linear elastic continuum and reduces wave reflections at the A-C interfaces by calculating the time-history-kernel (THK). This approach has proven to be effective, and variations of it have been introduced into

other concurrent multiscale frameworks such as CADD [78] and the Bridging Scale Method (BSM) [103]. However, because the THK method suffers from issues related to computational expense and scalability, various BSM frameworks have developed more efficient THK techniques, but such schemes are still only effective for linear solids [192, 196, 197]. Other approaches to reduce wave reflections include minimizing the reflection coefficient at the A-C boundaries [193, 198] as well as applying digital filters to remove high-frequency phonons that travel back into the fine-scaled region [199, 200].

Because all of these methods either minimize or absorb waves impinging on the A-C interfaces, information from short-wavelength phonons is lost. Furthermore, damping methods will inevitably eliminate fine-scaled wave data which should instead be transmitted across the boundaries [126]. One of the first attempts to solve this problem came in [201] which enhances a space-time discontinuous Galerkin finite element method by incorporating an enrichment function into the system. This technique has since been used to study both wave and crack propagation through materials, and it can successfully conserve energy and transmit high-frequency waves across the A-C interfaces [202]. Unfortunately, the framework in [201] requires extra degrees of freedom in the coarse-scaled regions, and the enriched functions must be removed at the continuum nodes in order to incorporate the short-wavelength phonons. Therefore, conserving the correct wave phase is challenging, so this technique cannot be easily used to study dynamic problems which require phonon coherency. As a result, a concurrent multiscale method is needed which would preserve phonon coherency and permit the full range of phonons to travel across the A-C interfaces.

Previous work has developed a technique to transfer high-frequency phonons across length scales within the CAC framework [126]. As stated earlier, CAC is a dynamic multiscale method which follows the solid state physics model of crystals whereby the structure is continuous at the lattice level but discrete at the atomic level, and a single set of governing equations is used throughout the entire domain [128]. As a result, the wave transfer problem reduces to a numerical problem caused by the discrepancy in finite element mesh sizes between the atomistic and continuum regions. This is a long-standing obstacle in continuum modeling and was regarded by Zienkiewicz as one of the great unsolved problems in the Finite Element

Method [203]. The work in [126] developed a supplemental basis for the CAC solution along with a new LD-based finite element scheme to pass a single high-frequency phonon between the atomistic and continuum regions. This technique allowed a wave packet with any wavevector and frequency to travel across the A-C interfaces without introducing new degrees of freedom into the coarse-scaled regions. However, this method could only be used for a single phonon and was demonstrated in a non-periodic domain.

In this chapter, we develop a technique based upon the work in [126] to pass multiple high-frequency phonon wave packets between the atomistic and continuum regions of a periodic CAC framework. This method uses the LD interpolation scheme to incorporate short-wavelength displacements into the continuum regions and introduces novel numerical techniques into the formulation to track a variety of wave packets across time. Specifically, two Fourier transforms are performed (both before and after the phonon is generated), and the difference in amplitude coefficients are stored in a master array in order to track waves of any wavevector at various time steps. Such a technique will be useful in real-world applications which involve the interaction and transmission of multiple waves within a single atomistic-continuum domain.

6.2 Lattice dynamics finite element formulation

6.2.1 Lattice dynamics method

In this section, we present a technique that was first formulated in [126] to overcome the issue of spurious wave reflections at the A-C interfaces, and we add extra details where necessary. This scheme uses an LD description of traveling waves to derive a new phonon wave-based finite element approximation of the CAC governing equations. Specifically, a novel interpolation method is employed to allow the transmission of high-frequency waves that would ordinarily be reflected at the A-C interface due to the linear shape functions. While the conventional finite element approximation discussed in Ch. 4 can only model low-frequency waves (with $\mathbf{k} < \mathbf{k}_C$) in the coarse-scaled regions, the current LD formulation allows the complete transmission of high-frequency waves (with $\mathbf{k} > \mathbf{k}_C$) from the atomistic to continuum region and vice versa.

If we consider a typical polyatomic crystalline system with N^α particles in each unit cell, then the standard approximation of the displacement field is given by Eq. (4.15). However, the LD-based method modifies this equation such that the particle displacements are now approximated as follows:

$$\mathbf{u}^\alpha(\mathbf{x},t) = \sum_{j=1}^{2^d} \mathbf{\Phi}_j(\mathbf{x}) \left[\mathbf{U}_j^\alpha(t) - \mathbf{U}_{sj}^\alpha(t)\right] + \mathbf{u}_s^\alpha(\mathbf{x},t) \qquad \alpha = 1,2,\ldots,N^\alpha. \tag{6.1}$$

In this equation, $\mathbf{u}^\alpha(\mathbf{x},t)$ is the new displacement at time *t* of the α^{th} atom within a given unit cell located at position **x**; d is the dimensionality of the system; 2^d is the total number of nodes in an element; $\mathbf{\Phi}_j(\mathbf{x})$ is the conventional tri-linear shape function; $\mathbf{U}_j^\alpha(t)$ is the total displacement of the α^{th} atom in the j^{th} element node at time t; $\mathbf{U}_{sj}^\alpha(t)$ is the short-wavelength displacement (denoted by the subscript s) of the α^{th} atom embedded in the j^{th} element node at time t; and $\mathbf{u}_s^\alpha(\mathbf{x},t)$ is the short-wavelength displacement at time t of the α^{th} atom within a unit cell at any material point **x** (not necessarily a nodal position). Since the tri-linear shape functions satisfy partition of unity $\left(\sum_{j=1}^{2^d} \mathbf{\Phi}_j(\mathbf{x}) = 1\right)$, we can rewrite Eq. (6.1) as follows:

$$\mathbf{u}^\alpha(\mathbf{x},t) = \sum_{j=1}^{2^d} \mathbf{\Phi}_j(\mathbf{x}) \left[\mathbf{U}_j^\alpha(t) - \mathbf{U}_{sj}^\alpha(t) + \mathbf{u}_s^\alpha(\mathbf{x},t)\right]. \tag{6.2}$$

As a result of this new basis, the CAC governing equation must be updated to account for the modified displacement interpolation which is now a function of time:

$$\rho^\alpha \ddot{\mathbf{u}}^\alpha(\mathbf{x},t) = \mathbf{f}_{int}^\alpha(\mathbf{x}) + \mathbf{f}^\alpha(\mathbf{x}). \tag{6.3}$$

In Eq. (6.2), the additional components of the displacement field approximation are $\mathbf{U}_{sj}^\alpha(t)$ and $\mathbf{u}_s^\alpha(\mathbf{x},t)$ which represent the short-wavelength displacements that need to be calculated. We note that at a given node j, $\mathbf{U}_{sj}^\alpha(t) = \mathbf{u}_s^\alpha(\mathbf{x},t)$, and Eq. (6.2) reduces to the following:

$$\mathbf{u}_j^\alpha(\mathbf{x},t) = \sum_{j=1}^{2^d} \mathbf{\Phi}_j(\mathbf{x}) \mathbf{U}_j^\alpha(t). \tag{6.4}$$

We can further reduce this expression for the α^{th} atom embedded in node j by recalling that the shape function $\mathbf{\Phi}_j(\mathbf{x})$ will equal 1 at node j and 0 everywhere else:

$$\mathbf{u}_j^{\alpha}(\mathbf{x}, t) = \mathbf{U}_j^{\alpha}(t). \tag{6.5}$$

Therefore, the displacements of particles at nodal locations remain unchanged when introducing the short-wavelength basis function. Instead, only the neighboring particles at non-nodal unit cells located at material points $\mathbf{x}$ within an element get modified by Eq. (6.2). These enhanced displacements will influence the force calculations at nodal locations which will allow short-wavelength phonons to pass through the coarse-scaled region.

Although the motion of a particle in a crystalline system is an oscillatory function of time, atomic motion is traditionally described by lattice vibrations [204]. Specifically, for a harmonic approximation, atomic displacement can be decomposed into a linear combination of normal modes with a discrete set of wavevectors where the number of wavevectors equals the number of unit cells [205]. If we only consider the contributions from short-wavelength phonons with $\mathbf{k} > \mathbf{k}_C$, then the displacement of the α^{th} particle in a unit cell at undeformed position $\mathbf{x}$ is given as follows:

$$\mathbf{u}_s^{\alpha}(\mathbf{x}, t) = \frac{1}{(N_l m^{\alpha})^{1/2}} \sum_{\mathbf{k},\nu(\mathbf{k}>\mathbf{k}_C)} \mathbf{e}_{\mathbf{k}\nu}^{\alpha} Q_{\mathbf{k}\nu} \exp\left[i\left(\mathbf{k}\cdot\mathbf{x} - \omega_{\mathbf{k}\nu} t\right)\right]. \tag{6.6}$$

In Eq. (6.6), each linear combination of normal modes represents the contribution from a wave with wavevector $\mathbf{k}$ and phonon branch ν. Additionally, N_l is the total number of unit cells in the system; m^{α} is the mass of the α^{th} particle in the l^{th} unit cell; $\mathbf{e}_{\mathbf{k}\nu}^{\alpha}$ is the polarization vector that determines which direction each particle moves; $Q_{\mathbf{k}\nu}$ is the normal mode coordinate which gives both the amplitude of the wave and the time dependence; and $\omega_{\mathbf{k}\nu}$ is the angular frequency corresponding to wavevector $\mathbf{k}$. We can then rewrite Eq. (6.6) to obtain the following

expressions for $\mathbf{U}_{sj}^{\alpha}(t)$ and $\mathbf{u}_{s}^{\alpha}(\mathbf{x},t)$ [126]:

$$\mathbf{U}_{sj}^{\alpha}(t)=\frac{1}{N_A}\sum_{\mathbf{k},\nu(\mathbf{k}>\mathbf{k}_C)}\mathbf{e}_{\mathbf{k}\nu}^{\alpha}U_{\mathbf{k}\nu}^{\alpha}\exp\left[i\left(\mathbf{k}\cdot\mathbf{x}_j-\omega_{\mathbf{k}\nu}t\right)\right] \tag{6.7}$$

$$\mathbf{u}_{s}^{\alpha}(\mathbf{x},t)=\frac{1}{N_A}\sum_{\mathbf{k},\nu(\mathbf{k}>\mathbf{k}_C)}\mathbf{e}_{\mathbf{k}\nu}^{\alpha}U_{\mathbf{k}\nu}^{\alpha}\exp\left[i\left(\mathbf{k}\cdot\mathbf{x}-\omega_{\mathbf{k}\nu}t\right)\right] \tag{6.8}$$

where N_A represents the total number of unit cells in only the *atomistic* region, and $U_{\mathbf{k}\nu}^{\alpha}$ is the amplitude. The only difference between the above two equations is that Eq. (6.7) is calculated for a particle α located in a unit cell at node j, while Eq. (6.8) is calculated for a particle α located in a unit cell at any elemental point **x**. Hence, Eq. (6.7) is only a function of *t* while Eq. (6.8) is a function of both **x** and *t*.

We use Eq. (6.2) to enrich the displacement field in the coarse-scaled region with high-frequency waves. This is achieved by linking the short-wavelength displacement at an unknown position **x** and time *t* in the coarse-scaled region to information at a known position $\mathbf{x}_0$ and time t_0 in the fine-scaled region as follows:

$$\begin{aligned}\mathbf{u}_{s}^{\alpha}(\mathbf{x},t)&=\frac{1}{N_A}\sum_{\mathbf{k},\nu(\mathbf{k}>\mathbf{k}_C)}\mathbf{e}_{\mathbf{k}\nu}^{\alpha}U_{\mathbf{k}\nu}^{\alpha}(\mathbf{x}_0,t_0)\exp\left\{i\left[\mathbf{k}\cdot(\mathbf{x}-\mathbf{x}_0)-\omega_{\mathbf{k}\nu}(t-t_0)\right]\right\}\\&=\frac{1}{N_A}\sum_{\mathbf{k},\nu(\mathbf{k}>\mathbf{k}_C)}\mathbf{e}_{\mathbf{k}\nu}^{\alpha}U_{\mathbf{k}\nu}^{\alpha}(\mathbf{x}_0,t_0)\exp\left[i\left(\mathbf{k}\cdot\Delta\mathbf{x}-\omega_{\mathbf{k}\nu}\Delta t\right)\right].\end{aligned} \tag{6.9}$$

Here, we have only shown the expression for $\mathbf{u}_{s}^{\alpha}(\mathbf{x},t)$ as the expression for $\mathbf{U}_{sj}^{\alpha}(t)$ would have the same form. In Eq. (6.9), $\Delta\mathbf{x}=\mathbf{x}-\mathbf{x}_0$ represents the spatial distance between the current unit cell at location **x** in the continuum region and the reference unit cell at *undeformed* location $\mathbf{x}_0$ in the atomistic region. Additionally, $\Delta t=t-t_0$ represents the difference between the current time *t* and the time t_0 at which $U_{\mathbf{k}\nu}^{\alpha}(\mathbf{x}_0,t_0)$ was calculated.

We can use Eq. (6.9) to calculate $\mathbf{u}_{s}^{\alpha}(\mathbf{x},t)$ [and $\mathbf{U}_{sj}^{\alpha}(t)$] and then substitute these expressions into Eq. (6.2). As a result, short-wavelength effects will now be incorporated into $\mathbf{u}^{\beta}(\mathbf{x}')$ from Eq. (4.14) which will enhance the internal force calculation. Specifically, the forces at the nodes will now contain information from the entire spectrum of phonon waves: low-frequency data from linear interpolation and high-frequency data from LD calculations. Therefore, it is

clear that an accurate determination of $\mathbf{u}_s^\alpha(\mathbf{x},t)$ and $\mathbf{U}_{sj}^\alpha(t)$ is crucial to achieve proper force matching, and this requires calculating the amplitude $U_{\mathbf{k}\nu}^\alpha(\mathbf{x}_0,t_0)$ of each short-wavelength phonon mode. We derive this amplitude in the following section.

6.2.2 Determining the amplitude of the short-wavelength phonon mode

In order to enhance the displacement approximation to include the effects of high-frequency phonon waves, we must calculate the amplitude $U_{\mathbf{k}\nu}^\alpha(\mathbf{x}_0,t_0)$ by analyzing the displacements in the fine-scaled region. This is achieved by taking the Fourier transform of each atom in the fine-scaled region one unit cell at a time. We can represent the short-wavelength displacement of the α^{th} particle at undeformed position $\mathbf{x}_j$ and time t as follows:

$$\mathbf{u}_s^\alpha(\mathbf{x}_j,t)=\sum_{\mathbf{k},\nu}A_{\mathbf{k}\nu}^\alpha\mathbf{e}_{\mathbf{k}\nu}^\alpha\exp\left[i\left(\mathbf{k}\cdot\mathbf{x}_j-\omega_{\mathbf{k}\nu}t\right)\right]+B_{\mathbf{k}\nu}^\alpha\mathbf{e}_{\mathbf{k}\nu}^\alpha\exp\left[i\left(\mathbf{k}\cdot\mathbf{x}_j+\omega_{\mathbf{k}\nu}t\right)\right]. \tag{6.10}$$

As before, we have only shown the expression for $\mathbf{u}_s^\alpha(\mathbf{x}_j,t)$ as the same analysis applies to $\mathbf{U}_{sj}^\alpha(t)$. Eq. (6.10) is a general expression for the short-wavelength displacement, but it is understood that $\mathbf{x}_j=\mathbf{x}_0$ and $t=t_0$ in this example. Here, $A_{\mathbf{k}\nu}^\alpha$ and $B_{\mathbf{k}\nu}^\alpha$ are the two unknown coefficients computed for each mode which represent both parts of the coefficient $U_{\mathbf{k}\nu}^\alpha(\mathbf{x}_0,t_0)$. Hence, the goal is to calculate $A_{\mathbf{k}\nu}^\alpha$ and $B_{\mathbf{k}\nu}^\alpha$ at t_0 as these coefficients will then be applied to the short-wavelength calculation (Eq. 6.9) at every subsequent time step.

To find these amplitudes, we must take the discrete Fourier transform (DFT) of both the initial displacements $\mathbf{u}_j^\alpha$ and initial velocities $\mathbf{v}_j^\alpha$ in the atomistic region. This analysis will give us $\mathbf{C}_\mathbf{k}^\alpha$ and $\mathbf{D}_\mathbf{k}^\alpha$ which represent the amplitude vectors of the displacement and velocity data respectively. We can define the DFT as follows:

$$\mathbf{X}_\mathbf{k}^\alpha=\sum_{j=0}^{N_A-1}\mathbf{x}_j^\alpha\exp\left[-i\left(\mathbf{k}\cdot j\mathbf{r}_0\right)\right] \tag{6.11}$$

where $\mathbf{r}_0$ is the equilibrium displacement between unit cells, and the index j specifies that the summation occurs over the α^{th} atom within each unit cell in the atomistic region. If we let $\mathbf{x}_j=j\mathbf{r}_0$ be the position of the j^{th} unit cell in the undeformed configuration, we get the

following DFTs for displacements and velocities:

$$\mathbf{C}_{\mathbf{k}}^{\alpha} = \sum_{j=0}^{N_A-1} \mathbf{u}_j^{\alpha} \exp\left[-i\left(\mathbf{k}\cdot\mathbf{x}_j\right)\right] \tag{6.12}$$

$$\mathbf{D}_{\mathbf{k}}^{\alpha} = \sum_{j=0}^{N_A-1} \mathbf{v}_j^{\alpha} \exp\left[-i\left(\mathbf{k}\cdot\mathbf{x}_j\right)\right]. \tag{6.13}$$

We can then relate the modal amplitude in Eq. (6.12) to the phonon modes in Eq. (6.10) evaluated at $t = 0$ for a specific wavevector $\mathbf{k}$:

$$\begin{aligned}
\mathbf{C}_{\mathbf{k}}^{\alpha} &= \sum_{\nu} \mathbf{u}_s^{\alpha}(\mathbf{x}_j, 0) \exp\left[-i(\mathbf{k}\cdot\mathbf{x}_j)\right] \\
&= \sum_{\nu} A_{\mathbf{k}\nu}^{\alpha} \mathbf{e}_{\mathbf{k}\nu}^{\alpha} \exp\left[i\left(\mathbf{k}\cdot\mathbf{x}_j - \mathbf{k}\cdot\mathbf{x}_j - \omega_{\mathbf{k}\nu}0\right)\right] + B_{\mathbf{k}\nu}^{\alpha} \mathbf{e}_{\mathbf{k}\nu}^{\alpha} \exp\left[i\left(\mathbf{k}\cdot\mathbf{x}_j - \mathbf{k}\cdot\mathbf{x}_j + \omega_{\mathbf{k}\nu}0\right)\right] \\
&= \sum_{\nu} \left(A_{\mathbf{k}\nu}^{\alpha} + B_{\mathbf{k}\nu}^{\alpha}\right) \mathbf{e}_{\mathbf{k}\nu}^{\alpha}.
\end{aligned} \tag{6.14}$$

Next, we can perform a similar analysis for the modal amplitude of the velocities in Eq. (6.13) by taking the derivative of Eq. (6.10) with respect to t:

$$\begin{aligned}
\mathbf{D}_{\mathbf{k}}^{\alpha} &= \sum_{\nu} \mathbf{v}_s^{\alpha}(\mathbf{x}_j, 0) \exp\left[-i(\mathbf{k}\cdot\mathbf{x}_j)\right] \\
&= \sum_{\nu} -i\omega_{\mathbf{k}\nu} A_{\mathbf{k}\nu}^{\alpha} \mathbf{e}_{\mathbf{k}\nu}^{\alpha} \exp\left[i\left(\mathbf{k}\cdot\mathbf{x}_j - \mathbf{k}\cdot\mathbf{x}_j - \omega_{\mathbf{k}\nu}0\right)\right] + i\omega_{\mathbf{k}\nu} B_{\mathbf{k}\nu}^{\alpha} \mathbf{e}_{\mathbf{k}\nu}^{\alpha} \exp\left[i\left(\mathbf{k}\cdot\mathbf{x}_j - \mathbf{k}\cdot\mathbf{x}_j + \omega_{\mathbf{k}\nu}0\right)\right] \\
&= \sum_{\nu} \left(B_{\mathbf{k}\nu}^{\alpha} - A_{\mathbf{k}\nu}^{\alpha}\right) i\omega_{\mathbf{k}\nu} \mathbf{e}_{\mathbf{k}\nu}^{\alpha}.
\end{aligned} \tag{6.15}$$

Finally, we arrive at a system of two equations with the two unknowns $A_{\mathbf{k}\nu}^{\alpha}$ and $B_{\mathbf{k}\nu}^{\alpha}$:

$$\mathbf{C}_{\mathbf{k}}^{\alpha} = \sum_{j=0}^{N_A-1} \mathbf{u}_j^{\alpha} \exp\left[-i\left(\mathbf{k}\cdot\mathbf{x}_j\right)\right] = \sum_{\nu} \left(A_{\mathbf{k}\nu}^{\alpha} + B_{\mathbf{k}\nu}^{\alpha}\right) \mathbf{e}_{\mathbf{k}\nu}^{\alpha} \tag{6.16}$$

$$\mathbf{D}_{\mathbf{k}}^{\alpha} = \sum_{j=0}^{N_A-1} \mathbf{v}_j^{\alpha} \exp\left[-i\left(\mathbf{k}\cdot\mathbf{x}_j\right)\right] = \sum_{\nu} \left(B_{\mathbf{k}\nu}^{\alpha} - A_{\mathbf{k}\nu}^{\alpha}\right) i\omega_{\mathbf{k}\nu} \mathbf{e}_{\mathbf{k}\nu}^{\alpha}. \tag{6.17}$$

Therefore, the DFTs of displacement and velocity for the α^{th} particle within each unit cell produce a 2ν by 2ν matrix to solve for the coefficients $A^{\alpha}_{\mathbf{k}\nu}$ and $B^{\alpha}_{\mathbf{k}\nu}$ corresponding to a given wavevector $\mathbf{k}$.

6.2.3 Calculating the short-wavelength amplitude in 1D

Since we are demonstrating this technique using a one-dimensional monatomic chain, we now solve these equations assuming such an environment. In 1D, there is only one phonon branch ($\nu = 1$), particles can only travel in the $\pm\mathbf{x}$ direction ($\mathbf{e}^{\alpha}_{\mathbf{k}\nu} = 1$), and there is only one atom per unit cell ($N_{\alpha} = 1$). As a result, Eqs. (6.16) and (6.17) reduce to the following:

$$C_k = \sum_{j=0}^{N_A-1} u_j \exp\left[-i\left(k \cdot x_j\right)\right] = A_k + B_k \tag{6.18}$$

$$D_k = \sum_{j=0}^{N_A-1} v_j \exp\left[-i\left(k \cdot x_j\right)\right] = (B_k - A_k) i\omega_k. \tag{6.19}$$

Solving Eqs. (6.18) and (6.19) for A_k and B_k gives the following:

$$A_k = \frac{C_k}{2} + i\frac{D_k}{2\omega_k} \tag{6.20}$$

$$B_k = \frac{C_k}{2} - i\frac{D_k}{2\omega_k}. \tag{6.21}$$

Substituting these expressions for A_k and B_k back into Eq. (6.10) when $x_j = x_0$ and $t = 0$, we get the following:

$$u_s(x_0, 0) = \sum_k (A_k + B_k) e^{ikx_0} \tag{6.22}$$

$$= \left[\frac{C_k}{2} + i\frac{D_k}{2\omega_k} + \frac{C_k}{2} - i\frac{D_k}{2\omega_k}\right] e^{ikx_0} \tag{6.23}$$

$$= C_k e^{ikx_0}. \tag{6.24}$$

Hence, we arrive at the following expression for the amplitude of the short-wavelength phonon mode in 1D:

$$U_k(x_0, t_0) = C_k e^{ikx_0} = \sum_{j=0}^{N_A-1} u_j e^{-ikx_j} e^{ikx_0}. \tag{6.25}$$

Substituting this back into Eq. (6.9) for the one-dimensional monatomic chain:

$$u_s(x,t) = \frac{1}{N_A} \sum_{k(k>k_C)} C_k e^{ikx_0} \exp\left[i\left(k \cdot \Delta x - \omega_k \Delta t\right)\right] \tag{6.26}$$

$$= \frac{1}{N_A} \sum_{k(k>k_C)} C_k \exp\left\{i\left[k \cdot (x_0 + \Delta x) - \omega_k \Delta t\right]\right\} \tag{6.27}$$

$$= \frac{1}{N_A} \sum_{k(k>k_C)} C_k \exp\left[i\left(k \cdot x - \omega_k \Delta t\right)\right] \tag{6.28}$$

where $x = x_0 + \Delta x$ is the location of the node in the continuum region. Additionally, C_k is given by the following expression:

$$C_k = \sum_{j=0}^{N_A-1} u_j e^{-ikx_j} = \sum_{j=0}^{N_A-1} u_j \left[\cos(k \cdot x_j) - i\sin(k \cdot x_j)\right]. \tag{6.29}$$

As a result, we can rewrite $u_s(x,t)$ in trigonometric form as follows:

$$u_s(x,t) = \frac{1}{N_A} \sum_{k(k>k_C)} \left[\mathrm{Re}(C_k) - i\mathrm{Im}(C_k)\right] \left[\cos(k \cdot x - \omega_k \Delta t) + i\sin(k \cdot x - \omega_k \Delta t)\right] \tag{6.30}$$

where

$$\mathrm{Re}(C_k) = \sum_{j=0}^{N_A-1} u_j \cos(k \cdot x_j) \tag{6.31}$$

$$\mathrm{Im}(C_k) = \sum_{j=0}^{N_A-1} u_j \sin(k \cdot x_j). \tag{6.32}$$

Keeping only the real parts, we arrive at our final expression for the short-wavelength displacement in 1D:

$$u_s(x,t) = \frac{1}{N_A} \sum_{k(k>k_C)} \left[\mathrm{Re}(C_k)\cos(k \cdot x - \omega_k \Delta t) + \mathrm{Im}(C_k)\sin(k \cdot x - \omega_k \Delta t)\right] \tag{6.33}$$

Therefore, when simulating a high-frequency phonon wave packet using the described LD technique, we utilize the velocity-Verlet algorithm from Sec. 2.4.2 to evolve the wave initialized in the atomistic region. Next, we store the displacements of each particle in an array at time $t = 0$ ps and follow the procedure outlined previously to calculate $U^{\alpha}_{\mathbf{k}\nu}$. Then, at each time step t, we use Eq. (6.9) to compute $\mathbf{u}^{\alpha}_{s}(\mathbf{x}, t)$ at a given position $\mathbf{x}$, and we calculate the total displacement of each continuum node using Eq. (6.2). Finally, we calculate the internal force of each particle as a function of relative displacements using Eq. (4.14) and update the time step. This technique allows high-frequency phonons that would ordinarily be reflected at the A-C interface to pass smoothly between the atomistic and continuum regions.

6.2.4 Passing a single high-frequency wave packet from atomistic to continuum

We now present a 1D wave packet simulation performed with the LD interpolation method. The results can be seen in Fig. 6.1, and $k = 0.2\,\pi/r_0$ in this case. Hence, we can directly compare the results in Fig. 6.1 to the results in Fig. 5.2d. We observe that the LD interpolation scheme permits the entire phonon wave packet to travel across the A-C interface from the atomistic to the continuum region with a nearly imperceptible reflection. This is in contrast to the complete reflection seen in Fig. 5.2d and is congruent with the results from previous studies [126]. Additionally, by enabling periodic boundary conditions, we observe that the LD interpolation method allows the high-frequency phonon wave packet to travel between the two outer continuum regions and back to the center atomistic region. The transmission demonstrated in Fig. 6.1 validates the implementation of the LD interpolation method.

6.3 Lattice dynamics technique for multiple waves

6.3.1 Background and preliminary approach

While the method presented in the previous section has been shown to efficiently pass high-frequency phonons between the atomistic and continuum regions of a CAC domain, the scheme is limited to single wave packets of a specified wavevector. This is because the short-wavelength amplitude information can only be stored for one wave at a time to prevent data from being

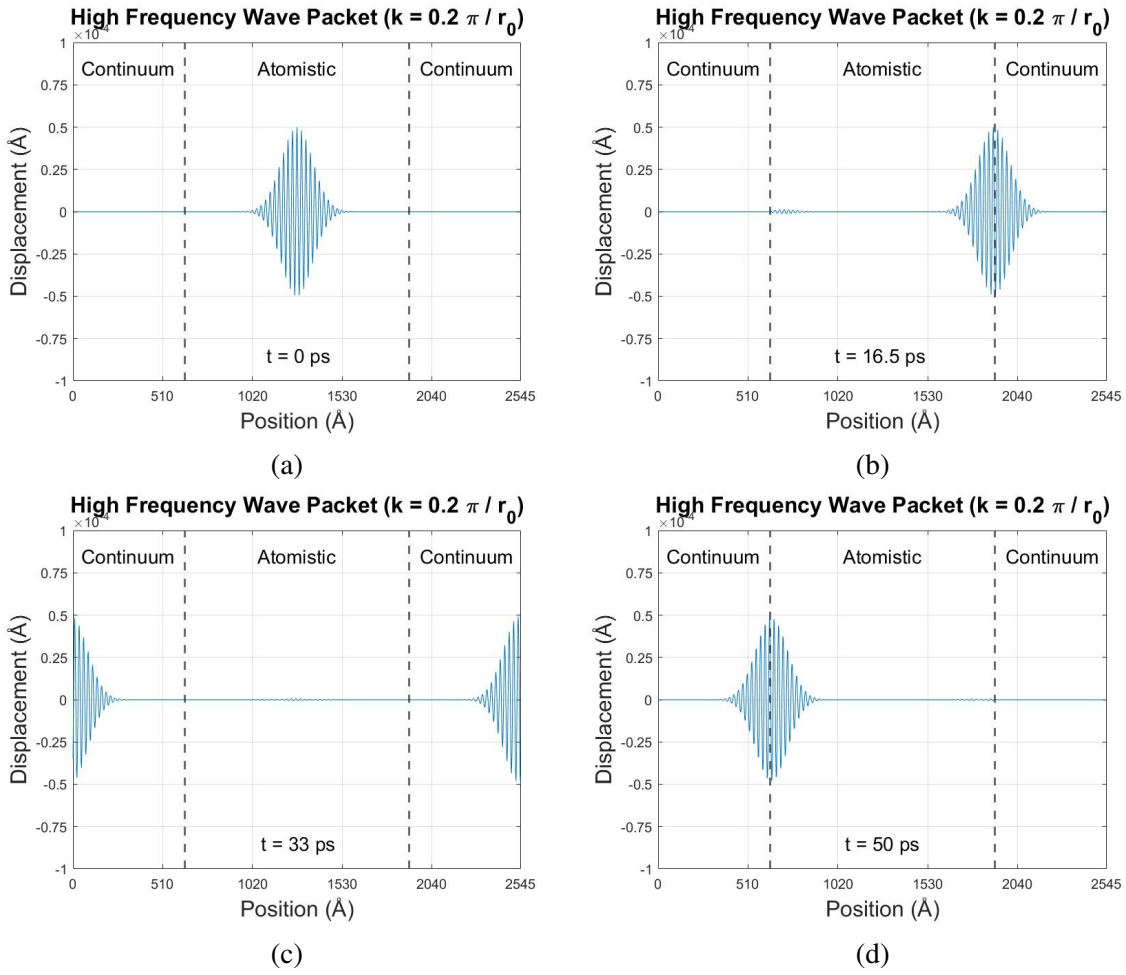

Figure 6.1: High-frequency phonon wave packet simulation performed with the LD interpolation method ($k = 0.2\,\pi/r_0$).

overwritten. However, many MD simulations produce multiple waves and other transient phenomena, so a scheme which could keep track of more than one wave packet and pass each wave across the A-C interface in a multiscale setting would be invaluable. In this section, we present an LD interpolation method to be used with multiple waves and wavevectors in a single CAC domain.

We recall the expression for the displacement field approximation from Sec. 6.2.1:

$$\mathbf{u}^{\alpha}(\mathbf{x},t) = \sum_{j=1}^{2^d} \mathbf{\Phi}_j(\mathbf{x}) \left[\mathbf{U}_j^{\alpha}(t) - \mathbf{U}_{sj}^{\alpha}(t) + \mathbf{u}_s^{\alpha}(\mathbf{x},t) \right]. \tag{6.34}$$

Here, we note that both $\mathbf{U}_{sj}^{\alpha}(t)$ and $\mathbf{u}_s^{\alpha}(\mathbf{x},t)$ contain all the short-wavelength information of a given wave packet at time t. Again, since the same analysis applies to both terms, we only focus on $\mathbf{u}_s^{\alpha}(\mathbf{x},t)$ in this section. Equation (6.10) gives the short-wavelength displacement of the α^{th} particle at an undeformed position $\mathbf{x}_j$ and time t, and the primary terms in that equation are the coefficients $A_{\mathbf{k}\nu}^{\alpha}$ and $B_{\mathbf{k}\nu}^{\alpha}$ as we saw in Sec. 6.2.2. Let us now assume that multiple wave packets will be generated in the domain where t is the current time in the simulation, and t_l is the time at which a given wave packet l is nucleated. Then, in principle, Eq. (6.10) could be expanded to account for these different wave packets at various time steps as follows:

$$\begin{aligned} \mathbf{u}_s^{\alpha}(\mathbf{x}_j,t) = \sum_{\mathbf{k},\nu} \sum_{l} & A_{\mathbf{k}\nu,l}^{\alpha} \mathbf{e}_{\mathbf{k}\nu}^{\alpha} \exp\left\{ i \left[\mathbf{k}\cdot\mathbf{x}_j - \omega_{\mathbf{k}\nu}(t-t_l) \right] \right\} \\ & + B_{\mathbf{k}\nu,l}^{\alpha} \mathbf{e}_{\mathbf{k}\nu}^{\alpha} \exp\left\{ i \left[\mathbf{k}\cdot\mathbf{x}_j + \omega_{\mathbf{k}\nu}(t-t_l) \right] \right\} \end{aligned} \tag{6.35}$$

where the inner summation occurs over all wave packets l. Now, the coefficients $A_{\mathbf{k}\nu,l}^{\alpha}$ and $B_{\mathbf{k}\nu,l}^{\alpha}$ correspond to each wave packet l. We refer to this as the preliminary or "naive" approach because the amplitude coefficients still do not have a time component, and hence each wave generated at time t_l cannot be tracked over time. As a result, any new phonon initialized at time $t_l \neq 0$ will be reflected off the A-C interface as seen in Fig. 6.2. Specifically, the main issue lies in keeping track of each individual phonon generated at time t_l without losing information from other phonons. In an attempt to overcome this difficult problem, we provide a detailed solution below.

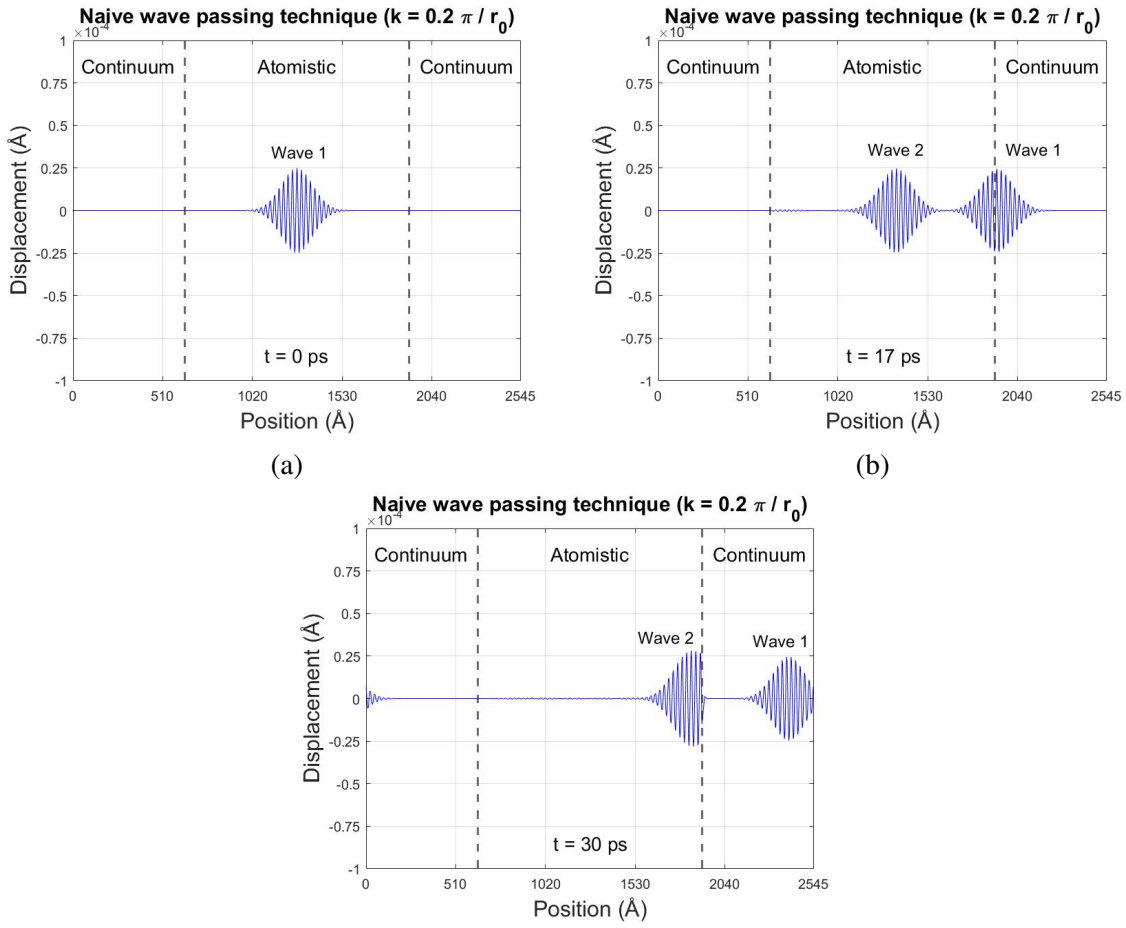

Figure 6.2: Naive approach to passing multiple waves across the A-C interface in which wave 1 crosses but wave 2 gets reflected ($k = 0.2\,\pi/r_0$).

6.3.2 Solution to the preliminary approach

Each wave packet can be characterized by its wavevector and frequency combination (**k**, ω), its short-wavelength amplitudes ($A^{\alpha}_{\mathbf{k}\nu,l}$ and $B^{\alpha}_{\mathbf{k}\nu,l}$), and the time at which is was initialized (t_l). These terms must be tracked and stored correctly in order to allow multiple waves to pass across the A-C interfaces. To this end, we first rewrite Eq. (6.35) as follows:

$$\mathbf{u}^{\alpha}_{s}(\mathbf{x}_j,t) = \sum_{\mathbf{k},\nu}\sum_{l} A^{\alpha}_{\mathbf{k}\nu,l}\text{exp}[i\cdot\omega_{\mathbf{k}\nu}t_l]\mathbf{e}^{\alpha}_{\mathbf{k}\nu}\text{exp}\left[i\left(\mathbf{k}\cdot\mathbf{x}_j-\omega_{\mathbf{k}\nu}t\right)\right] \tag{6.36}$$
$$+\, B^{\alpha}_{\mathbf{k}\nu,l}\text{exp}[-i\cdot\omega_{\mathbf{k}\nu}t_l]\mathbf{e}^{\alpha}_{\mathbf{k}\nu}\text{exp}\left[i\left(\mathbf{k}\cdot\mathbf{x}_j+\omega_{\mathbf{k}\nu}t\right)\right].$$

Thus, we now have "time-stamped" coefficients $A^{\alpha}_{\mathbf{k}\nu,l}\text{exp}[i\cdot\omega_{\mathbf{k}\nu}t_l]$ and $B^{\alpha}_{\mathbf{k}\nu,l}\text{exp}[-i\cdot\omega_{\mathbf{k}\nu}t_l]$ which contain the unique information for each phonon and encode the time at which the wave is nucleated. During each time step (before a new wave is generated), we take a "snapshot" of the domain in ***k-space*** whereby the amplitude coefficients are obtained from the Fourier transform discussed in Sec. 6.2.2. After the generation of a new phonon, a second Fourier transform of the domain is taken, and the first set of coefficients is subtracted from the second. This allows us to see which frequencies are "new" and thus gives us information about the current wave without the influence from previous phonons. Finally, we add the difference in these coefficients to a global "master" array and use a modified form of Eq. (6.9) to calculate the displacement of each particle:

$$\mathbf{u}^{\alpha}_{s}(\mathbf{x},t) = \frac{1}{N_A}\sum_{\mathbf{k},\nu(\mathbf{k}>\mathbf{k}_C)}\sum_{l}\mathbf{e}^{\alpha}_{\mathbf{k}\nu}U^{\alpha}_{\mathbf{k}\nu,l}\text{exp}[i\cdot\omega_{\mathbf{k}\nu}t_l]\text{exp}\left[i\left(\mathbf{k}\cdot\Delta\mathbf{x}-\omega_{\mathbf{k}\nu}\Delta t\right)\right]. \tag{6.37}$$

As a result, the displacement field approximation is updated based upon multiple waves, and no information gets lost.

6.3.3 Detailed explanation in 1D

We now elaborate on this process for a one-dimensional monatomic chain as is utilized in the present work. Fig. 6.3 gives a visual representation of two high-frequency wave packets with

wavevector-frequency pairs of (k_1, ω_1) and (k_2, ω_2) traveling within the 1D CAC framework described in Sec. 2.4.1. The first phonon is generated at time t_1, the second phonon is generated

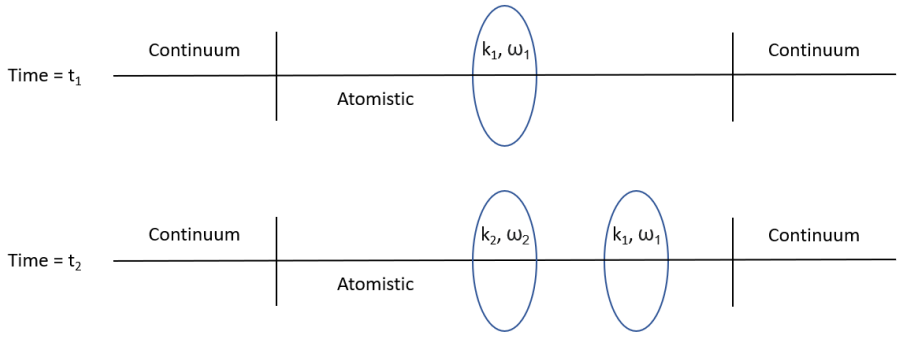

Figure 6.3: Schematic of two phonon wave packets traveling through a CAC domain.

at time t_2, and without loss of generality, we assume that each wave originates at the center of the atomistic region. For a one-dimensional system, Eq. (6.36) reduces to the following:

$$u_s(x_j,t) = \sum_k \sum_l A_{k,l}\text{exp}[i\cdot\omega_k t_l]\text{exp}\left[i\left(k\cdot x_j - \omega_k t\right)\right] \\ + B_{k,l}\text{exp}[-i\cdot\omega_k t_l]\text{exp}\left[i\left(k\cdot x_j + \omega_k t\right)\right]. \tag{6.38}$$

By following the procedure discussed in Sec. 6.2.3, we can solve for the coefficients and substitute these back into Eq. (6.9) to achieve the following short-wavelength displacement approximation in 1D:

$$u_s(x,t) = \frac{1}{N_A}\sum_{k(k>k_C)} \sum_l C_{k,l}\text{exp}[i\cdot\omega_k t_l]\text{exp}\left[i\left(k\cdot x - \omega_k t\right)\right] \tag{6.39}$$

where t is the global simulation time, and $C_{k,l}$ is the derived coefficient given by Eq. (6.29). Recall that $C_{k,l}$ is purely a function of the atomic displacements, undeformed positions, and wavevectors. Furthermore, Eq. (6.39) is the same as Eq. (6.28) but with the added exponential term and summation over l.

Therefore, we have the new *time-stamped* coefficient $E_{k,l} = C_{k,l}\text{exp}[i\cdot\omega_k t_l]$. Expanding out $C_{k,l}$ into its real and imaginary parts, we get the following:

$$E_{k,l} = C_{k,l}\text{exp}[i\cdot\omega_k t_l] = \left[\text{Re}(C_{k,l}) - i\text{Im}(C_{k,l})\right]\left[\cos(\omega_k t_l) + i\sin(\omega_k t_l)\right] \tag{6.40}$$

where Re($C_{k,l}$) and Im($C_{k,l}$) are given by Eqs. (6.31) and (6.32) respectively. Next, we can define the real and imaginary components of the coefficient $E_{k,l}$:

$$\mathrm{Re}(E_{k,l}) = \mathrm{Re}(C_{k,l})\cos(\omega_k t_l) + \mathrm{Im}(C_{k,l})\sin(\omega_k t_l) \tag{6.41}$$

$$\mathrm{Im}(E_{k,l}) = \mathrm{Re}(C_{k,l})\sin(\omega_k t_l) - \mathrm{Im}(C_{k,l})\cos(\omega_k t_l). \tag{6.42}$$

Substituting the two parts of this coefficient back into Eq. (6.39) and writing the expression in trigonometric form, we get the following:

$$u_s(x,t) = \frac{1}{N_A} \sum_{k(k>k_C)} \sum_{l} \left[\mathrm{Re}(E_{k,l}) + i\mathrm{Im}(E_{k,l})\right] \left[\cos(k \cdot x - \omega_k t) + i\sin(k \cdot x - \omega_k t)\right]. \tag{6.43}$$

Then, keeping only the real parts of Eq. (6.43), we arrive at the final expression for the multi-wave, short-wavelength displacement in 1D:

$$u_s(x,t) = \frac{1}{N_A} \sum_{k(k>k_C)} \sum_{l} \left[\mathrm{Re}(E_{k,l})\cos(k \cdot x - \omega_k t) - \mathrm{Im}(E_{k,l})\sin(k \cdot x - \omega_k t)\right]. \tag{6.44}$$

Equation (6.44) allows us to update the atomic displacements given multiple high-frequency waves in the CAC domain.

6.3.4 Using the LD technique with time integration

We now discuss how the process described above is incorporated into the time integration algorithm, and we use the two waves from Fig. 6.3 as a reference. Additionally, we assume that $t = t_2$ and the first phonon (wave 1) has already been nucleated in the atomistic region. The steps are enumerated as follows.

1. After the particle velocity update, we calculate the *time-independent* amplitude coefficients $C_{k,l}$. Specifically, we find the real and imaginary components of the coefficient $C_{k,l}$ using Eqs. (6.31) and (6.32) and store them in a *k*-based array in which each index is a different wavevector. This effectively allows us to take a "snapshot" of the framework

in *k*-space and thus capture the information from any phonon currently within the domain. Referring back to Fig. 6.3, we calculate and store the $C_{k,1}$ coefficients to preserve the displacements/velocities induced by wave 1.

2. If desired, we then generate the second phonon (wave 2) after obtaining $C_{k,1}$ and update the particle displacements and velocities accordingly. In other words, displacements and velocities resulting from wave 2 are added to those values induced by wave 1 such that both phonons are still present in the domain and information from each is preserved.

3. At the end of the time step, we then calculate the time-independent amplitude coefficient of wave 2 ($C_{k,2}$). We note that the wavevector of wave 2 can be any value – it does not have to be the same as wave 1.

4. Next, we subtract the real and imaginary components of $C_{k,1}$ from the corresponding components of $C_{k,2}$. This gives us the exclusive frequencies from wave 2 as seen below:

$$\mathrm{Re}(C_{k,21}) = \mathrm{Re}(C_{k,2}) - \mathrm{Re}(C_{k,1}) \tag{6.45}$$

$$\mathrm{Im}(C_{k,21}) = \mathrm{Im}(C_{k,2}) - \mathrm{Im}(C_{k,1}). \tag{6.46}$$

5. Finally, we substitute $\mathrm{Re}(C_{k,21})$ and $\mathrm{Im}(C_{k,21})$ into Eqs. (6.41) and (6.42) to obtain the new *time-stamped* coefficient $E_{k,2}$. This coefficient contains all the "new" information from wave 2 including its generation time.

The real and imaginary parts of $E_{k,2}$ are added to a global *k*-based array where each array index contains the sum of the $E_{k,l}$ coefficients from every generated phonon (the $E_{k,1}$ coefficients from wave 1 would have already been obtained at $t = t_1$). This array serves as a "master template" by storing the time-stamped coefficients from every phonon, and a visual representation for wave 1 and wave 2 can be seen in Fig. 6.4. We note that the nondegenerate wavevectors are limited to $k_x = \pi n_x / r_0 N_A$ where n_x is an integer ranging from 0 to $N_A - 1$ [178]. Thus, for any given wavevector, we know the corresponding total amplitude coefficient. We can then use these coefficients in Eq. (6.44) during all subsequent time steps to calculate the short wavelength displacement induced by multiple wave packets.

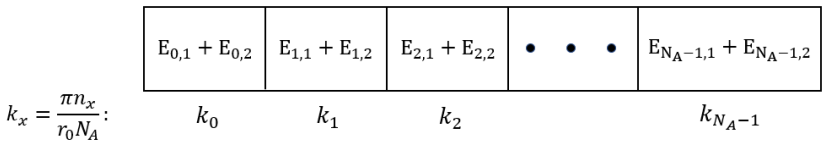

Figure 6.4: Master template for the time-stamped wave passing coefficients.

The flow chart shown in Fig. 6.5 provides an overview of the various steps required to pass more than one phonon wave packet between the atomistic and continuum regions of a CAC domain using the velocity Verlet time integration algorithm. We note that the second Fourier transform always occurs at the end of each time step regardless of whether or not a new wave is nucleated. If there is not a new phonon present in the domain, the first and second $C_{k,l}$ coefficients will cancel out and $E_{k,l}$ will equal zero. As a result, no "extra" data is ever added to the master template.

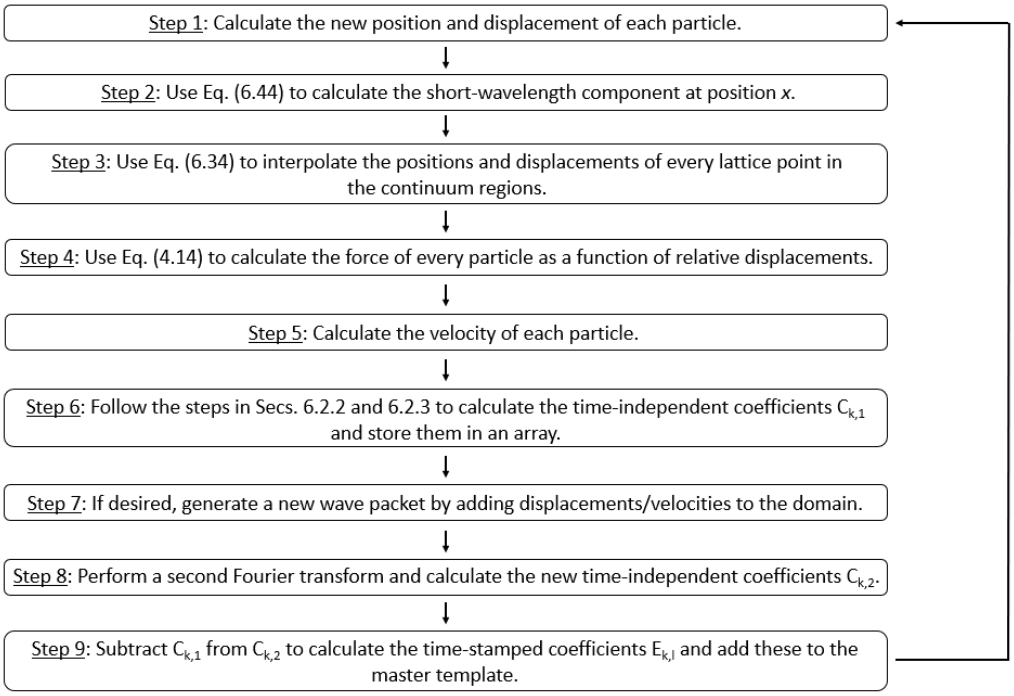

Figure 6.5: Flow chart showing the various steps taken to pass multiple waves between the atomistic and continuum regions of a CAC domain.

6.4 Benchmark examples with multiple waves

To verify the implementation and effectiveness of the technique discussed in Sec. 6.3, we perform simulations with multiple waves using the CAC framework described in Sec. 2.4.1. Specifically, we utilize the new technique to pass various high-frequency wave packets between the atomistic and continuum regions of the multiscale domain. Results from these simulations can be seen in both Fig. 6.6 as well as in Fig. 6.7. In each simulation, we nucleate four waves in the atomistic region and allow them to propagate to the right and travel across the A-C interfaces. The waves are generated in time increments of 15 ps, and each has a high wavevector value that would ordinarily cause the phonon to be completely reflected (as demonstrated in Fig. 5.2). We note that in Fig. 6.6, each phonon has the same wavevector ($k = 0.2\,\pi/r_0$) while in Fig. 6.7, the phonons increase in wavevector from $k = 0.2\,\pi/r_0$ to $k = 0.5\,\pi/r_0$. This is done in order to showcase how the new method can be used with multiple waves of a variety of frequencies within the same domain.

In both figures, we observe that the new method outlined in Sec. 6.3 permits each short-wavelength phonon wave packet to travel across the A-C interface with no observable reflection. Additionally, this scheme facilitates periodic boundary conditions whereby the waves can travel between the two outer continuum regions and back into the inner atomistic region. Hence, this method may be used in practical applications which require a periodic domain. Finally, we note that this technique can be utilized to track phonons with a variety of frequencies within a single domain, and these waves may interact with each other freely without undermining any stored data. Therefore, we can use this method to transmit many waves across length scales as they contact each other as well as the domain boundary.

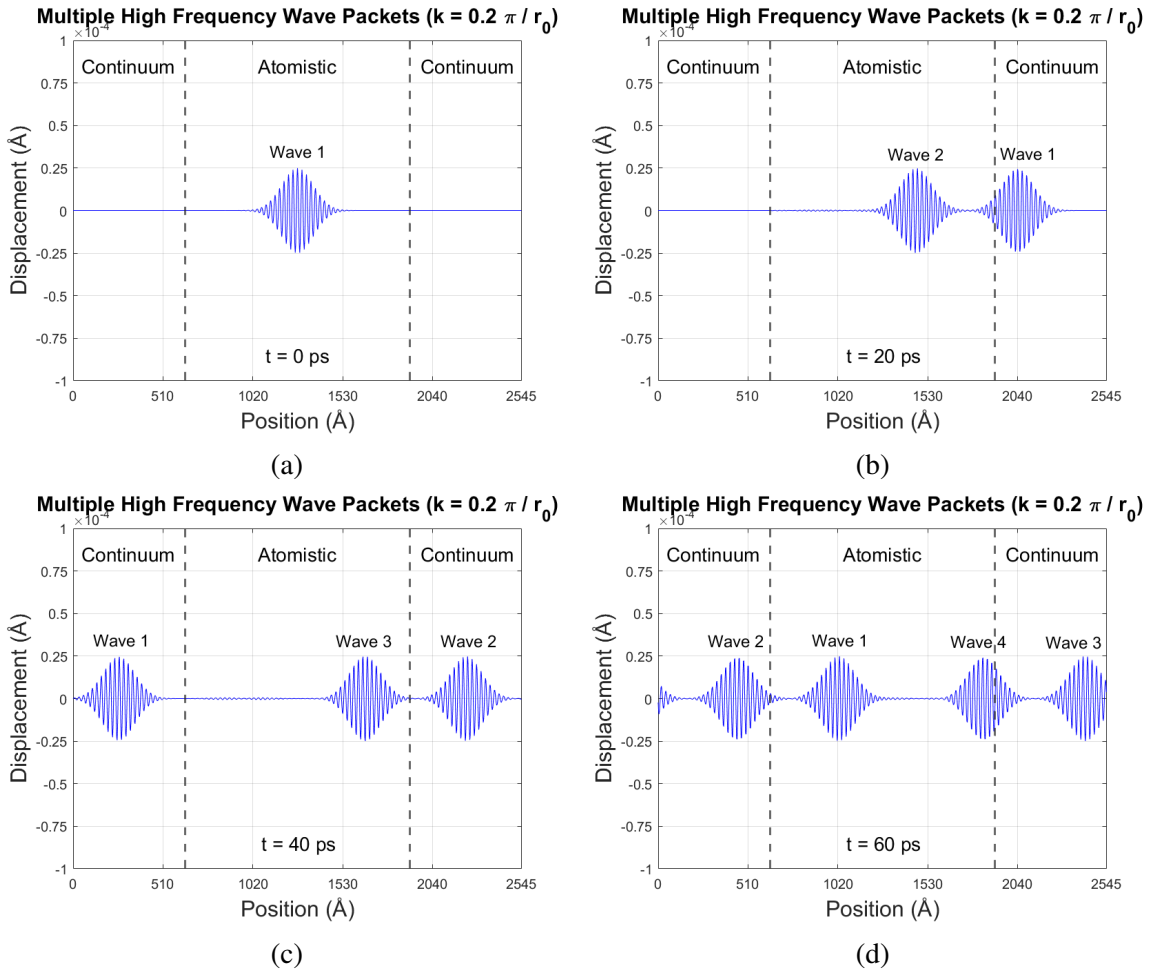

Figure 6.6: Multiple high-frequency phonon wave packets traveling through a single CAC domain. In this case, each phonon has the same wavevector: $k = 0.2\,\pi/r_0$.

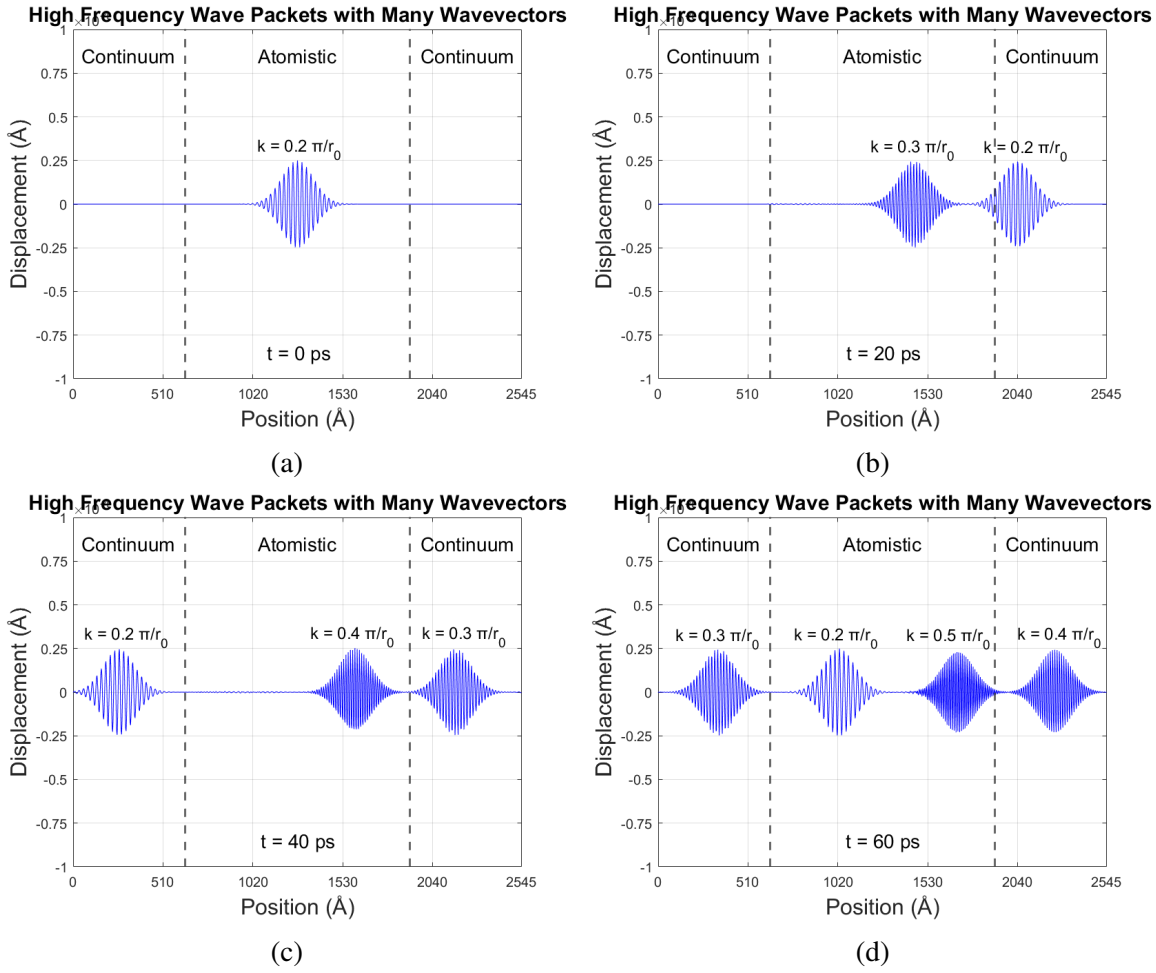

Figure 6.7: Multiple high-frequency phonon wave packets traveling through a single CAC domain. In this case, each phonon has a different wavevector as is shown.

Chapter 7

Results with the 2D CAC Framework

The results found in this chapter have also been published in *Computational Mechanics* [4]. As stated previously, the study of shock wave propagation using the CAC method has been limited due to the highly dynamic nature of such phenomena. In Ch. 5, we incorporated two moving window techniques into a CAC framework to track a nonlinear shock wave for long runtimes, but this formulation only considered a 1D chain of particles and was thus limited in scope.

7.1 Two-dimensional computational framework

7.1.1 2D abstract

In this chapter, we develop a multiscale framework using the CAC method to simulate long-time shock wave propagation through a two-dimensional lattice. Specifically, we utilize both the Hugoniot shock equations [11] as well as the nonlinear Eulerian shock equations [136] to analyze the well-known Riemann problem of an individual discontinuity traveling through a material. Furthermore, we enhance the moving window techniques first presented in [2] to track the shock over long simulation times and engineering-scale domains. Each method keeps the shock front in the middle of the atomistic region for the entire runtime, so the wave front never encounters the A-C interfaces. This allows us to model shock propagation for greater simulation times than traditional NEMD and multiscale methods and thus gain valuable information about the long-term, time-averaged material response to shock loading of two different FCC ductile metals: Cu and Al. The results from each set of shock equations are compared to analytical models as well as empirical data to highlight the directional anisotropies in single

crystals subject to shock loading. Next, parametric studies are performed related to the shock front's structure and its planarity. Finally, the capability of the CAC moving window technique compared to classic NEMD is showcased through speedup and efficiency tests.

7.1.2 2D geometry and boundary conditions

We use our personal C++ code to develop, test, operate, and update the two-dimensional CAC framework, and the monatomic lattice is divided into three primary regions as seen in Fig. 7.1. The two coarse-scaled (continuum) regions are composed of rhombus elements, and the four particles which make up any particular element are classified as *nodes* in this work. We choose rhombus elements because they align with the primitive unit cell of the FCC lattice (see Sec. 7.2.1) and thus facilitate a smooth transition between the fine-scaled and coarse-scaled regions. Specifically, the x-direction corresponds to the [112] lattice orientation while the y-direction corresponds to the $[\bar{1}10]$ lattice orientation. Since element connectivity is not required in CAC [117], each node is a member of only one element, and this greatly reduces the complexity of the finite element formulation. Furthermore, the edges of the grid in the continuum regions are "filled in" with particles which we refer to as *boundary atoms* in this work. This is done in order to facilitate periodic boundary conditions as shown in [146].

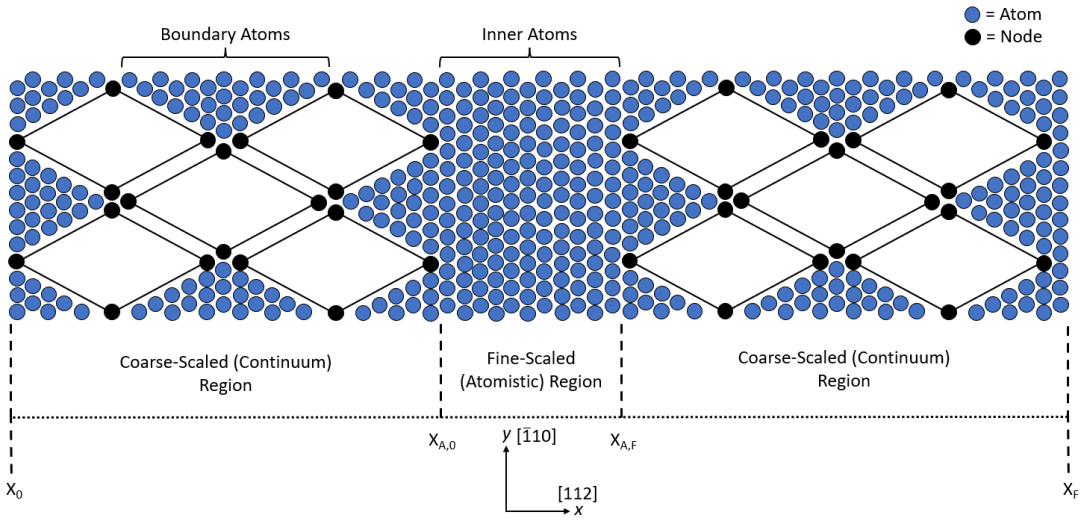

Figure 7.1: Schematic of the two-dimensional CAC framework.

The two continuum regions border the central fine-scaled (atomistic) region on the left and right-hand side, and we classify the particles in this region as either *inner atoms* or just *atoms* in

the present work. The "elements" in the fine-scaled region are reduced to their smallest possible configuration such that only four atoms constitute the entire area of each element. Hence, both the fine-scaled and coarse-scaled regions are technically made up of rhombuses with the only differences being the area and mass of their respective elements. As a consequence, one governing equation along with a single mass matrix is utilized for both regions, the interatomic potential is the only constitutive relation, and all force calculations are nonlocal [123]. Thus, as mentioned in Sec. 2.4, the particles at the A-C interfaces ($x_{A,0}$ and $x_{A,F}$) have a direct communication with each other without creating ghost forces [127, 146].

We note that to avoid introducing non-physical strains into the domain during shock simulations, semi-periodic boundary conditions are employed in the x-direction whereby the particles at the extreme ends of the lattice (x_0 and x_F) are neighbors with the nodes at the A-C interfaces ($x_{A,0}$ and $x_{A,F}$ respectively) [2]. Additionally, since the present work only considers uniaxial compression, we utilize periodic boundary conditions in the y-direction when modeling a longitudinal shock wave.

7.1.3 Shock parameters

In Table 7.1, we present the empirical Hugoniot shock parameters as well as the second, third, and fourth-order elastic constants (in a normal and Eulerian setting) for both Cu and Al. The Hugoniot parameters are obtained from [15], the second and third-order elastic constants for Cu and Al are obtained from [206] and [207] respectively, and the fourth-order elastic constants are obtained from [137]. For these values, the temperature is assumed to be 295 K, C_0 is given in km/sec, S is unitless, and the elastic constants are given in GPa. The Hugoniot parameters are derived for a shock wave propagating through a bulk, polycrystalline material. Furthermore, the elastic constants represent the pure-mode directions such that a planar shock impact results in an exclusively longitudinal component (along the [100] direction) with no transmitted shear stress, and hence the one-dimensional analysis is valid. We use these parameters as initial input in our shock simulations and compare the results from the CAC model to analytical and empirical data in Sec. 7.4.

Table 7.1: Hugoniot and Eulerian shock parameters for Cu and Al ($\theta = 295$ K, C_0 in km/sec, and $C_{\alpha\beta}$ in GPa).

Property	*Cu [100]*	*Al [100]*
C_0	3.94	5.33
S	1.49	1.34
C_{11}	166	107
C_{111}	-1270	-1080
$\hat{C}_{111}$	722	204
C_{1111}	11900	25000
$\hat{C}_{1111}$	2000	10500

7.1.4 'Elastic' shock waves

To legitimately utilize the shock equations from Sec. 2.2 as well as avoid intractability with the moving window techniques, we perform shock simulations with relatively small strains such that the resulting stresses are below the HEL of the material (see Appx. C.0.2). To maintain consistency, we refer to these as *elastic* shock waves in the present work. Elastic shock waves are often modeled in defect-free crystals with NEMD techniques to study a particular phenomenon, test a new framework, or validate a given potential [1, 41, 140], and their distinguishing characteristic is the lack of any permanent dislocations (inelastic deformation) behind the wave front. This is possible because the HEL is typically higher than what is seen in experimental settings [119], and the wave speed is still greater than the sound velocity in the material at the low strains. Modeling shock propagation with the CAC moving window framework using thermoelastic-viscoplastic models [208, 209] is a worthy pursuit but would add an extra layer of complexity to the current model and is thus reserved for future studies.

7.2 Two-dimensional CAC method

For a discussion of AFT and the finite element implementation of CAC, see Sec. 4. We note here that a unique feature of 2D CAC is that element connectivity is not required because the nonlocal interatomic force field is the only constitutive relation [117]. This is similar to aspects of the cohesive zone model [210] and greatly simplifies the implementation of both the mass matrix as well as the force calculations.

7.2.1 Element formulation in 2D

Rhombohedral elements are utilized within the CAC formulation to replicate the primitive unit cell of a monocrystalline lattice (FCC in the present work). A sketch of this can be seen in Fig. 7.2, where we observe the primitive unit cell (blue lines) within the broader FCC crystal structure. Furthermore, the shaded region represents the two-dimensional atomic plane

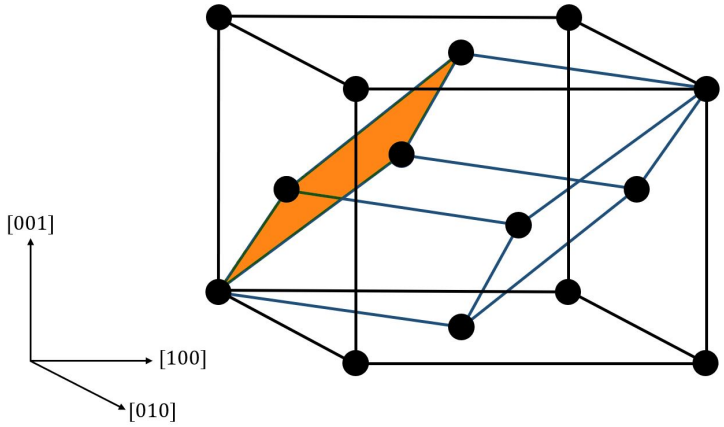

Figure 7.2: Rhombohedral element constituting the primitive unit cell (blue lines) of an FCC lattice. The shaded region represents the two-dimensional rhombus element utilized in the present formulation.

used in our formulation whereby rhombus elements are incorporated throughout the domain. Since the same constitutive relation is used both within elements as well as between elements, dislocations and cracks emerge naturally through the separation of finite elements [117]. This is a direct result of the CAC governing equations, and it allows such defects to pass smoothly across the A-C interfaces without deforming individual elements. As a result, some mesh sensitivity may be introduced into simulations with very high strains whereby different grid resolutions alter the convergence of the solution.

A schematic of the two-dimensional rhombus element can be seen in Fig. 7.3. Here, the black circles represent the four nodes where the governing equations are applied, and the grey circles represent the lattice points which serve as nodal neighbors and thus aid in the force calculations. For monatomic crystals, each nodal location (unit cell) only contains one atom, and the positions of the lattice points are interpolated using Eq. (4.15) throughout the element. We emphasize that the lattice points are excluded from the Verlet algorithm. Finally, since no

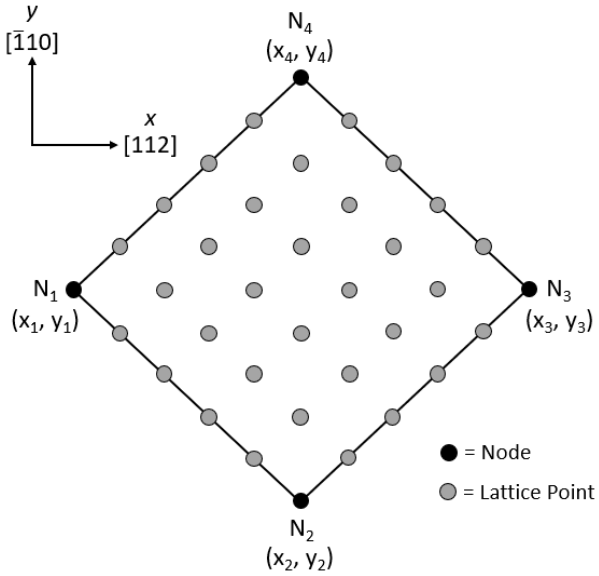

Figure 7.3: Schematic of the two-dimensional rhombus element.

external forces are applied in this work, the governing equations from Sec. 4.2 reduce to the following:

$$\mathbf{M}\ddot{\mathbf{U}} - \mathbf{F}^{int} = \mathbf{0} \tag{7.1}$$

where the terms $\mathbf{M}$ and $\mathbf{F}^{int}$ are given as

$$\mathbf{M} = \int_{\Omega(\mathbf{x})} \left[\rho \mathbf{\Phi}(\mathbf{x}) \mathbf{\Phi}(\mathbf{x})\right] d\mathbf{x} \tag{7.2}$$

$$\mathbf{F}^{int} = \int_{\Omega(\mathbf{x})} \mathbf{\Phi}(\mathbf{x}) \int_{\Omega(\mathbf{x}')} \sum_{j=1}^{n_\alpha} \mathbf{f}\left[\mathbf{\Phi}(\mathbf{x})\mathbf{U}_i - \mathbf{\Phi}(\mathbf{x}')\mathbf{U}_j\right] d\mathbf{x}' d\mathbf{x} = \int_{\Omega(\mathbf{x})} \mathbf{\Phi}(\mathbf{x}) \mathbf{f}^{int}(\mathbf{x}) d\mathbf{x}. \tag{7.3}$$

In Eq. (7.1), $\mathbf{M}$ is the mass matrix, and Sec. 7.2.2 provides a full derivation of this term. In brief, we utilize the lumped mass matrix approach in the present formulation which effectively reduces $\mathbf{M}$ to the following expression for each element:

$$\mathbf{M} = \frac{m N_{ppe}}{N_{npe}} \tag{7.4}$$

where m is the atomic mass, N_{ppe} is the number of particles per element (including lattice points), and N_{npe} is the number of nodes per element [146].

The terms $\ddot{\mathbf{U}}$ and $\mathbf{F}^{int}$ are the respective accelerations and internal forces for each atom/node in the lattice, and n_α represents the total number of neighbors of particle i within a specified cutoff radius. Furthermore, the local force $\mathbf{f}^{int}(\mathbf{x})$ on particle i at position $\mathbf{x}$ is obtained exclusively from the interatomic potential through relative displacements of particles, and the total force is obtained through Gaussian quadrature rules (see Sec. 7.2.3). We note that the surrounding lattice points act as atomic neighbors when calculating the force $\mathbf{f}^{int}(\mathbf{x})$ of a node in the continuum regions, whereas in the fine-scaled region, atomic neighbors are merely other atoms.

7.2.2 Mass matrix in 2D

We now elaborate on the isoparametric formulation of the mass matrix for a given continuum element in the two-dimensional CAC framework. As stated in Sec. 7.2, element connectivity is not required in CAC. Hence, this derivation is general and can be applied to any element in the domain assuming the physical nodal coordinates of that element are known.

The isoparametric shape functions of a four-node element are given as follows:

$$\phi_1(\xi,\eta) = \frac{1}{4}(1-\xi)(1-\eta) \tag{7.5}$$

$$\phi_2(\xi,\eta) = \frac{1}{4}(1+\xi)(1-\eta) \tag{7.6}$$

$$\phi_3(\xi,\eta) = \frac{1}{4}(1-\xi)(1+\eta) \tag{7.7}$$

$$\phi_4(\xi,\eta) = \frac{1}{4}(1+\xi)(1+\eta) \tag{7.8}$$

which can be stored in a matrix as

$$\mathbf{\Phi}(\xi,\eta) = \begin{bmatrix} \phi_1 & 0 & \phi_2 & 0 & \phi_3 & 0 & \phi_4 & 0 \\ 0 & \phi_1 & 0 & \phi_2 & 0 & \phi_3 & 0 & \phi_4 \end{bmatrix} \tag{7.9}$$

where $\phi_i = \phi_i(\xi, \eta)$. In order to map the element between the global and natural coordinate system, we need the Jacobian which is given as follows:

$$\boldsymbol{J} = \begin{bmatrix} \partial\phi_1/\partial\xi & \partial\phi_2/\partial\xi & \partial\phi_3/\partial\xi & \partial\phi_4/\partial\xi \\ \partial\phi_1/\partial\eta & \partial\phi_2/\partial\eta & \partial\phi_3/\partial\eta & \partial\phi_4/\partial\eta \end{bmatrix} \begin{bmatrix} x_1 & y_1 \\ x_2 & y_2 \\ x_3 & y_3 \\ x_4 & y_4 \end{bmatrix} \tag{7.10}$$

where (x_1, y_1), (x_2, y_2), (x_3, y_3), and (x_4, y_4) are the positions of the four element nodes in the global coordinate system. We note that the numbering goes counterclockwise starting from the left node as seen in Fig. 7.4. Expanding out Eq. (7.10) and taking the appropriate derivatives

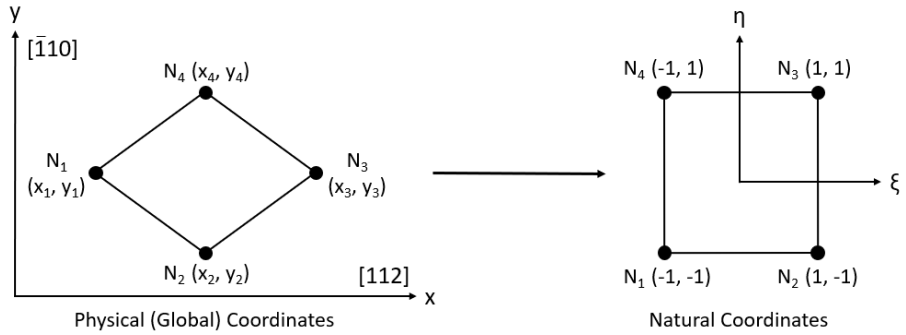

Figure 7.4: Mapping from global to natural coordinates of a two-dimensional CAC element.

of the shape functions, we obtain the four components of the Jacobian:

$$J_1 = \frac{x_1}{4}(\eta - 1) + \frac{x_2}{4}(1 - \eta) + \frac{x_3}{4}(\eta + 1) - \frac{x_4}{4}(\eta + 1) \tag{7.11}$$

$$J_2 = \frac{y_1}{4}(\eta - 1) + \frac{y_2}{4}(1 - \eta) + \frac{y_3}{4}(\eta + 1) - \frac{y_4}{4}(\eta + 1) \tag{7.12}$$

$$J_3 = \frac{x_1}{4}(\xi - 1) - \frac{x_2}{4}(\xi + 1) + \frac{x_3}{4}(\xi + 1) + \frac{x_4}{4}(1 - \xi) \tag{7.13}$$

$$J_4 = \frac{y_1}{4}(\xi - 1) - \frac{y_2}{4}(\xi + 1) + \frac{y_3}{4}(\xi + 1) + \frac{y_4}{4}(1 - \xi). \tag{7.14}$$

Hence, the Jacobian determinant is

$$det(\mathbf{J}) = \begin{vmatrix} J_1 & J_2 \\ J_3 & J_4 \end{vmatrix} = J_1 J_4 - J_2 J_3 \tag{7.15}$$

which can be simplified using a software program like Wolfram Mathematica.

The expression for the mass matrix of the 2D element in global coordinates is given as follows:

$$\mathbf{M} = \rho \int_A \mathbf{\Phi}^T \mathbf{\Phi} \; dA. \tag{7.16}$$

Writing this in natural coordinates:

$$\mathbf{M} = \rho \int_{-1}^{1} \int_{-1}^{1} \left[\mathbf{\Phi}^T \mathbf{\Phi} \cdot det(\mathbf{J}) \right] d\xi d\eta \tag{7.17}$$

where

$$\mathbf{\Phi}^T \mathbf{\Phi} = \begin{bmatrix} \phi_1 & 0 \\ 0 & \phi_1 \\ \phi_2 & 0 \\ 0 & \phi_2 \\ \phi_3 & 0 \\ 0 & \phi_3 \\ \phi_4 & 0 \\ 0 & \phi_4 \end{bmatrix} \begin{bmatrix} \phi_1 & 0 & \phi_2 & 0 & \phi_3 & 0 & \phi_4 & 0 \\ 0 & \phi_1 & 0 & \phi_2 & 0 & \phi_3 & 0 & \phi_4 \end{bmatrix} \tag{7.18}$$

and ρ is the area of the element. As a result, we can use the expressions for the shape functions as well as $det(\mathbf{J})$ from Eq. (7.15) to calculate all sixty-four components of the mass matrix for the given element. It turns out, however, that only ten of these components are unique, so we can simplify the mass matrix significantly as follows:

$$\mathbf{M} = \begin{bmatrix} M_{11} & M_{13} & M_{15} & M_{17} \\ M_{13} & M_{33} & M_{35} & M_{37} \\ M_{15} & M_{35} & M_{55} & M_{57} \\ M_{17} & M_{37} & M_{57} & M_{77} \end{bmatrix} \tag{7.19}$$

where

$$M_{ij} = \rho \int_{-1}^{1} \int_{-1}^{1} \left[\phi_i \phi_j \cdot det(\mathbf{J}) \right] d\xi d\eta. \tag{7.20}$$

After obtaining the cumulative force on each node in the element through Gaussian integration (see Sec. 7.2.3), we can then calculate the respective accelerations as follows:

$$\begin{bmatrix} \ddot{\mathbf{u}}_1 \\ \ddot{\mathbf{u}}_2 \\ \ddot{\mathbf{u}}_3 \\ \ddot{\mathbf{u}}_4 \end{bmatrix} = \begin{bmatrix} M_{11} & M_{13} & M_{15} & M_{17} \\ M_{13} & M_{33} & M_{35} & M_{37} \\ M_{15} & M_{35} & M_{55} & M_{57} \\ M_{17} & M_{37} & M_{57} & M_{77} \end{bmatrix}^{-1} \begin{bmatrix} \mathbf{f}_1 \\ \mathbf{f}_2 \\ \mathbf{f}_3 \\ \mathbf{f}_4 \end{bmatrix}. \tag{7.21}$$

In this work, we use the lumped mass matrix approximation, and specifically, the row-sum method. Hence, we can further simplify our calculations and sum the rows of the mass matrix such that

$$M_1 = M_{11} + M_{13} + M_{15} + M_{17} \tag{7.22}$$

$$M_2 = M_{13} + M_{33} + M_{35} + M_{37} \tag{7.23}$$

$$M_3 = M_{15} + M_{35} + M_{55} + M_{57} \tag{7.24}$$

$$M_4 = M_{17} + M_{37} + M_{57} + M_{77}. \tag{7.25}$$

Therefore, we arrive at the final result for the accelerations of the four nodes:

$$\begin{bmatrix} \ddot{\mathbf{u}}_1 \\ \ddot{\mathbf{u}}_2 \\ \ddot{\mathbf{u}}_3 \\ \ddot{\mathbf{u}}_4 \end{bmatrix} = \begin{bmatrix} \mathbf{f}_1/M_1 \\ \mathbf{f}_2/M_2 \\ \mathbf{f}_3/M_3 \\ \mathbf{f}_4/M_4 \end{bmatrix}. \tag{7.26}$$

For the sake of completeness, we provide the expressions for the ten unique components of the two-dimensional mass matrix below:

$$M_{11} = \frac{\rho}{36}\left[(3x_1 - x_3)(y_2 - y_4) + x_2(2y_4 + y_3 - 3y_1) + x_4(3y_1 - 2y_2 - y_3)\right] \tag{7.27}$$

$$M_{13} = \frac{\rho}{72}\left[x_1(3y_2 - y_3 - 2y_4) + x_2(y_4 + 2y_3 - 3y_1) + x_3(y_1 - 2y_2 + y_4) + x_4(2y_1 - y_2 - y_3)\right] \tag{7.28}$$

$$M_{15} = \frac{\rho}{72}\left[(x_1 - x_3)(y_2 - y_4) - (x_2 - x_4)(y_1 - y_3)\right] \tag{7.29}$$

$$M_{17} = \frac{\rho}{72}\left[x_1(2y_2 + y_3 - 3y_4) + x_2(y_4 + y_3 - 2y_1) - x_3(y_1 + y_2 - 2y_4) + x_4(3y_1 - y_2 - 2y_3)\right] \tag{7.30}$$

$$M_{33} = \frac{\rho}{36}\left[x_1(3y_2 - 2y_3 - y_4) + 3x_2(y_3 - y_1) + x_3(2y_1 - 3y_2 + y_4) + x_4(y_1 - y_3)\right] \tag{7.31}$$

$$M_{35} = \frac{\rho}{72}\left[x_1(2y_2 - y_3 - y_4) - x_2(2y_1 - 3y_3 + y_4) + x_3(y_1 - 3y_2 + 2y_4) + x_4(y_1 + y_2 - 2y_3)\right] \tag{7.32}$$

$$M_{37} = \frac{\rho}{72}\left[(x_1 - x_3)(y_2 - y_4) - (x_2 - x_4)(y_1 - y_3)\right] \tag{7.33}$$

$$M_{55} = \frac{\rho}{36}\left[(x_1 - 3x_3)(y_2 - y_4) - x_2(y_1 - 3y_3 + 2y_4) + x_4(y_1 + 2y_2 - 3y_3)\right] \tag{7.34}$$

$$M_{57} = \frac{\rho}{72}\left[x_1(y_2 + y_3 - 2y_4) - x_2(y_1 - 2y_3 + y_4) - x_3(y_1 + 2y_2 - 3y_4) + x_4(2y_1 + y_2 - 3y_3)\right] \tag{7.35}$$

$$M_{77} = \frac{\rho}{36}\left[x_1(y_2 + 2y_3 - 3y_4) + x_2(y_3 - y_1) - x_3(2y_1 + y_2 - 3y_4) + 3x_4(y_1 - y_3)\right] \tag{7.36}$$

As can be seen, each of these terms is strictly a function of the four nodal positions of the element in the global coordinate system as well as the density ρ. Thus, assuming that we know the global coordinates, we can calculate each component of the mass matrix and thereby obtain the acceleration of each node.

7.2.3 Gaussian integration in 2D

When employing the two-dimensional framework, we calculate the internal force density using Gaussian integration, so we now elaborate on this method for a 2D coarse-scaled element. In Gaussian integration, the elemental forces are approximated by the forces at both the nodes as well as the integration points. Thus, while more complex to implement, Gaussian integration typically results in more accurate force calculations when using complex geometries or large elements. For all of our simulations, we use twelve-point Gaussian integration such that each element, in addition to the four nodes, contains twelve integration points. These integration points are chosen such that there are two along each edge of the element and four on the interior surface as seen in Fig. 7.5. In particular, both the edge and surface integration points are chosen to be equal to the lattice points which directly neighbor the nodes, and this is comparable to techniques used in other multiscale schemes such as cluster-QC [10] and three-dimensional CAC [146].

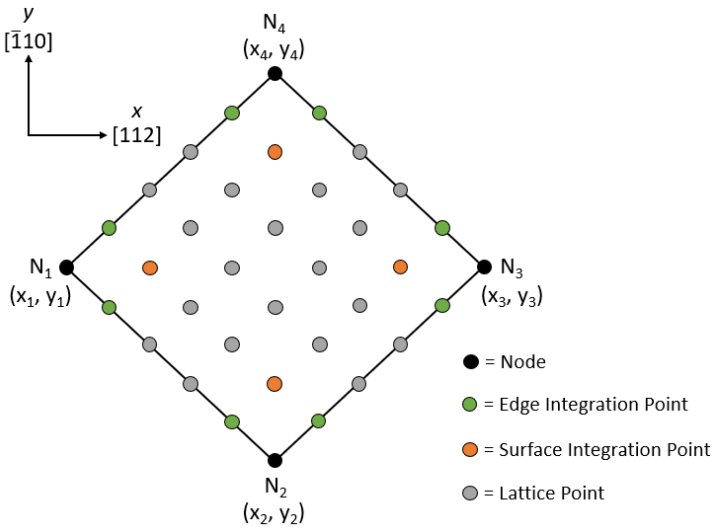

Figure 7.5: Two-dimensional CAC coarse-scaled element. Nodes are shown in black, edge integration points are shown in green, surface integration points are shown in orange, and lattice points are shown in grey.

The forces within the 2D element are thus split into three distinct parts associated with the (1) nodes, (2) edges, and (3) surfaces as seen in the equation below:

$$\mathbf{F}_{int} = \mathbf{FN}_{int} + \mathbf{FE}_{int} + \mathbf{FS}_{int}. \tag{7.37}$$

The first term in Eq. (7.37) represents the forces at the nodes and is calculated as follows:

$$\begin{aligned}
\mathbf{FN}_{int} &= w_{N_1}\mathbf{\Phi}(N_1)\mathbf{f}_{int}(N_1) + w_{N_2}\mathbf{\Phi}(N_2)\mathbf{f}_{int}(N_2) + w_{N_3}\mathbf{\Phi}(N_3)\mathbf{f}_{int}(N_3) + w_{N_4}\mathbf{\Phi}(N_4)\mathbf{f}_{int}(N_4) \\
&= \begin{bmatrix} \phi_1(N_1) \\ \phi_2(N_1) \\ \phi_3(N_1) \\ \phi_4(N_1) \end{bmatrix} \mathbf{f}_{int}(N_1) + \begin{bmatrix} \phi_1(N_2) \\ \phi_2(N_2) \\ \phi_3(N_2) \\ \phi_4(N_2) \end{bmatrix} \mathbf{f}_{int}(N_2) + \begin{bmatrix} \phi_1(N_3) \\ \phi_2(N_3) \\ \phi_3(N_3) \\ \phi_4(N_3) \end{bmatrix} \mathbf{f}_{int}(N_3) + \begin{bmatrix} \phi_1(N_4) \\ \phi_2(N_4) \\ \phi_3(N_4) \\ \phi_4(N_4) \end{bmatrix} \mathbf{f}_{int}(N_4) \\
&= \begin{bmatrix} 1 \\ 0 \\ 0 \\ 0 \end{bmatrix} \mathbf{f}_{int}(x_1, y_1) + \begin{bmatrix} 0 \\ 1 \\ 0 \\ 0 \end{bmatrix} \mathbf{f}_{int}(x_2, y_2) + \begin{bmatrix} 0 \\ 0 \\ 1 \\ 0 \end{bmatrix} \mathbf{f}_{int}(x_3, y_3) + \begin{bmatrix} 0 \\ 0 \\ 0 \\ 1 \end{bmatrix} \mathbf{f}_{int}(x_4, y_4) \\
&= \begin{bmatrix} \mathbf{f}_{int}(x_1, y_1) \\ \mathbf{f}_{int}(x_2, y_2) \\ \mathbf{f}_{int}(x_3, y_3) \\ \mathbf{f}_{int}(x_4, y_4) \end{bmatrix}
\end{aligned} \tag{7.38}$$

where we note that all of the weights equal one. Additionally, each shape function equals one at its nodal location and zero everywhere else. Equation (7.38) would be the only force used in nodal integration – a technique which effectively does not alter the forces obtained using the interatomic potential function and relative displacement of particles. Although nodal integration is more computationally efficient, it is less robust than Gaussian integration and only accurate for simple geometries and relatively small elements, so it is not used in 2D CAC.

The second two forces in Eq. (7.37) are given as follows:

$$\mathbf{FE}_{int} = \sum_{j=1}^{8} (w_{j,x} \cdot w_{j,y}) \mathbf{\Phi}(j) \mathbf{f}_{int}(j) \tag{7.39}$$

$$\mathbf{FS}_{int} = \sum_{j=9}^{12} (w_{j,x} \cdot w_{j,y}) \mathbf{\Phi}(j) \mathbf{f}_{int}(j). \tag{7.40}$$

In Eqs. (7.39) and (7.40), the summations occur over the eight edge integration points and four surface integration points respectively. Furthermore, the terms $w_{j,x}$ and $w_{j,y}$ are the weights of the integration points along the x and y directions. Finally, $\mathbf{\Phi}(j)$ is the shape function vector at the given integration point while $\mathbf{f}_{int}(j)$ is the force of the integration point obtained through the potential function. For the sake simplicity, we do not write out the full expressions of these terms, but the expansion would be similar to that shown for the nodal forces in Eq. (7.38).

7.3 Two-dimensional shock propagation technique

7.3.1 Shock initialization in 2D

For each simulation, the shock wave is characterized using either the Hugoniot (Sec. 2.1) or Eulerian (Sec. 2.2) governing equations, and the shock front is achieved by dividing the grid from Fig. 7.1 into different regions as seen in Fig. 7.6. The boundary particles within each continuum domain (red circles) constitute the *thermostat regions* and are categorized as "damped" atoms since they apply a constant temperature to the lattice through the Langevin thermostat. Furthermore, a narrow band of inner atoms at each A-C interface are also damped to ensure that the *window region* made up of "undamped" atoms (blue circles) achieves the correct canonical ensemble [2]. We note that as in [78], the nodes (black circles) are left undamped to prevent spurious behavior within each element. The shock wave front (SWF) starts at the midpoint of the WR and travels to the right along the positive x-direction with a speed of U_S. We delineate material to the right of the SWF as the unshocked region and material to the left of the SWF as the shocked region.

To initialize the shock, we assign a final strain ϵ^+ to the shocked region and use either Eqs. (2.12) and (2.14) for the Hugoniot formulation or Eqs. (2.49) and (2.50) for the Eulerian formulation to calculate the mean particle velocity v^+ and SWF velocity U_S. The Hugoniot parameters C_0 and S as well as the elastic constants C_{11}, $\hat{C}_{111}$, and $\hat{C}_{1111}$ are initially assigned their literature values given in Table 7.1. The particle velocity v^+ is the new equilibrium velocity for the shocked region, and the strain ϵ^+ causes the lattice to compress uniaxially such

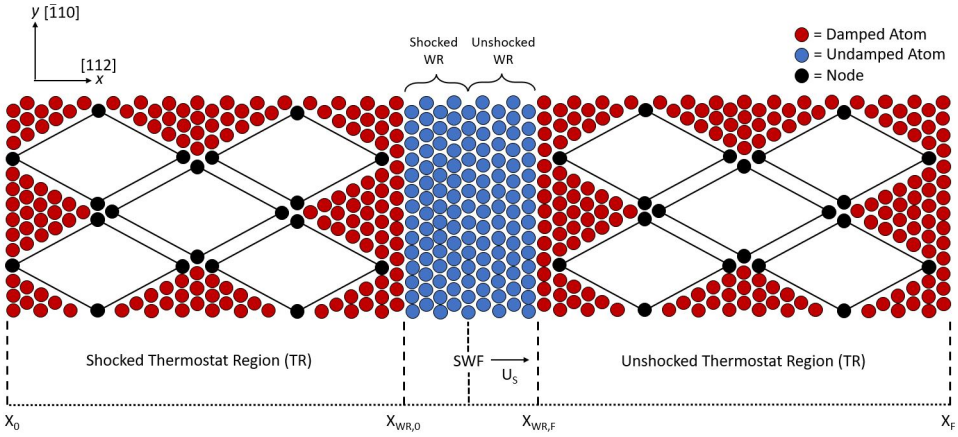

Figure 7.6: Two-dimensional CAC geometry used for shock wave simulations. Here, the red circles represent damped atoms, the blue circles represent undamped atoms, and the black circles represent nodes.

that particles behind the SWF obey the Cauchy-Born rule [156]. As a result, the shocked region achieves its final state and the SWF starts to propagate forward beginning in the middle of the WR. The temperature θ^+ calculated from either Eq. (2.32) or Eq. (2.51) is applied to the shocked TR, and each TR is far enough away from the non-equilibrium SWF to be considered within a region of "local" equilibrium. Hence, we can legitimately apply the Langevin thermostat to the strained portion of the domain [70].

In the following sections, we discuss how the moving window techniques are incorporated into the two-dimensional CAC framework.

7.3.2 Conveyor method in 2D

Figure 7.7 provides a schematic of the conveyor technique for the two-dimensional CAC framework. This technique is similar to the scheme found in [2] for one dimension, but there are more intricacies and complexities associated with the higher-dimensional lattice. After the SWF has traveled one lattice spacing (a_{lat}) along the positive x-direction from the center of the WR, the initial position, displacement, velocity, and acceleration of particles in the first two columns of the grid are set equal to the parameters of their rightmost neighbors within the same row. The neighbors may be either boundary atoms, nodes, or lattice points, but if they are lattice points, the Verlet parameters are first interpolated as discussed in Sec. 4.2. Effectively, the parameters

of particles within the first two columns of the lattice are removed from the simulation as is noted in the figure by the leftmost arrow.

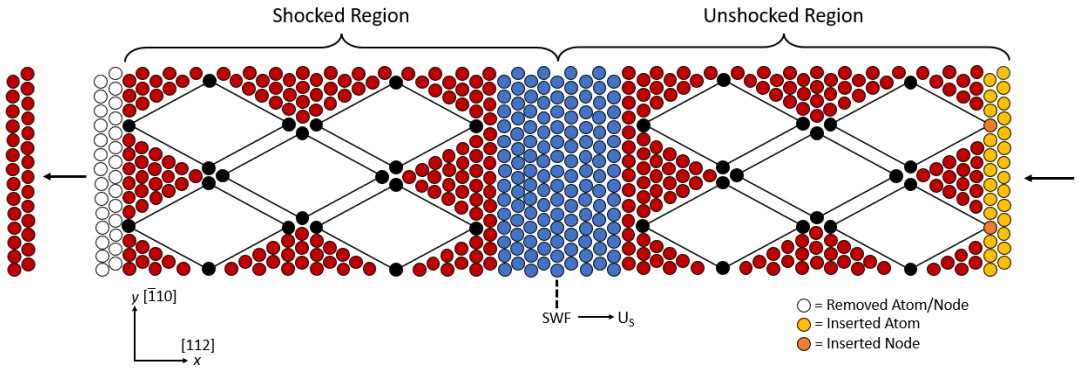

Figure 7.7: Schematic of the moving window *conveyor* technique for the 2D CAC framework. The white circles represent removed particle locations while the gold/orange circles represent inserted particle locations.

This process continues throughout the entire domain from the beginning of the shocked region to the end of the unshocked region, and we note that only the initial position of lattice points are updated since their displacements, velocities, and accelerations are interpolated during the integration algorithm. Particles in the final column of the domain (denoted by the gold and orange circles in Fig. 7.7) are given new initial x-positions which are one lattice spacing greater than their current initial x-positions, and their y-positions remain the same. Furthermore, their displacements, velocities, and accelerations are all set equal to zero, and the Langevin thermostat dampens any energy fluctuations generated near x_F as in [77]. This conveyor mechanism occurs with a frequency of $\tau^{-1} = U_S/a_{lat}$, and if the simulated and analytical shock velocities are the same, the SWF will remain stationary in the middle of the WR for the entire runtime. The resulting time resolution of a_{lat}/U_S is thus optimized for the given shock propagation velocity, but higher time resolutions are achievable depending on the speed of the phenomenon in question.

7.3.3 Coarsen-refine method in 2D

A schematic of the two-dimensional coarsen-refine method can be seen in Fig. 7.8, and it is again similar in principle to the 1D technique from [2]. Here, after the SWF has traveled a distance equal to the length of the element diagonal (e_{diag}) plus the lattice spacing divided

by two, the moving window mechanism begins whereby material in the shocked continuum region gets coarsened and material in the unshocked continuum region gets refined. In the shocked region, coarsening is achieved by transforming the relevant particles into nodes and lattice points such that new elements appear in the previous atomic locations. On the other hand, in the unshocked region, refinement takes place by changing nodes and lattice points into fine-scaled particles through both parameter re-assignment and linear interpolation – similar to what is done with the conveyor technique. This procedure effectively transmits the fine-scaled region forward to the new SWF location as seen in Fig. 7.8.

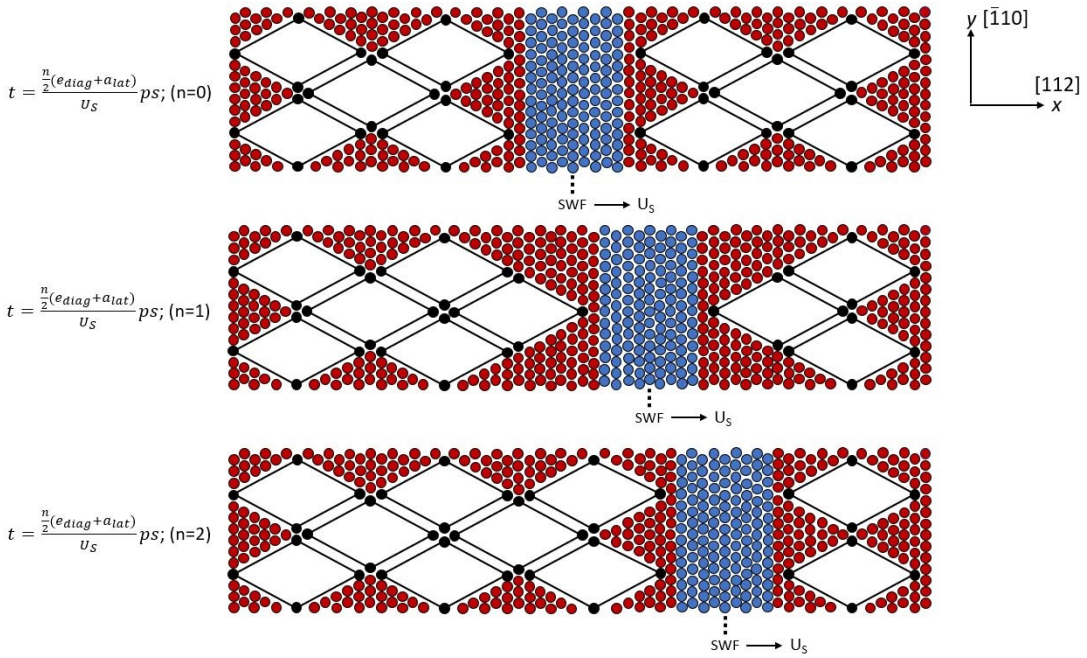

Figure 7.8: Schematic of the moving window *coarsen-refine* technique for the 2D CAC framework.

After this process completes, undamped particles at the A-C interfaces in the shocked material are redefined as damped particles and vice versa for particles in the unshocked material. Furthermore, the mass matrix is modified to exhibit the new mass distribution within the lattice. This technique occurs iteratively with a frequency of $\tau^{-1} = U_S/\frac{1}{2}\left(e_{diag} + a_{lat}\right)$, and the integer time counter n is increased by one each time the mechanism terminates (as shown in Fig. 7.8). When utilizing the coarsen-refine method, the entire two-dimensional grid remains stationary and merely the location of the fine-scaled region is shifted. As a result, most the the domain can be populated with finite elements while a comparatively small section of atoms

track the propagating shock wave through the lattice. This technique thus ultimately endeavors to balance total efficiency and total accuracy of nonlinear shock wave modeling.

7.4 Elastic Anisotropy: Crystal Orientation Dependence of Shock Propagation Response

In this section, we elaborate on the shock velocity and longitudinal stress results obtained with both the Hugoniot and Eulerian formulations and discuss how they relate to the directional anisotropy of materials subject to shock impact. Recent NEMD works have studied shock propagation along different lattice directions of single crystals and observed a significant orientation dependence on the material's shock response [13, 14, 50, 82]. This phenomenon has also been documented for elastic shock waves in small-scale, atomistic domains [140]. Interestingly, large-scale experimental studies have not shown the same orientation dependence of shock parameters [83], but this may be due to the fact that bulk crystals naturally have more defects than what can be feasibly represented using atomistic techniques [14]. The present work provides a unique insight on this phenomenon because the CAC domain is modeled after the primitive unit cell of an FCC lattice and thus promotes a smooth transition between the atomistic and continuum regions. Hence, the shock travels along the [112] longitudinal direction, and the $[\bar{1}10]$ direction is transverse to the direction of propagation. To the authors' knowledge, this is one of the first studies to analyze shock evolution along this particular orientation.

7.4.1 Simulation specifications

The results in this section are obtained from shock wave simulations performed with the *conveyor* moving window technique using the CAC domain described in Fig. 7.6. For every simulation, the left and right coarse-scaled regions each contain 250 particle columns for a total length of $250a_{lat}$, and each element diagonal has a length of $8a_{lat}$. Furthermore, the fine-scaled region contains 2,500 particle columns, and the length of each element diagonal is merely the lattice spacing (a_{lat}). Additionally, each atomistic TR band contains 20 columns to ensure that the WR reaches the desired temperature [78]. Simulations are conducted for compressive strains (ϵ^+) ranging from 1% to 9% and 1% to 8% for Cu and Al respectively (see Appx. C.0.2), and the total runtime is 2 ns. A velocity profile of the two-dimensional shocked lattice can be

seen in Fig. 7.9a. Specifically, we track the SWF over time in MATLAB by taking a column average of the particle velocities as shown in Fig. 7.9b.

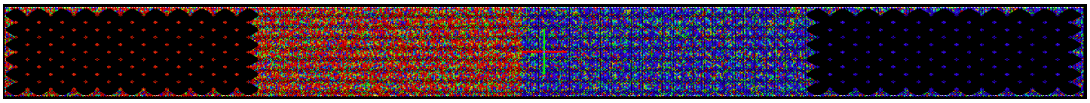

(a)

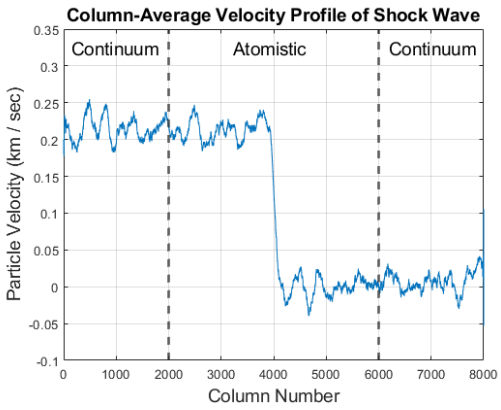

(b)

Figure 7.9: Velocity profiles of the propagating shock in the CAC framework. (a) SWF in the two-dimensional grid (not to scale); (b) SWF obtained from averaging the column velocities of the lattice.

7.4.2 Shock velocity results

Shock velocity results obtained for both Hugoniot and Eulerian theory can be seen in Figs. 7.10 and 7.11 respectively. Specifically, Fig. 7.10 displays the shock velocity vs. particle velocity data (as well as the derived Hugoniot equations) of four different sets of simulations using both (a) Cu and (b) Al. Here, the blue line represents the polycrystalline Hugoniot calculated in [15], and the green data points are the average velocity results for shocks propagating through the standard CAC domain. As a comparison, we also invert the lattice such that the $[\bar{1}10]$ orientation lies along the x-direction, and the [112] orientation lies along the y-direction. These results are given by the red data points. As in Appx. C.0.2, we performed stress vs. strain studies for this inverted lattice and found yielding to occur at 9% strain for Cu and 8% strain for Al, so we maintain ϵ^+ values below these elastic limits when simulating shocks along the $[\bar{1}10]$ direction. Finally, we also present one-dimensional atomistic shock data obtained from [1] for Cu and calculated in this work for Al.

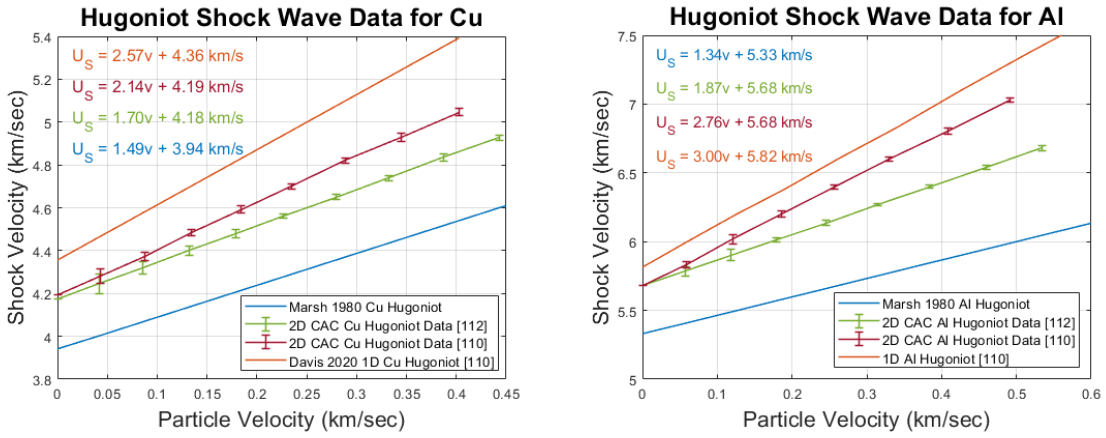

(a) (b)

Figure 7.10: Hugoniot shock wave results for both (a) Cu and (b) Al. The polycrystalline shock Hugoniot obtained from [15] is shown in blue. Two-dimensional CAC Hugoniot data obtained for shocks propagating along the [112] and $[\bar{1}10]$ lattice directions are shown in green and red respectively. One-dimensional shock Hugoniots are given in orange. The Cu Hugoniot comes from [1], and the Al Hugoniot is calculated in the present work.

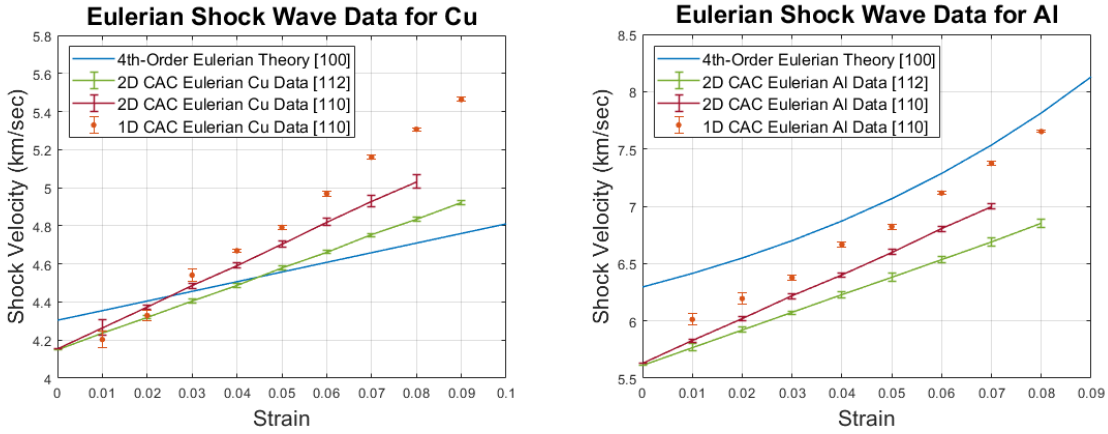

(a) (b)

Figure 7.11: Eulerian shock results for both (a) Cu and (b) Al. The blue line represents velocities obtained from fourth-order Eulerian theory. Two-dimensional CAC data obtained for shocks propagating along the [112] and $[\bar{1}10]$ lattice directions are shown in green and red respectively. One-dimensional CAC data obtained from [2] are in orange.

The data and associated Hugoniot equations in Fig. 7.10 clearly show the dependency of a shock's propagation velocity on the given lattice orientation. In particular, both of the two-dimensional CAC Hugoniots have C_0 and S values which are greater than the standard polycrystalline Hugoniot. This is most likely due to the fact that the FCC primitive unit cell is rhombohedral instead of cubic, so the entire CAC lattice is more compressed than a traditional structured FCC grid. This causes the particles in the domain to be more compact which results in larger forces from the interatomic potential and hence higher shock velocities. Additionally, the polycrystalline Hugoniot data are fitted to strong shock waves for which yielding reduces the effects of the shear modulus. Hence, we would anticipate the shocks from [15] to be slower than the elastic CAC shocks since shear stress is limited to plastic yield strength. Next, as expected, the inverted CAC lattice produces slightly higher shock velocities than the lattice from Fig. 7.6 since the $[\bar{1}10]$ lattice spacing is shorter than the [112] spacing. Finally, the one-dimensional shock velocities are greater than the those from the two-dimensional simulations due to the lack of any transverse motion which naturally dampens the shock speed. Instead, the 1D results are comparable to plane-plane collisions in a bulk lattice [33].

We observe a similar phenomenon for the Eulerian results in Fig. 7.11 where we now plot average shock velocity vs. applied strain. Here, the green and red data points are from the same types of 2D simulations as those from Fig. 7.10. However, the blue line now represents the analytical results from fourth-order Eulerian theory, and the orange data points are 1D CAC shock results obtained from [2]. Since we utilize elastic constants obtained for shocks propagating along the [100] direction and the CAC formulation analyzes shocks along the [112] and $[\bar{1}10]$ directions, elastic anisotropy in the crystal lattice is a major reason why the results from the various models differ.

As seen previously, the 1D shock velocities are slightly greater than the 2D velocities from the present study, and the inverted CAC lattice has a higher slope than the standard CAC lattice. For Cu, the shock velocities predicted at higher strains by Eulerian theory are indeed lower than the 2D and 1D CAC results, but this is not the case for Al. The reason for the anomalous results with Al is not necessarily clear, but it could be due to the fact that the third- and fourth-order elastic constants are not always measurable to high accuracy, so uncertainties in their values

would lead to uncertainty in the results predicted by fourth-order Eulerian theory. Nonetheless, we observe qualitative compatibility between the Hugoniot and Eulerian formulations which gives us confidence that the current CAC framework produces accurate results and can thus be reliably used to measure the response of materials to shock propagation along various lattice directions.

7.4.3 Longitudinal stress results

To supplement the anisotropic shock velocity results from Sec. 7.4.2, we perform longitudinal stress vs. strain studies using the shocked data for both Cu and Al, and these results can be seen in Fig. 7.12. Specifically, we calculate the time-averaged virial (thermodynamic) stress (σ_{xx}) in the shocked region using Eq. (C.1), and we relate the Cauchy stress (P_{xx}) to the virial stress as follows [140]:

$$P_{xx} = (1 - \epsilon)\sigma_{xx} \tag{7.41}$$

where we note that compressive stress/strain is considered positive.

Fig. 7.12 shows the shock stress P_{xx} normalized by the second-order elastic constant C_{11} as a function of the applied strain. The data from Hugoniot and Eulerian theory were practically identical, so without loss of generality, we only exhibit the Eulerian results. The [100] second, third, and fourth-order Eulerian models are represented by the blue, orange, and green lines respectively, while the [112] and $[\bar{1}10]$ shock stress data are represented by the purple circles and gold diamonds respectively. As in Sec. 7.4.2, we clearly observe the orientation dependence and elastic anisotropy of the shock stress as the CAC data is significantly higher than that predicted by the various Eulerian models for shocks along the [100] direction. Furthermore, the $[\bar{1}10]$ CAC simulations produced shock stresses which were slightly higher than those from the [112] simulations. Again, this is primarily due to the higher compression velocities caused by the larger 'compactness' of CAC domains. This anisotropic stress data is congruent with a previous work which analyzed elastic shocks along various lattice directions using a number of different potential functions [140].

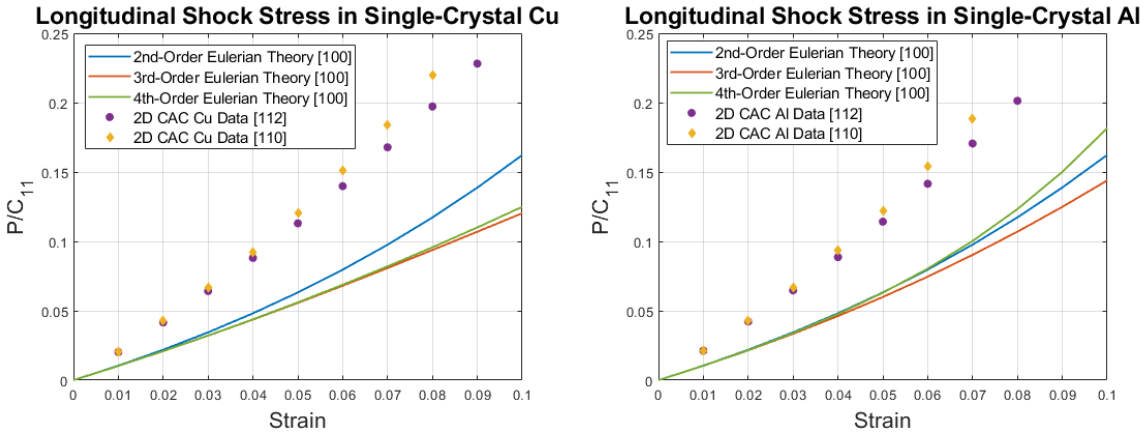

(a) (b)

Figure 7.12: Longitudinal stress data for both (a) Cu and (b) Al. The blue, orange, and green lines represent the [100] results from 2nd, 3rd, and 4th-order Eulerian theory respectively. The purple circles and gold diamonds represent the [112] and $[\bar{1}10]$ CAC data respectively.

7.5 2D Results with the Coarsen-Refine Method and Formulation Efficiency

Without loss of generality, we only reference data from Eulerian theory in this section as both shock models gave similar quantitative results.

7.5.1 Coarsen-refine simulations

In Fig. 7.13, we present results from a shock wave simulation performed using the *coarsen-refine* technique over 6 ns. Here, we can observe the atomistic portion of the domain successfully follow the evolving shock front throughout the CAC framework with no spurious wave behavior at the A-C interfaces. Due the elastic nature of the shock as discussed in Sec. 7.1.4, no dislocations are present to the left of the wave front, but we do see the shocked material maintain the mean particle velocity of v^+ for the entire runtime. These results are in contrast to those performed using the conveyor technique because now the SWF may travel through the entire CAC domain while staying within the fine-scaled region. Although previous work has used mesh refinement to study phenomena within both finite-element [189] and multiscale [116, 123, 190] schemes, utilizing simultaneous refine/coarsen techniques to study dynamic, high-temperature phenomena is still a challenging area of research [2]. Thus, the present formulation provides a novel means for tracking propagating shocks over long runtimes, and may

be used to research even more complex lattice structures in the future such as nanoscale composites or high-entropy alloys (HEAs).

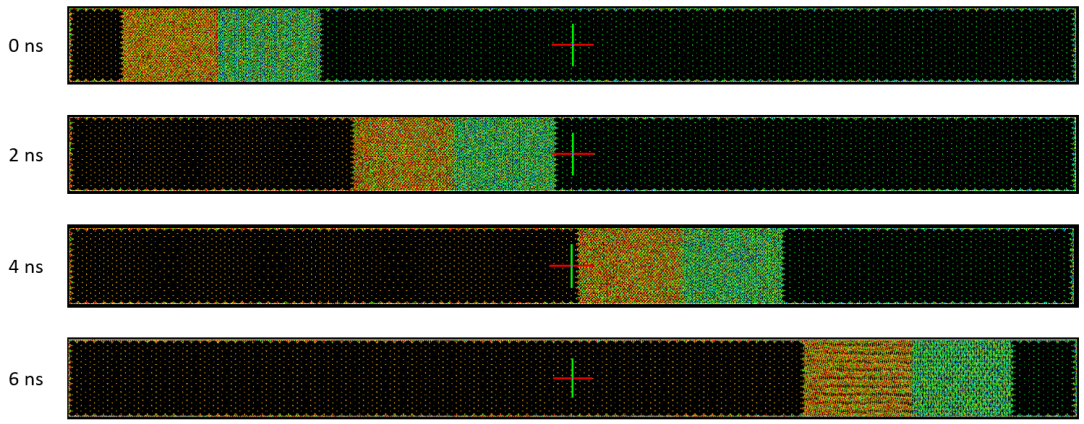

Figure 7.13: 2D shock simulation using the coarsen-refine moving window technique.

7.5.2 Shock structure and planarity

We now use the coarsen-refine simulations to analyze the shock front's spatial width over 5 ns, and the results for $\epsilon^+ = -0.06$ can be seen in Fig. 7.14. As a comparison, we also show the 1D CAC results from [2]. Unlike the 1D data, the present work shows a clear steadiness in the shock wave behavior as evidenced by the fact that the shock width remains constant throughout the simulation with very little deviation from the mean. We also do not observe a significant change in the shock front's planarity throughout the simulation's duration. Finally, similar results were found for both Cu and Al over the range of strains studied with the present formulation. Clearly, for shock waves modeled at the microscale, the ability of particles to oscillate transversely to the direction of shock propagation plays a large role in the overall steadiness of the wave. These results are similar to findings from previous NEMD studies which observed a change in shock structure and steadiness when transitioning from a 1D to 3D regime [28]. In particular, the transition from unsteady to steady waves was due to the "increase in coupling between vibrational excitations normal and transverse to the direction of shock wave propagation" [42]. Our work shows this for two dimensions as well.

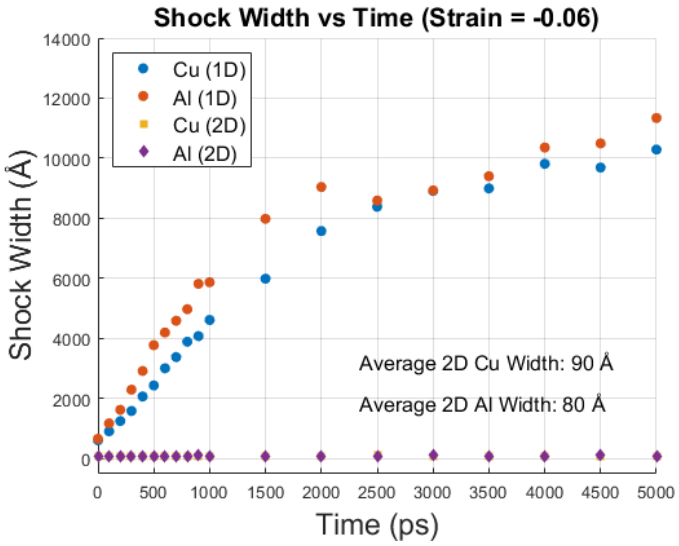

Figure 7.14: Spatial shock width over time. The blue and red circles represent the 1D CAC data from [2] for both Cu and Al respectively. The gold squares and purple diamonds represent the 2D CAC data for Cu and Al from the present work.

7.5.3 Framework speedup and efficiency

For the sake of completeness, we now present results for speedup/efficiency tests which compare the two-dimensional moving window CAC framework to equally-sized NEMD domains. The data from these two studies can be seen in Fig. 7.15. Specifically, in Fig. 7.15a, we maintain a constant ratio in the CAC lattice such that the fine-scaled region is always one-tenth the length of the entire grid, and we run simulations for increasing domain sizes. We observe the CAC vs. MD speedup reach an asymptotic value around 4.0x (further increases in domain size did not significantly effect the speedup). Next, in Fig. 7.15b, we keep the total lattice size constant and vary the length of the coarse-scaled region from 0% to 100% of the total area. Clearly, as the percentage of the lattice that is coarse-scaled increases, the speedup does as well up to a maximum value of approximately 6.5x. These studies demonstrate the utility of using the present CAC framework to enhance performance in large-scale simulations.

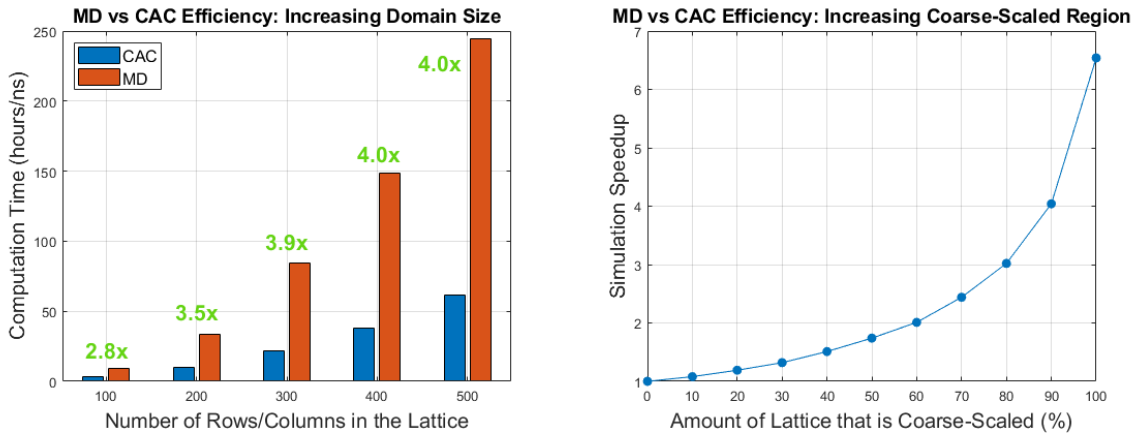

(a) (b)

Figure 7.15: Efficiency of the CAC framework vs equally-sized MD domains. In (a), the total runtimes are compared for increasing system sizes. Here, the central fine-scaled region of the CAC lattice is always 1/10 the length of the entire grid. In (b), the simulation speedup is shown when the size of the domain remains constant, but the coarse-scaled region increases from 0% to 100% of the lattice.

Chapter 8

Conclusion

In this final chapter, we summarize all the work explained in this dissertation, discuss the scientific contributions made with these projects, and consider current and future goals for this research.

8.1 Summary

8.1.1 One-dimensional atomistic framework

In the first part of this dissertation, we developed a moving window framework using MD to model long-time shock wave propagation through a one-dimensional monatomic chain. The framework was composed of a window region containing the shock wave flanked by thermostat boundary regions on either end of the domain. The dynamics of the window region were governed by the classic MD equations of motion while continuum shock conditions were incorporated into the boundary regions. The boundary regions utilized the Langevin thermostat along with a linear damping technique to prevent spurious reflections and absorb any artifact waves that impinged on the WA/CA interfaces. The moving window focused the shock wave front at the center of the WA region by adding/removing atoms to/from the WA and CA regions. This allowed us to use relatively small domain sizes to model shock wave propagation much longer than conventional NEMD shock simulations. Before presenting the results, we introduced a classical single-wave Riemann problem and defined the one-dimensional scheme. We then discussed the Langevin damping band method as well as the moving window formulation, and we extensively verified that each component of the framework was functioning properly.

In Sec. 3.3, we used the moving window framework to follow the propagating shock wave and calculate the shock velocity vs. particle velocity Hugoniot of the close packed framework. We observed that the EOS parameters obtained from the Morse and EAM potentials were in good agreement with the results from other MD studies. We then performed moving window shock simulations with the new EOS parameters to obtain a stationary shock wave front. This allowed us to track the shock wave for a few nanoseconds (much longer than conventional NEMD shock simulations) and characterize the shock's structure. We observed a linear increase in the width of the shock front up to 500 ps followed by a gradual increase until the end of the simulation. This increase in the shock front thickness was attributed to the fact that the one-dimensional framework is unable to account for transverse atomic displacements. These results were consistent with early MD studies which used a one-dimensional chain of atoms to model shock wave propagation [28].

With this work, we demonstrated that the moving window formulation could follow a propagating shock wave for long simulation times ($\geq$ 1 ns). Additionally, we showed that a shock propagating through a "close packed" one-dimensional monatomic chain could serve as a good approximation for a planar shock wave propagating along the [110] direction of a bulk single-crystal lattice. Transverse effects appear to be less influential along this lattice orientation [50], and our derived Hugoniot parameters were shown to be in good agreement with other MD studies [13, 14]. Existing NEMD shock techniques demonstrate distinct Hugoniot equations along the various lattice directions of a bulk crystal [13, 14, 50, 82] while experimental methods show no such distinction [83]. A higher-dimensional moving window formulation could be used to resolve such a discrepancy. The results achieved with the moving window atomistic framework served as a stepping stone and proof-of-concept for the development of the fully-coupled CAC framework for shock wave propagation discussed in the next part of this dissertation.

8.1.2 One-dimensional CAC framework

In the second part of this dissertation, we developed a moving window multiscale framework using the CAC method to model shock wave propagation through a one-dimensional

monatomic chain. Specifically, we studied the classic Riemann problem of a single propagating shock wave in an infinite medium. We characterized the shock at the continuum level using the third-order nonlinear Eulerian thermoelastic equations for shock compression in anisotropic crystals [136, 137]. We then incorporated two different moving window techniques into the framework which tracked the moving shock front in distinct ways. In the first method, the entire domain followed the wave front in a conveyor fashion, while in the second method, the fine-scaled region traveled through the chain by simultaneous coarsening and refinement.

We performed many verification studies with the framework including the replication of phonon dispersion curves and the simulation of phonon wave packets. Shock wave studies revealed that the CAC framework could accurately model propagating shocks with velocities very similar to those predicted by third-order Eulerian continuum theory. Additionally, these studies showed that the conveyor technique could maintain the wave front in the middle of the fine-scaled region for very long simulation times. Finally, simulations performed with the coarsen-refine technique demonstrated that the fine-scaled region could travel with the shock through the domain and thus prevent the shock wave from encountering the atomistic-continuum interface.

This work showcased the ability of the CAC framework to simulate highly non-equilibrium, transient events like shock waves through engineering-scale domains over realistic time scales. Atomistic methods have modeled many features of shock propagation in materials over the past several decades, but the scalability of such schemes is restricted by computational resources. While multiscale methods like CAC overcome size-scalability issues, studies which use these atomistic-continuum frameworks to model shock-like events have been limited. This is partly because fast-moving, nonlinear phenomena like shock waves can be hard to capture even in fairly large computational frameworks. When such events are simulated, the total runtime is nevertheless bounded because the shock will eventually leave the domain. The CAC method along with the two moving window techniques discussed in this paper significantly reduces the computational expense of such simulations and provides a means to model a propagating wave

over extended time scales. The present formulation will also be very valuable when studying other phenomena in a 1D chain such as nonlinear transition waves, Hertzian contact, and phonon transport [121, 126, 211, 212, 213].

8.1.3 CAC phonon wave passing formulation

In the third part of this dissertation, we developed a technique to transmit multiple high-frequency phonon waves across length scales within a periodic CAC domain. Specifically, we utilized the LD interpolation scheme from [126] and introduced novel numerical techniques into the framework to update the continuum region with short-wavelength data and track multiple waves across time. We first replicated the phonon dispersion relation of the system in order to find the critical wavevector k_C above which the curves of the coarse-scaled region and fine-scaled region diverged. Wave packet simulations confirmed that phonons with wavevectors $< k_C$ fully transmit across the A-C interface while phonons with wavevectors $> k_C$ completely reflect. Next, we described the LD-based finite element scheme developed in [126] to transmit a single short-wavelength phonon across length scales. A wave packet simulation confirmed the ability of this method to transmit a high-frequency $k = 0.2\pi/r_0$ phonon from the atomistic to the continuum region with nearly imperceptible reflection.

We then described the technique to pass multiple high-frequency phonons between the atomistic and continuum regions of the CAC framework. To implement this method, we first expanded the short-wavelength displacement equation to account for a variety of wave packets nucleated at different time steps. However, the coefficients in this equation were still time-independent, and we showcased how this "naive" approach could only store information for one phonon at a time. Next, we modified the displacement equation to incorporate "time-stamped" coefficients which encoded the initialization time of each wave. During the integration algorithm, we performed two separate Fourier transforms both before and after a new phonon was generated. By obtaining the amplitude coefficients, we effectively took a "snapshot" of the domain in ***k**-space* which allowed us to know which information was new. The difference in these coefficients was used to calculate the updated time-stamped coefficients which were then stored in a "master" array. Hence, information from multiple phonons was tracked over time, and the

displacement field could be updated to incorporate each of these waves into the continuum regions. Simulations performed with this technique confirmed its effectiveness in transmitting multiple short-wavelength phonons across the A-C interfaces.

While this technique can be used to transmit multiple short-wavelength waves, we note some limitations of this scheme. The framework, in its current state, is incapable of transmitting short-wavelength waves generated due to physical processes such as scattering. For example, during impact simulations, a shock wave may interact with a microstructural interface and produce high-frequency transient waves which travel throughout the domain. Such a wave will appear in the system during the Verlet integration. However, in the current framework, the short-wavelength wave packet nucleation occurs at a very specific step in the flowchart (Fig. 6.5) external to the Verlet integration. As such, any high-frequency wave generated during Verlet integration will not be captured and thus not added to the master template. We emphasize, however, that the current technique is not meant to be a decisive solution to a complex problem of wave scattering/transmission in multiscale modeling. Rather, this method is a step towards tracking a variety of high-frequency waves which are nucleated in a concurrent domain over time.

In the future, we hope to extend this technique to higher-dimensions and use it to study waves in systems with complex microstructures. Such microstructures could arise from particles being randomly oriented within a monatomic lattice or alloyed materials giving rise to intricate particle arrangements within polyatomic crystals. For diatomic systems in particular, there would be two branches of the analytical dispersion relation, and in principle, the present formulation could be used to transmit high-frequency optical phonons between the fine-scaled and coarse-scaled regions of the CAC domain and vice versa. We also hope to expand this method to account for different wave types such as elastic waves and orthogonal wavelets. Finally, we intend to eventually solve the scattering problem whereby we could transmit across length scales multiple high-frequency waves generated from a physical process such as a moving dislocation or shock impact.

8.1.4 Two-dimensional CAC framework

In the fourth part of this dissertation, we developed a dynamic moving window CAC framework to simulate shock wave propagation through a two-dimensional, single-crystal lattice. Specifically, we characterized the shock using both the linear Hugoniot [21] and nonlinear Eulerian [136] shock equations to analyze the well-known Riemann problem of a single discontinuity traveling through an infinite medium. The CAC multiscale formulation was utilized for its ability to seamlessly transition between the fine-scaled and coarse-scaled regions, and many verifications and analyses were conducted on the higher-dimensional system. We elaborated on the technique to initialize the shock front in the lattice as well as described two moving window methods which were incorporated into the domain. These schemes provided a mechanism to study the evolution of the shock over very long simulation times by preventing non-physical wave reflections at the A-C interfaces.

We performed many shock wave simulations within the CAC framework and used the moving window techniques to track the shock front through two different FCC materials: Cu and Al. The unique lattice directions inherent to the CAC formulation provided us the opportunity to study how directional anisotropies in single crystals can give rise to orientation-dependent shock velocities. We observed that longitudinal shocks traveling along the [112] and $[\bar{1}10]$ directions of the CAC domain propagated at distinct velocities for a given strain and particle velocity. These shock velocities were also different from those predicted by polycrystalline Hugoniot and Eulerian analytical models as well as previous one-dimensional atomistic and multiscale data. From these results, we were able to derive new Hugoniot parameters for the CAC formulation, and longitudinal stress calculations further validated the observed anisotropic material response. Our data agreed qualitatively with the results from previous NEMD studies which identified this orientation-dependence of shock evolution in solids [13, 14, 50, 82].

Next, in Sec. 7.5, we exhibited the capability and novelty of the present framework by using the coarsen-refine technique to track a propagating shock wave through the entire grid. By leveraging concepts from previous atomistic and finite element schemes as well as exploiting

the unique qualities of the CAC formulation, the fine-scaled region could travel through the domain at the speed of the moving wave front, and we noted the significance of this for advancing non-equilibrium multiscale research. We utilized this techinique to study the shock's structure and planarity over very long runtimes which are typically unattainable in traditional NEMD methods. Finally, we presented multiple plots comparing the efficiency of an NEMD system to an equally-sized CAC lattice. We observed that the present moving window multiscale scheme had significantly faster runtimes for various domain sizes – a necessary quality for realistic and scalable atomistic-continuum models.

The present 2D work is innovative in its own right, but it also opens the door to more complex research involving the use of multiscale domains to simulate dynamic, nonlinear phenomena over engineering length scales. While we focused only on elastic shock waves in this work, we hope to expand this formulation to model elastic-plastic shocks [208] in polycrystalline materials to study the role of grain boundaries on shock evolution. Additionally, recent works have used both atomistic [214, 215] as well as multiscale [16, 216, 217] methods to predict material behavior in medium-entropy and high-entropy alloys. This work provides a framework to study shock propagation through such materials. Furthermore, we would also like to utilize machine learning algorithms in this scheme to pass information from the mesoscale to macroscale [218]. Finally, we hope to eventually incorporate the high-frequency wave passing technique into the present formulation to study shock scattering and the role of scattered waves in subsequent material behavior.

8.2 Scientific contributions of this work

We now comment on a select number of scientific contributions made in this dissertation. The potential research avenues opened up by this research are numerous and are touched on more in Sec. 8.3, but in this section, we merely discuss the immediate advancements to knowledge and computational methods brought about by this work.

1. First, we developed a new technique to characterize a discontinuous shock wave within an atomistic framework and model long time shock propagation through the domain using a

moving window. As stated previously, traditional NEMD shock simulations suffer from limited simulation times due to phenomena such as boundary reflections. Techniques like the Hugoniostat [70] and MSST [74] overcome some of these issues but still suffer from problems related to scalability. Furthermore, while moving window methods have been implemented into other atomistic schemes [76], the shock is still generated through piston-driven techniques and is thus harder to analyze. To our knowledge, the atomistic moving window framework presented at the beginning of this dissertation is one of the first formulations to allow one to accurately and reliably study shock wave propagation and evolution over engineering time scales.

2. With the one-dimensional atomistic framework, we were also able to validate previous NEMD studies of weak, structured shock waves by analyzing the shock front drift as well as the increase in the shock front thickness over time. Because of the close-packed nature of the one-dimensional chain, our system could be compared to other works which studied shock wave propagation along the [110] direction of an FCC lattice. By using the moving window technique to monitor the shock front drift over long simulation times, we were able to optimize the shock velocity vs. particle velocity Hugoniot parameters for our domain, and these corresponded well to the parameters obtained from two previous NEMD studies [13, 14]. Furthermore, since the one-dimensional framework was incapable of incorporating transverse atomic motion, we could only study weak elastic shock waves, and we expected these shocks to develop a structure as they evolved as was seen in previous studies [42]. We did observe this phenomena because the shock front thickness increased over very long simulation times (3 ns), and this confirmed the structured nature of such 1D shocks.

3. Next, with the one-dimensional CAC research, we developed one of the first frameworks to use a domain refinement/coarsening mechanism to track a propagating shock wave over very long simulation times and engineering length scales. Coupled atomistic-continuum methods have been developed since the early 1990s in order to overcome

some of the intrinsic constraints of traditional atomistic techniques such as limited domain sizes and large computational overhead. However, such multiscale formulations have been hindered in their study of dynamic wave propagation due to the difference in material description between the coarse-scaled and fine-scaled regions as well as the fact that the wave may reflect off the A-C interface. We overcame such issues by characterizing our domain using CAC which utilizes a single governing equation to describe both the atomistic and continuum regions. Furthermore, we incorporated two moving window techniques into the framework to follow the shock as it evolved within the inner fine-scaled zone. Effectively, the atomistic region traveled with the shock front as it propagated through the larger continuum medium, and such a scheme had not been accomplished previously in the literature.

4. Using the one-dimensional moving window CAC framework, we were able to perform valuable shock wave studies which would not have been possible through either experiments or traditional atomistic simulations. First, we analyzed the average shock propagation velocity over 1 ns for a range of compressive strains. We found that the velocities obtained from our CAC simulations corresponded very well to the data from third-order Eulerian theory with the largest error being $\sim 3\%$ [137]. This was true not only for Cu but also for Al, Ag, and Ni. Next, we analyzed the growth in the spatial width of the shock front over 5 ns and observed good agreement with previous NEMD studies of weak 1D shocks [42, 28, 1, 19]. Finally, we compared the CAC simulations to equally-sized NEMD simulations and showed that our framework was much more computationally efficient with a speedup of nearly 6x.

5. With the high-frequency wave passing technique, we developed (to the authors' knowledge) the first concurrent atomistic-continuum formulation to transmit multiple short-wavelength phonons between the fine-scaled and coarse-scaled regions and vice versa. While a previous study has also published in this area [126], their particular method could only be used for a single phonon in a non-periodic domain. In the present work, we introduced novel numerical techniques into an LD scheme for CAC in order to enhance the

interpolation method in the continuum regions to allow multiple waves to pass through unimpeded. The phenomena of spurious wave reflections at the A-C interfaces is one of the biggest unsolved problems in modern multiscale modeling, and it is particularly relevant for simulations that involve shock scattering. While our framework cannot solve the scattering problem, it nevertheless provides valuable insight and results for an extremely complex topic.

6. We have emphasized throughout this dissertation that the study of shock wave propagation using multiscale methods has been limited due to the highly dynamic nature of such phenomena. While the 1D research addressed this complication by incorporating two moving window techniques into a CAC framework to track a nonlinear shock wave, this formulation only considered a one-dimensional chain of particles and was thus limited in scope. The 2D framework developed in this work is the first of its kind to model long-time, large-domain shock wave propagation through a multi-dimensional atomistic-continuum domain using moving window techniques. As a result, our understanding of the connection between microscale behavior and the continuum response of materials subjected to shock impact is significantly enhanced. The potential research avenues available to the community through this framework are numerous, and the knowledge gained using such a formulation may be used in the future to develop more durable armor for use in both military and space applications.

8.3 Ongoing research in the Mechanics of Materials Laboratory

8.3.1 Current work: three-dimensional alloys

At present, we have expanded the two-dimensional framework into three dimensions as well as significantly enhanced the parallelization scheme to increase the efficiency of Gaussian force calculations in large-scale CAC simulations. In particular, we can now choose to run the code using either the shared-memory architecture of OpenMP or the distributed memory architecture of MPI depending on the scope and specific requirements of the given problem. Additionally, we have implemented data structures to read-in information from EAM interatomic potential

files for three-dimensional frameworks, and we continue to use nearest-neighbor pair potentials (i.e. Lennard-Jones and Morse) for both one and two-dimensional grids. Furthermore, we have the capability to perform simulations using either periodic, fixed, or free boundary conditions in each direction, and we can execute various essential tasks such as calculating the spectral energy density, virial stress, and elasticity tensor as well as modeling a shock through a normal or inverted grid using moving window techniques. Most of the reasoning and analysis presented in Sec. 7.2 for 2D elements is similar in principle for 3D, but the main difference is that an extra dimension is created along the $[\bar{1}1\bar{1}]$ lattice orientation in the z-direction which increases the complexity of the mass matrix and Gaussian integration formulations. For visualization, a screenshot of the three-dimensional monatomic grid can be seen in Fig. 8.1, and all of our code can be found at github.com/vinagr/movingwindow.

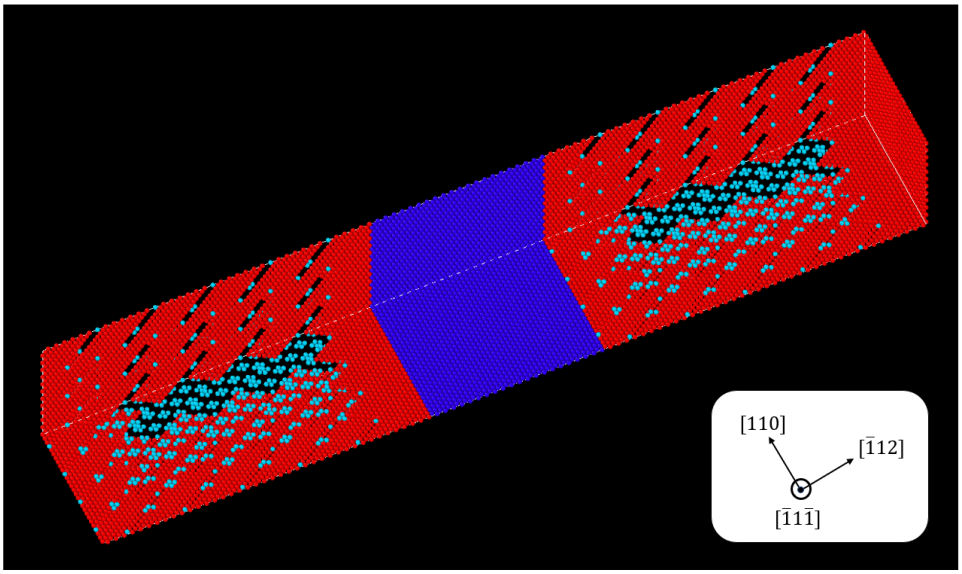

Figure 8.1: Ovito visualization of the three-dimensional monatomic grid.

The most substantial modification we have made to the CAC code in the past few months is the capability to simulate alloyed materials using complex EAM multi-body potentials. Specifically, we have been modeling the medium-entropy alloy (MEA) FeNiCr within our three-dimensional CAC framework using the advanced EAM potential developed in 2018 for this material [219]. In recent years, computational research of complex multicomponent alloys has experienced a revival due to the attractive properties of such solids [220, 221, 222, 223, 224]; and in 2016, an average-atom (A-atom) approach was developed for the EAM potential to

study the "complex defect/defect interactions that are nearly impossible to extract from direct simulations on explicit random alloys at high concentration" [225]. Various MD simulations have been performed using the A-atom method over the past few years [226, 227], but the first study to incorporate this technique into a multiscale CAC framework occurred just last year [16]. This state-of-the-art formulation maintains a true-random system in the fine-scaled region but transitions to A-atom bulk elements in the coarse-scaled regions as seen in Fig. 8.2. Here, we observe that the lattice directions change slightly when introducing the z-dimension, and this necessitates modifications in the generation of the grid as well as the orientation of the elements. We have incorporated these changes as well as others in our updated version of the three-dimensional MEA CAC framework for use in shock and dislocation simulations.

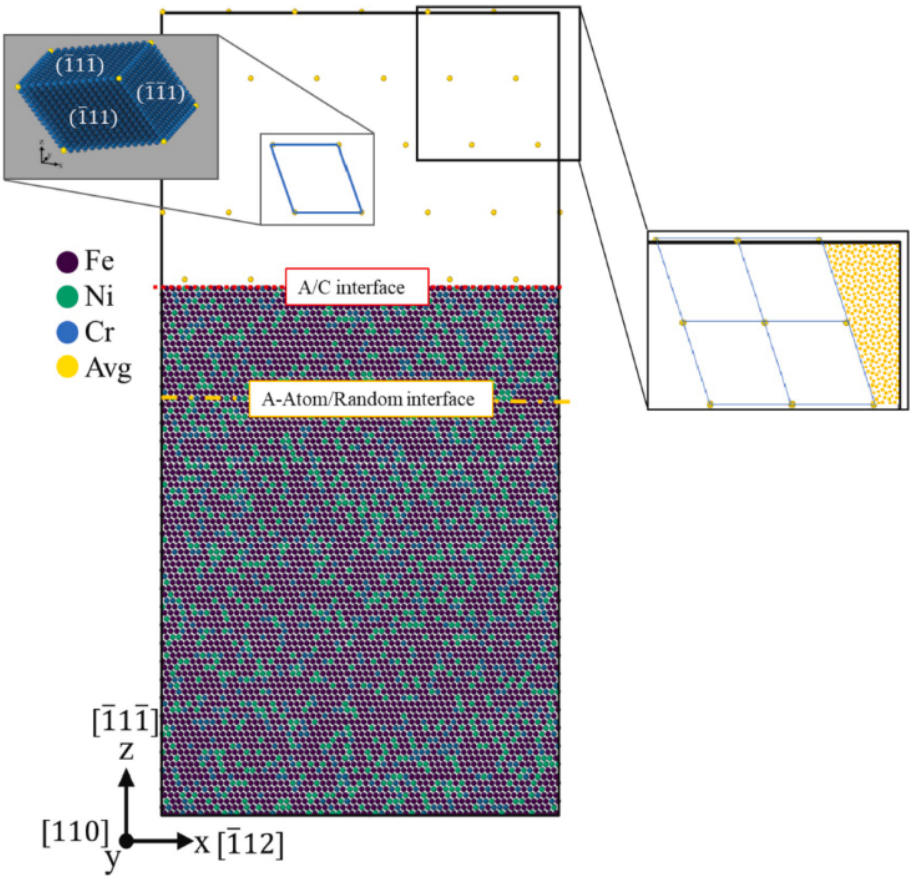

Figure 8.2: Schematic of the MEA CAC framework using the A-atom method. The A-C and A-atom interfaces are represented by the red and yellow lines respectively. Furthermore, the inset shows the relative finite element orientation as well as the boundary particles [16][8].

[8]Reprinted from *Computational Materials Science*, vol. 201; K. Chu, A. Diaz, Y. Chen, T. Zhu, and D.L. McDowell; "Multiscale Concurrent Atomistic-Continuum (CAC) modeling of multicomponent alloys," pp. 110873, 2022. Obtained with permission from Elsevier.

As stated, we are now utilizing the three-dimensional CAC framework along with the A-atom approach to model austenitic stainless steels with nominal FeNiCr components. An austenitic stainless steel is one of the five types of crystalline structures of stainless steels (along with ferritic, martensitic, duplex, and precipitation hardened), and its main arrangement is austenite (face-centered cubic) [228]. Hence, the x, y, and z directions change from their standard CAC configuration to the following: $x = [\bar{1}12]$, $y = [110]$, and $z = [\bar{1}1\bar{1}]$. Such a difference necessitates a rather significant update to the grid, integration points, and Gaussian force calculations, which we accomplished while also maintaining the ability to simulate non-alloy materials. Furthermore, the EAM potential becomes more complex because we must now account for different types of interacting particles α and β as seen in the equation below:

$$\Pi_i = F_\alpha \left(\sum_{j \neq i} \rho_{\alpha\beta} \left(r_{ij} \right) \right) + \frac{1}{2} \sum_{j \neq i} V_{\alpha\beta} \left(r_{ij} \right) \tag{8.1}$$

where $\rho_{\alpha\beta}$ is the electron density contributed from neighbor j of element β to atom i of element α. Depending on the potential file, ρ can either be a functional specific to the elements of both particles i and j (eam/fs files) or just the element of particle i (eam/alloy files). Please see the LAMMPS documentation page for more details about the various types of EAM files.

For an extensive derivation of the force equations from the EAM potential, the reader is referred to either the appendix of [109] or the PyCAC website [127]. To summarize those works, if $\rho_{ij} \neq \rho_{ji}$ (i.e. an eam/fs file):

$$\mathbf{f}_i = \sum_{j(j \neq i)} \left[\frac{\partial V_{ij}(r_{ij})}{\partial r_{ij}} + \frac{\partial F(\bar{\rho}_i)}{\partial \bar{\rho}_i} \frac{\partial \rho_{ij}(r_{ij})}{\partial r_{ij}} + \frac{\partial F(\bar{\rho}_j)}{\partial \bar{\rho}_j} \frac{\partial \rho_{ji}(r_{ij})}{\partial r_{ij}} \right] \frac{\mathbf{r}_{ij}}{r_{ij}} \tag{8.2}$$

where $\bar{\rho}_i$ is the total electron density for particle i, and r_{ij} is the magnitude of the vector $\mathbf{r}_{ij}$. However, if $\rho_{ij} = \rho_{ji}$ (i.e. an eam/alloy file), Eq. (8.2) simplifies to the following:

$$\mathbf{f}_i = \sum_{j(j \neq i)} \left[\frac{\partial V_{ij}(r_{ij})}{\partial r_{ij}} + \left(\frac{\partial F(\bar{\rho}_i)}{\partial \bar{\rho}_i} + \frac{\partial F(\bar{\rho}_j)}{\partial \bar{\rho}_j} \right) \frac{\partial \rho_{ij}(r_{ij})}{\partial r_{ij}} \right] \frac{\mathbf{r}_{ij}}{r_{ij}} \tag{8.3}$$

Since we are utilizing an A-atom approach within the coarse-scaled regions of the CAC domain, the EAM potential must be modified slightly to accurately represent such averaged-atoms as shown in [225]. Here, we follow the derivation found in that work. In particular, we simulate an N-component alloy where the average concentration of each element X is c_X and $\sum_{X=1}^{N} c_X = 1$. In each alloyed material, individual particles occupy various particle sites $\{i\}$. We express this site occupation using the variable s_i^X where $s_i^X = 1$ if a particle of type X exists at atomic site i, and $s_i^X = 0$ in all other cases. Using this nomenclature, we can express the EAM potential as follows [225]:

$$E\left(\left\{s_i^X\right\}\right) = \sum_{i,X} s_i^X F^X(\rho_i) + \frac{1}{2} \sum_{i,j\neq i,X,Y} V_{ij}^{XY} s_i^X s_j^Y \tag{8.4}$$

where we know that

$$\rho_i = \sum_{j\neq i,X} s_j^X \rho_{ij}^X \tag{8.5}$$

In Eq. (8.4), X and Y specify different particle types, V_{ij}^{XY} is the pair potential between particles of type X and Y at sites i and j, and $F^X(\rho_i)$ is the standard embedding energy at position i for particle X.

We can recover the average energy of a given collection of atomic positions $\{i\}$ by "averaging over all possible site occupations consistent with the overall alloy composition" [225]. Doing this results in the following average energy:

$$\langle E_0 \rangle = \sum_{i,X} c_X \langle F^X\left(\rho_i\right) \rangle + \frac{1}{2} \sum_{i,j\neq i,X,Y} V_{ij}^{XY} c_X c_Y \tag{8.6}$$

where $\langle s_i^X \rangle = c_X$ in Eq. (8.6). If we then perform a Taylor expansion around the average electron density $\bar{\rho}_i$ and ignore second and higher-order terms, we get the following:

$$\langle E_0 \rangle = \sum_{i} F^A\left(\bar{\rho}_i\right) + \frac{1}{2} \sum_{i,j\neq i} V_{ij}^{AA} \tag{8.7}$$

where

$$F^A\left(\bar{\rho}_i\right) = \sum_X c_X F^X\left(\bar{\rho}_i\right) \tag{8.8}$$

$$V_{ij}^{AA} = \sum_{X,Y} c_X c_Y V_{ij}^{XY} \tag{8.9}$$

$$\bar{\rho}_i = \sum_{j \neq i} \sum_X c_X \rho_{ij}^X \tag{8.10}$$

In the above equations, A refers to an average-atom with embedding function F^A and pair potential V_{ij}^{AA}. Equation (8.7) has the same form as the traditional EAM potential, but the difference is that average atomic properties are now used to generate a new particle species. Because the averaging procedure smooths local energy fluctuations inherent to a true random alloy, the energies and forces of A-atoms are merely approximate. As a result, various mechanical and structural properties may differ slightly between a true random alloy and an A-atom lattice [225].

The A-atom technique permits one to model random alloys of *arbitrary* composition by performing an analytic average over all possible particle sites to acquire the mean properties of the disordered alloy. Such a scheme creates a new *averaged* particle species which transforms the EAM function into a "single-atom average-atom" potential. While purely atomistic simulations are valuable for understanding the defect interactions and mechanical properties of complex materials like multicomponent alloys, developing accurate interatomic potentials for such MD simulations remains a major challenge, and this is especially true for alloys [152, 229, 230, 231, 232, 233, 234, 235]. Multiscale schemes like CAC may be utilized to compute discrete atomic values explicitly while also extending the domain to continuum length scales where A-atoms are incorporated. Using such an approach, we can simulate a dynamic multicomponent framework without losing the intricate details of defect interactions and other important phenomena.

8.3.2 Future project ideas

The novel work presented in this dissertation opens up numerous research avenues for future projects, and I will discuss just a handful of them here. The first and most obvious extension of this work would be to utilize the three-dimensional MEA framework along with the A-atom approach to simulate moving dislocations and/or propagating shocks through a multiscale framework using the moving window techniques. Although simulations of alloys have been performed at the atomic- and meso-scales over the past few years [220, 221, 222], the first *concurrent* formulation to model an MEA appeared in the literature just last year [16]. Hence, our understanding of how phenomena like shocks and dislocations influence the overall material response of an MEA or HEA across length scales in lacking. A corollary of such research would be to use the CAC moving window technique to analyze shock propagation across grain boundaries and/or interfaces of a composite as seen in Fig. 8.3a. When a shock encounters such boundaries, transient elastic waves will travel throughout the material as seen in Fig 8.3b, and the formulation developed in this dissertation could be used to study these interactions.

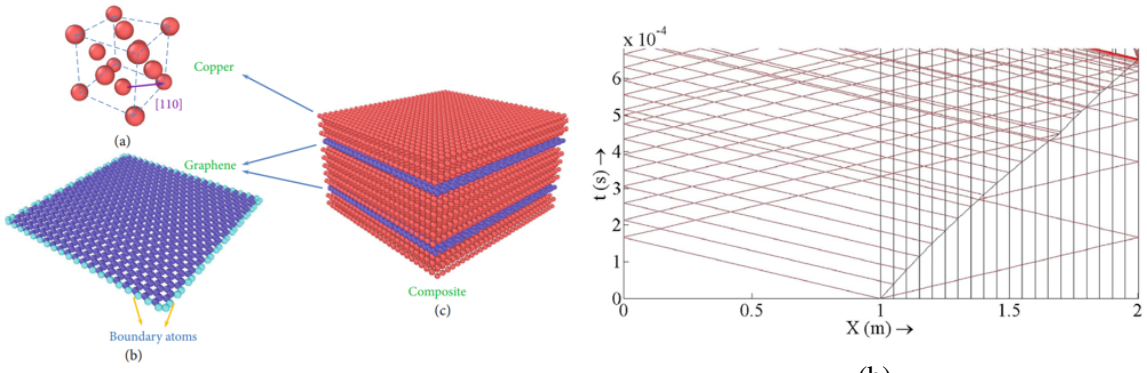

(a) (b)

Figure 8.3: (a) Graphene-reinforced Cu composite showing the interface regions as well as the boundary atoms [17][9]. (b) Shock wave (black line) interacting with various microstructural interfaces and producing transient elastic waves (red lines) [18][10].

[9]Reprinted from *Research*; Y. Fan, Y. Xiang, and H.-S. Shen; "Temperature-dependent mechanical properties of graphene/cu nanocomposites with in-plane negative poisson's ratios," 2020. Open access article. Figure obtained with permission from the terms and conditions of the Creative Commons Attribution license.

[10]Reprinted from *International Journal of Solids and Structures*, vol. 51, no. 21-22; V. Agrawal and K. Bhattacharya; "Shock wave propagation through a model one-dimensional heterogeneous medium," pp. 3604-3618, 2014. Obtained with permission from Elsevier.

Another noteworthy research endeavor would involve utilizing the CAC coarsen-refine technique to model strong shock waves with thermoelastic-viscoplastic models like those developed in [208] and [209]. While 3D multiscale moving window simulations of such realistic shock waves would be very unique and valuable, the shocked region would produce numerous dislocations and stacking faults as seen in Fig. 8.4. Although domain refinement ahead of the shock wave front would be fairly straightforward for such models, coarsening the grid in the shocked material would be extremely challenging if not impossible with current formulations. In studying these strong shocks, one would also need to develop a technique to pass dislocations between the fine-scaled and coarse-scaled regions while simultaneously coarsening the grid. Hence, a secondary research project could involve optimizing the continuum element sizes for dislocation transmission within an adaptive mesh-refinement CAC framework.

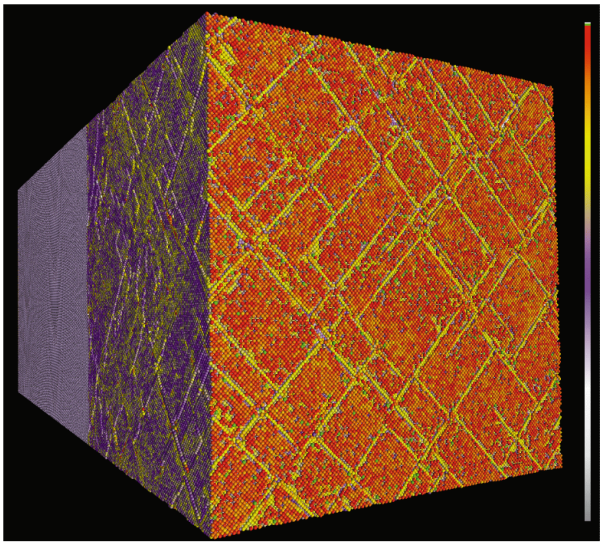

Figure 8.4: Shock-induced dislocations and intersecting stacking faults at piston face. Atoms are colored according to potential energy [19][11].

If we are considering "pie-in-the-sky" research goals, the two that come to mind are related to high-frequency wave transmission across the A-C interfaces as well as a "non-arbitrary" temperature formulation for multiscale systems. The issue of wave reflections at the intersection of fine-scaled and coarse-scaled domains is a problem inherent to multiscale modeling,

[11]Reprinted from *Science*, vol. 280, no. 5372; B.L. Holian and P.S. Lomdahl; "Plasticity induced by shock waves in nonequilibrium molecular-dynamics simulations," pp. 2085-2088, 1998. Obtained with permission from the American Association for the Advancement of Science.

and simulating nonlinear shock propagation enhances this problem since shocks produce transient waves during impact. Although the current dissertation developed a unique method to tackle this puzzle, developing a robust technique to solve the scattering problem and seamlessly transmit randomly generated high-frequency phonons across length scales would be amazing. Furthermore, most concurrent schemes rely on thermostats to apply temperature to the domain. While certain methods such as *max-ent QC* have been developed in recent years [113], a non-arbitrary temperature formulation for multiscale systems is still needed. Such a scheme would ideally follow the mathematics developed in [236] (one of the most complicated papers I have ever read).

Finally, a long-term research goal would be to develop frameworks which connect atomistic and multiscale modeling with machine learning and continuum mechanics (see Fig. 8.5). Machine learning (ML) has become extremely popular in recent years [237], and techniques which utilize atomistic and/or multiscale techniques to inform ML algorithms are actively being developed [238]. In particular, one could create methods to simulate material behavior at the atomic scale, input that data into advanced ML algorithms, and utilize such results to inform continuum models of phenomena like void growth or crack propagation. Such a technique would enhance our understanding of material behavior at various length scales and also advance knowledge in fields such as experimental mechanics and even planetary science.

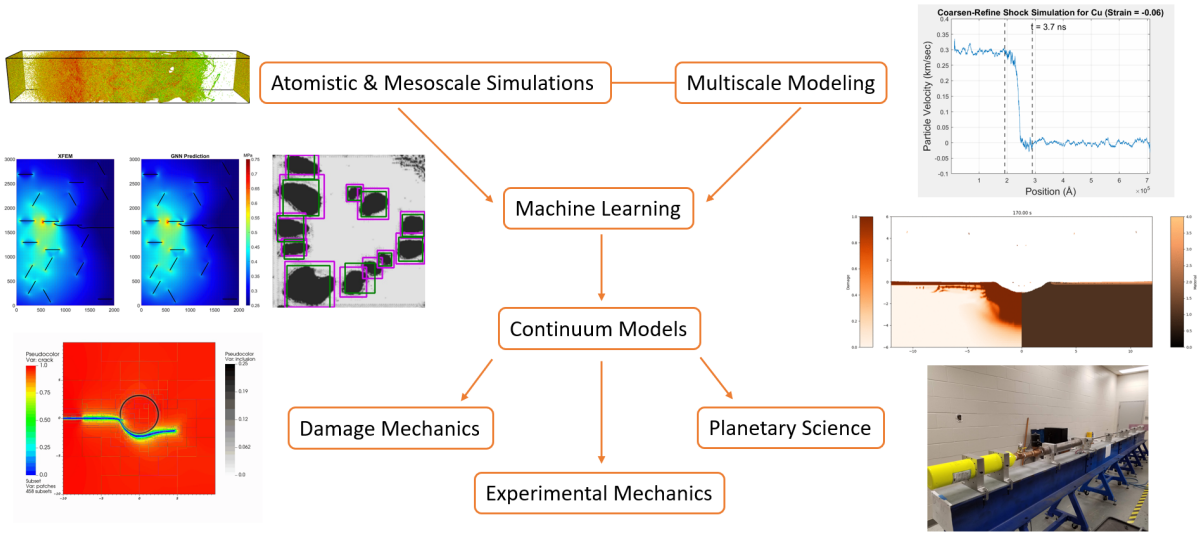

Figure 8.5: Connection between atomistic simulations, multiscale schemes, machine learning, and continuum models.

References

[1] A. S. Davis and V. Agrawal, "One-dimensional moving window atomistic framework to model long-time shock wave propagation," *Computer Methods in Applied Mechanics and Engineering*, vol. 371, 2020.

[2] A. S. Davis, J. T. Lloyd, and V. Agrawal, "Moving window techniques to model shock wave propagation using the concurrent atomistic–continuum method," *Computer Methods in Applied Mechanics and Engineering*, vol. 389, 2022.

[3] A. S. Davis and V. Agrawal, "Transmitting multiple high-frequency phonons across length scales using the concurrent atomistic–continuum method," *Computational Materials Science*, vol. 214, 2022.

[4] A. S. Davis and V. Agrawal, "Investigating shock wave propagation, evolution, and anisotropy using a moving window concurrent atomistic-continuum framework," *Computational Mechanics*, vol. 71, pp. 721–742, 2023.

[5] T. De Rességuier, D. Loison, A. Dragon, and E. Lescoute, "Laser driven compression to investigate shock-induced melting of metals," *Metals*, vol. 4, no. 4, pp. 490–502, 2014.

[6] J. S. Amelang, G. N. Venturini, and D. M. Kochmann, "Summation rules for a fully nonlocal energy-based quasicontinuum method," *Journal of the Mechanics and Physics of Solids*, vol. 82, pp. 378–413, 2015.

[7] I. Tembhekar, *The Fully Nonlocal, Finite-Temperature, Adaptive 3D Quasicontinuum Method for Bridging Across Scales*. PhD thesis, California Institute of Technology, 2018.

[8] R. E. Rudd and J. Q. Broughton, "Concurrent coupling of length scales in solid state systems," *Computer Simulation of Materials at Atomic Level*, pp. 251–291, 2000.

[9] R. E. Miller and E. B. Tadmor, "A unified framework and performance benchmark of fourteen multiscale atomistic/continuum coupling methods," *Modelling and Simulation in Materials Science and Engineering*, vol. 17, no. 5, 2009.

[10] J. Knap and M. Ortiz, "An analysis of the quasicontinuum method," *Journal of the Mechanics and Physics of Solids*, vol. 49, no. 9, pp. 1899–1923, 2001.

[11] M. A. Meyers, *Dynamic Behavior of Materials*. John Wiley & Sons, 1994.

[12] A. Mitchell, W. Nellis, J. Moriarty, R. Heinle, N. Holmes, R. Tipton, and G. Repp, "Equation of state of al, cu, mo, and pb at shock pressures up to 2.4 tpa (24 mbar)," *Journal of Applied Physics*, vol. 69, no. 5, pp. 2981–2986, 1991.

[13] E. Bringa, J. Cazamias, P. Erhart, J. Stölken, N. Tanushev, B. Wirth, R. Rudd, and M. Caturla, "Atomistic shock hugoniot simulation of single-crystal copper," *Journal of Applied Physics*, vol. 96, no. 7, pp. 3793–3799, 2004.

[14] E. Lin, H. Shi, and L. Niu, "Effects of orientation and vacancy defects on the shock hugoniot behavior and spallation of single-crystal copper," *Modelling and Simulation in Materials Science and Engineering*, vol. 22, no. 3, 2014.

[15] S. P. Marsh, *LASL shock Hugoniot data*. University of California press, 1980.

[16] K. Chu, A. Diaz, Y. Chen, T. Zhu, and D. L. McDowell, "Multiscale concurrent atomistic-continuum (cac) modeling of multicomponent alloys," *Computational Materials Science*, vol. 201, 2022.

[17] Y. Fan, Y. Xiang, and H.-S. Shen, "Temperature-dependent mechanical properties of graphene/cu nanocomposites with in-plane negative poisson's ratios," *Research*, vol. 2020, 2020.

[18] V. Agrawal and K. Bhattacharya, "Shock wave propagation through a model one dimensional heterogeneous medium," *International Journal of Solids and Structures*, vol. 51, no. 21-22, pp. 3604–3618, 2014.

[19] B. L. Holian and P. S. Lomdahl, "Plasticity induced by shock waves in nonequilibrium molecular-dynamics simulations," *Science*, vol. 280, no. 5372, pp. 2085–2088, 1998.

[20] R. A. MacDonald and W. M. MacDonald, "Thermodynamic properties of fcc metals at high temperatures," *Physical Review B*, vol. 24, no. 4, pp. 1715–1724, 1981.

[21] L. Davison, *Fundamentals of Shock Wave Propagation in Solids*. Springer Science & Business Media, 2008.

[22] G. T. Gray III, "High-strain-rate deformation: mechanical behavior and deformation substructures induced," *Annual Review of Materials Research*, vol. 42, pp. 285–303, 2012.

[23] S. Fensin, J. Escobedo, G. Gray III, B. Patterson, C. Trujillo, and E. Cerreta, "Dynamic damage nucleation and evolution in multiphase materials," *Journal of Applied Physics*, vol. 115, no. 20, 2014.

[24] J. F. Bingert, R. M. Suter, J. Lind, S. F. Li, R. Pokharel, and C. P. Trujillo, "High-energy diffraction microscopy characterization of spall damage," in *Dynamic Behavior of Materials, Volume 1*, pp. 397–403, Springer, 2014.

[25] R. E. Miller and E. B. Tadmor, "The quasicontinuum method: Overview, applications and current directions," *Journal of Computer-Aided Materials Design*, vol. 9, no. 3, pp. 203–239, 2002.

[26] R. McQueen, S. Marsh, J. Taylor, J. Fritz, and W. Carter, "The equation of state of solids from shock wave studies," *High velocity impact phenomena*, vol. 293, pp. 294–417, 1970.

[27] R. Thurston, "Waves in solids," *In: Mechanics of solids IV (Festkoerpermechanik IV). Berlin*, vol. 4, pp. 109–308, 1974.

[28] B. Holian, "Atomistic computer simulations of shock waves," *Shock Waves*, vol. 5, no. 3, pp. 149–157, 1995.

[29] B. J. Alder and T. E. Wainwright, "Phase transition for a hard sphere system," *The Journal of Chemical Physics*, vol. 27, no. 5, pp. 1208–1209, 1957.

[30] B. Alder and T. Wainwright, "Molecular dynamics by electronic computers," *Transport Processes in Statistical Mechanics*, pp. 97–131, 1958.

[31] J. Gibson, A. Goland, M. Milgram, and G. Vineyard, "Dynamics of radiation damage," *Physical Review*, vol. 120, no. 4, pp. 1229–1253, 1960.

[32] L. Verlet, "Computer "experiments" on classical fluids. i. thermodynamical properties of lennard-jones molecules," *Physical Review*, vol. 159, no. 1, pp. 98–103, 1967.

[33] D. Tsai and C. Beckett, "Shock wave propagation in cubic lattices," *Journal of Geophysical Research*, vol. 71, no. 10, pp. 2601–2608, 1966.

[34] G. E. Duvall, R. Manvi, and S. C. Lowell, "Steady shock profile in a one-dimensional lattice," *Journal of Applied Physics*, vol. 40, no. 9, pp. 3771–3775, 1969.

[35] R. Manvi, G. Duvall, and S. Lowell, "Finite amplitude longitudinal waves in lattices," *International Journal of Mechanical Sciences*, vol. 11, no. 1, pp. 1–8, 1969.

[36] R. Manvi and G. Duvall, "Shock waves in a one-dimensional non-dissipating lattice," *Journal of Physics D: Applied Physics*, vol. 2, no. 10, pp. 1389–1396, 1969.

[37] A. Paskin and G. Dienes, "Molecular dynamic simulations of shock waves in a three-dimensional solid," *Journal of Applied Physics*, vol. 43, no. 4, pp. 1605–1610, 1972.

[38] A. Paskin and G. Dienes, "Molecular dynamic simulation of shock waves in 3 dimensions," in *Bulletin of the American Physical Society*, vol. 20, American Institute of Physics, 1975.

[39] A. Paskin, A. Gohar, and G. Dienes, "Simulations of shock waves in solids," *Journal of Physics C: Solid State Physics*, vol. 10, no. 19, pp. 563–566, 1977.

[40] A. Paskin, A. Gohar, and G. Dienes, "Simulations of shock waves in solids," *Journal of Physics and Chemistry of Solids*, vol. 39, no. 12, pp. 1307–1311, 1978.

[41] B. Holian and G. Straub, "Molecular dynamics of shock waves in one-dimensional chains," *Physical Review B*, vol. 18, no. 4, pp. 1593–1608, 1978.

[42] B. L. Holian and G. K. Straub, "Molecular dynamics of shock waves in three-dimensional solids: Transition from nonsteady to steady waves in perfect crystals and implications for the rankine-hugoniot conditions," *Physical Review Letters*, vol. 43, no. 21, pp. 1598–1600, 1979.

[43] G. Straub, B. Holian, and R. Swanson, "Molecular-dynamics of shock-waves in 3-dimensional lennard-jones systems in the solid-phase," in *Bulletin of the American Physical Society*, vol. 25, American Institute of Physics, 1980.

[44] B. L. Holian, "Modeling shock-wave deformation via molecular dynamics," *Physical Review A*, vol. 37, no. 7, pp. 2562–2568, 1988.

[45] B. Holian, A. Voter, N. Wagner, R. Ravelo, S. Chen, W. Hoover, C. Hoover, J. Hammerberg, and T. Dontje, "Effects of pairwise versus many-body forces on high-stress plastic deformation," *Physical Review A*, vol. 43, no. 6, pp. 2655–2661, 1991.

[46] C. E. Morris, "Shock-wave equation-of-state studies at los alamos," *Shock Waves*, vol. 1, no. 3, pp. 213–222, 1991.

[47] N. J. Wagner, B. L. Holian, and A. F. Voter, "Molecular-dynamics simulations of two-dimensional materials at high strain rates," *Physical Review A*, vol. 45, no. 12, pp. 8457–8471, 1992.

[48] N. J. Wagner and B. L. Holian, "Massively parallel molecular dynamics simulations of two-dimensional materials at high strain rates," *MRS Online Proceedings Library*, vol. 291, 1992.

[49] B. L. Holian and R. Ravelo, "Fracture simulations using large-scale molecular dynamics," *Physical Review B*, vol. 51, no. 17, pp. 275–292, 1995.

[50] T. C. Germann, B. L. Holian, P. S. Lomdahl, and R. Ravelo, "Orientation dependence in molecular dynamics simulations of shocked single crystals," *Physical Review Letters*, vol. 84, no. 23, pp. 5351–5354, 2000.

[51] T. C. Germann, B. L. Holian, P. S. Lomdahl, D. Tanguy, M. Mareschal, and R. Ravelo, "Dislocation structure behind a shock front in fcc perfect crystals: Atomistic simulation results," *Metallurgical and Materials Transactions A*, vol. 35, no. 9, pp. 2609–2615, 2004.

[52] E. Bringa, K. Rosolankova, R. Rudd, B. Remington, J. Wark, M. Duchaineau, D. Kalantar, J. Hawreliak, and J. Belak, "Shock deformation of face-centred-cubic metals on subnanosecond timescales," *Nature Materials*, vol. 5, no. 10, pp. 805–809, 2006.

[53] S. Srinivasan, M. Baskes, and G. Wagner, "Atomistic simulations of shock induced microstructural evolution and spallation in single crystal nickel," *Journal of Applied Physics*, vol. 101, no. 4, 2007.

[54] G. E. Norman, A. Y. Kuksin, V. V. Stegailov, and A. V. Yanilkin, "Atomistic simulation of plasticity and fracture of crystalline and polycrystalline metals under high strain rate," in *AIP Conference Proceedings*, vol. 955, pp. 329–334, American Institute of Physics, 2007.

[55] E. M. Bringa, S. Traiviratana, and M. A. Meyers, "Void initiation in fcc metals: effect of loading orientation and nanocrystalline effects," *Acta Materialia*, vol. 58, no. 13, pp. 4458–4477, 2010.

[56] S. Fensin, J. Escobedo-Diaz, C. Brandl, E. Cerreta, G. Gray III, T. Germann, and S. Valone, "Effect of loading direction on grain boundary failure under shock loading," *Acta Materialia*, vol. 64, pp. 113–122, 2014.

[57] R. Perriot, V. V. Zhakhovsky, N. A. Inogamov, and I. I. Oleynik, "Evolution of elastic precursor and plastic shock wave in copper via molecular dynamics simulations," in *Journal of Physics: Conference Series*, vol. 500, IOP Publishing, 2014.

[58] A. Bisht, A. Neogi, N. Mitra, G. Jagadeesh, and S. Suwas, "Investigation of the elastically shock-compressed region and elastic–plastic shock transition in single-crystalline copper to understand the dislocation nucleation mechanism under shock compression," *Shock Waves*, vol. 29, no. 7, pp. 913–927, 2019.

[59] X. Tian, K. Ma, G. Ji, J. Cui, Y. Liao, and M. Xiang, "Anisotropic shock responses of nanoporous al by molecular dynamics simulations," *Plos One*, vol. 16, no. 3, 2021.

[60] D. Tramontina, E. Hahn, M. Meyers, and E. Bringa, "Simulation of tantalum nanocrystals under shock-wave loading: Dislocations and twinning," in *AIP Conference Proceedings*, vol. 1793, AIP Publishing LLC, 2017.

[61] G. Righi, C. J. Ruestes, C. V. Stan, S. J. Ali, R. E. Rudd, M. Kawasaki, H.-S. Park, and M. A. Meyers, "Towards the ultimate strength of iron: spalling through laser shock," *Acta Materialia*, vol. 215, 2021.

[62] Q. Zhu, J.-L. Shao, H. Pan, and P. Wang, "Collapse of stacking fault tetrahedron and dislocation evolution in copper under shock compression," *Journal of Nuclear Materials*, vol. 554, 2021.

[63] A. Higginbotham, M. Suggit, E. M. Bringa, P. Erhart, J. Hawreliak, G. Mogni, N. Park, B. Remington, and J. Wark, "Molecular dynamics simulations of shock-induced deformation twinning of a body-centered-cubic metal," *Physical Review B*, vol. 88, no. 10, 2013.

[64] D. Wu, K. Chen, Y. Zhu, L. Zhao, M. Huang, and Z. Li, "Unveiling grain size effect on shock-induced plasticity and its underlying mechanisms in nano-polycrystalline ta," *Mechanics of Materials*, vol. 160, 2021.

[65] Y. Zhu, D. Wu, L. Zhao, S. Liang, M. Huang, and Z. Li, "A novel shock-induced multistage phase transformation and underlying mechanism in textured nano-twinned cu," *Extreme Mechanics Letters*, vol. 48, 2021.

[66] S. Fensin, S. Valone, E. Cerreta, J. Escobedo-Diaz, G. Gray, K. Kang, and J. Wang, "Effect of grain boundary structure on plastic deformation during shock compression using molecular dynamics," *Modelling and Simulation in Materials Science and Engineering*, vol. 21, no. 1, 2012.

[67] X.-X. Wang, A.-M. He, T.-T. Zhou, and P. Wang, "Spall damage in single crystal tin under shock wave loading: A molecular dynamics simulation," *Mechanics of Materials*, vol. 160, 2021.

[68] Y. Chen, Z. Jian, S. Xiao, L. Wang, X. Li, K. Wang, H. Deng, and W. Hu, "Molecular dynamics simulation of shock wave propagation and spall failure in single crystal copper under cylindrical impact," *Applied Physics Express*, vol. 14, no. 7, 2021.

[69] M. Dewapriya and R. Miller, "Molecular dynamics simulations of shock propagation and spallation in amorphous polymers," *Journal of Applied Mechanics*, vol. 88, no. 10, 2021.

[70] J.-B. Maillet, M. Mareschal, L. Soulard, R. Ravelo, P. S. Lomdahl, T. C. Germann, and B. L. Holian, "Uniaxial hugoniostat: A method for atomistic simulations of shocked materials," *Physical Review E*, vol. 63, no. 1, 2000.

[71] J.-B. Maillet and S. Bernard, "Uniaxial hugoniostat: method and applications," in *AIP Conference Proceedings*, vol. 620, pp. 367–370, American Institute of Physics, 2002.

[72] R. Ravelo, B. Holian, T. Germann, and P. Lomdahl, "Constant-stress hugoniostat method for following the dynamical evolution of shocked matter," *Physical Review B*, vol. 70, no. 1, 2004.

[73] D. Bedrov, J. B. Hooper, G. D. Smith, and T. D. Sewell, "Shock-induced transformations in crystalline rdx: A uniaxial constant-stress hugoniostat molecular dynamics simulation study," *The Journal of Chemical Physics*, vol. 131, no. 3, 2009.

[74] E. J. Reed, L. E. Fried, and J. Joannopoulos, "A method for tractable dynamical studies of single and double shock compression," *Physical Review Letters*, vol. 90, no. 23, 2003.

[75] E. J. Reed, L. E. Fried, W. D. Henshaw, and C. M. Tarver, "Analysis of simulation technique for steady shock waves in materials with analytical equations of state," *Physical Review E*, vol. 74, no. 5, 2006.

[76] V. Zhakhovskii, K. Nishihara, and S. Anisimov, "Shock wave structure in dense gases," *Journal of Experimental and Theoretical Physics Letters*, vol. 66, no. 2, pp. 99–105, 1997.

[77] V. V. Zhakhovsky, M. M. Budzevich, N. A. Inogamov, I. I. Oleynik, and C. T. White, "Two-zone elastic-plastic single shock waves in solids," *Physical Review Letters*, vol. 107, no. 13, 2011.

[78] S. Qu, V. Shastry, W. Curtin, and R. E. Miller, "A finite-temperature dynamic coupled atomistic/discrete dislocation method," *Modelling and Simulation in Materials Science and Engineering*, vol. 13, no. 7, pp. 1101–1118, 2005.

[79] D. Holland and M. Marder, "Ideal brittle fracture of silicon studied with molecular dynamics," *Physical Review Letters*, vol. 80, no. 4, pp. 746–749, 1998.

[80] R. L. Selinger and J. M. Corbett, "Dynamic fracture in disordered media," *MRS Bulletin*, vol. 25, no. 5, pp. 46–50, 2000.

[81] J. Knowles, "On the relation between particle velocity and shock wave speed for thermoelastic materials," *Shock Waves*, vol. 12, no. 2, pp. 137–144, 2002.

[82] A. Neogi and N. Mitra, "Shock induced deformation response of single crystal copper: Effect of crystallographic orientation," *Computational Materials Science*, vol. 135, pp. 141–151, 2017.

[83] R. Chau, J. Stölken, P. Asoka-Kumar, M. Kumar, and N. Holmes, "Shock hugoniot of single crystal copper," *Journal of Applied Physics*, vol. 107, no. 2, 2010.

[84] G. Straub, B. Holian, and R. Petschek, "Molecular dynamics of shock waves in one-dimensional chains. ii. thermalization," *Physical Review B*, vol. 19, no. 8, pp. 4049–4055, 1979.

[85] A. Davis, "Development of a one-dimensional moving window atomistic framework to model steady state shock wave propagation," Master's thesis, Auburn University, 2020.

[86] R. J. Hardy, "Formulas for determining local properties in molecular-dynamics simulations: Shock waves," *The Journal of Chemical Physics*, vol. 76, no. 1, pp. 622–628, 1982.

[87] J. Irving and J. G. Kirkwood, "The statistical mechanical theory of transport processes. iv. the equations of hydrodynamics," *The Journal of Chemical Physics*, vol. 18, no. 6, pp. 817–829, 1950.

[88] S. Kohlhoff, P. Gumbsch, and H. Fischmeister, "Crack propagation in bcc crystals studied with a combined finite-element and atomistic model," *Philosophical Magazine A*, vol. 64, no. 4, pp. 851–878, 1991.

[89] C. Miehe, J. Schröder, and J. Schotte, "Computational homogenization analysis in finite plasticity simulation of texture development in polycrystalline materials," *Computer Methods in Applied Mechanics and Engineering*, vol. 171, no. 3-4, pp. 387–418, 1999.

[90] F. Feyel and J.-L. Chaboche, "Fe2 multiscale approach for modelling the elastoviscoplastic behaviour of long fibre sic/ti composite materials," *Computer Methods in Applied Mechanics and Engineering*, vol. 183, no. 3-4, pp. 309–330, 2000.

[91] N. Lange, G. Hütter, and B. Kiefer, "An efficient monolithic solution scheme for fe2 problems," *Computer Methods in Applied Mechanics and Engineering*, vol. 382, 2021.

[92] R. J. Amodeo and N. M. Ghoniem, "Dislocation dynamics. i. a proposed methodology for deformation micromechanics," *Physical Review B*, vol. 41, no. 10, pp. 6958–6967, 1990.

[93] E. Van der Giessen and A. Needleman, "Discrete dislocation plasticity: a simple planar model," *Modelling and Simulation in Materials Science and Engineering*, vol. 3, no. 5, 1995.

[94] H. M. Zbib, M. Rhee, and J. P. Hirth, "On plastic deformation and the dynamics of 3d dislocations," *International Journal of Mechanical Sciences*, vol. 40, no. 2-3, pp. 113–127, 1998.

[95] X. Zhang, S. Lu, B. Zhang, X. Tian, Q. Kan, and G. Kang, "Dislocation–grain boundary interaction-based discrete dislocation dynamics modeling and its application to bicrystals with different misorientations," *Acta Materialia*, vol. 202, pp. 88–98, 2021.

[96] D. J. Luscher, D. L. McDowell, and C. A. Bronkhorst, "A second gradient theoretical framework for hierarchical multiscale modeling of materials," *International Journal of Plasticity*, vol. 26, no. 8, pp. 1248–1275, 2010.

[97] E. B. Tadmor and R. E. Miller, *Modeling materials: continuum, atomistic and multiscale techniques*. Cambridge University Press, 2011.

[98] R. E. Rudd and J. Q. Broughton, "Coarse-grained molecular dynamics and the atomic limit of finite elements," *Physical Review B*, vol. 58, no. 10, pp. 893–896, 1998.

[99] F. F. Abraham, J. Q. Broughton, N. Bernstein, and E. Kaxiras, "Spanning the length scales in dynamic simulation," *Computers in Physics*, vol. 12, no. 6, pp. 538–546, 1998.

[100] J. Q. Broughton, F. F. Abraham, N. Bernstein, and E. Kaxiras, "Concurrent coupling of length scales: methodology and application," *Physical Review B*, vol. 60, no. 4, pp. 2391–2403, 1999.

[101] R. E. Rudd, "The atomic limit of finite element modeling in mems: Coupling of length scales," *Analog Integrated Circuits and Signal Processing*, vol. 29, no. 1-2, pp. 17–26, 2001.

[102] S. Xiao and T. Belytschko, "A bridging domain method for coupling continua with molecular dynamics," *Computer Methods in Applied Mechanics and Engineering*, vol. 193, no. 17-20, pp. 1645–1669, 2004.

[103] G. J. Wagner and W. K. Liu, "Coupling of atomistic and continuum simulations using a bridging scale decomposition," *Journal of Computational Physics*, vol. 190, no. 1, pp. 249–274, 2003.

[104] D. Qian, G. J. Wagner, and W. K. Liu, "A multiscale projection method for the analysis of carbon nanotubes," *Computer Methods in Applied Mechanics and Engineering*, vol. 193, no. 17-20, pp. 1603–1632, 2004.

[105] L. Shilkrot, R. E. Miller, and W. Curtin, "Coupled atomistic and discrete dislocation plasticity," *Physical Review Letters*, vol. 89, no. 2, 2002.

[106] W. A. Curtin and R. E. Miller, "Atomistic/continuum coupling in computational materials science," *Modelling and Simulation in Materials Science and Engineering*, vol. 11, no. 3, pp. 33–68, 2003.

[107] L. Shilkrot, R. E. Miller, and W. A. Curtin, "Multiscale plasticity modeling: coupled atomistics and discrete dislocation mechanics," *Journal of the Mechanics and Physics of Solids*, vol. 52, no. 4, pp. 755–787, 2004.

[108] R. E. Miller, L. Shilkrot, and W. A. Curtin, "A coupled atomistics and discrete dislocation plasticity simulation of nanoindentation into single crystal thin films," *Acta Materialia*, vol. 52, no. 2, pp. 271–284, 2004.

[109] L. Xiong, *A concurrent atomistic-continuum methodolody and its applications*. PhD thesis, University of Florida, 2011.

[110] S. Xu and X. Chen, "Modeling dislocations and heat conduction in crystalline materials: atomistic/continuum coupling approaches," *International Materials Reviews*, vol. 64, no. 7, pp. 407–438, 2019.

[111] E. B. Tadmor, M. Ortiz, and R. Phillips, "Quasicontinuum analysis of defects in solids," *Philosophical Magazine A*, vol. 73, no. 6, pp. 1529–1563, 1996.

[112] V. Shenoy, V. Shenoy, and R. Phillips, "Finite temperature quasicontinuum methods," *MRS Online Proceedings Library Archive*, vol. 538, 1998.

[113] Y. Kulkarni, J. Knap, and M. Ortiz, "A variational approach to coarse graining of equilibrium and non-equilibrium atomistic description at finite temperature," *Journal of the Mechanics and Physics of Solids*, vol. 56, no. 4, pp. 1417–1449, 2008.

[114] J. S. Amelang and D. M. Kochmann, "Surface effects in nanoscale structures investigated by a fully-nonlocal energy-based quasicontinuum method," *Mechanics of Materials*, vol. 90, pp. 166–184, 2015.

[115] J. Amelang, *A fully-nonlocal energy-based formulation and high-performance realization of the quasicontinuum method*. PhD thesis, California Institute of Technology, 2016.

[116] I. Tembhekar, J. S. Amelang, L. Munk, and D. M. Kochmann, "Automatic adaptivity in the fully nonlocal quasicontinuum method for coarse-grained atomistic simulations," *International Journal for Numerical Methods in Engineering*, vol. 110, no. 9, pp. 878–900, 2017.

[117] L. Xiong, G. Tucker, D. L. McDowell, and Y. Chen, "Coarse-grained atomistic simulation of dislocations," *Journal of the Mechanics and Physics of Solids*, vol. 59, no. 2, pp. 160–177, 2011.

[118] L. Xiong, Q. Deng, G. Tucker, D. L. McDowell, and Y. Chen, "A concurrent scheme for passing dislocations from atomistic to continuum domains," *Acta Materialia*, vol. 60, no. 3, pp. 899–913, 2012.

[119] S. Yang, L. Xiong, Q. Deng, and Y. Chen, "Concurrent atomistic and continuum simulation of strontium titanate," *Acta Materialia*, vol. 61, no. 1, pp. 89–102, 2013.

[120] L. Xiong, D. L. McDowell, and Y. Chen, "Sub-thz phonon drag on dislocations by coarse-grained atomistic simulations," *International Journal of Plasticity*, vol. 55, pp. 268–278, 2014.

[121] L. Xiong, X. Chen, N. Zhang, D. L. McDowell, and Y. Chen, "Prediction of phonon properties of 1d polyatomic systems using concurrent atomistic–continuum simulation," *Archive of Applied Mechanics*, vol. 84, no. 9, pp. 1665–1675, 2014.

[122] L. Xiong, S. Xu, D. L. McDowell, and Y. Chen, "Concurrent atomistic–continuum simulations of dislocation–void interactions in fcc crystals," *International Journal of Plasticity*, vol. 65, pp. 33–42, 2015.

[123] S. Xu, L. Xiong, Q. Deng, and D. L. McDowell, "Mesh refinement schemes for the concurrent atomistic-continuum method," *International Journal of Solids and Structures*, vol. 90, pp. 144–152, 2016.

[124] S. Xu, L. Xiong, Y. Chen, and D. L. McDowell, "Sequential slip transfer of mixed-character dislocations across $\sigma 3$ coherent twin boundary in fcc metals: a concurrent atomistic-continuum study," *NPJ Computational Materials*, vol. 2, no. 1, pp. 1–9, 2016.

[125] X. Chen, W. Li, A. Diaz, Y. Li, Y. Chen, and D. L. McDowell, "Recent progress in the concurrent atomistic-continuum method and its application in phonon transport," *MRS Communications*, vol. 7, no. 4, pp. 785–797, 2017.

[126] X. Chen, A. Diaz, L. Xiong, D. L. McDowell, and Y. Chen, "Passing waves from atomistic to continuum," *Journal of Computational Physics*, vol. 354, pp. 393–402, 2018.

[127] S. Xu, T. G. Payne, H. Chen, Y. Liu, L. Xiong, Y. Chen, and D. L. McDowell, "Pycac: The concurrent atomistic-continuum simulation environment," *Journal of Materials Research*, vol. 33, no. 7, pp. 857–871, 2018.

[128] Y. Chen, S. Shabanov, and D. L. McDowell, "Concurrent atomistic-continuum modeling of crystalline materials," *Journal of Applied Physics*, vol. 126, no. 10, 2019.

[129] Y. Chen and J. Lee, "Atomistic formulation of a multiscale field theory for nano/micro solids," *Philosophical Magazine*, vol. 85, no. 33-35, pp. 4095–4126, 2005.

[130] Y. Chen, "Reformulation of microscopic balance equations for multiscale materials modeling," *The Journal of Chemical Physics*, vol. 130, no. 13, 2009.

[131] X. Chen, L. Xiong, D. L. McDowell, and Y. Chen, "Effects of phonons on mobility of dislocations and dislocation arrays," *Scripta Materialia*, vol. 137, pp. 22–26, 2017.

[132] S. Xu, L. Smith, J. R. Mianroodi, A. Hunter, B. Svendsen, and I. J. Beyerlein, "A comparison of different continuum approaches in modeling mixed-type dislocations in al," *Modelling and Simulation in Materials Science and Engineering*, vol. 27, no. 7, p. 074004, 2019.

[133] S. Xu, D. L. McDowell, and I. J. Beyerlein, "Sequential obstacle interactions with dislocations in a planar array," *Acta Materialia*, vol. 174, pp. 160–172, 2019.

[134] Y. Li, Z. Fan, W. Li, D. L. McDowell, and Y. Chen, "A multiscale study of misfit dislocations in pbte/pbse (001) heteroepitaxy," *Journal of Materials Research*, vol. 34, no. 13, pp. 2306–2314, 2019.

[135] A. Selimov, S. Xu, Y. Chen, and D. McDowell, "Lattice dislocation induced misfit dislocation evolution in semi-coherent $\{111\}$ bimetal interfaces," *Journal of Materials Research*, vol. 36, pp. 2763–2778, 2021.

[136] J. D. Clayton, "Nonlinear eulerian thermoelasticity for anisotropic crystals," *Journal of the Mechanics and Physics of Solids*, vol. 61, no. 10, pp. 1983–2014, 2013.

[137] J. Clayton, "Shock compression of metal crystals: a comparison of eulerian and lagrangian elastic-plastic theories," *International Journal of Applied Mechanics*, vol. 6, no. 05, 2014.

[138] M. Rice, R. G. McQueen, and J. Walsh, "Compression of solids by strong shock waves," in *Solid State Physics*, vol. 6, pp. 1–63, Elsevier, 1958.

[139] G. I. Kerley, "The linear us-up relation in shock-wave physics," *arXiv preprint arXiv:1306.6916*, 2013.

[140] J. A. Zimmerman, J. M. Winey, and Y. M. Gupta, "Elastic anisotropy of shocked aluminum single crystals: Use of molecular dynamics simulations," *Physical Review B*, vol. 83, 2011.

[141] F. Birch, "Finite elastic strain of cubic crystals," *Physical Review*, vol. 71, no. 11, pp. 809–824, 1947.

[142] P. Germain and E. Lee, "On shock waves in elastic-plastic solids," *Journal of the Mechanics and Physics of Solids*, vol. 21, no. 6, pp. 359–382, 1973.

[143] J. S. Weaver, "Application of finite strain theory to non-cubic crystals," *Journal of Physics and Chemistry of Solids*, vol. 37, no. 7, pp. 711–718, 1976.

[144] G. Perrin and M. Delannoy, "Application de la théorie des déformations finies à la détermination de propriétés élastiques des polycristaux de symétrie hexagonale sous haute pression," *Journal de Physique*, vol. 39, no. 10, pp. 1085–1095, 1978.

[145] D. C. Wallace, "Flow process of weak shocks in solids," *Physical Review B*, vol. 22, no. 4, pp. 1487–1494, 1980.

[146] S. Xu, R. Che, L. Xiong, Y. Chen, and D. L. McDowell, "A quasistatic implementation of the concurrent atomistic-continuum method for fcc crystals," *International Journal of Plasticity*, vol. 72, pp. 91–126, 2015.

[147] W. C. Swope, H. C. Andersen, P. H. Berens, and K. R. Wilson, "A computer simulation method for the calculation of equilibrium constants for the formation of physical clusters of molecules: Application to small water clusters," *The Journal of Chemical Physics*, vol. 76, no. 1, pp. 637–649, 1982.

[148] J. E. Jones, "On the determination of molecular fields.—ii. from the equation of state of a gas," *Proceedings of the Royal Society of London. Series A, Containing Papers of a Mathematical and Physical Character*, vol. 106, no. 738, pp. 463–477, 1924.

[149] P. M. Agrawal, B. M. Rice, and D. L. Thompson, "Predicting trends in rate parameters for self-diffusion on fcc metal surfaces," *Surface Science*, vol. 515, no. 1, pp. 21–35, 2002.

[150] A. Krivtsov and V. Kuz'kin, "Derivation of equations of state for ideal crystals of simple structure," *Mechanics of Solids*, vol. 46, no. 3, pp. 387–399, 2011.

[151] S. Foiles, M. Baskes, and M. S. Daw, "Embedded-atom-method functions for the fcc metals cu, ag, au, ni, pd, pt, and their alloys," *Physical Review B*, vol. 33, no. 12, pp. 7983–7991, 1986.

[152] M. S. Daw and M. I. Baskes, "Embedded-atom method: Derivation and application to impurities, surfaces, and other defects in metals," *Physical Review B*, vol. 29, no. 12, pp. 6443–6453, 1984.

[153] Y. Mishin, M. Mehl, D. Papaconstantopoulos, A. Voter, and J. Kress, "Structural stability and lattice defects in copper: Ab initio, tight-binding, and embedded-atom calculations," *Physical Review B*, vol. 63, no. 22, 2001.

[154] T. Schneider and E. Stoll, "Molecular-dynamics study of a three-dimensional one-component model for distortive phase transitions," *Physical Review B*, vol. 17, no. 3, pp. 1302–1322, 1978.

[155] R. E. Miller and E. B. Tadmor, "Hybrid continuum mechanics and atomistic methods for simulating materials deformation and failure," *MRS Bulletin*, vol. 32, no. 11, pp. 920–926, 2007.

[156] J. Ericksen, "On the cauchy—born rule," *Mathematics and mechanics of solids*, vol. 13, no. 3-4, pp. 199–220, 2008.

[157] B. L. Holian, A. F. Voter, and R. Ravelo, "Thermostatted molecular dynamics: How to avoid the toda demon hidden in nosé-hoover dynamics," *Physical Review E*, vol. 52, no. 3, pp. 2338–2347, 1995.

[158] L. C. Chhabildas and J. R. Asay, "Rise-time measurements of shock transitions in aluminum, copper, and steel," *Journal of Applied Physics*, vol. 50, no. 4, pp. 2749–2756, 1979.

[159] Q. Deng, *Coarse-graining atomistic dynamics of fracture by finite element method: Formulation, parallelization and applications*. PhD thesis, University of Florida, 2011.

[160] J. W. Gibbs, *Elementary principles in statistical mechanics*. Courier Corporation, 2014.

[161] J. G. Kirkwood, "The statistical mechanical theory of transport processes i. general theory," *The Journal of Chemical Physics*, vol. 14, no. 3, pp. 180–201, 1946.

[162] G. Chen, R. Yang, and X. Chen, "Nanoscale heat transfer and thermal-electric energy conversion," in *Journal de Physique IV (Proceedings)*, vol. 125, pp. 499–504, EDP Sciences, 2005.

[163] Y. Chen, "Local stress and heat flux in atomistic systems involving three-body forces," *The Journal of Chemical Physics*, vol. 124, no. 5, 2006.

[164] L. Xiong and Y. Chen, "Multiscale modeling and simulation of single-crystal mgo through an atomistic field theory," *International Journal of Solids and Structures*, vol. 46, no. 6, pp. 1448–1455, 2009.

[165] S. Yang, *A concurrent atomistic-continuum method for simulating defects in ionic materials*. PhD thesis, University of Florida, 2014.

[166] O. C. Zienkiewicz, R. L. Taylor, P. Nithiarasu, and J. Zhu, *The finite element method*, vol. 3. McGraw-Hill London, 1977.

[167] L. Xiong and Y. Chen, "Coarse-grained atomistic modeling and simulation of inelastic material behavior," *Acta Mechanica Solida Sinica*, vol. 25, no. 3, pp. 244–261, 2012.

[168] L. Xiong, J. Rigelesaiyin, X. Chen, S. Xu, D. L. McDowell, and Y. Chen, "Coarse-grained elastodynamics of fast moving dislocations," *Acta Materialia*, vol. 104, pp. 143–155, 2016.

[169] Q. Deng, L. Xiong, and Y. Chen, "Coarse-graining atomistic dynamics of brittle fracture by finite element method," *International Journal of Plasticity*, vol. 26, no. 9, pp. 1402–1414, 2010.

[170] Q. Deng and Y. Chen, "A coarse-grained atomistic method for 3d dynamic fracture simulation," *International Journal for Multiscale Computational Engineering*, vol. 11, no. 3, 2013.

[171] S. Yang, N. Zhang, and Y. Chen, "Concurrent atomistic–continuum simulation of polycrystalline strontium titanate," *Philosophical Magazine*, vol. 95, no. 24, pp. 2697–2716, 2015.

[172] L. Xiong and Y. Chen, "Coarse-grained simulations of single-crystal silicon," *Modelling and Simulation in Materials Science and Engineering*, vol. 17, no. 3, 2009.

[173] M. T. Dove and M. T. Dove, *Introduction to Lattice Dynamics*, vol. 4. Cambridge University Press, 1993.

[174] L. Kantorovich, *Quantum theory of the solid state: an introduction*, vol. 136. Springer Science & Business Media, 2004.

[175] G. Rutledge, D. Lacks, R. Martoňák, and K. Binder, "A comparison of quasi-harmonic lattice dynamics and monte carlo simulation of polymeric crystals using orthorhombic polyethylene," *The Journal of Chemical Physics*, vol. 108, no. 24, pp. 10274–10280, 1998.

[176] J. Turney, E. Landry, A. McGaughey, and C. Amon, "Predicting phonon properties and thermal conductivity from anharmonic lattice dynamics calculations and molecular dynamics simulations," *Physical Review B*, vol. 79, no. 6, 2009.

[177] G. E. Peckham, *Phonon Dispersion Relations in Crystals*. PhD thesis, University of Cambridge, 1964.

[178] J. A. Thomas, J. E. Turney, R. M. Iutzi, C. H. Amon, and A. J. McGaughey, "Predicting phonon dispersion relations and lifetimes from the spectral energy density," *Physical Review B*, vol. 81, no. 8, 2010.

[179] G. E. Shilov, R. A. Silverman, *et al.*, *Elementary real and complex analysis*. Courier Corporation, 1996.

[180] X. Chen, W. Li, L. Xiong, Y. Li, S. Yang, Z. Zheng, D. L. McDowell, and Y. Chen, "Ballistic-diffusive phonon heat transport across grain boundaries," *Acta Materialia*, vol. 136, pp. 355–365, 2017.

[181] P. Schelling, S. Phillpot, and P. Keblinski, "Phonon wave-packet dynamics at semiconductor interfaces by molecular-dynamics simulation," *Applied Physics Letters*, vol. 80, no. 14, pp. 2484–2486, 2002.

[182] P. Schelling, S. Phillpot, and P. Keblinski, "Kapitza conductance and phonon scattering at grain boundaries by simulation," *Journal of Applied Physics*, vol. 95, no. 11, pp. 6082–6091, 2004.

[183] X. Wei and T. Luo, "A phonon wave packet study of thermal energy transport across functionalized hard-soft interfaces," *Journal of Applied Physics*, vol. 126, no. 1, 2019.

[184] K. Gahagan, D. Moore, D. J. Funk, R. Rabie, S. Buelow, and J. Nicholson, "Measurement of shock wave rise times in metal thin films," *Physical Review Letters*, vol. 85, no. 15, pp. 3205–3208, 2000.

[185] M. Born, "On the stability of crystal lattices. i," in *Mathematical Proceedings of the Cambridge Philosophical Society*, vol. 36, pp. 160–172, Cambridge University Press, 1940.

[186] L. A. Girifalco and V. G. Weizer, "Application of the morse potential function to cubic metals," *Physical Review*, vol. 114, no. 3, pp. 687–690, 1959.

[187] R. Lincoln, K. Koliwad, and P. Ghate, "Morse-potential evaluation of second-and third-order elastic constants of some cubic metals," *Physical Review*, vol. 157, no. 3, pp. 463–466, 1967.

[188] V. Singh and B. Sharma, "Third order elastic constants and pressure derivatives of second order elastic constant of copper and aluminum," *Journal of Pure Applied and Industrial Physics*, vol. 10, no. 4, pp. 1–6, 2020.

[189] M. J. Berger and P. Colella, "Local adaptive mesh refinement for shock hydrodynamics," *Journal of Computational Physics*, vol. 82, no. 1, pp. 64–84, 1989.

[190] A. Amor-Martin and L. E. Garcia-Castillo, "Adaptive semi-structured mesh refinement techniques for the finite element method," *Applied Sciences*, vol. 11, no. 8, 2021.

[191] B. Eidel and A. Stukowski, "A variational formulation of the quasicontinuum method based on energy sampling in clusters," *Journal of the Mechanics and Physics of Solids*, vol. 57, no. 1, pp. 87–108, 2009.

[192] E. Karpov, G. J. Wagner, and W. K. Liu, "A green's function approach to deriving non-reflecting boundary conditions in molecular dynamics simulations," *International Journal for Numerical Methods in Engineering*, vol. 62, no. 9, pp. 1250–1262, 2005.

[193] X. Li and E. Weinan, "Variational boundary conditions for molecular dynamics simulations of crystalline solids at finite temperature: treatment of the thermal bath," *Physical Review B*, vol. 76, no. 10, 2007.

[194] K. Jolley and S. P. Gill, "Modelling transient heat conduction in solids at multiple length and time scales: A coupled non-equilibrium molecular dynamics/continuum approach," *Journal of Computational Physics*, vol. 228, no. 19, pp. 7412–7425, 2009.

[195] W. Cai, M. de Koning, V. V. Bulatov, and S. Yip, "Minimizing boundary reflections in coupled-domain simulations," *Physical Review Letters*, vol. 85, no. 15, pp. 3213–3216, 2000.

[196] H. S. Park, E. G. Karpov, and W. K. Liu, "Non-reflecting boundary conditions for atomistic, continuum and coupled atomistic/continuum simulations," *International Journal for Numerical Methods in Engineering*, vol. 64, no. 2, pp. 237–259, 2005.

[197] E. Karpov, H. S. Park, and W. K. Liu, "A phonon heat bath approach for the atomistic and multiscale simulation of solids," *International Journal for Numerical Methods in Engineering*, vol. 70, no. 3, pp. 351–378, 2007.

[198] E. Weinan and Z. Huang, "Matching conditions in atomistic-continuum modeling of materials," *Physical Review Letters*, vol. 87, no. 13, 2001.

[199] N. Mathew, R. Picu, and M. Bloomfield, "Concurrent coupling of atomistic and continuum models at finite temperature," *Computer Methods in Applied Mechanics and Engineering*, vol. 200, no. 5-8, pp. 765–773, 2011.

[200] S. B. Ramisetti, G. Anciaux, and J.-F. Molinari, "Spatial filters for bridging molecular dynamics with finite elements at finite temperatures," *Computer Methods in Applied Mechanics and Engineering*, vol. 253, pp. 28–38, 2013.

[201] S. U. Chirputkar, D. Qian, and C. Source, "Coupled atomistic/continuum simulation based on extended space-time finite element method," *Computer Modeling in Engineering and Sciences*, vol. 24, no. 2-3, 2008.

[202] J. Z. Yang, X. Wu, and X. Li, "A generalized irving–kirkwood formula for the calculation of stress in molecular dynamics models," *The Journal of Chemical Physics*, vol. 137, no. 13, 2012.

[203] O. C. Zienkiewicz, "Achievements and some unsolved problems of the finite element method," *International Journal for Numerical Methods in Engineering*, vol. 47, no. 1-3, pp. 9–28, 2000.

[204] M. Born, K. Huang, and M. Lax, "Dynamical theory of crystal lattices," *American Journal of Physics*, vol. 23, no. 7, 1955.

[205] A. Kumar and M. Ansari, "Lattice thermal conductivity of deformed crystals," *Physica B+C*, vol. 147, no. 2-3, pp. 267–281, 1988.

[206] Y. Hiki and A. Granato, "Anharmonicity in noble metals; higher order elastic constants," *Physical Review*, vol. 144, no. 2, pp. 411–419, 1966.

[207] J. F. Thomas Jr, "Third-order elastic constants of aluminum," *Physical Review*, vol. 175, no. 3, pp. 955–962, 1968.

[208] J. Lloyd, J. Clayton, R. Becker, and D. McDowell, "Simulation of shock wave propagation in single crystal and polycrystalline aluminum," *International Journal of Plasticity*, vol. 60, pp. 118–144, 2014.

[209] J. Lloyd, J. Clayton, R. Austin, and D. McDowell, "Plane wave simulation of elastic-viscoplastic single crystals," *Journal of the Mechanics and Physics of Solids*, vol. 69, pp. 14–32, 2014.

[210] A. Needleman, "A continuum model for void nucleation by inclusion debonding," *Journal of Applied Mechanics*, vol. 54, no. 3, pp. 525–531, 1987.

[211] C. Daraio, V. Nesterenko, E. Herbold, and S. Jin, "Strongly nonlinear waves in a chain of teflon beads," *Physical Review E*, vol. 72, no. 1, 2005.

[212] P. Kevrekidis, A. Vainchtein, M. S. Garcia, and C. Daraio, "Interaction of traveling waves with mass-with-mass defects within a hertzian chain," *Physical Review E*, vol. 87, no. 4, 2013.

[213] B. Deng, P. Wang, V. Tournat, and K. Bertoldi, "Nonlinear transition waves in free-standing bistable chains," *Journal of the Mechanics and Physics of Solids*, vol. 136, 2020.

[214] T. Shen, H. Song, M. An, and Y. Li, "Uncovering strengthening and softening mechanisms of nano-twinned cocrfecuni high entropy alloys by molecular dynamics simulation," *Journal of Applied Physics*, vol. 131, no. 9, 2022.

[215] J. Jiang, W. Sun, and N. Luo, "Molecular dynamics study of microscopic deformation mechanism and tensile properties in alxcocrfeni amorphous high-entropy alloys," *Materials Today Communications*, vol. 31, 2022.

[216] S. Elahi, R. Tavakoli, A. Boukellal, T. Isensee, I. Romero, and D. Tourret, "Multiscale simulation of powder-bed fusion processing of metallic alloys," *Computational Materials Science*, vol. 209, 2022.

[217] W. Yan, W. Huang, Q. Huang, J. Yang, G. Giunta, S. Belouettar, and H. Hu, "Data-driven multiscale method for composite plates," *Computational Mechanics*, vol. 70, pp. 1025–1040, 2022.

[218] S. Xiao, P. Deierling, S. Attarian, and A. El Tuhami, "Machine learning in multiscale modeling of spatially tailored materials with microstructure uncertainties," *Computers & Structures*, vol. 249, 2021.

[219] X. W. Zhou, M. E. Foster, and R. B. Sills, "An fe-ni-cr embedded atom method potential for austenitic and ferritic systems," *Journal of computational chemistry*, vol. 39, no. 29, pp. 2420–2431, 2018.

[220] C. Varvenne, G. P. M. Leyson, M. Ghazisaeidi, and W. A. Curtin, "Solute strengthening in random alloys," *Acta Materialia*, vol. 124, pp. 660–683, 2017.

[221] W.-R. Jian, Z. Xie, S. Xu, Y. Su, X. Yao, and I. J. Beyerlein, "Effects of lattice distortion and chemical short-range order on the mechanisms of deformation in medium entropy alloy cocrni," *Acta Materialia*, vol. 199, pp. 352–369, 2020.

[222] E. Antillon, C. Woodward, S. Rao, B. Akdim, and T. Parthasarathy, "Chemical short range order strengthening in a model fcc high entropy alloy," *Acta Materialia*, vol. 190, pp. 29–42, 2020.

[223] E. P. George, W. Curtin, and C. C. Tasan, "High entropy alloys: A focused review of mechanical properties and deformation mechanisms," *Acta Materialia*, vol. 188, pp. 435–474, 2020.

[224] S. Nag and W. A. Curtin, "Effect of solute-solute interactions on strengthening of random alloys from dilute to high entropy alloys," *Acta Materialia*, vol. 200, pp. 659–673, 2020.

[225] C. Varvenne, A. Luque, W. G. Nöhring, and W. A. Curtin, "Average-atom interatomic potential for random alloys," *Physical Review B*, vol. 93, no. 10, 2016.

[226] K. Chu, M. E. Foster, R. B. Sills, X. Zhou, T. Zhu, and D. L. McDowell, "Temperature and composition dependent screw dislocation mobility in austenitic stainless steels from

large-scale molecular dynamics," *npj Computational Materials*, vol. 6, no. 1, pp. 1–10, 2020.

[227] D. Farkas, "Deformation behavior of a model high entropy alloy from atomistic simulations," *Materials Science and Engineering: A*, vol. 812, 2021.

[228] J. Vaccari, "Standard wrought austenitic stainless-steels," *Materials Engineering*, vol. 80, no. 7, pp. 63–71, 1974.

[229] M. Finnis and J. Sinclair, "A simple empirical n-body potential for transition metals," *Philosophical Magazine A*, vol. 50, no. 1, pp. 45–55, 1984.

[230] V. Rosato, M. Guillope, and B. Legrand, "Thermodynamical and structural properties of fcc transition metals using a simple tight-binding model," *Philosophical Magazine A*, vol. 59, no. 2, pp. 321–336, 1989.

[231] A. Caro, D. Crowson, and M. Caro, "Classical many-body potential for concentrated alloys and the inversion of order in iron-chromium alloys," *Physical review letters*, vol. 95, no. 7, p. 075702, 2005.

[232] F. Apostol and Y. Mishin, "Interatomic potential for the al-cu system," *Physical Review B*, vol. 83, no. 5, 2011.

[233] G. P. Pun and Y. Mishin, "Embedded-atom potential for hcp and fcc cobalt," *Physical Review B*, vol. 86, no. 13, 2012.

[234] M. Čák, T. Hammerschmidt, J. Rogal, V. Vitek, and R. Drautz, "Analytic bond-order potentials for the bcc refractory metals nb, ta, mo and w," *Journal of Physics: Condensed Matter*, vol. 26, no. 19, 2014.

[235] J. Gehrmann, D. Pettifor, A. Kolmogorov, M. Reese, M. Mrovec, C. Elsässer, and R. Drautz, "Reduced tight-binding models for elemental si and n, and ordered binary si-n systems," *Physical Review B*, vol. 91, no. 5, 2015.

[236] E. B. Tadmor, F. Legoll, W. Kim, L. Dupuy, and R. E. Miller, "Finite-temperature quasi-continuum," *Applied Mechanics Reviews*, vol. 65, no. 1, 2013.

[237] R. Perera, D. Guzzetti, and V. Agrawal, "Graph neural networks for simulating crack coalescence and propagation in brittle materials," *Computer Methods in Applied Mechanics and Engineering*, vol. 395, p. 115021, 2022.

[238] A. Khoei and M. Kianezhad, "A machine learning-based atomistic-continuum multi-scale technique for modeling the mechanical behavior of ni3al," *International Journal of Mechanical Sciences*, vol. 239, p. 107858, 2023.

[239] K. Huang, *Statistical mechanics*. John Wiley & Sons, 2008.

[240] J. Lutsko, "Generalized expressions for the calculation of elastic constants by computer simulation," *Journal of Applied Physics*, vol. 65, no. 8, pp. 2991–2997, 1989.

[241] F. Bavaud, P. Choquard, and J.-R. Fontaine, "Statistical mechanics of elastic moduli," *Journal of Statistical Physics*, vol. 42, no. 3-4, pp. 621–646, 1986.

[242] J. R. Ray, M. C. Moody, and A. Rahman, "Calculation of elastic constants using isothermal molecular dynamics," *Physical Review B*, vol. 33, no. 2, pp. 895–899, 1986.

[243] J. R. Ray, "Elastic constants and statistical ensembles in molecular dynamics," *Computer Physics Reports*, vol. 8, no. 3, pp. 109–151, 1988.

[244] G. Gao, K. Van Workum, J. D. Schall, and J. A. Harrison, "Elastic constants of diamond from molecular dynamics simulations," *Journal of Physics: Condensed Matter*, vol. 18, no. 32, pp. 1737–1750, 2006.

[245] M. Wen, S. Whalen, R. S. Elliott, and E. B. Tadmor, "Interpolation effects in tabulated interatomic potentials," *Modelling and Simulation in Materials Science and Engineering*, vol. 23, no. 7, 2015.

[246] W. Cai, J. Li, and S. Yip, "1.09 molecular dynamics," *Comprehensive Nuclear Materials*, pp. 249–265, 2012.

Appendices

Appendix A

Additional Verification for the 1D Atomistic Framework

A.1 NVT ensemble

First, we perform constant temperature simulations for systems of 10,000 atoms using the Langevin thermostat which is designed to maintain a canonical ensemble. We can compute the microscopic temperature using the equipartition theorem [239]:

$$\sum_{n=1}^{N} KE = \sum_{n=1}^{N} \frac{1}{2} m v_i^2 = \frac{dim}{2} N k_B T. \tag{A.1}$$

In our case, $dim = 1$, N is the total number of atoms, and KE is the total kinetic energy of the group of atoms. We test the performance of the Langevin thermostat using all three potential functions (Lennard-Jones, modified Morse, and EAM) at temperatures ranging from 250 K - 1,250 K. Since the melting temperature of copper is 1,358 K, we do not perform simulations with higher input temperatures. The total run-time for each simulation is 3,000 ps with an equilibration time of 5 ps. In this case, standard periodic boundary conditions are enforced such that the leftmost atom interacts with the rightmost atom in the chain and vice versa. The results from these MD simulations can be seen in Fig. A.1.

For all three potential functions, the average temperatures oscillate around their corresponding initial input values for the entire run-time of 3,000 ps. However, we notice that the variance in the average temperature does increase with increasing input temperature. This effect occurs regardless of which potential function is used. Such a phenomenon makes physical sense because the frequency of oscillation of the particles in a solid increases as the temperature in the solid is raised. Additionally, we observe that at higher temperatures, the Langevin

thermostat equilibrates the system to the initial input temperature more slowly than at lower temperatures. This effect is seen for all three potential functions, and it is most prominent at an input temperature of 1,250 K. This is understandable as the Langevin thermostat is a local thermostat, and hence there is a lack of feedback between the target temperature and input temperature. From these results, it is apparent that we maintain an NVT ensemble for a wide range of input values.

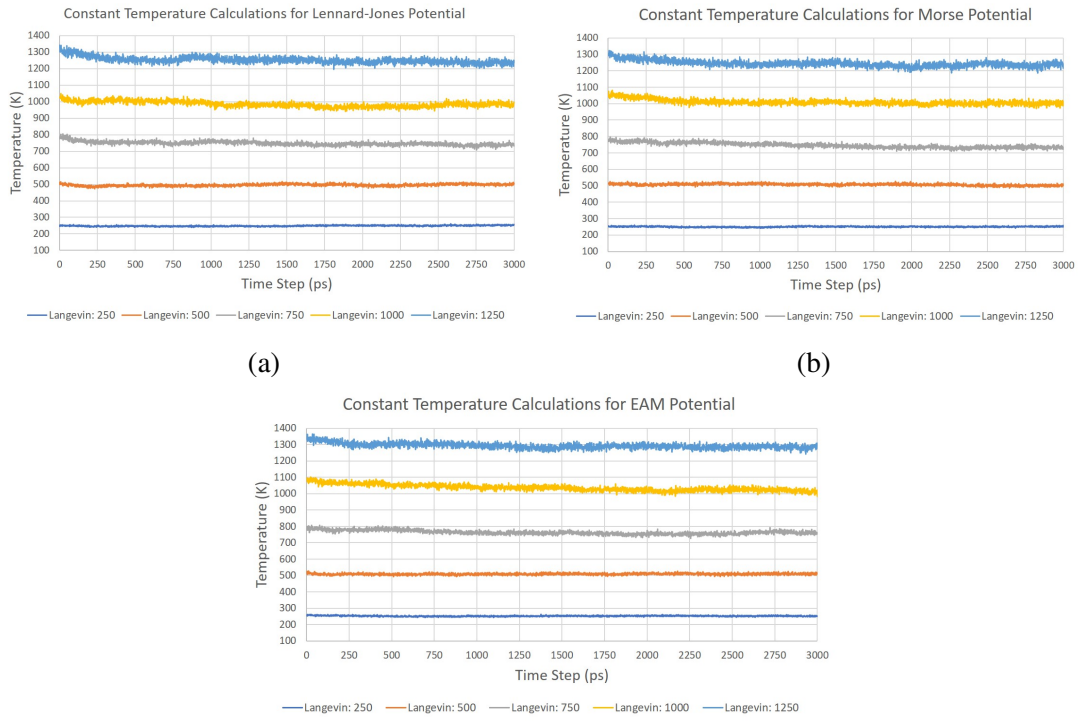

Figure A.1: Constant temperature NVT results with the 1D atomistic framework using (a) Lennard-Jones, (b) modified Morse and (c) EAM potentials.

A.2 Mechanical properties

Verification of the Lennard-Jones and modified Morse potentials is carried out by computing the tangent modulus of the system over a range of temperatures, while verification of the EAM potential is achieved by computing the cohesive energy and bulk modulus of the system at 0 K. In each case, we compare the simulated mechanical properties to their corresponding literature values for copper.

A.2.1 Lennard-Jones and Morse potentials

To compute the isothermal elastic modulus in 1D (tangent modulus), we utilize the microscopic elasticity tensor derived in [97]. The conventional expression for the microscopic elasticity tensor at a temperature *T* is given as follows [97]:

$$c_{ijkl} = \frac{1}{V}\left[2Nk_BT\left(\delta_{il}\delta_{jk} + \delta_{jl}\delta_{ik}\right) + \left\langle c^0_{ijkl}\right\rangle - \frac{V^2}{k_BT}Cov\left(\sigma^{inst}_{ij}, \sigma^{inst}_{kl}\right)\right] \tag{A.2}$$

where $\langle\cdot\rangle$ refers to a *phase* average, k_B is Boltzmann's Constant, *V* is the volume, and the covariance operator is defined by

$$Cov\left(A, B\right) \equiv \left\langle AB\right\rangle - \left\langle A\right\rangle\left\langle B\right\rangle. \tag{A.3}$$

Additionally, c^0_{ijkl} is defined as

$$c^0_{ijkl} = \frac{1}{V}\left[\frac{1}{4}\sum_{\alpha\neq\beta}\sum_{\gamma\neq\delta}\kappa^{\alpha\beta\gamma\delta}\frac{r^{\alpha\beta}_i r^{\alpha\beta}_j r^{\gamma\delta}_k r^{\gamma\delta}_l}{r^{\alpha\beta}r^{\gamma\delta}} - \frac{1}{2}\sum_{\alpha\neq\beta}\varphi^{\alpha\beta}\frac{r^{\alpha\beta}_i r^{\alpha\beta}_j r^{\alpha\beta}_k r^{\alpha\beta}_l}{\left(r^{\alpha\beta}\right)^3}\right] \tag{A.4}$$

where $\varphi^{\alpha\beta}$ is the interatomic force depending only on the distance $r^{\alpha\beta}$ between the atoms and $\kappa^{\alpha\beta\gamma\delta}$ is the *bond stiffness* defined by

$$\kappa^{\alpha\beta\gamma\delta} \equiv \frac{\partial\varphi^{\alpha\beta}}{\partial r^{\gamma\delta}} = \frac{\partial^2\Pi^{int}}{\partial r^{\alpha\beta}\partial r^{\gamma\delta}}. \tag{A.5}$$

This bond stiffness is interpreted for a simple pairwise potential, where the force on atom α due to atom β depends only on the distance $r^{\alpha\beta}$. Equation (A.2) can be further simplified by splitting the instantaneous stress terms into kinetic and potential parts as seen below:

$$\begin{aligned}\sigma^{K,inst}_{ij} &= -\frac{1}{V}\sum_{\alpha}\frac{p^\alpha_i p^\alpha_j}{m^\alpha}\\ \sigma^{V,inst}_{ij} &= \frac{1}{2V}\sum_{\alpha\neq\beta}\varphi^{\alpha\beta}\frac{r^{\alpha\beta}_i r^{\alpha\beta}_j}{r^{\alpha\beta}}.\end{aligned} \tag{A.6}$$

Substituting $\sigma^{inst} = \sigma^{K,inst} + \sigma^{V,inst}$ into the third term of Eq. (A.2) and noting that the cross-terms cancel,

$$\left\langle \sigma_{ij}^{K,inst} \sigma_{ij}^{V,inst} \right\rangle = \left\langle \sigma_{ij}^{K,inst} \right\rangle \left\langle \sigma_{ij}^{V,inst} \right\rangle \tag{A.7}$$

we get the following:

$$Cov\left(\sigma_{ij}^{inst}, \sigma_{kl}^{inst}\right) = Cov\left(\sigma_{ij}^{K,inst}, \sigma_{kl}^{K,inst}\right) + Cov\left(\sigma_{ij}^{V,inst}, \sigma_{kl}^{V,inst}\right). \tag{A.8}$$

Then, as shown in [97], the kinetic terms can be reduced as follows:

$$Cov\left(\sigma_{ij}^{K,inst}, \sigma_{kl}^{K,inst}\right) = \left(\delta_{ik}\delta_{jl} + \delta_{il}\delta_{jk}\right) N \left(k_B T\right)^2. \tag{A.9}$$

Substituting Eqs. (A.8) and (A.9) into Eq. (A.2), we get the simpler form of the elasticity tensor:

$$c_{ijkl} = \frac{1}{V}\left[\left\langle c_{ijkl}^0 \right\rangle - \frac{V^2}{k_B T} Cov\left(\sigma_{ij}^{V,inst}, \sigma_{kl}^{V,inst}\right) + N k_B T \left(\delta_{ik}\delta_{jl} + \delta_{il}\delta_{jk}\right)\right]. \tag{A.10}$$

Here, the first term is the elasticity at 0 K, the second term is the instantaneous potential energy, and the third term is the instantaneous kinetic energy. It is noted that the third term goes to zero as $T \to 0$ K. Additionally, [240] showed that the fluctuation term disappears as the stress and potential terms expand. In this case, $c = c^0$, where c^0 is given by Eq. (A.4). We note that the elastic constants associated with shear vanish in the thermodynamic limit, as shown in [241]. However, Eq. (A.10) still allows us to calculate the elastic constants of solids by replacing the phase averages with time averages.

The method just described to calculate the spatial elastic modulus is known as the stress fluctuation method [242, 243, 244]. We use this stress fluctuation method to calculate the microscopic elastic (tangent) modulus of a one-dimensional chain of atoms with constant length *L* and constant temperature *T*. For the 1D case, Eq. (A.10) reduces to the following [245]:

$$c = \frac{1}{L}\left[2N k_B T + L\left\langle c^0 \right\rangle - \frac{L^2}{k_B T} Cov\left(\sigma^{V,inst}, \sigma^{V,inst}\right)\right] \tag{A.11}$$

where *L* is the chain length, and "*Cov*" is the covariance operator given by Eq. (A.3). Then, the c^0 Born term in 1D is

$$c^0 = \frac{1}{L}\sum_{i=1}^{N}\sum_{j=i+1}^{N}\left[\varphi'(x_{ij})(x_{ij})^2 - \varphi(x_{ij})x_{ij}\right] \tag{A.12}$$

where $x_{ij} = x_j - x_i$. Finally, the potential part of the instantaneous stress in 1D is given as follows:

$$\sigma^{V,inst} = \frac{1}{L}\sum_{i=1}^{N}\sum_{j=i+1}^{N}\varphi(x_{ij})x_{ij}. \tag{A.13}$$

We compare the tangent modulus obtained from MD to the tangent modulus obtained from the Quasi-Harmonic (QH) approximation. The QH approximation for the temperature-dependent stress-free spatial tangent modulus of a one-dimensional chain of atoms is [97, 245]

$$c = r_0\left[\Pi''(r_0) + \frac{k_B T}{2}\frac{\Pi^{(4)}(r_0)\Pi''(r_0) - (\Pi'''(r_0))^2}{(\Pi''(r_0))^2}\right] \tag{A.14}$$

where $r_0 = r_0(T)$ is the stress-free equilibrium lattice constant at temperature *T*. In this case, the temperature dependence of the equilibrium lattice constant is obtained through the following equation [97]:

$$\Pi'(r_0) + \frac{k_B T}{2}\frac{\Pi'''(r_0)}{\Pi''(r_0)} = 0. \tag{A.15}$$

This requires calculation of third and fourth derivatives of the potential function Π, making calculations for EAM cumbersome. We use Eq. (A.14) to obtain the analytic tangent modulus values for the Lennard-Jones and modified Morse potentials.

We utilize Eq. (A.11) to calculate the microscopic tangent modulus of a one-dimensional chain of 10,000 Cu atoms using the Lennard-Jones and modified Morse potential functions. We test the performance of each of these potentials using the Langevin thermostat at various temperatures. For each of the input temperatures, we calculate the corresponding equilibrium lattice spacing using Eq. (A.15). Using these temperature-dependent lattice spacings, we can obtain the tangent modulus from MD simulations with Eq. (A.11) and compare this to the value obtained analytically with Eq. (A.14).

Plots showing the MD and analytic tangent modulus results can be seen in Fig. A.2. Here, we present the analytic tangent modulus values (blue line) for temperatures ranging from 0 - 900 K, but we limit the MD calculations for Lennard-Jones and Morse to 400 K and 450 K respectively. As shown in [245], the MD-derived tangent modulus of the system becomes non-physical for input temperatures above $\approx$ 450 K. The total run-time for each MD simulation is 3,000 ps with an equilibration time of 10 ps. As in section A.1, each atom is treated as a thermostat atom, and normal periodic boundary conditions are enforced such that the leftmost atom interacts with the rightmost atom and vice versa. In Fig. A.2, we observe that the calculated tangent modulus values from MD are in close agreement with the analytic values obtained from the QH approximation. This validates the implementation of Lennard-Jones and modified Morse potentials in the program.

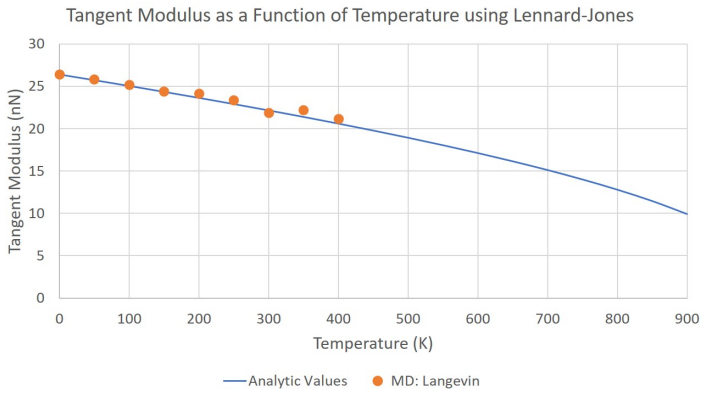

(a)

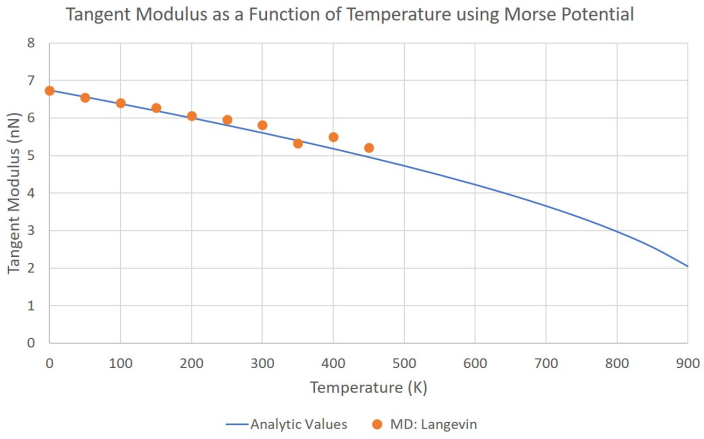

(b)

Figure A.2: Tangent modulus results for the Langevin thermostat using the (a) Lennard-Jones and (b) modified Morse potentials.

A.2.2 EAM potential

To verify the EAM potential, we calculate the cohesive energy E_0 as well as the bulk modulus B of the system at 0 K. The cutoff radius for the EAM potential is 5.507 Å, and we consider a periodic chain of 500 atoms where each atom is treated as a window (non-thermostat) atom. The experimental value of the equilibrium lattice spacing of Cu is 3.615 Å, so we vary the lattice constant from 3.605 Å to 3.625 Å in steps of 0.001 Å. The potential energy per atom as a function of the cubic lattice spacing is plotted in Fig. A.3, and the data can be fitted to a parabola.

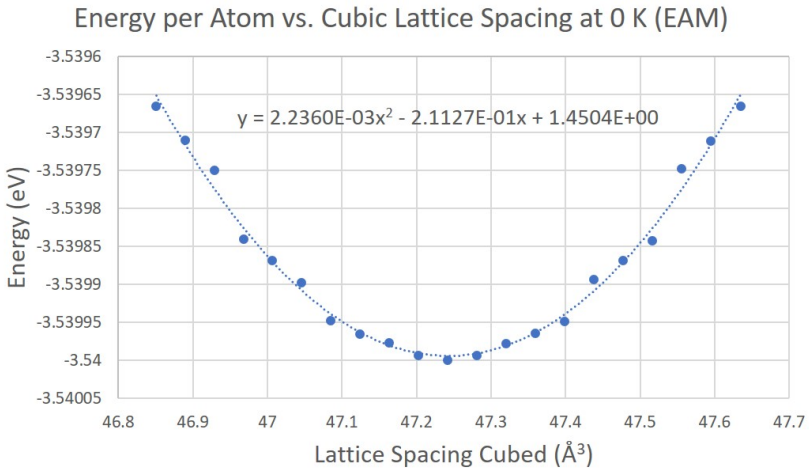

Figure A.3: Potential energy per atom vs. cubic lattice spacing in steps of 0.001 Å. Circles are data computed from the EAM potential, and the line is a parabola fitted to the data.

The minimum of this parabola corresponds to the cube of the equilibrium lattice spacing, $r_0 = 3.615$ Å. This matches the experimental data exactly because r_0 is one of the fitted parameters of the EAM potential. The energy per atom at r_0 is the cohesive energy, $E_{coh} =$ -3.540 eV, which is another fitted parameter [153]. Hence, our implementation of the EAM potential gives an accurate representation of the cohesive energy of Cu.

As discussed in [246], the curvature of the parabola at r_0 can be used to calculate the bulk modulus using

$$B(V) = V\left(\frac{\partial^2 E}{\partial V^2}\right)_{T,S} = 4(r_0)^3(2a) \tag{A.16}$$

where a is the parabola coefficient, and we multiply by four to account for every atom in the given lattice volume. Applying this equation to the data in Fig. A.3, we obtained a bulk modulus value of $B = 135.4$ GPa, which is not very accurate when compared to the literature value of 140 GPa [153]. To obtain a more accurate bulk modulus, we compute the $E(V)$ curve again in the range of $|r - r_0| < 10^{-4}$ Å. Specifically, we perform the calculations in steps of 0.0008 Å. This plot can be seen in Fig. A.4. The curvature of this new parabola at r_0 gives a bulk modulus value of $B = 140.6$ GPa, which is the fitted bulk modulus of this potential model.

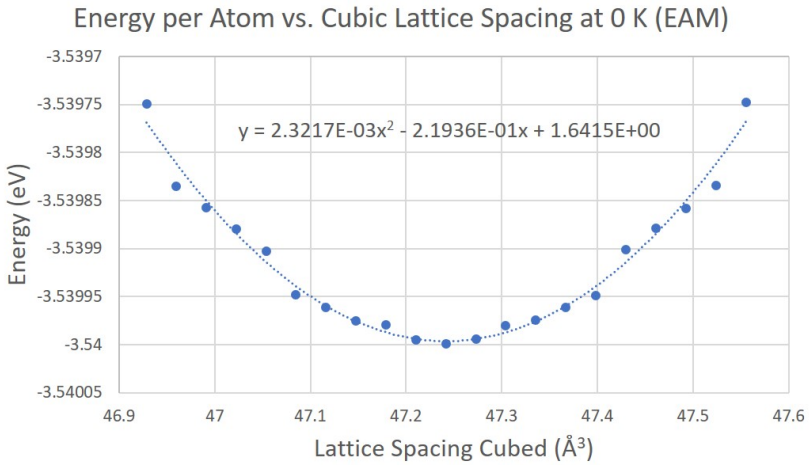

Figure A.4: Potential energy per atom vs. cubic lattice spacing in steps of 0.0008 Å. Circles are data computed from the EAM potential, and the line is a parabola fitted to the data.

Appendix B

Additional Verification for the 1D CAC Framework

B.1 Force vs. displacement tests

To ensure that the one-dimensional CAC framework achieves proper force matching at the A-C interfaces and thus does not produce any spurious wave phenomena, we perform force vs. displacement tests. This is accomplished by pulling the first particle in the chain very slowly at a constant rate and plotting the net force acting on it as a function of its absolute displacement over time. Specifically, we displace the particle at a rate of 1.6695×10^{-7} Å/ps for 10,000 ps. We perform these simulations using fine-scaled, coarse-scaled, and CAC domains with a total of 595 particles and lattice points in each system. Hence, the fine-scaled domain consists of 595 atoms, the coarse-scaled domain consists of 100 nodes with each element having a length of $6r_0$, and the CAC domain consists of an inner atomistic region containing 360 atoms and two outer continuum regions each containing 20 nodes. The results from these force vs. displacement studies can be seen in Fig. B.1.

We observe that the coarse-scaled and CAC domains produce slopes which are nearly identical to the slope obtained from the fine-scaled domain with relative errors of 0.0% and 0.84% respectively. We note that even smaller relative errors were achieved with larger domain sizes. This implies that the spring constant is approximately the same in all three frameworks. From these results, we conclude that the nodal integration and linear interpolation schemes used in our 1D CAC framework yield accurate forces on the individual particles. Therefore, Eq. (4.14) is implemented correctly, and our system does not produce any spurious phenomena

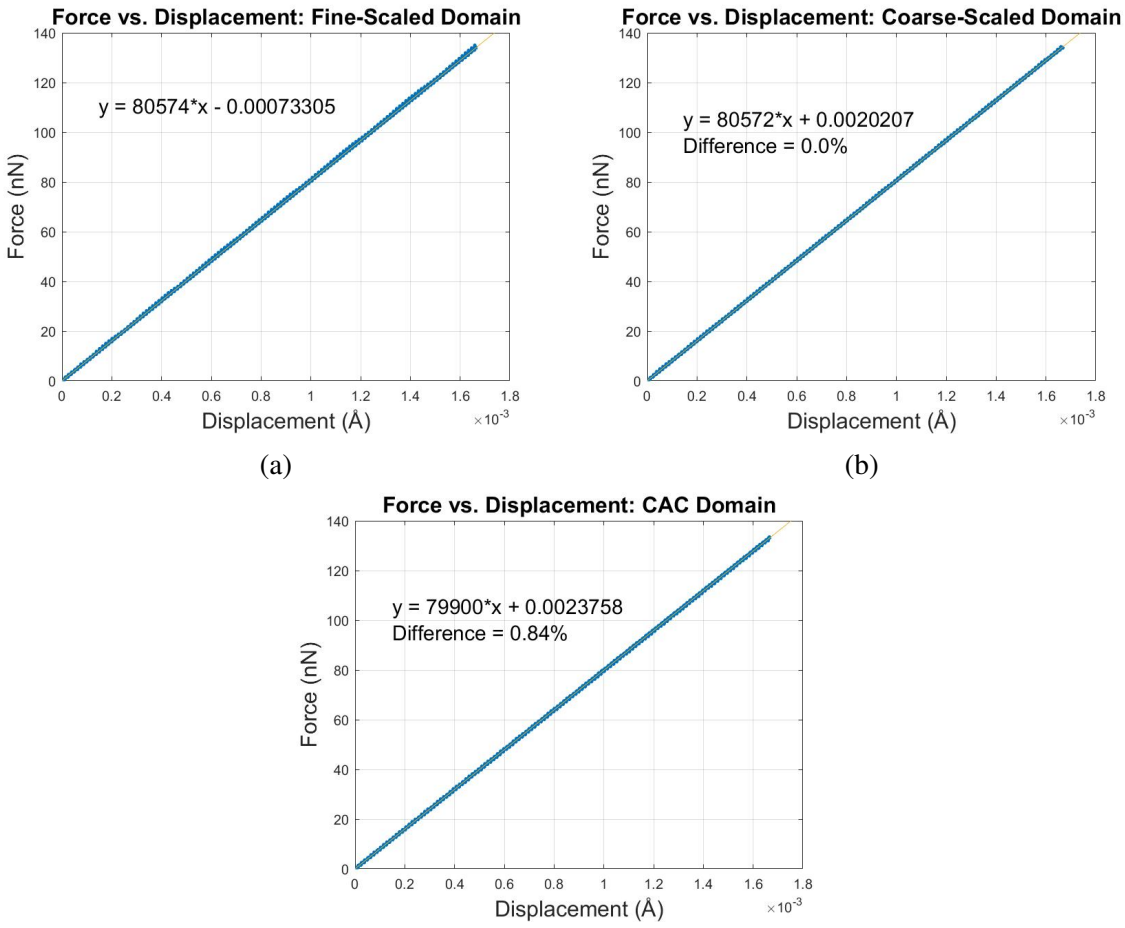

Figure B.1: Force vs. displacement test results for (a) fine-scaled, (b) coarse-scaled, and (c) CAC domains.

at the A-C boundaries. Additionally, the spring constant remains largely unchanged when transitioning from a fine-scaled domain to an equally-sized coarse-scaled or CAC domain.

B.2 Temperature equilibration tests

In this section, we verify that the CAC system from Fig. 4.2 can achieve the correct NVT ensemble in the undamped WR when the Langevin thermostat is applied to each TR. Specifically, we ensure that the temperature of the WR remains stable for various desired temperatures under equilibrium conditions. The input temperature θ_0 is specified, and the particles initially have random velocities such that the CAC domain contains the correct total energy for an equilibrium system at θ_0. Ideally, under equilibrium conditions, the system should achieve steady state with the appropriate equipartition of kinetic and potential energies. As with the 1D atomistic framework, each TR is at least the range of the forces, and the maximum damping parameter ζ_0 is one-half the Debye frequency ($\frac{1}{2}\omega_D$). Results for the temperature equilibration studies can be seen in Fig. B.2.

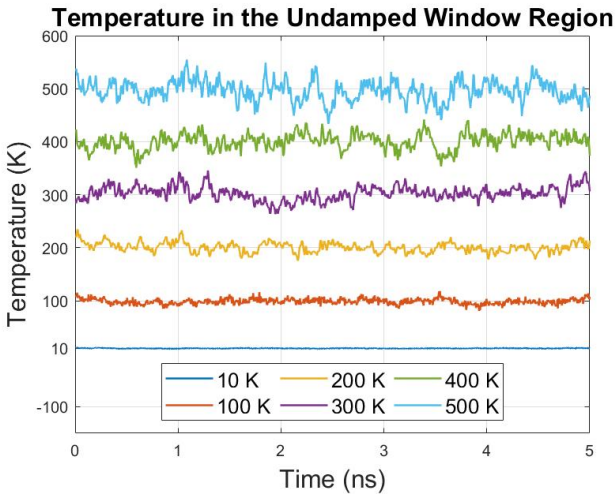

Figure B.2: Temperature in the undamped WR vs. time. Here, the *Langevin* thermostat is applied to the TRs for the following input temperatures: 10 K, 100 K, 200 K, 300 K, 400 K, and 500 K.

For each of these simulations, the CAC domain contains a total of 1,000 particles with 100 nodes in each coarse-scaled TR, 50 atoms in each fine-scaled TR, and 700 atoms in the WR. We then evolve the system for 5 ns and calculate the temperature of the undamped WR at each time step using the equipartition theorem. The temperature in each TR remains steady

at the input temperature θ_0 and thus acts as a constant-temperature reservoir. In Fig. B.2, we plot the temperature in the WR vs. time for the following input values: 10 K, 100 K, 200 K, 300 K, 400 K, and 500 K. In each case, we observe the temperature stabilize after a short time and achieve a steady state around the respective input temperature. We note that the variance in the temperature increases with larger input values because the particles oscillate more rapidly at higher temperatures. This effect can also be seen in Table B.1 which shows the time-average temperature and its corresponding standard deviation in the WR for each simulation. These results confirm that when an input temperature θ_0 is applied to each TR, the undamped WR maintains an equilibrium steady state around this value.

Table B.1: Time-average temperature in the WR and its associated standard deviation for various input temperatures θ_0 applied to each TR.

θ_0 (K)	$\langle\theta\rangle$	$\langle\delta\theta\rangle$
10	10.19	0.52
100	98.64	5.37
200	200.65	11.24
300	302.72	16.52
400	400.66	19.35
500	496.39	24.56

Appendix C

Additional Verification for the 2D CAC Framework

In this section, we present results from additional studies which verify that the two-dimensional CAC framework functions correctly.

C.0.1 Temperature equilibration

First, we verify that the two-dimensional CAC framework used in the shock wave simulations (Fig. 7.6) can achieve the correct canonical ensemble in the undamped WR when the Langevin thermostat is applied to each TR. In particular, we demonstrate that the system equilibrates to the proper steady-state value over long simulation times for a range of input temperatures. The initial random velocities of the particles are such that the system has the correct total energy for a given temperature θ_0. Furthermore, we ensure that each TR has a length which is at least equal to the force range of the interatomic potential, and we set the damping parameter ζ equal to one-half the Debye frequency of the material ($\frac{1}{2}\omega_D$). These specifications are based off results from previous multiscale studies which used CADD [78] as well as CAC [2] to characterize the domain. The temperature equilibration results for both Cu and Al can be seen in Fig. C.1.

The domain size for these simulations is as follows: 200 total columns (100 in the atomistic region and 50 in each continuum region) and 40 total rows. Within the fine-scaled region, there are 5 columns in each TR and hence 90 columns in the undamped WR. Each simulation is performed for 1 ns, and the temperature in the WR is obtained at every time step using the equipartition theorem. For the two-dimensional CAC framework, the maximum temperature

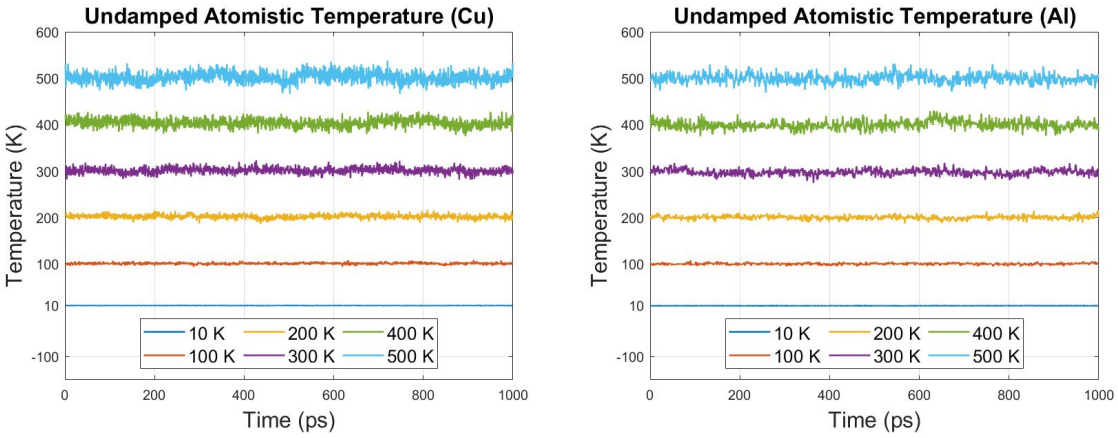

(a) (b)

Figure C.1: Temperature in the undamped atomistic region of the 2D CAC framework vs. time using the $Morse$ potential for both (a) Cu and (b) Al. The $Langevin$ thermostat is applied to the TRs for the following input temperatures: 10 K, 100 K, 200 K, 300 K, 400 K, and 500 K.

obtained from shock loading is $\sim$ 450 K, so we perform analysis for the following input temperatures: 10 K, 100 K, 200 K, 300 K, 400 K, and 500 K. In Fig. C.1, we observe that in each simulation, the temperature achieves a steady state around its mean value with very little deviation. Hence, this confirms the implementation of the framework from Fig. 7.6 and shows that the WR can maintain the correct equilibrium temperature during long runtimes with both materials.

C.0.2 Stress-strain relations

Next, we identify the elastic zone of the framework and ensure that the yield strength between a purely atomistic domain and equally-sized CAC domain is comparable. This is done to establish that the CAC force calculations are accurate as well as provide a range of input strains for the shock equations. Specifically, we compress the grid uniaxially along the x-direction ([112] lattice orientation) with strains ranging from 0.01 - 0.2 and calculate the virial stress of the domain for each input strain using the following expression [97]:

$$\sigma_{kl} = \frac{1}{A}\left\langle -\sum_{\alpha} m^{\alpha}\left(\dot{u}_k^{\alpha} - \bar{\dot{u}}_k\right)\left(\dot{u}_l^{\alpha} - \bar{\dot{u}}_l\right) + \frac{1}{2}\sum_{\substack{\alpha,\beta \\ (\alpha\neq\beta)}} \varphi^{\alpha\beta}\frac{r_k^{\alpha\beta} r_l^{\alpha\beta}}{r^{\alpha\beta}}\right\rangle. \tag{C.1}$$

In Eq. (C.1), $\boldsymbol{\sigma}$ is the virial (thermodynamic) stress, A is the area of the grid, m^{α} is the mass of particle α, $\dot{u}_k^{\alpha}$ is the velocity in the k^{th} direction of particle α, $\bar{\dot{u}}_k$ is the average velocity in the k^{th} direction of all particles in the given area, $\varphi^{\alpha\beta}$ is the first derivative of the potential energy at a distance $r^{\alpha\beta}$ between particles α and β ($\varphi^{\alpha\beta} = \frac{\partial \Pi}{\partial r^{\alpha\beta}}$), and $r_k^{\alpha\beta}$ is the distance in the k^{th} direction between particles α and β. Since we consider uniaxial compressive strains for the shock simulations, we only calculate the longitudinal stress ($\sigma_{kk} = \sigma_{xx}$) in this section and do not perform any tensile tests. The stress vs. strain results for both Cu and Al at 450 K can be seen in Fig C.2.

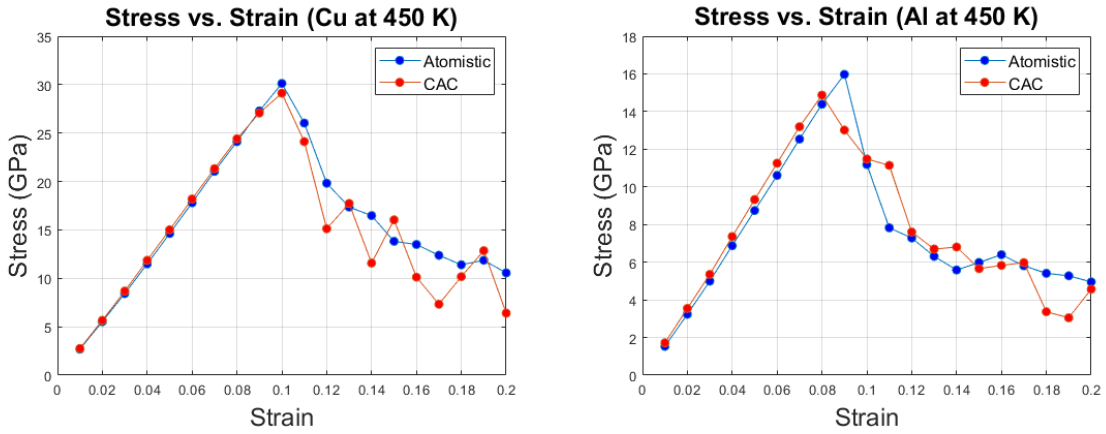

(a) (b)

Figure C.2: Virial stress of the domain as a function of strain for both (a) Cu and (b) Al. Simulations were performed for both a purely atomistic (blue) and CAC (red) framework. In each case, the system is equilibrated to 450 K, and the compression is applied uniaxially along the x-direction.

For each atomistic simulation, the domain contains 100 columns and 20 rows, and the runtime is 100 ps with an equilibration time of 50 ps. The parameters for the CAC simulations are the same, but the lattice described in Sec. 7.1.2 (with damped atoms) is utilized instead of the fully atomistic grid. Since 450 K is the highest temperature achieved in the shock simulations, we specifically wanted to identify the yield point at this extreme temperature to inform our shock calculations. In Fig. C.2, we observe that the linear elastic region of the CAC framework is nearly identical to that of the atomistic framework for both Cu and Al with yielding occurring at compressive strains of approximately 10% and 9% respectively. After this point, dislocations begin appearing throughout the lattice in both the coarse-scaled and fine-scaled

regions, so we maintain compressive strains $\leq 9\%$ for Cu and $\leq 8\%$ for Al when using the Hugoniot and Eulerian shock equations. We note that experimental HEL values for Cu and Al are on the order of 10s to 100s of MPa largely due to pre-existing defects present in bulk metals. Since homogeneously nucleating a dislocation in a perfect crystal is much harder than moving a dislocation which already exists in the microstructure, it makes sense that the HEL values observed in the present work are higher than those obtained experimentally.

These results confirm the validity of the CAC force calculations, and they are also congruent with results from previous CAC studies [117].

C.0.3 Young's modulus

Finally, we compare the Young's modulus of equally-sized atomistic and CAC frameworks for both Cu and Al over temperatures ranging from 10 K to 500 K. Young's modulus represents the slope of the linear portion of the stress-strain curve, and it generally decreases with increasing temperature as the particles in the material oscillate faster [245]. Therefore, we perform this study to supplement the results from C.0.2 and thus confirm that the CAC framework functions properly in the elastic regime at various temperatures. To calculate Young's modulus for the atomistic domain, we use the 2D elasticity tensor equation [97]:

$$C_{klmn} = \frac{1}{A}\left[Nk_B\theta\left(\delta_{km}\delta_{ln} + \delta_{kn}\delta_{lm}\right) + A\left\langle C^0_{klmn}\right\rangle - \frac{A^2}{k_BT}\mathrm{Cov}\left(\sigma^{V,inst}_{kl}, \sigma^{V,inst}_{mn}\right)\right]. \quad \text{(C.2)}$$

Here, A is the area of the grid, N is the total number of particles, θ is the temperature, and 'Cov' is the covariance operator defined by

$$\mathrm{Cov}\left(A, B\right) \equiv \left\langle AB\right\rangle - \left\langle A\right\rangle\left\langle B\right\rangle \quad \text{(C.3)}$$

where $\langle\cdot\rangle$ is a phase average (time average in our case). Since we only consider uniaxial compressive strain along the x-direction in the present work, we can obtain Young's modulus by

calculating C_{1111} as follows:

$$C_{1111} = \frac{1}{A}\left[2Nk_B\theta + A\left\langle C^0_{1111}\right\rangle - \frac{A^2}{k_BT}\mathrm{Cov}\left(\sigma^{V,inst}_{11}, \sigma^{V,inst}_{11}\right)\right] \tag{C.4}$$

where we understand that $1 = x$ here. In Eq. (C.4), $\sigma^{V,inst}_{11}$ is merely the second part of Eq. (C.1):

$$\sigma^{V,inst}_{11} = \frac{1}{2A}\sum_{\substack{\alpha,\beta \\ (\alpha\neq\beta)}} \varphi^{\alpha\beta}\frac{\left(r^{\alpha\beta}_1\right)^2}{r^{\alpha\beta}} \tag{C.5}$$

and C^0_{1111} is given as follows:

$$C^0_{1111} = \frac{1}{A}\left[\frac{1}{2}\sum_{\substack{\alpha,\beta \\ (\alpha\neq\beta)}} \frac{\partial\varphi^{\alpha\beta}}{\partial r^{\alpha\beta}}\frac{\left(r^{\alpha\beta}_1\right)^4}{\left(r^{\alpha\beta}\right)^2} - \frac{1}{2}\sum_{\substack{\alpha,\beta \\ (\alpha\neq\beta)}} \varphi^{\alpha\beta}\frac{\left(r^{\alpha\beta}_1\right)^4}{\left(r^{\alpha\beta}\right)^3}\right]. \tag{C.6}$$

Here again, $\varphi^{\alpha\beta} = \frac{\partial\Pi}{\partial r^{\alpha\beta}}$, and $r^{\alpha\beta}$ is the distance between two particles α and β. Results from the Young's modulus studies can be seen in Fig. C.3.

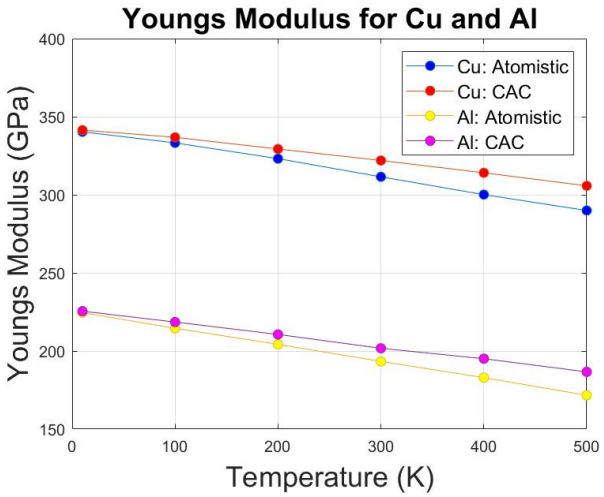

Figure C.3: Young's modulus vs. temperature for both Cu and Al. For each material, simulations were performed using both a fully atomistic domain as well as a CAC domain.

In Fig. C.3, we have shown the atomistic Young's modulus obtained from Eq. (C.4) as well as the CAC Young's modulus obtained from the slope of the stress-strain curves for both Cu and Al. The domain sizes are the same as those described in C.0.2. In this figure, we again observe the coherency between the two formulations because the Young's modulus of the CAC

framework is nearly the same as the Young's modulus of the atomistic framework over the full range of temperatures. As expected, we see more agreement at low temperatures than at higher temperatures where the vibration of particles introduces slightly more error. However, even at the upper end of 500 K, the largest difference is $\sim 5\%$ which is small considering the approximations inherent in the CAC finite element formulation. Hence, from each of these verification studies, we can conclude that the CAC framework is implemented correctly and can accurately represent the temperature and material parameters of an equally-sized atomistic grid.

Appendix D

Unsolicited Advice to Future Engineering Students

Here, I consider some of the lessons I learned while pursuing my PhD and reflect on how the struggles inherent in such an endeavor influenced my overall outlook on life. Hopefully, these musings will be beneficial to future students who are interested in obtaining a PhD in a STEM field.

1. **Have perseverance and a long time horizon**

   Obtaining a PhD in any science or engineering field, while ultimately fulfilling in the long run, is a prolonged and arduous task. Depending on the discipline, it will typically take between 4 and 7 years to complete your degree after 4 years of undergrad. Therefore, if you are a senior about to finish high school, plan on spending another 8 - 11 years in school before starting your career in the "real world." During this time, you will take very demanding classes that push the limits of your analytical ability and require many weekends devoted to studying rather than hanging out with friends or family. In addition, you are expected to perform innovative and publishable research while getting paid $\frac{1}{3}$ to $\frac{1}{4}$ of what you could be making with an industry job. However, throughout this process, you will also learn a tremendous amount, meet incredibly smart people at the top of your field, make life-long contacts through conferences and internships, publish new and exciting research, and become an expert in a particular topic in science. Thus, while I do believe the payout is worth it, achieving a PhD is a strenuous journey that requires you to cultivate immense perseverance and set aside short-term pleasures for long-term gain.

2. **Be passionate and have a purpose**

Along these same lines, you must be extremely diligent and passionate about your work as well as have your mind focused on your purpose for pursuing scientific research in order to complete a PhD. Talk to any doctoral student, and they will most likely tell you that the hardest part about a PhD is not the research per se but the mental and psychological fortitude required for the research. There will be many times when you have been working on a simulation or experiment for months, a deadline set by your advisor is coming up in a few weeks, and you are up at 3 a.m. with no new results and a faulty framework. Then, you will look on social media and see your peers from college starting new jobs, buying houses, taking the weekends off, and seemingly living "the good life." These moments will test you psychologically, and it is during these stressful times that you will be tempted to throw in the towel. In fact, many students do just this as evidenced by the fact that only 50% of people who begin a doctoral program actually finish it. Therefore, you must find a research topic that interests you and ignites your passion, and you must constantly remind yourself of the reasons for choosing this path. If you can do that, you will not only be successful in your PhD, but you will also develop enough psychological stamina to weather future stress points in your career and life.

3. **Develop a plan but be flexible**

During the first semester of grad school, my advisor and I decided on a topic for my PhD research and developed a road map for achieving these goals over the next few years. This was a crucial step as it organized my thinking and has continued to guide me in my work even as I near the end of my doctoral research. However, I can safely say that while the main objectives of that plan have stayed constant, there have been many twists and turns along the way. Big ideas that I had when I started have been scraped entirely because upon further study, they were either impossible to accomplish or so overly complex that they would require many more years of intense research past the 4-7 years of a PhD. In fact, I worked on one side project for an entire year that, while it produced some interesting results, could not accomplish what I had hoped for initially. Conversely, I have worked on other projects that I did not even consider in the initial road map such

as performing higher-dimensional shock simulations within a multiscale framework. All that to say, develop a long-term strategy and have the discipline to stick to it but also know that your research will evolve over time so be in constant communication with your advisor about your changing goals and perspectives.

4. **Pick the right advisor**

   I cannot emphasize enough how important it is to pick the right PhD advisor as this one action will determine whether your graduate school experience is pleasant and memorable or dreadful and emotionally scarring. I have been very lucky and blessed to have the same advisor throughout my entire PhD who I work very well with and whose research goals are closely aligned with mine. However, I have talked with several doctoral graduates who did not have such an advisor, and the stories they tell sound terrible. The reason your advisor can make or break your success as a PhD student is because he is not only your boss and the person through whom you typically receive funding, but he is also your closest "colleague" for potentially 7 years and the main person who helps you actualize your work. Therefore, when choosing a PhD advisor, consider a few things: (1) Does this person have funding for me, or will I have to find funding through an outside source? (2) Do I want an advisor who is very hands-on and guides me every step of the way, or do I want an advisor who is rather hands-off and expects me to figure out most things myself? (3) Do I share common research and career goals with this person, or do we have different visions? (4) Do I want to be a member of a big lab where many people work on the same project, or do I primarily want to work by myself? (5) Do I want an advisor who expects me to work on one particular project and nothing else, or do I want an advisor who has a more exploratory attitude towards research? If you can find an advisor who you get along with and whose work style matches yours, your PhD experience will be a little less painful.

5. **Dream big but be realistic**

   It's very important to set your goals and expectations high in order to stay motivated during the often laborious tenure of a PhD. However, also realize that scientific research

is hard, and you should celebrate every little accomplishment in your work. Focus on making small, incremental advances to your field and don't worry if you don't make some revolutionary new discovery in science. We're constantly told stories of people like Isaac Newton, Nikola Tesla, Albert Einstein, Richard Feynman, and Stephen Hawking who had already changed our view of reality by the time they were 30. I made the mistake of idolizing people like this when I first began studying physics in college, and I used them as the standard for what constitutes success in research. However, these men were the top 0.01% and possessed nearly inhuman levels of analytical ability and general intelligence. Most of us will never reach the levels of greatness that they did, but that is perfectly okay because science also advances through the everyday mathematics, experiments, and simulations done by millions of people across the world. So, view your PhD as participating in a small part of this grand symphony of scientific research, and you will enjoy it much more.

6. **Remain humble about what you can achieve**

   Going off the previous point, humility is potentially the most important virtue to cultivate while engaged in PhD research. Without a humble spirit, you will greatly overestimate your abilities, have overly-ambitious objectives, and set yourself up for failure. Thus, before beginning graduate school, write down a list of challenging, but realistic, goals that you would like to achieve during your tenure as a doctoral student. Some of mine were as follows: (1) Study hard in all of my classes and try to maintain a 4.0 GPa. (2) Pick a good advisor my first semester who shares my research interests. (3) Apply for multiple fellowships in an attempt to obtain independent funding for my work. (4) Take my Qualifying and Candidacy exams early enough so that I can focus on research. (5) Defend a Master's thesis as preparation for the final PhD defense. (6) Publish 2-3 research articles in highly-reputable journals. (7) Attend multiple conferences each year to practice my public speaking skills and network with other scientists. (8) Participate in at least one summer internship to expand my research and make contacts at a national lab. (9) Become very knowledgeable about an area of science/engineering that interests

me. (10) Make valuable friends and lifelong connections. Your individual goals may be different, but as long as you remain humble, your graduate school experience will be very memorable and profitable.

7. **Create a daily schedule**

   The life of a PhD student is very open-ended and can thus often feel unstructured. The positive aspect of this is that you get to work at your own pace and pursue research avenues that you find interesting and important. The downside is that you may think that you *always* need to be working, and you can feel guilty when taking any time off. Therefore, it is important to develop a daily schedule that keeps you grounded and do your best to stick to that schedule. This will help you not only be more efficient in your research but will also prevent you from neglecting other important parts of your life such as family, friends, and personal health. I'll provide a few suggestions here. First, try to wake up and go to sleep at the same time every day even if you don't technically need to. Next, set aside specific hours in the day to pursue your research and really endeavor to stay within those bounds. Finally, when you're not working, either pursue a hobby, workout, or spend time with friends and family to allow your brain to relax and recharge. I myself have struggled with sticking to a schedule while in graduate school, but the times that I have been consistent with my schedule are typically the times when I feel the most effective and peaceful.

8. **Make connections with professional scientists and engineers**

   One of the many benefits of pursuing a PhD in a STEM field is the fact that you will be surrounded by extremely intelligent people who you would not ordinarily encounter in your everyday life. Although you may think that your particular research is extremely specialized and niche, you would be surprised at how many other people are working on similar topics around the globe. When I entered graduate school, I thought that nobody would care about my research, but as I've advanced in my studies, I've talked and worked with many people who have similar research interests. Therefore, it's very important to take advantage of networking with as many people in your field as you can during your

PhD. This can occur through a variety of avenues including internships, conferences, seminars, and on-campus recruitment events. Furthermore, try to meet people who have a career path that you would like to emulate. For example, if you want to work at a national lab after you graduate, seek out people at these labs who are working on projects that align with your expertise and just strike up a conversation through email. You can also ask your advisor to introduce you to them if you feel uncomfortable emailing someone directly like that. Many times, researchers at these facilities enjoy discussing their work with graduate students, and they can help boost your odds of finding a postdoc position.

9. **Keep your personal health a priority**

   This is a point that regularly gets overlooked by individuals, not only in graduate school, but as they pursue their career and life goals in general. We can so often get bogged down in the everyday struggles of work and family that we forget to take care of ourselves both physically and mentally. For example, my work is exclusively computational, so I can find myself sitting at a desk in front of a computer screen for hours on-end each day. While a relatively comfortable lifestyle, this type of work can nevertheless have detrimental effects on the body and mind if not coupled with regular exercise and a temperate diet. Therefore, I have cultivated a routine where each morning before I start work, I go to the gym and either lift weights or take a long run for an hour or so. I have discovered that this time away from work is definitely worth it because I feel so much more productive on the days when I workout as opposed to the days when I cannot. Furthermore, I try to maintain a moderate diet where I eat mostly high-protein foods along with fruits and vegetables, but I also allow myself to enjoy occasional nights out on the weekends. Finally, scientific research can be mentally draining, so I try to take active steps to maintain my mental health through the toils of graduate school as well.

10. **Enjoy the journey**

    During my junior year at Samford when I was talking to one of my professors about whether to get a Master's or a PhD after undergrad, he said, "Get a PhD. It will be very difficult, but it will also open up many opportunities that you can't even imagine right

now. I've never regretted getting my PhD. I wouldn't go back and do it again, but I'm glad I did it." This was some of the best advice I have ever received, and at this point in my career, I'm so glad my 21-year-old self followed it. Pursuing a PhD has been, by far, the most challenging thing I have ever done in my life, but it has also been the most rewarding. I have learned so much, met so many amazing people, and undergone many incredible experiences which have helped to boost my confidence in research and shape my scientific understanding as a whole. Furthermore, I have had numerous career doors open up that I know would not have been attainable without a PhD. Therefore, if you're a good student, like scientific research, and are on the fence about pursuing a PhD, I would say do it. You won't come back later in life and get a PhD because life obligations (money, family, job, etc.) become too pressing, so do it while you're young when you are already accustomed to the academic lifestyle and have very few responsibilities. It's essentially a once-in-a-lifetime opportunity that can expose you to many amazing life paths. The PhD is a roller coaster ride that is often arduous and stressful but also extremely rewarding in the end. So, my last piece of advice would just be to have a positive attitude throughout the whole experience and enjoy the journey.

Obtaining a PhD in aerospace engineering has been the greatest professional accomplishment of my life thus far, and I am so grateful for being given the opportunity to work under Dr. Agrawal at Auburn over these past six years. He has been an incredible mentor, and I cannot thank him enough for seeing the potential in me and always encouraging me to seek out the next interesting idea in science. The skills I have learned while pursuing this degree have given me the confidence to know that wherever my engineering career takes me, I will be able to excel and make meaningful contributions. Finally, none of my studies of the physical world would have been possible without the Incarnate Logos, through Whom natural processes originate and are thus made intelligible to the human mind. Therefore, I will conclude this dissertation with my favorite Scripture verse – the one which arguably got me through graduate school, and the one which I always remember when I am feeling doubtful or hopeless:

"Have I not commanded you? Be strong and courageous. Do not be frightened and do not be dismayed, for the LORD your God is with you wherever you go." – Joshua 1:9